



REFERENCE ONLY

UNIVERSITY OF LONDON THESIS

Degree *phd*

Year *2005*

Name of Author *ETT WESLEY U-T*

COPYRIGHT

This is a thesis accepted for a Higher Degree of the University of London. It is an unpublished typescript and the copyright is held by the author. All persons consulting the thesis must read and abide by the Copyright Declaration below.

COPYRIGHT DECLARATION

I recognise that the copyright of the above-described thesis rests with the author and that no quotation from it or information derived from it may be published without the prior written consent of the author.

LOANS

Theses may not be lent to individuals, but the Senate House Library may lend a copy to approved libraries within the United Kingdom, for consultation solely on the premises of those libraries. Application should be made to: Inter-Library Loans, Senate House Library, Senate House, Malet Street, London WC1E 7HU.

REPRODUCTION

University of London theses may not be reproduced without explicit written permission from the Senate House Library. Enquiries should be addressed to the Theses Section of the Library. Regulations concerning reproduction vary according to the date of acceptance of the thesis and are listed below as guidelines.

- A. Before 1962. Permission granted only upon the prior written consent of the author. (The Senate House Library will provide addresses where possible).
- B. 1962 - 1974. In many cases the author has agreed to permit copying upon completion of a Copyright Declaration.
- C. 1975 - 1988. Most theses may be copied upon completion of a Copyright Declaration.
- D. 1989 onwards. Most theses may be copied.

This thesis comes within category D.

This copy has been deposited in the Library of *UCL*

This copy has been deposited in the Senate House Library, Senate House, Malet Street, London WC1E 7HU.

**THE EFFECTIVE MOISTURE HISTORY OF THE AMAZON
BASIN FOR THE LAST 40,000 YEARS, RECONSTRUCTED
FROM ODP SITE 942 ON THE AMAZON FAN**

VIRGINIA JANE ETTWEIN

**A THESIS SUBMITTED FOR THE DEGREE OF
DOCTOR OF PHILOSOPHY**

UNIVERSITY COLLEGE LONDON

MARCH 2005

UMI Number: U591976

All rights reserved

INFORMATION TO ALL USERS

The quality of this reproduction is dependent upon the quality of the copy submitted.

In the unlikely event that the author did not send a complete manuscript and there are missing pages, these will be noted. Also, if material had to be removed, a note will indicate the deletion.



UMI U591976

Published by ProQuest LLC 2013. Copyright in the Dissertation held by the Author.
Microform Edition © ProQuest LLC.

All rights reserved. This work is protected against
unauthorized copying under Title 17, United States Code.



ProQuest LLC
789 East Eisenhower Parkway
P.O. Box 1346
Ann Arbor, MI 48106-1346

This Ph.D. thesis is dedicated to:

Barnaby Jonathan Ettwein

and

Holly Bojangles Ettwein

(1985-2004)

ABSTRACT

The Amazon Basin is the site of the Earth's largest land-based atmospheric convection centre, and acts as a large source of latent heat release, particularly during the summer months when the South American Summer Monsoon (SASM) is most developed. Convectonal rainfall over the Amazon Basin therefore plays a fundamental role in the transport of heat to the higher latitudes, and the regulation of global climate. The Pleistocene moisture history of the Amazon Basin is comparatively poorly known. However, sediments from the Amazon Fan have the potential to record a basin-wide average of past changes in the effective moisture of the Amazon Basin within single, continuous sequences, which accumulate rapidly.

Oxygen isotopes ($\delta^{18}\text{O}$) records were measured for five planktonic foraminifera species from ODP Site 942 on the Amazon Fan. Data were constrained by an age model constructed around 36 AMS radiocarbon dates, which were converted to calibrated calendar ages. Past changes in the outflow of the Amazon River were reconstructed by attempting to isolate the relative shift in $\delta^{18}\text{O}_{942}$ brought about by freshwater-driven changes in salinity in the surface water over the Site. $\delta^{18}\text{O}_{942}$ records were adjusted for fractionation effects associated with changes in global ice volume, however removing the sea surface temperature (SST) effect was more problematic.

$\Delta\delta^{18}\text{O}_{942}$ data implied that the Amazon Basin was more arid during the glacial stage relative to the Holocene. Co-variance with November-December insolation at 10°S implied that this was associated with insolation-driven variations in the intensity of the SASM. Particularly high-resolution records were measured for the last glacial-interglacial transition. Maximum aridity was reconstructed around the onset of the Younger Dryas (YD) in the Northern Hemisphere, after which effective moisture levels exhibited an increasing trend thereafter throughout the period, correlating with a warming trend in Antarctica. A similarity between the $\Delta\delta^{18}\text{O}_{942}$ data and the Vostock ice core temperature record (δD) suggests a possible Antarctic forcing over the climate of the Amazon Basin. It was hypothesised that Northern and Southern hemisphere temperature gradients exert independent control over the northerly and southerly limits of SASM convection over the Amazon Basin.

An isotopic balancing model was used to attempt to semi-quantify the Amazon River outflow. Assuming a SST cooling of 2 to 3°C , the Amazon River outflow was modelled to have been reduced by up to ~30-50% at the YD onset, and by up to ~20-30% during the Last Glacial Maximum. However semi-quantified reconstructions are limited by the assumptions of the model.

ACKNOWLEDGEMENTS

I would like to thank Mark Maslin, for supervising my PhD and for all his help and support over the years, and also my unofficial mentors Steve Burns and Tom Guilderson who gave me lots of help and endless encouragement with the research. Isotope data was measured with the help of Steve Burns (UMass) and Melanie Leng (NIGL). I would like to extend a special thankyou to Connie Weyhenmeyer (CAMS/ LLNL) for not only offering to measure some of my AMS dates, but also spending extra time sitting on the accelerator to minimise the errors.

I would like to also thank the following people: Members of the ECRC, University College London, for assistance with sample preparation; Walter Hale, everyone at Bremen ODP Core repository and Juliet Ettwein for assistance with sediment sampling; Maraten Blaaw for endless enthusiasm about my AMS dates; Sharon Cowling, Peter Cox and Richard Betts for stimulating discussions about climate modelling; Chris Boot and Richard Pancost for useful conversations of the potential use of organic chemistry for studying the Amazon Fan; all my friends for their support, especially Liz, Sairah, the Carolines, the Mikes, Andrew, Phil, CK and C2; Cait, Howely, Shannon, Kelly, Katie and all the others for giving me a much needed distraction from work in the evenings; the people at Starbucks for making the coffee exactly how I like it; Gillian, Viking, Newman, Duchess, Tarot, Trinity and everyone else at Hall Place Equestrian Centre for giving me the most delightful hour's break from work each week; Ruth, Andrew and David for teaching me yoga and literally changing my life; and Pat for all the stress-relieving reflexology (I hasten to use the word 'relaxing' as it hurt).

I would like to say a very, very special thankyou to Darren Hillegonds for all his endless encouragement, support and above all, patience, all of which were above and beyond the call of duty.

Most importantly, I would like to thank my family and cats for encouraging me so much over the past couple of years, especially my Dad for being so helpful in the final stages with all the proof reading, and my Mum for keeping me alive with food and cups of tea, not to mention providing an emergency taxi service. Finally, I would like to thank Mrs Byrne, a teacher at Kendrick Grammar School, 1988-1995, who nurtured my kindling interest and inspired me to study Geography.

This PhD research was supported by NERC Studentship GT4/00/165

TABLE OF CONTENTS

<u>ABSTRACT.....</u>	<u>I</u>
<u>ACKNOWLEDGEMENTS.....</u>	<u>II</u>
<u>TABLE OF CONTENTS.....</u>	<u>III</u>
<u>LIST OF FIGURES</u>	<u>VIII</u>
<u>LIST OF TABLES</u>	<u>XVIII</u>
<u>1. INTRODUCTION.....</u>	<u>1</u>
1.0 Background	1
1.2 Aims and Objectives	3
1.3 Thesis Outline.....	3
1.4 References.....	4
<u>2. STUDY SETTING</u>	<u>5</u>
2.1 Introduction.....	5
2.2 The Depositional Setting of the Amazon Fan	6
2.2.1 Introduction to the Amazon Fan	6
2.2.2 Sediment Source and Supply	9
2.2.3 Glacial – Interglacial Sedimentary Regime and the ‘On-Off’ Switch	10
2.3 The Hydrographic Setting of the Amazon Fan	14
2.3.1 Introduction	14
2.3.2 The North Brazilian Current (NBC)	14
2.3.3 Origins and Structure of the NBC.....	19
2.3.4 Interhemispheric Ocean Transport.....	21
2.4 Setting of ODP Site 942 on the Amazon Fan	24
2.4.1 Site Location and Sedimentary Setting.....	24
2.4.2 Sampling Strategy and Sediment Description	25

2.4.2a Iron-Rich Crust in 942 Sediments	25
2.4.2 Hydrographic setting	27
2.5 References.....	28
<u>3. A REVIEW OF THE MODERN CLIMATOLOGY OF THE AMAZON</u>	
<u>BASIN AND SURROUNDING REGIONS</u>	<u>35</u>
3.1 Introduction.....	35
3.2 The Modern Meteorology of the Amazon Basin.....	35
3.2.1 Introduction	35
3.2.2 Temporal Organisation of Rainfall Over the Amazon Basin.....	41
3.2.3 Spatial Organisation of Rainfall Over the Amazon Basin	45
3.2.4 The Influence of ENSO on the Precipitation Regime over the Amazon Basin	46
3.3 The Modern Meteorology of the Altiplano Region	46
3.3.1 Introduction	46
3.3.2 The Modern Meteorology of the Altiplano Region	46
3.3.3 The Influence of ENSO on the Precipitation Regime over the Altiplano Region	49
3.4 References.....	49
<u>4. A REVIEW OF THE 0 TO 40 KA PALAEOCLIMATE</u>	
<u>RECONSTRUCTIONS OF TROPICAL AND SUBTROPICAL SOUTH</u>	
<u>AMERICA</u>	<u>52</u>
4.1 Introduction to Reconstructions of Palaeoclimate	52
4.1.1 Introduction	52
4.1.2 Limitations to Palaeoclimate Reconstruction	52
4.2 Palaeotemperature Reconstructions of the Amazon Basin	59
4.3 Palaeomoisture Reconstructions of the Amazon Basin.....	63
4.3.1 Morphological Observations	64
4.3.2 Palaeoecological Records	66
4.3.3 Inorganic Sedimentary Lake Records.....	69
4.3.4 Marine Geochemical Records.....	71
4.3.5 Speleothem Records	72
4.3.6 Extrapolations of Climate Information From More Distal Regions	74
4.3.6a South of Amazonia: the Altiplano	74

4.3.6b North of Amazonia: the Cariaco Basin	80
4.3.7 Summary of the Palaeomoisture Reconstructions for the Amazon Basin	81
4.4 Summary of Glacial and LGIT Palaeoclimate Records from Tropical and Subtropical South America.....	83
4.5 References.....	85
<u>5. ODP SITE 942 COMPOSITE AGE MODEL.....</u>	<u>94</u>
5.1 Age Model Construction Using AMS ¹⁴C dates.....	94
5.1.1 Conversion of AMS Radiocarbon Dates to Calibrated Calendar Years	94
5.1.2 Accounting for the Marine Reservoir Correction at ODP Site 942	95
5.1.3 Sample Reproducibility	97
5.2 Splicing Together the A-B-C Cores.....	100
5.2.1 Splicing of Datasets Using Shipboard Magnetic Susceptibility Records	100
5.2.2 Calibrated Age-Depth Plot of ODP 942	101
5.3 Sedimentation Rate Over ODP Site 942.....	105
5.3.1 The Pleistocene-Holocene Sedimentary Regime Over Site 942.....	105
5.3.2 Chronological and Sea-Level Timing of the ‘On/Off Switch’ in Fan Deposition	108
5.4 Summary.....	108
5.5 References.....	109
<u>6: OXYGEN ISOTOPE RECORDS FROM ODP SITE 942 ON THE AMAZON FAN</u>	<u>112</u>
6.1 Introduction to Reconstructing Amazon River Outflow Using $\delta^{18}\text{O}$ Records.....	112
6.2 $\delta^{18}\text{O}$ Methodology for This Study.....	116
6.2.1 Sample Preparation.....	116
6.2.2 Foraminifera Species Analysed in This Study.....	118
6.2.3 Stable Isotope Analysis for This Study.....	119
6.3 High Resolution $\delta^{18}\text{O}$ Records from ODP Site 942.....	120
6.3.1 High Resolution $\delta^{18}\text{O}$ Records	120
6.3.2 Smoothed Isotope Data.....	123
6.3.4 Isolating the $\delta^{18}\text{O}_{\text{Amazon}}$ Signal from the $\delta^{18}\text{O}_{942}$ Record	126
6.4 Qualitative Interpretations of Amazon River Outflow from $\Delta\delta^{18}\text{O}_{942}$	128

6.4.1 How to Interpret the $\Delta\delta^{18}\text{O}_{942}$ Record.....	128
6.4.2 General Comparisons Between $\Delta\delta^{18}\text{O}_{942}$ Records of Different Species	130
6.4.3 Interpretations of the Glacial-Holocene Amplitude in $\Delta\delta^{18}\text{O}_{942}$	134
6.4.4 Interpretations of the Glacial Records (40 to ~15 Cal kyr).....	136
6.4.5 Interpretations of the ~15 to ~13 Cal ka Records	139
6.4.6 Interpretations of the ~13 to ~11 Cal ka Records	141
6.4.7 Interpretations of the Holocene Records (~11 Cal ka to Present).....	145
6.5 Summary of the Qualitative Interpretations of the $\Delta\delta^{18}\text{O}_{942}$ records.....	146
6.6 References.....	149
<u>7: SEMI-QUANTITATIVE RECONSTRUCTION OF PAST CHANGES IN AMAZON RIVER OUTFLOW.....</u>	<u>155</u>
7.1 Introduction.....	155
7.2 Quantifying the Isotopic Fractionation Effects	155
7.3 Construction of the Amazon River Outflow Model	158
7.4 Variables Used in the Refined Outflow Model	159
7.5 Amazon River Outflow Model Results.....	161
7.6 Limitations of the Amazon River Outflow Model.....	167
7.7 Summary.....	168
7.8 References.....	168
<u>8: SYNTHESIS AND DISCUSSION.....</u>	<u>172</u>
8.1 Introduction.....	172
8.2 Comparison of $\Delta\delta^{18}\text{O}_{942}$ to Other Proxy Records From Tropical and Subtropical South America.....	173
8.2.1 Comparison to Proxy Records From Within the Amazon Basin	173
8.2.3 Comparison to Large-Scale Proxy Records from Tropical and Subtropical South America.	174
8.3 Interpretation of Climate From Large-Scale Proxy Records from Tropical and Subtropical South America.....	177

8.3 Comparison of $\Delta\delta^{18}\text{O}_{942}$ Records With Polar Ice Cores: Possible Inter-Hemispheric Drivers for Tropical South American Palaeoclimate	179
8.4 Comparison of Tropical South American Palaeoclimate Records for the Onset of the Younger Dryas	183
8.5 Comparison of the Holocene $\Delta\delta^{18}\text{O}_{942}$ Amazon Basin Effective Moisture Record with Records of ENSO Variability.....	185
8.6 Comparison of the $\Delta\delta^{18}\text{O}_{942}$ Amazon Basin Effective Moisture Record with Records of Atmospheric Methane	186
8. References.....	187
<u>9. CONCLUSIONS AND RECOMMENDATIONS FOR FURTHER WORK..</u>	191
9.1 Conclusions.....	191
9.2 Recommendations for Further Work.....	194
9.3 References.....	196
<u>APPENDIX: ISOTOPE DATA.....</u>	198
Appendix 1: <i>G. ruber</i>.....	198
Appendix 2: <i>G. sacculifer</i> (sac form)	207
Appendix 3: <i>G. sacculifer</i> (non sac form).....	216
Appendix 4: <i>N. dutertrei</i>	225
Appendix 5: <i>G. truncatulinoides</i>.....	234

LIST OF FIGURES

Corresponding page numbers are listed to the right.

- Figure 1.1:** A sketch map of South America to show the approximate location and extent of the Amazon River drainage basin, shaded in yellow. Other key reference locations are also labelled (modified from Houghton Mifflin Company, 2002). 1
- Figure 2.1:** Map of Sites drilled from the Amazon Fan during ODP Leg 155. Site 942 is situated to the west of the main fan complex (modified from Flood *et al.*, 1995). 5
- Figure 2.2:** A sketch map to show the geographical setting of the Amazon Fan in relation to other bathymetric features off the coast of Brazil (after Damuth, 1977). 7
- Figure 2.3:** A diagram to show the main features of the Amazon Fan, and its location off the edge of the continental shelf, adjacent to the mouth of the Amazon River. Bathymetry is shown in metres. ‘GR’ denotes gradient (after Damuth *et al.*, 1983b). 8
- Figure 2.4:** Cartoon to illustrate the glacial/sea level low stand deposition of riverine sediments. Sediments are transported directly onto the Amazon Fan. OM= organic matter. “NBCC” = NBC = North Brazil Current (after Schlünz *et al.*, 1999). 10
- Figure 2.5:** Cartoon to illustrate the interglacial/sea level high-stand deposition of riverine sediments. OM= organic matter. “NBCC” = NBC = North Brazil Current. Sediments are entrained in the North Brazilian Current and transported northwestwards, away from the fan and deposited on the continental shelf. Very little terrestrial material accumulates on the fan (after Schlünz *et al.*, 1999). 11
- Figure 2.6:** A diagram to show the relationship between sea level change and fan sedimentation (after Maslin *et al.*, 2000). Sea level change data are those compiled by (McGuire *et al.*, 1997) based upon Barbados (Fairbanks, 1989) and Pacific (Shackleton, 1987) data, and are compared against marine transgression over the continental shelf (see A-D) described by Milliman *et al.* (1975) and the Amazon River sediment influx (hatching on graph) reconstructed by Maslin *et al.* (2000). 12
- Figure 2.7:** Cartoon to illustrate the significance of the North Brazilian Current (NBC) to oceanic circulation in the north Atlantic (modified from Colling, 2001). ‘C’ denotes ‘current’. 16

-
- Figure 2.8:** SeaWiFS satellite colour reflectance imagery of the Amazon River plume, shown as black and red/yellow/green colours (NASA, 2002). 16
- Figure 2.9:** Map of sea-surface salinity for the period 24 July to 11 September 1964. Arrows indicate the inferred path of low-salinity Amazon water and major currents (after Müller-Karger *et al.*, 1988). 17
- Figure 2.10:** Schematic representation of the Amazon River plume as observed in seasonal composites of NASA's Coastal Zone Colour Scanner (CZCS) images for (a) 1979, (b) 1980, and (c) 1981. Shaded areas show plume extent for June-January, broken lines show plume extent for February-May (after Müller-Karger *et al.*, 1988). 18
- Figure 2.11:** A schematic diagram of the modern mean upper ocean circulation pattern of the western tropical Atlantic Ocean (after Wilson *et al.*, 1994). 19
- Figure 2.12:** Circulation in the Western Tropical Atlantic in density layers derived from repeated sections of water mass properties and current measurements by Meteor sections (green dashed lines) and moored arrays (red dots). The Surface layer reaches from the surface to the 24.5 isopycnal, the Central layer is defined between the 24.5 and 26.8 isopycnals, and the Intermediate layer from 26.8 down to 1000 m depth. Numbers are for the transports (in $Sv = 10^6 m^3 s^{-1}$) of current branches. Abbreviated as follows: NBC: North Brazilian Current; NBUC: North Brazil Undercurrent; SEC: South Equatorial Current; NEC: North Equatorial Current; GUC: Guyana Undercurrent; NECC: North Equatorial Countercurrent; SECC: South Equatorial Countercurrent; NEUC: North Equatorial Undercurrent; SEUC: South Equatorial Undercurrent; EUC: Equatorial Undercurrent; NICC: Northern Intermediate Countercurrent; SICC: Southern Intermediate Countercurrent; EIC: Equatorial (Intermediate) Undercurrent (modified from <http://www.ifm.uni-kiel.de/fb/fb1/po1/research/woce/woce-ao.html>). 20
- Figure 2.13:** A cartoon detailing the main features of the North Brazilian Current (NBCC on figure) for the periods February–June (left) and July–January (modified from Maslin *et al.*, 2000) in relation to ODP Site 942 on the Amazon Fan. NEC = North Equatorial Countercurrent. NEC = North Equatorial Current. Depth contours refer to the relief of the sea floor. Small squares indicate locations of other Sites drilled during ODP Leg 155. 22
- Figure 2.14:** A cartoon illustrating the formation of North Brazilian Current Rings during retroreflection periods (after Goni *et al.*, 2003). NBC = North Brazil Current. NEC = North Equatorial Current. NECC = North Equatorial Countercurrent. nSEC/cSEC = northern/central South Equatorial Current. CC = Caribbean Current. BC = Brazilian Current. GC = Guiana Current. 23
-

Figure 2.15: The location of ODP Site 942 on the Middle Levee Complex, as shown on a cross-section through the Amazon Fan (modified from Flood and Piper, 1997).	24
Figure 2.16: 3.5-KHz seismic profile illustrating the sedimentary stratigraphy at Site 942 (after Shipboard Scientific Party, 1995).	25
Figure 2.17: A proposed sequence of iron-rich crust formation for environments such as the Amazon Fan (modified from McGearry and Damuth, 1973).	26
Figure 3.1: Goddard Earth Observing System-1 (GEOS-1) assimilation of upper level (200-hPa) circulation composite monitoring the formation and decline of the Bolivian High. (a) October to November; (b) mid-November to December; (c) December to early February (wet season); (d) early February to mid-March; (e) mid-March to end April. H = area of high atmospheric pressure; L = area of low atmospheric pressure (modified from Zhou and Lau, 1998).	37
Figure 3.2: GEOS-1 and NCEP re-analysis climatology of lower level (900-hPa) wind ($m s^{-1}$) for (a) annual mean, (b) January minus annual mean, and (c) July minus annual mean (modified from Zhou and Lau, 1998).	39
Figure 3.3: Map of the distribution of annual rainfall across the Amazon Basin (modified from Marengo, 1995).	40
Figure 3.4: Mean monthly river discharges illustrating the onset of the wet season across different parts of the Amazon Basin, measured at (A) Estirao do Repouso, Rio Javari, western Amazonia; (B) Porto Velho, Rio Madeira, southern Amazonia; (C) Obidos, Rio Amazonas, near to the mouth of the Amazon River; (D) Caracarai, Rio Branco, north of the equator. Monthly averages are calculated for the period from January 1928 to March 1996 (modified from Global Runoff Data Centre, 2005).	41
Figure 3.5: A cartoon to show the mean position of the ITCZ/meteorological equator (dashed line) and the coeval zone of atmospheric convection over tropical South America for January, April, July and October (modified from Davison, 1999).	43
Figure 4.1: Diagram to illustrate the effects of tuning the Sajama and Huascarán Andean ice core records to the sequence of Northern Hemisphere climate change. ^{14}C cal dates, the $\delta^{18}O_{atm}$ match points, and the time interval over which $\delta^{18}O_{ice}$ was matched to that in the GISP2 core are shown along the top (modified from Thompson <i>et al.</i> 2000).	54

Figure 4.2: Methane-synchronised isotope records of the Greenland GRIP, and Antarctic Vostock and Byrd Station ice cores to show the relative timing of the Antarctic Cold Reversal and the Younger Dryas period (Blunier *et al.*, 1997), together with the increase in atmospheric CO₂ record from Byrd (modified from Raynaud *et al.*, 2000). 54

Figure 4.3: Palaeoclimate records from tropical and subtropical South America compared to the polar ice core records, which suggest that deglacial warming in tropical South America preceded the deglacial warming in the northern high latitudes by several thousand years (modified from Seltzer *et al.*, 2002). It should be noted that the GRIP timescale quoted by Seltzer *et al.* (2002) has since been revised to match the GISP2 chronology back to 40 ka (Johnsen *et al.*, 2001) and so is now no longer younger than the GISP2 for ages >15 kyr BP as shown in this figure. Data shown are magnetic susceptibility records from Lake Junin, Peru (A) and Lake Titicaca (B and C); and $\delta^{18}\text{O}_{\text{ice}}$ ice core records from Byrd Station, Antarctica (D) and GRIP, Greenland (E). 56

Figure 4.4: Diagram from Clark (2002) to show the synchronicity of deglaciation between the Northern Hemisphere and tropical Andes. The vertical grey box represents the timing of tropical deglaciation established in Seltzer *et al.* (2002). (A) GISP2 record of atmospheric methane. Black markers show the relative ages (with errors) of deglaciation of five glacier systems in western North America (no vertical scale). WR = Wind River Mountains, Wyoming; SN = Sierra Nevada Mountains, California; OM = Olympic Mountains, Washington; CIS = southern margin of the Cordilleran Ice Sheet, Fraser Lowlands, British Columbia; YIC = northern outlet glacier of the Yellowstone Ice Cap, Wyoming. (B) Smooth curves: midmonth insolation at 60°N (June) and 30°S (December). Jagged curves: GISP2 oxygen isotope record, presented at lower and higher-resolutions. (C) Oxygen isotope record from Byrd Station, Antarctica, displayed on the GISP2 timescale. For more details about how this diagram was constructed, please refer to Clark (2002). 58

Figure 4.5: A map to show the locations of the ice cores drilled to date in the Tropical Andes. 61

Huascarán Col (9°07' S, 77°37'W, elev. 6048 m)

Quelccaya Ice Cap (13°56' S, 70°50' W, elev. 5670 m)

Coropuna Ice Cap (15° 32' S, 72° 39' W, elev. 6450 m)

Nevado Sajama (18°07' S, 68°53' W, elev. 6642 m)

(<http://researchnews.osu.edu/archive/quelcoropics.htm> [accessed 04.06.04])

-
- Figure 4.6:** $\delta^{18}\text{O}$, nitrate and insoluble dust concentrations from the Huascarán ice core, Peru (modified from Thompson *et al.*, 2000). 62
- Figure 4.7:** $\delta^{18}\text{O}$, nitrate and insoluble dust concentrations from the Sajama ice core, Bolivia (Thompson *et al.*, 2000). 62
- Figure 4.8:** A comparison of proxy records for effective moisture in tropical South America from Lake Junin (Peruvian Andes), and ODP Site 942C on the Amazon Fan (modified from Maslin and Burns, 2000). $\Delta\delta^{18}\text{O} = \delta^{18}\text{O}$ measured at ODP Site 942, corrected for global ice volume and sea surface temperature. For details of how $\Delta\delta^{18}\text{O}$ was derived, see Maslin and Burns (2000). 71
- Figure 4.9:** The Location of the Sajama ice cap in Bolivia in relation to modern lakes (black) and salt flats (white). Dark grey areas represent the areas covered by palaeolakes during the LGS (modified from Thompson *et al.*, 1998). 76
- Figure 4.10:** Snow accumulation record from the Sajama ice core (modified from Thompson *et al.*, 1998). 76
- Figure 4.11:** Chemical, isotopic, and biotic analyses of sediments from Lake Titicaca, where more elevated data generally signifies higher lake level or fresher water (modified from Baker *et al.*, 2001b). Data are presented from three cores, represented by grey, blue and black curves. (A) relative abundance of benthic diatoms; (B) relative abundance of planktonic freshwater diatoms; (C) weight percentage calcium carbonate; (D) relative abundance of saline diatoms; (E) $\delta^{13}\text{C}$ of total organic carbon; (F) January insolation at 15°S . For more details, see Baker *et al.* (2001b). 78
- Figure 4.12:** Sketch maps to show the main lacustrine basins of the modern Altiplano (left), and the extension of Palaeolake Tauca, labelled on map as “Paleolake Pocuyu” referring to the cumulative basins of Lakes Poopó, Coipasa and Uyuni (Modified from Argollo and Mourguiart, 2000). 79
- Figure 4.13:** Downcore record of natural γ -radiation from the Salar de Uyuni showing effective moisture through time. More positive values indicate increased moisture (after Baker *et al.*, 2001a; Fritz *et al.*, 2004). 80
- Figure 4.14:** Bulk sedimentary Ti content of Cariaco Basin sediments from ODP Site 1002 for the last 14,000 years (three point moving average). Higher Ti content reflects greater terrestrial input from riverine runoff, which is interpreted to reflect greater precipitation over the Cariaco Basin, and a more northerly position of the ITCZ (modified from Haug *et al.*, 2001). 81
-

-
- Figure 4.15:** A latitudinal comparison of palaeomoisture records from the Cariaco Basin (Haug *et al.*, 2001); ODP Site 942 on the Amazon Fan (Maslin and Burns, 2000; Maslin *et al.*, 2000); Lake Junin in the Peruvian Andes (Seltzer *et al.*, 2000); and the Salar de Uyuni on the Bolivian Altiplano (Baker *et al.*, 2001a). Also shown are the GISP2 methane record (Brook *et al.*, 1996) and solar insolation at 10°S (Berger, 1978a; Berger, 1978b; Berger and Loutre, 1991). 84
- Figure 5.1:** An example of a radiocarbon date converted to a calibrated calendar age using the probability distribution method. A radiocarbon age of 3014 ± 56 ^{14}C kyr BP yields a calibrated calendar age range of $\sim 3282 - 3438$ Cal ka at a probability distribution of one sigma. 95
- Figure 5.2:** Tuning of shipboard magnetic susceptibility curves to transfer AMS dates from 942C onto the 942B depth scale. Maximum lateral displacement of C Core MS = ~ 6 cm. Triangles indicate the relative positions of radiocarbon-dated samples. 100
- Figure 5.3:** Tuning of shipboard magnetic susceptibility curves to transfer AMS dates from 942C onto the 942A depth scale. No lateral displacement of cores. Triangles indicate the relative positions of radiocarbon-dated samples. 101
- Figure 5.4a:** Age-depth plot of calibrated radiocarbon dates from ODP 942 with their respective errors (one sigma). Depth scale is that of Core 942B. Connected diamonds indicate those samples used in age model, unconnected circles indicate those which were excluded. 'x2' indicates replicate samples. Dates above the wavy line were calibrated using Calib 4.3 (Stuiver and Reimer, 1993). Dates below the wavy line were calibrated against the data presented in Beck *et al.* (2000). 102
- Figure 5.4b:** 0-13 Cal kyr BP detail age-depth plot of calibrated radiocarbon dates from ODP 942 with their respective errors (one sigma). Depth scale is that of Core 942B. Connected diamonds indicate those samples used in age model, unconnected circles indicate those which were excluded. 'x2' indicates replicate samples. 103
- Figure 5.5:** Inter-radiocarbon age sedimentation rates for ODP Site 942. Sedimentation rates are in metres per thousand calendar years. Triangles indicate relative stratigraphic position of radiocarbon-dated samples. '^'^ indicates data plotted off the chart (up to $\sim 18\text{m Cal kyr}^{-1}$). 105
- Figure 5.6:** Site 942 sedimentation rate plotted alongside the sea level change curve (after Fairbanks, 1989; Shackleton, 1987) illustrating the chronological- and sea level- timing of the 'on/off switch' in Amazon Fan sedimentation. '^'^ indicates data plotted off the chart (up to $\sim 18\text{m Cal kyr}^{-1}$). 108
-

-
- Figure 6.1:** A typical vertical temperature ($t^{\circ}\text{C}$), salinity (S‰) and density (σ_t) profile for the tropical oceans (modified from Bradley, 1999). 113
- Figure 6.2:** Map of South America to show relative locations of ODP Site 942 and GeoB 3104-1. Dark blue arrows represent the direction of surface ocean currents; light blue arrow represents the Amazon River freshwater outflow. 114
- Figure 6.3:** From top to bottom: *Neogloboquadrina dutertrei* $\Delta\delta^{18}\text{O}$ data from ODP Site 942C on the Amazon Fan as a proxy for Amazon River discharge; the Peruvian Lake Junin $\Delta\delta^{18}\text{O}$ record of effective moisture; the atmospheric methane record from Greenland Ice Sheet Project 2 (GISP2) in parts per billion by volume (ppbv); and summer insolation changes at 10°S (modified from Maslin and Burns, 2000). 115
- Figure 6.4: Sequence of sample preparation for ODP Site 942 sediments. 117
- Figure 6.5a:** Normalised composite $\delta^{18}\text{O}_{942}$ records for each of the five species measured, plotted against metres below sea floor. Markers indicate individual sample levels. All data were normalised against the stratigraphically most recent value to express change relative to modern (where modern = 0.0 to 0.01 mbsf). 121
- Figure 6.5b:** Normalised composite $\delta^{18}\text{O}_{942}$ records for each of the five species measured, plotted against calendar years BP. Individual sample levels are indicated by markers. Yellow diamonds indicate the relative stratigraphic placement of AMS radiocarbon dates, with their respective error margins. All data were normalised against the stratigraphically most recent value to express change relative to modern (where modern = 1 Cal yr BP). 122
- Figure 6.6a:** Composite smoothed $\delta^{18}\text{O}_{942}$ records for each of the five species measured plotted against metres below sea floor. Individual sample levels are indicated by red dots. All data were normalised against the stratigraphically most recent value to express change relative to modern (where modern = 0.00 to 0.01 mbsf). 124
- Figure 6.6b:** Composite smoothed $\delta^{18}\text{O}_{942}$ records for each of the five species measured plotted against Calendar years BP. Individual sample levels are indicated by red dots. Yellow diamonds indicate the relative stratigraphic placement of AMS radiocarbon dates, with their respective error margins. All data were normalised against the stratigraphically most recent value to express change relative to modern (where modern = 1 Cal yr BP). 125
- Figure 6.7:** Glacio-eustatic sea level change and associated change in $\delta^{18}\text{O}$, as a proxy for the global ice volume effect (after Fairbanks, 1989; Shackleton, 1987). 126
- Figure 6.8:** Composite smoothed $\Delta\delta^{18}\text{O}_{942}$ records for each of the five species measured, with the global ice volume effect removed, plotted against Calendar years BP. Individual 127
-

sample levels are indicated with markers. Yellow diamonds indicate the relative stratigraphic placement of AMS radiocarbon dates, with their respective error margins. All data were normalised against the stratigraphically most recent value to express change relative to modern (where modern = 1 Cal yr BP).

Figure 6.9: Graph of *G. sacculifer* (sac) $\delta^{18}\text{O}$ to illustrate the different system states in the isotopic signal. 132

Figure 6.10: Composite smoothed $\Delta\delta^{18}\text{O}$ records for *G. ruber*, *G. sacculifer* sp. and *N. dutertrei*, plotted against Calendar years BP. Individual sample levels markers have been omitted for clarity. Yellow diamonds indicate the relative stratigraphic placement of AMS radiocarbon dates, with their respective error margins. All data were normalised against the stratigraphically most recent value to express change relative to modern (where modern = 1 Cal yr BP). Shading denotes the timeframes approximating to the last glacial maximum (~23 to ~21 Cal ka) and Younger Dryas (~ 13 to ~11.5 Cal ka). YD= Younger Dryas; ACR= Antarctic Cold Reversal; LGIT= Last Glacial-Interglacial Transition. 133

Figure 6.11: A comparison between sedimentation rates and *G. sacculifer* (sac) $\Delta\delta^{18}\text{O}$ at ODP Site 942. Blue and yellow shading denotes the Lateglacial Interstadial and Younger Dryas periods, respectively. 140

Figure 6.12: 13 to 11.5 Cal ka composite smoothed $\Delta\delta^{18}\text{O}$ records, for *G. ruber*, *G. sacculifer* sp. and *N. dutertrei*. Individual sample levels are shown with markers. The 13-12.5 Cal ka period is shown in more detail on the right. Yellow diamonds indicate the relative stratigraphic placement of AMS radiocarbon dates, with their respective error margins. All data were normalised against the stratigraphically most recent value to express change relative to modern (where modern = 1 Cal yr BP). 142

Figure 6.13: a comparison between *G. ruber* $\Delta\delta^{18}\text{O}_{942}$ and the Bond *et al.* (2001) stacked record of drift-ice deposits expressed as a percentage of ice-rafted lithic grains in the 63 to 150 μm size range (modified from Maslin *et al.*, 2003). 146

Figure 7.1: Factors influencing the tropical Atlantic and Amazon River components of the $\delta^{18}\text{O}_{942}$ signal, as well as those influencing the overall $\delta^{18}\text{O}_{942}$ ('RA Effect' = Reverse Amount Effect; 'GIV' = Global Ice Volume; 'SOS' = Surface Ocean Salinity; 'SST' = Sea Surface Temperature). 156

Figure 8.1: Long, continuous regional-scale proxy records from tropical and subtropical South America, stacked in approximate latitudinal order against Cal kyr BP, alongside calculated November and December insolation at 10°S (Berger 1978a; Berger 1978b; Berger and Loutre, 1991). From top to bottom: Cariaco Basin (%Ti; Haug *et al.*, 2001); Amazon Fan, ODP Site 942 ($\Delta\delta^{18}\text{O}_{942}$ *G. sacculifer* (sac); this study); Lake Junin, Peru ($\delta^{18}\text{O}$; Maslin and Burns, 2000; Seltzer *et al.*, 2000); Botuverá Cave, southeast Brazil ($\delta^{18}\text{O}$; Cruz *et al.*, 2005); Lake Titicaca, Peruvian/Bolivian Altiplano (% benthic diatoms; Baker *et al.*, 2001b); Salar de Uyuni, Bolivian Altiplano (natural γ -radiation; Baker *et al.*, 2001a). Shaded area denotes the Younger Dryas period as determined by GISP2 $\delta^{18}\text{O}$ records (Grootes and Stuiver, 1997). The Botuverá Cave record (Cruz *et al.* 2005) monitors relative changes in the source area of precipitation (ppn). 175

Figure 8.2 : Long, continuous regional-scale proxy records from tropical and subtropical South America, stacked in approximate latitudinal order against Cal kyr BP, alongside polar ice core data. From top to bottom: GISP2 ice core ($\delta^{18}\text{O}$; Grootes and Stuiver, 1997); Cariaco Basin (%Ti; Haug *et al.*, 2001); Amazon Fan, ODP Site 942 ($\Delta\delta^{18}\text{O}_{942}$ *G. sacculifer* (sac); this study); Lake Junin, Peru ($\delta^{18}\text{O}$; Maslin and Burns, 2000; Seltzer *et al.*, 2000); Botuverá Cave, southeast Brazil ($\delta^{18}\text{O}$; Cruz *et al.*, 2005); Lake Titicaca, Peruvian/Bolivian Altiplano (% benthic diatoms; Baker *et al.*, 2001b); Salar de Uyuni, Bolivian Altiplano (natural γ -radiation; Baker *et al.*, 2001a); Vostok ice core (δD ; Blunier, 1998). Shaded area denotes the Younger Dryas period as determined by GISP2 $\delta^{18}\text{O}$ records (Grootes and Stuiver, 1997). The Botuverá Cave record (Cruz *et al.* 2005) monitors relative changes in the source area of precipitation (ppn). 180

Figure 8.3: A comparison between $\delta^{18}\text{O}$ records from the Huascarán ice core (A), and Lake Junin (B; Peru). Chronological bias to the Northern Hemisphere in the Huascarán age model may account for the noticeable dissimilarity between the isotopic records from ~11 to ~14 ka, which results in relatively more enriched $\Delta\delta^{18}\text{O}$ values around this time (B), where $\Delta\delta^{18}\text{O}$ represents the difference between the two records (modified from Seltzer *et al.*, 2000). 182

-
- Figure 8.4:** ~10 to ~15 ka detail. Long, continuous regional-scale proxy records from tropical and subtropical South America, stacked in approximate latitudinal order against Cal kyr BP, alongside polar ice core data. From top to bottom: GISP2 ice core ($\delta^{18}\text{O}$; Grootes and Stuiver, 1997); Cariaco Basin (%Ti; Haug *et al.*, 2001); Amazon Fan, ODP Site 942 ($\Delta\delta^{18}\text{O}_{942}$ *G. sacculifer* (sac); this study); Lake Junin, Peru ($\Delta\delta^{18}\text{O}$; Maslin and Burns, 2000; Seltzer *et al.*, 2000); Botuverá Cave, southeast Brazil ($\delta^{18}\text{O}$; Cruz *et al.*, 2005); Lake Titicaca, Peruvian/Bolivian Altiplano (% benthic diatoms; Baker *et al.*, 2001b); Salar de Uyuni, Bolivian Altiplano (natural γ -radiation; Baker *et al.*, 2001a); Vostok ice core (δD ; Blunier, 1998). Shaded area indicates the time of rapid sediment accumulation on the Amazon Fan ($\sim 18 \text{ m Cal ka}^{-1}$). The Botuverá Cave record (Cruz *et al.*, 2005) monitors relative changes in the source area of precipitation (ppn). 184
- Figure 8.5:** A comparison of the *G. ruber* $\Delta\delta^{18}\text{O}_{942}$ record of effective moisture in the Amazon Basin against the reconstruction of ENSO frequency from Laguna Pallcacocha in the southern Ecuadorian Andes (after Moy *et al.*, 2002). 186
- Figure 8.6.** A comparison of the *G. sacculifer* (sac) $\Delta\delta^{18}\text{O}_{942}$ record from the Amazon Fan as a proxy for tropical humidity, and the GISP2 atmospheric methane record (Brook *et al.*, 1996). 187
-

LIST OF TABLES

Corresponding page numbers are listed to the right.

Table 2.1: Details of ODP Site 942 on the Amazon Fan. *All details are exactly as quoted in (Shipboard Scientific Party, 1995).	6
Table 2.2: Summary of stratigraphic nomenclature of the Amazon Fan (after Damuth <i>et al.</i> , 1983a; Flood and Piper, 1997; Manley and Flood, 1988).	14
Table 4.1: A comparison of average $\delta^{18}\text{O}$ values for various time intervals and for different ice cores. Vostock measurements are in δD with comparable $\delta^{18}\text{O}$ values shown in parenthesis (modified from Thompson <i>et al.</i> , 2000; see also references therein).	63
Table 4.2: A review of the morphological evidence for palaeomoisture in the Amazon Basin.	65
Table 4.2: A summary of the proxy evidence for palaeomoisture in the Amazon Basin.	82
Table 5.1: Details of samples measured for radiocarbon dating. Asterisks (*) denote where data is unknown. Data in bold indicates B-Core samples; grey shading denotes samples not used to construct age model. 'mbsf' denotes metres below sea floor. #Calibration datasets used: (1) Stuiver <i>et al.</i> , (1993; version 4.3); (2) Beck <i>et al.</i> (2001). 'G. sacc.' denotes the foraminiferan species <i>Globigerinoides sacculifer</i> (sp); 'P. obliq.' denotes the foraminiferan species <i>Pulleniatina obliquiloculata</i> . '1 σ ' denotes one sigma.	98-99
Table 5.2: The effect of contamination by modern carbon on the true radiocarbon age of a sample (after Lowe and Walker, 1997, p246).	104
Table 5.3: Sedimentation rates (m ka^{-1}) calculated between each age horizon for Site 942. Figures in boxes emphasise periods of extreme sediment accumulation. SR = sedimentation rate.	107
Table 6.1: Details of foraminifera species analysed for $\delta^{18}\text{O}$ (after Anand <i>et al.</i> , 2003; Bradley, 1999; Hilbrecht, 1996; Ravelo and Fairbanks, 1992).	118
Table 6.2: Details of $\delta^{18}\text{O}$ sample analyses at different laboratories.	119
Table 7.1: Definition of variables used in the Amazon River outflow model.	159

Table 7.2: Published palaeoclimate variables and their associated isotopic fractionation effects.	160
Table 7.3: Amazon River outflow model input variable, and output data for <i>G. sacculifer</i> (sac).	162
Table 7.4: Amazon River outflow model input variable, and output data for <i>G. sacculifer</i> (non sac).	163
Table 7.5: Summary of Amazon River outflow model output for <i>G. sacculifer</i> (both sac forms).	164
Table 7.6: Amazon River outflow model input variable, and output data for <i>G. sacculifer</i> (sac), for the time period 12.4 to 12 Cal ka.	166
Table 7.7: Amazon River outflow model input variable, and output data for <i>G. sacculifer</i> (non sac), for the time period 12.4 to 12 Cal ka.	166
Table 7.8: Summary of Amazon River outflow model output for <i>G. sacculifer</i> (both sac forms), for the time period 12.4 to 12 Cal ka.	167
Table 8.1: Details of long, continuous regional-scale proxy records from tropical and subtropical South America.	176

1. INTRODUCTION

1.0 Background

The Amazon Basin, shown for scale in Figure 1.1, is the largest single source of fresh water on Earth (Marengo *et al.*, 2001). The Amazon River drains an area of approximately 7 050 000 km² (Franzinelli and Potter, 1983), with an annual discharge rate in excess of 6300 km³ yr⁻¹ (ca. 0.2 Sv; Meade, 1994). This constitutes approximately 20% of all the world's freshwater carried to the oceans (Franzinelli and Potter, 1983).



Figure 1.1: A sketch map of South America to show the approximate location and extent of the Amazon River drainage basin, shaded in yellow. Other key reference locations are also labelled (modified from Houghton Mifflin Company, 2002).

The Amazon region is of particular interest to studies of palaeoclimatology as it represents a large source of heat in the tropics, and has been shown to have a significant impact on extra-tropical circulation (Marengo *et al.*, 2001). The Amazon Basin is the Earth's largest and

most intense land-based convection centre (Barry and Chorley, 1995). During the Southern Hemisphere summer, when convection is best developed, the Amazon Basin is one of the wettest regions on the planet (Marengo *et al.*, 2001).

Records of continental palaeoclimate from tropical South America are of critical importance to the understanding of climate change throughout the Quaternary. Equatorial regions play a fundamental role in the atmospheric transport of heat to the higher latitudes (Flood *et al.*, 1995). However, the Pleistocene climate history of the Amazon Basin is comparatively poorly known. Until now, Amazon Basin aridity has been largely inferred from highly localised and qualitative indicators of effective moisture. The relatively few sites that are available are widely dispersed, poorly constrained in time, are often discontinuous, and moreover, are frequently open to a wide range of interpretation. However, analysing marine sediments from the Amazon Fan can circumvent these limitations. Oxygen isotope ($\delta^{18}\text{O}$) records from the Amazon Fan have the potential to record a basin-wide average of past changes in the effective moisture of the Amazon Basin within single, continuous sequences that can be radiocarbon dated. Furthermore, high rates of sedimentation have the potential to yield records of a resolution comparable to the ice core records.

Reconstructions of palaeoclimate for the Amazon Basin are essential for a number of reasons:

- Effective moisture availability is a key physiological control on the distribution of vegetation (Cowling *et al.*, 2001) and therefore provides a means of testing the Pleistocene tropical rainforest refuge hypothesis {proposed by Haffer, 1969 #713; updated by Prance, 1987 #715}, which attempts to explain the immense diversity and species endemism of the Amazon Basin.
- Amazonian wetlands represent a major source of atmospheric methane; thus it has been suggested that tropical aridity is the primary control on the reduced glacial levels of atmospheric methane as measured in the ice core records (Brook *et al.*, 1996).
- Reconstructed levels of effective moisture from within the Amazon Basin can provide an indication of overall tropical moisture, and thus tropical atmospheric water vapour, another important greenhouse gas.

- Tropical palaeoclimate records may be able to provide insights into the global phasing of large-scale climate change.

1.2 Aims and Objectives

A previously published reconstruction of the effective moisture history of the Amazon Basin from ODP Site 942 on the Amazon Fan provided the precursor for this PhD research (Maslin and Burns, 2000; Maslin *et al.*, 2000). However, these previous reconstructions only detailed the last 14 Cal kyr. The study presented in this thesis attempts to expand the timeframe of these previous records back through the last glacial cycle, and enhance the sample resolution of the records previously published.

The principal aim of this study therefore, is to reconstruct a high-resolution record of continental palaeoclimate for tropical South America, for the last 40 Cal ka, using oxygen isotope measurements from ODP Site 942 on the Amazon Fan.

This PhD research is important, as it constitutes one of the first long, high-resolution records of the effective moisture history of the Amazon Basin.

1.3 Thesis Outline

This thesis can essentially be divided into two parts. The first section provides a review of the existing knowledge, whereas the second part focuses more specifically on the interpretation of data generated by this research. Details of the depositional and hydrographic setting of Site 942 are given in Chapter 2. Chapter 3 provides an overview of the modern climatology of tropical South America, whereas previous studies of the palaeoclimatology are reviewed in Chapter 4. The high-resolution composite age model for Site 942 is described in Chapter 5. Chapters 6 and 7 present interpretations of the data generated in this study. Chapter 6 explains how Amazon River outflow signal was isolated from the $\delta^{18}\text{O}$ records measured, and the interpretations of the down-core record are discussed. Attempts to quantify the past outflow of the Amazon River for selected time periods are detailed in Chapter 7. Chapter 8 provides a synthesis of the palaeoclimate history of tropical South America. The $\delta^{18}\text{O}_{942}$ records generated in this study are examined in the context of large-scale climate change in tropical South America, and possible mechanisms of past climate change are discussed. Particular attention is paid to the Last Glacial Maximum, and last glacial-interglacial transition periods. The principal findings of this research are summarised

in Chapter 9, along with recommendations for future work. An appendix follows at the end of the thesis, which details all the data discussed.

1.4 References

- Barry, R. G., and Chorley, R. J. (1995). Tropical Weather and Climate. *In* "Atmosphere, Weather and Climate." pp. 224. Routledge, London.
- Brook, E. J., Sowers, T. A., and Orchardo, J. (1996). Rapid variations in atmospheric methane concentration during the past 110,000 years. *Science* **273**, 1087-1091.
- Cowling, S. A., Sykes, M. T., and Maslin, M. A. (2001). Paleovegetation simulations of lowland Amazonia and implications for neotropical allopatry and speciation. *Quaternary Research* **55**, 140-149.
- Flood, R. D., Piper, D. J. W., and Shipboard Scientific Party. (1995). Introduction. *In* "Proceedings of the Ocean Drilling Program, Initial Reports, Vol. 155." (R. D. Flood, D. J. W. Piper, A. Klaus, and others, Eds.), pp. 5-16, College Station, TX (Ocean Drilling Program).
- Franzinelli, E., and Potter, P. (1983). Petrology, chemistry and texture of Amazon River sands. Amazon River system. *Journal of Geology* **91**, 23-39.
- Haffer, J. (1969). Speciation in Amazon Forest Birds. *Science* **165**, 131-137.
- Houghton Mifflin Company. (2002). Political Map of South America. available online: <http://www.eduplace.com>, (accessed 28/08/05).
- Marengo, J. A., Nobre, C. A., McClain, M. E., Victoria, R. L., and Richey, J. E. (2001). General Characteristics and Variability of Climate in the Amazon Basin and its Links to the Global Climate System. *In* "The Biogeochemistry of the Amazon Basin." pp. 17-41. Oxford University Press, Oxford.
- Maslin, M. A., and Burns, S. J. (2000). Reconstruction of the Amazon Basin effective moisture availability over the past 14,000 years. *Science* **290**, 2285-2287.
- Maslin, M. A., Durham, E., Burns, S. J., Platzman, E., Grootes, P., Greig, S. E. J., Nadeau, M. J., Schleicher, M., Pflaumann, U., Lomax, B., and Rimington, N. (2000). Palaeoreconstruction of the Amazon River freshwater and sediment discharge using sediments recovered at site 942 on the Amazon Fan. *Journal of Quaternary Science* **15**, 419-434.
- Meade, R. H. (1994). Suspended sediment of the modern Amazon and Orinoco Rivers. *Quaternary International* **21**, 29-39.
- Prance, G. T. (1987). Vegetation. *In* "Biogeography and Quaternary History in Tropical America." (T. C. Whitmore, and G. T. Prance, Eds.), pp. 28-44. Oxford Science Publications, Oxford.
-

2. STUDY SETTING

2.1 Introduction

Site 942 was drilled as part of Ocean Drilling Program (ODP) Leg 155, which drilled a total of 17 sites on the Amazon Fan (see Figure 2.1). In total, three holes were drilled at the Site: 942A, 942B and 942C, spaced approximately 50m apart. Each hole was drilled at a slight depth offset to obtain a continuous composite linear sequence for the Site (Flood *et al.*, 1995; Shipboard Scientific Party, 1995). Details of cores drilled at Site 942 are given in Table 2.1.

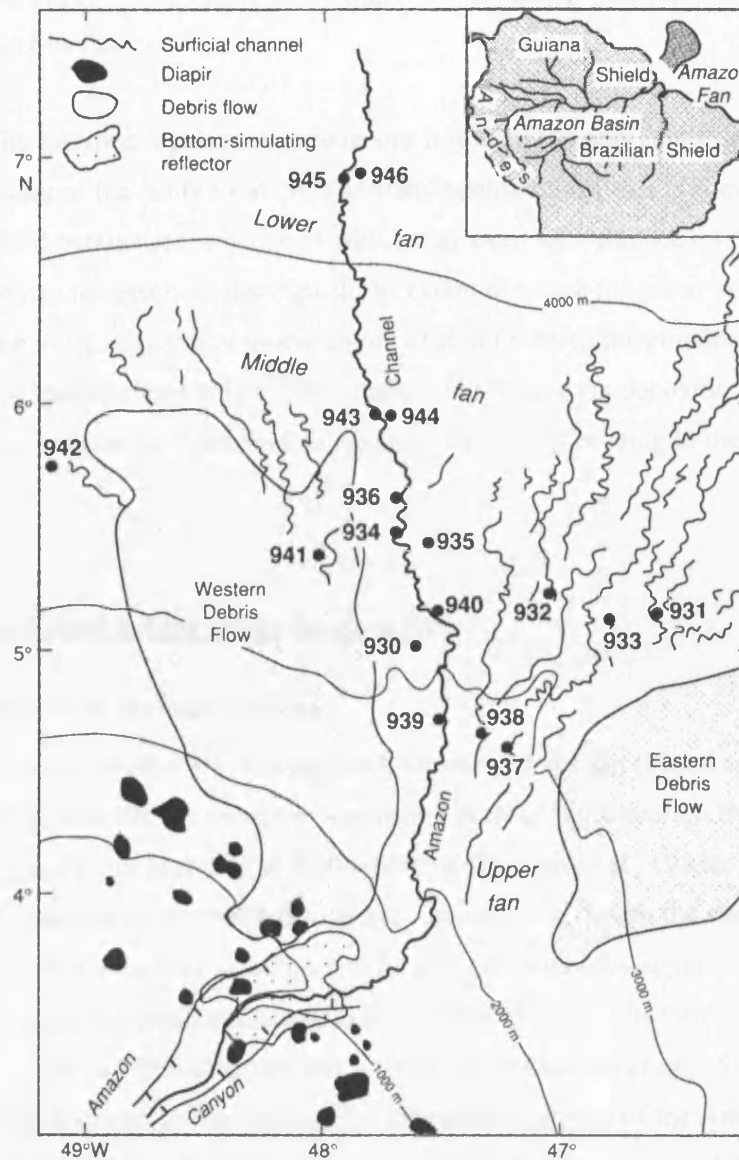


Figure 2.1: Map of Sites drilled from the Amazon Fan during ODP Leg 155. Site 942 is situated to the west of the main fan complex (modified from Flood *et al.*, 1995).

	942 A	942 B	942 C
Position	5°44.546'N 49°5.464'W	5°44.557'N 49°5.460'W	5°44.552'N 49°5.452'W
Water Depth (drill pipe measurement from sea level)	3346.3 m	3345.7 m	3348.8 m
Penetration (m)	177.60	74.00	71.50
Number of cores (inc those with no recovery)	20	8	5
Total length of cored section (m)	177.60	74.00	42.30*
Total core recovered (m)	152.60	56.91	44.03*

Table 2.1: Details of ODP Site 942 on the Amazon Fan. *All details are exactly as quoted in (Shipboard Scientific Party, 1995).

In order to fully interpret a palaeoclimate record it is useful to appreciate the local, regional, and global setting of the study location. The study setting of any site is comprised of a suite of environmental parameters, any one of which may exert an influence on the proxy record analysed. It is also necessary to distinguish the extent to which the proxy record is responding to a local, regional or global signal of change. Such information will enhance the interpretation of palaeoclimate data. This chapter will review the depositional and hydrographic setting of the Amazon Fan, and specific details relating to the setting of Site 942.

2.2 The Depositional Setting of the Amazon Fan

2.2.1 Introduction to the Amazon Fan

The Amazon Fan is the world's third largest modern deep-sea fan (Flood and Damuth, 1987), extending 650-700 km from the continental shelf off northeastern Brazil, as far as the Demerara Abyssal Plain at depths of 4,600-4850 m (Damuth *et al.*, 1983a; Damuth and Kumar, 1975; Damuth *et al.*, 1983b; Flood and Damuth, 1987) with the easternmost portion extending over the Ceara Rise (see Figure 2.2). The Fan measures approximately 380 km in width at the continental shelf, spreading to about 600 km wide at its base, with a longitudinal gradient of ~1:100 to 1:500 (Damuth and Kumar, 1975; Damuth *et al.*, 1983b). Based on morphology and acoustic characteristics, the longitudinal profile of the Amazon Fan is commonly subdivided into three different morphological units, characteristic of nearly all deep-sea fans (see Damuth and Kumar, 1975): the upper fan (shelf break to 2500 – 3000 m); the middle fan (2500 – 3000 to 4000 – 4200 m); and the lower fan (4000 – 4200 to ~4700 m; Damuth and Flood, 1984; Damuth *et al.*, 1988; Damuth *et al.*, 1983a; Damuth and Kumar, 1975; Flood and Damuth, 1987). Details of the fan are shown in Figure 2.3.

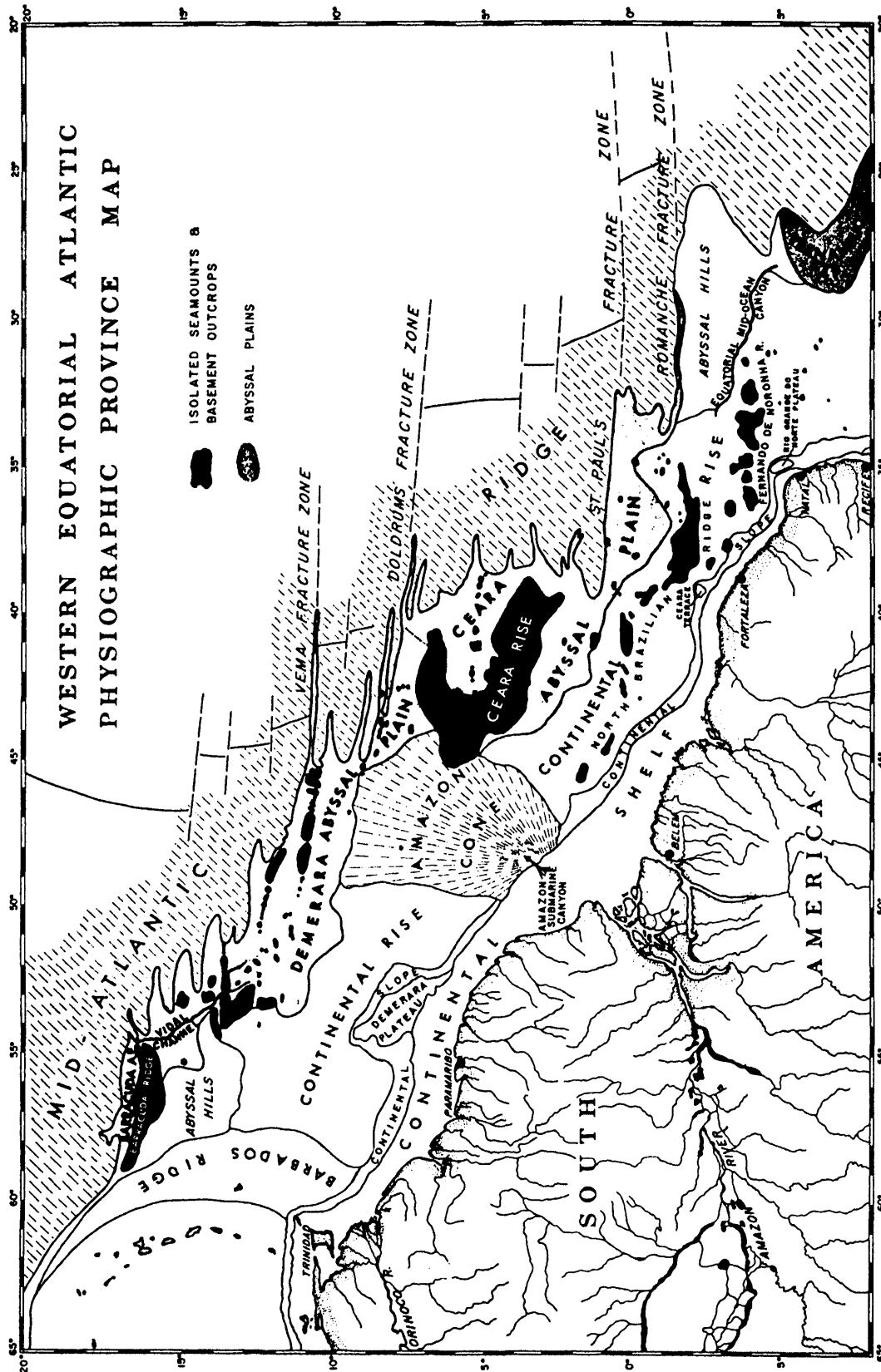


Figure 2.2: A sketch map to show the geographical setting of the Amazon Fan in relation to other bathymetric features off the coast of Brazil (after Damuth, 1977).

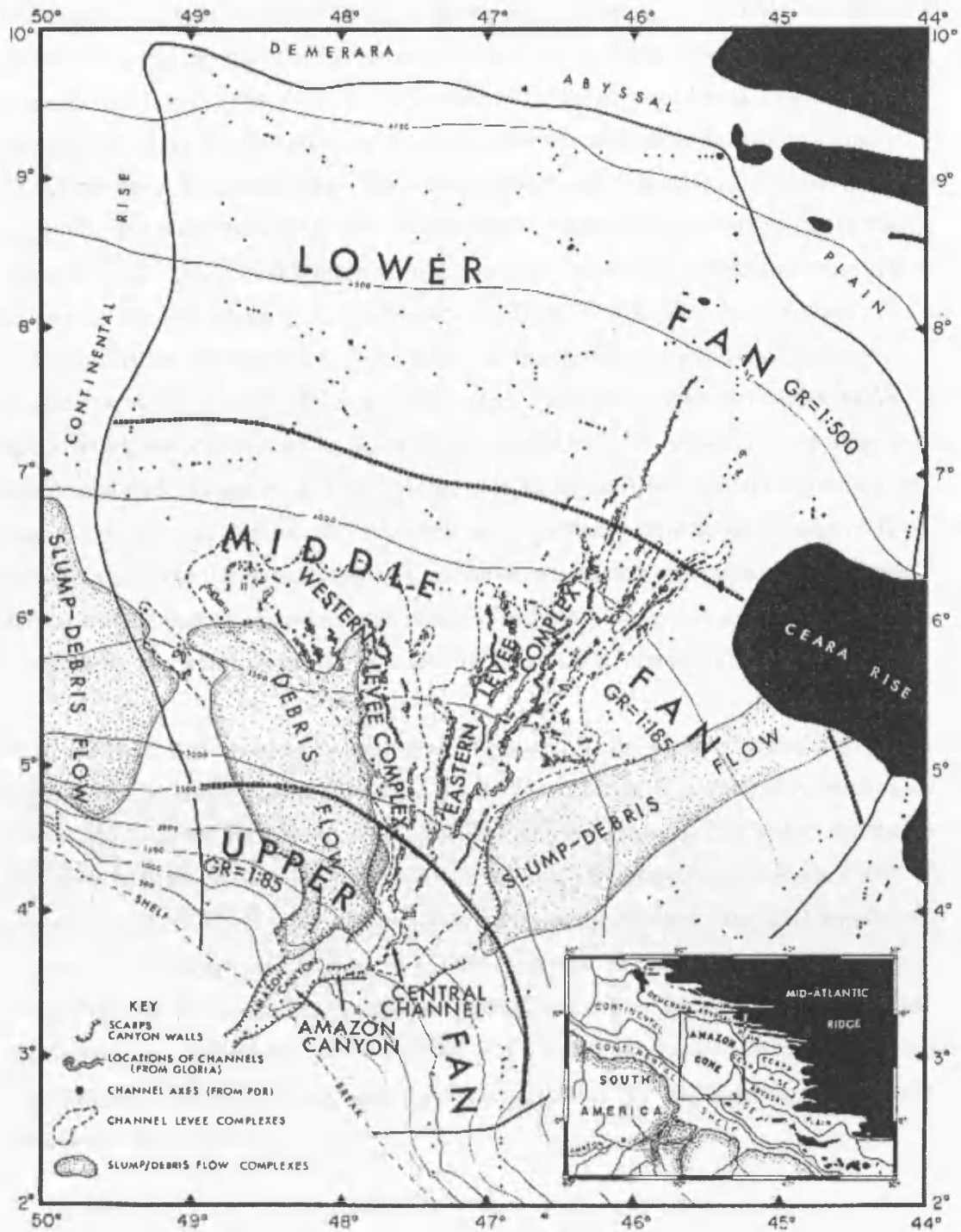


Figure 2.3: A diagram to show the main features of the Amazon Fan, and its location off the edge of the continental shelf, adjacent to the mouth of the Amazon River. Bathymetry is shown in metres. 'GR' denotes gradient (after Damuth *et al.*, 1983b).

The deposition of the Amazon Fan began during the early Miocene (16.5 Ma) in response to the Andean orogeny when the Eastern Cordillera of the northwest Andes was uplifted (Damuth and Flood, 1984; Damuth and Kumar, 1975; Manley and Flood, 1988). Such mountain building diverted the flow of continental water away from the palaeo-Orinoco fluvial system in northwest Amazonia, which drained north toward the Caribbean (Hoorn *et al.*, 1995), and away from the proto-Amazon system, which flowed west toward the Pacific Ocean (Lovejoy *et al.*, 1998). Instead, the active tectonism forced continental water to flow toward the Atlantic Ocean in the east, via the newly evolved Amazon River system (Damuth and Flood, 1984; Damuth and Kumar, 1975). Continental erosion associated with this orogeny would have supplied vast quantities of sediment to the newly evolved Amazon River, which due to lower sea level at this time, would have flowed across the emergent continental shelf (Hoorn *et al.*, 1995). At the shelf edge, the Amazon River incised a deep canyon into the edge of the continental shelf, and deposited sediments on the canyon floor, spreading out onto the abyssal plain to form the deep sea fan. Consequently the channels form a striking feature of the fan, with nearly all radiating outward in a single distributary system from the Amazon Submarine Canyon (Damuth and Kumar, 1975).

With reference to the modern setting shown in Figure 2.3, the Amazon Submarine Canyon extends from at least the 50-m isobath on the continental shelf, to a depth of approximately 1400-1500 m on the fan (Damuth *et al.*, 1983b; Flood and Damuth, 1987). Between the 30- and 50-m isobaths on the outer shelf, a network of small tributary canyons (up to 150 m of relief) converges to form what is known collectively as the Amazon Canyon (Damuth and Kumar, 1975). Bathymetric studies (Ealey, 1969), seismic profiles (Damuth and Kumar, 1975) (Manley and Flood, 1988), and echograms (Damuth and Kumar, 1975) indicate that the canyon has a maximum relief of 500-600 m at 1000 m water depth, taking the form of an 'asymmetric V' in cross-section, with the southeast wall of the canyon being much steeper than that of the northwest.

2.2.2 Sediment Source and Supply

The sediments that make up the fan are principally supplied by the Amazon River, the largest drainage system in the world, discharging approximately 6300 km³ of freshwater into the tropical Atlantic each year (ca. 0.2 Sv, where 1 Sv = 10⁶ m³ s⁻¹; Meade, 1994), which amounts to about 15-20% of the annual global river discharge into the world's oceans (Müller-Karger *et al.*, 1988). The amount of sediment released annually into the Atlantic Ocean is approximately 1.2 × 10⁹ metric tons (1.2 Gt; Meade, 1985; Meade *et al.*, 1985). Although for the majority of its course the Amazon River flows within the lowland basin

(90% of the flow is <2000 m), over 80% of the sediment it carries originates from the Andes (Meade, 1994).

2.2.3 Glacial – Interglacial Sedimentary Regime and the ‘On-Off’ Switch

The Amazon Fan is unique and unusually well structured with numerous channel-levee systems because the supply of sediment to the fan is controlled by glacio-eustatic changes in sea level. Sediment is only able to reach the fan during low stands of sea level when there is increased exposure of the continental shelf. The Amazon River flows across the shelf to eventually deposit its load off the edge of the shelf break (see Figure 2.4). Sediment becomes dispersed onto the fan mainly through the development of distributary-channel-levee systems, and through turbidity flows (Manley and Flood, 1988).

Glacial/Sea Level Low Stand

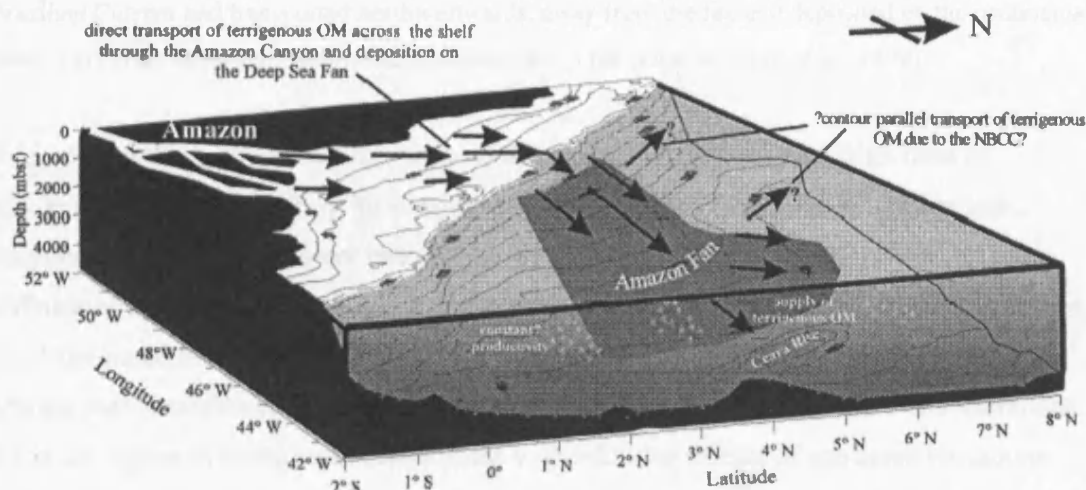


Figure 2.4: Cartoon to illustrate the glacial/sea level low stand deposition of riverine sediments. Sediments are transported directly onto the Amazon Fan. OM= organic matter. “NBCC” = NBC = North Brazil Current (after Schlünz *et al.*, 1999).

During sea level high-stands when the edge of the continental shelf is flooded, the outflow of the Amazon River is focussed relatively further inland. Here, longshore currents transport the sediments northwestwards along the coastline where they are deposited on the continental shelf, inshore of the shelf break (see Figure 2.5). The fan is thus effectively deprived of terrestrial sediment, and consequently does not accrete during sea level high-stands (Damuth and Fairbridge, 1970; Damuth and Kumar, 1975).

Interglacial/Sea Level High Stand

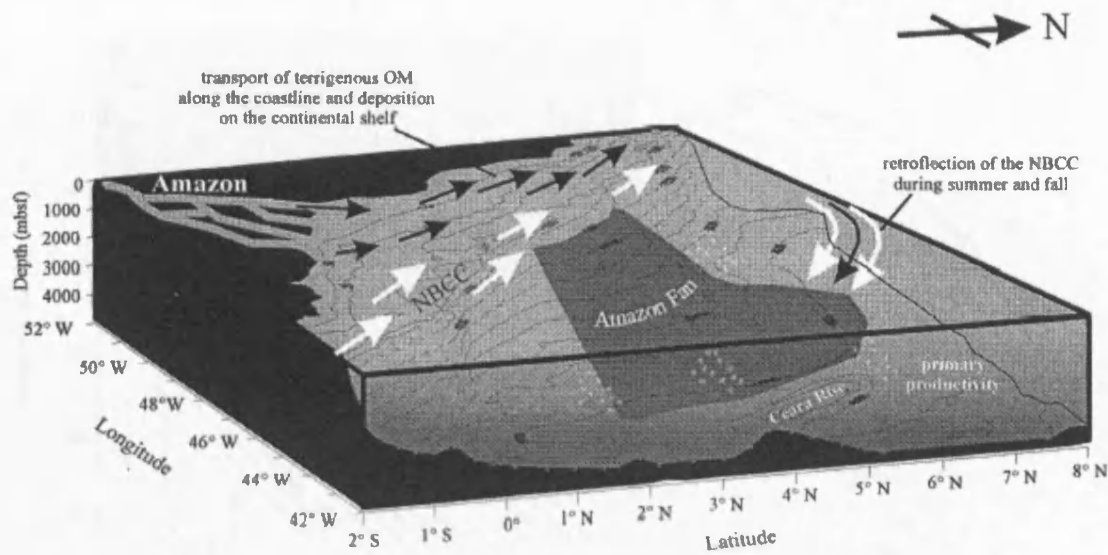


Figure 2.5: Cartoon to illustrate the interglacial/sea level high-stand deposition of riverine sediments. OM= organic matter. “NBCC” = NBC = North Brazil Current. Sediments are entrained in the North Brazilian Current and transported northwestwards, away from the fan and deposited on the continental shelf. Very little terrestrial material accumulates on the fan (after Schlünz *et al.*, 1999).

As a consequence, glacial sedimentation is dominantly terrigenous with high rates of accumulation ($100 \rightarrow 5000 \text{ cm ka}^{-1}$), whereas interglacial sedimentation is hemi-pelagic, accumulating at a much slower rate ($5\text{-}10 \text{ cm ka}^{-1}$; Mikkelsen *et al.*, 1997). Thus, sedimentation on the Amazon fan can be described as being ‘switched on’ during glacial/sea level low-stand periods, and ‘switched off’ during interglacial/sea level high-stand periods. Marine sedimentation remains continuous throughout, although foraminifera concentrations are much higher in interglacial deposits due to the diluting effects of enhanced terrigenous sedimentation during the glacial. The relationship between fan deposition and sea level over the last 80 cal kyr is shown in Figure 2.6. According to Milliman *et al.* (1975), the Amazon Fan was ‘switched on’ when sea levels were at least 30 m lower than present, whereas Schlünz *et al.* (1999) suggest that sea level would have to have been 30-50 m lower. Maslin *et al.* (2000) revised this further to suggest that the Amazon Fan sedimentation would only have switched on when sea level had fallen by 40-50 m. However the different estimates of change required may be attributed to the different sea-level records used in each account.

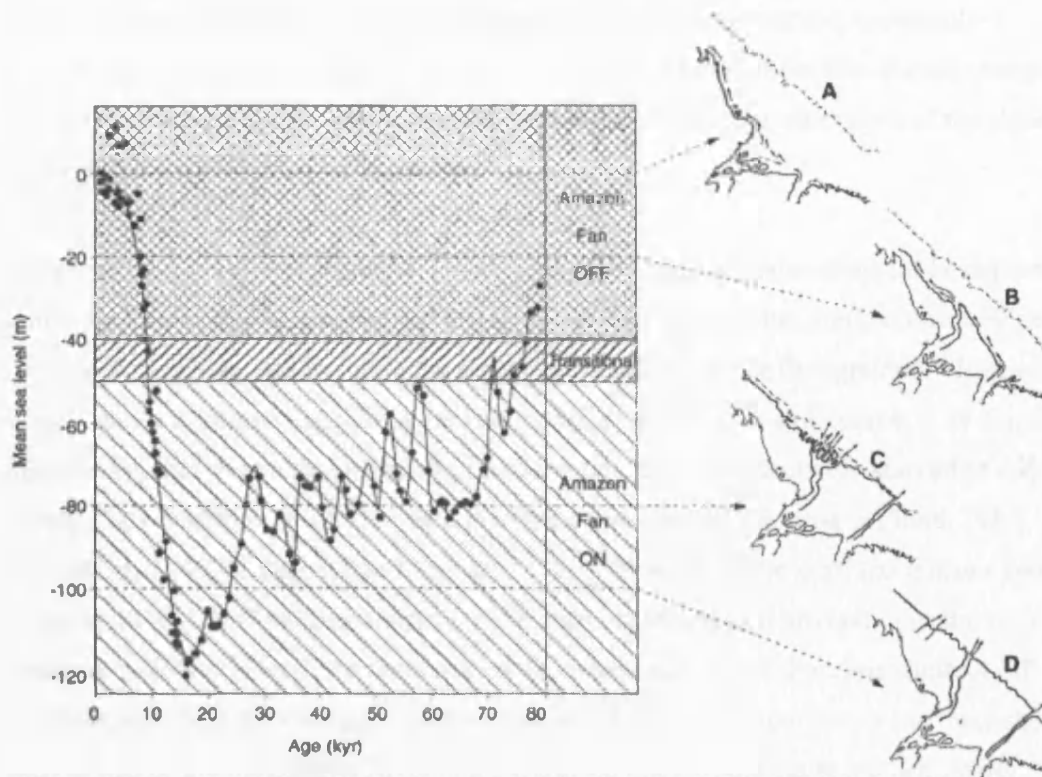


Figure 2.6: A diagram to show the relationship between sea level change and fan sedimentation (after Maslin *et al.*, 2000). Sea level change data are those compiled by (McGuire *et al.*, 1997) based upon Barbados (Fairbanks, 1989) and Pacific (Shackleton, 1987) data, and are compared against marine transgression over the continental shelf (see A-D) described by Milliman *et al.* (1975) and the Amazon River sediment influx (hatching on graph) reconstructed by Maslin *et al.* (2000).

It has been suggested that only one channel-levee system is active at any one given time (Damuth *et al.*, 1988; Damuth *et al.*, 1983a; Damuth *et al.*, 1983b), with the different levee complexes being formed during different low stands. In this way, the following model of fan development has been hypothesised (after Manley and Flood, 1988): as sea level falls, sediments previously trapped on the shelf during sea level high-stands would become transported directly to the deep sea. The consequent increase in sedimentation would lead to the over-steepening of slope deposits, thus inducing large-scale sediment failures on the upper slopes, which in turn would initiate large mass movements and turbidity flows down the fan. Furthermore, renewed sedimentation and a lowering of sea level might destabilise some of the gas hydrate (by altering the depth of some of the gas-hydrate-boundary in the sediment) which would lead to further mass movements (Maslin *et al.*, 1998; McIver, 1982). These debris flows and turbidity currents would then fill the topographic lows, reducing the pre-existing fan topography. With a continued fall in sea level, the Amazon River would start to discharge directly into the deep sea, incising a submarine canyon at the shelf break. Such a localised focus of input of fluvial sediments would create a single point source for

turbidity flows, from which large channel-levee systems would evolve, commonly bifurcating through avulsion to create a levee complex. During these low-stands, slumps, debris flows and turbidity currents would continue to develop on other parts of the slope, although they would be more localised.

With a subsequent rise in sea level, the more coarsely grained material would be deposited relatively further inland, trapped in the aggrading river delta on the shelf, and so sediments entering the canyon, and reaching the fan will be relatively more fine-grained. When sea level is at a maximum (e.g. during the Holocene), all of the river sediment will be deposited directly onto the river delta on the shelf, and the fan becomes effectively starved of sediment supply, thus rendering it inactive, as it is in the modern day (Damuth and Flood, 1985; Damuth *et al.*, 1988; Damuth and Kumar, 1975). The width of the shelf has a major control on the shutting off of sediment supply to the deep ocean and thus abyssal fans: the wide Amazon shelf would lead to a rapid seaward transgression of the shoreline shutting off sediment supply at the very early stages of sea level rise. In comparison, a narrower shelf, such as that of the Magdalena River in the Caribbean Sea would cause a much slower transgression resulting in a more gradual cessation of sediment supply, and sedimentation would thus continue for longer during a period of sea level rise (McGeary and Damuth, 1973). Other factors affecting sediment supply would include the depth of the shelf edge, the volume and velocity of river flow, and the amount of continental erosion.

However, if the river delta prograded to the shelf break during a sea level high-stand the, fan sedimentation could be re-established with further channel levee development. Throughout the present interglacial high-stand (~10 kyr) however, the modern Amazon River delta has prograded only one third the distance across the shelf break (Nittrouer *et al.*, 1986), although if the high-stand persists for an extended time, then the delta may well accrete to the shelf edge. Progradation could also be enhanced if the Amazon Canyon cuts further landward across the outer shelf (Farre *et al.*, 1983).

However, although this may explain the cyclic pattern of deposition observed in both ancient and modern submarine fan systems (see for example Droz and Beallaiche, 1985; Feeley *et al.*, 1985; Mitchum, 1985; Mutti, 1985; Mutti and Zuffa, 1985; Weimer and Buffler, 1989), attempts at relating these cycles to changes in sea level has frequently been limited by poor age control (Manley and Flood, 1988).

At times, successive channel-levee systems may follow the same upstream path, which gives rise to the grouping of individual channel-levee units into channel-levee complexes: the Upper, Middle, Lower and Bottom Levee Complexes. These occupy geographically distinct areas of the fan and are commonly separated from each other by mass-transport deposits and flat-lying seismic reflections (see Figure 2.3; Damuth *et al.*, 1983a; Flood and Piper, 1997). Previous workers on the Amazon Fan (Damuth *et al.*, 1983a; Manley and Flood, 1988) have assigned names to all the recognised channel-levee systems as shown in stratigraphic order in Table 2.2. Of these, the systems of the Upper Levee Complex were thought to have been active during the last 40 kyr (Flood and Piper, 1997).

	Western fan*	Central fan	Eastern fan
Upper Levee Complex		Amazon Brown Aqua	} (=1) Channel 5* Channel 6A* Channel 6B* Channel 6C*
	Purple (= 2)	Blue (= 3) Yellow (= 4)	
		Orange*	
		Unit R Debris Flow	
Middle Levee Complex		Red	
		Debris flow	
Lower Levee Complex		Green Gold Lime Gray	
		Debris flow	
Bottom Levee Complex			

Notes: *High-resolution seismic data are not available from most of the western fan.
*The age relationship between Orange and Channels 5 and 6A, 6B, and 6C has not been clearly delineated from seismic profiles.

Table 2.2: Summary of stratigraphic nomenclature of the Amazon Fan (after Damuth *et al.*, 1983a; Flood and Piper, 1997; Manley and Flood, 1988).

2.3 The Hydrographic Setting of the Amazon Fan

2.3.1 Introduction

The Amazon Fan is situated beneath the modern trajectory of the North Brazilian Current (NBC), details of which are reviewed in the following section.

2.3.2 The North Brazilian Current (NBC)

The western Tropical Atlantic is an important area for global thermohaline circulation as a number of important currents flow in this region. Of these, the NBC is perhaps one of the most important. The modern NBC is a warm water western boundary current flowing north

of 10°S along the Brazilian continental slope (da Silveira *et al.*, 1994). Western boundary currents are characteristically fast, intense, deep and narrow in their nature (Colling, 2001) and results to date document the NBC as transporting 14-18 Sv within the upper 500 m of the water column (da Silveira *et al.*, 1994). In the literature, the NBC has been referred to by a variety of names (e.g. the North Brazilian Current, North Brazilian Coastal Current, Brazilian Coastal Current), but herein after it shall be referred to as the North Brazilian Current (NBC), the convention employed by the FOCAL/SEQUAL (Programme Français Océan et Climat dans l'Atlantique Equatorial/Seasonal Response of the Equatorial Atlantic) and WOCE (World Ocean Circulation Experiment) programs.

The NBC is extremely significant to studies of the Amazon Fan as it is the dominant ocean current influencing the distribution of the fresh water and sediment plume discharged by the Amazon River. The NBC is highly unique in that it is the only known modern surface water current to cross the equator as part of the Atlantic meridional overturning cell (Johns *et al.*, 1998; Metcalf and Stalcup, 1967; Richardson and Walsh, 1986). It therefore acts as an important upper-ocean vector of both heat and salinity between the two hemispheres (Flood and Piper, 1997). Numerous investigations into the Northern Hemisphere fate of Amazon River water have confirmed its presence in the Caribbean Sea, (e.g. Borstad, 1982; Bowles and Fleischer, 1985; Dessier and Donguy, 1993; Deuser *et al.*, 1988; Froelich *et al.*, 1978; Hellweger and Gordon, 2002; Kelly *et al.*, 2000; Moore *et al.*, 1986; Müller-Karger *et al.*, 1988; Signorini *et al.*, 1999; Steven and Brooks, 1972), an area of significant importance to global oceanography, as shown in Figure 2.7.

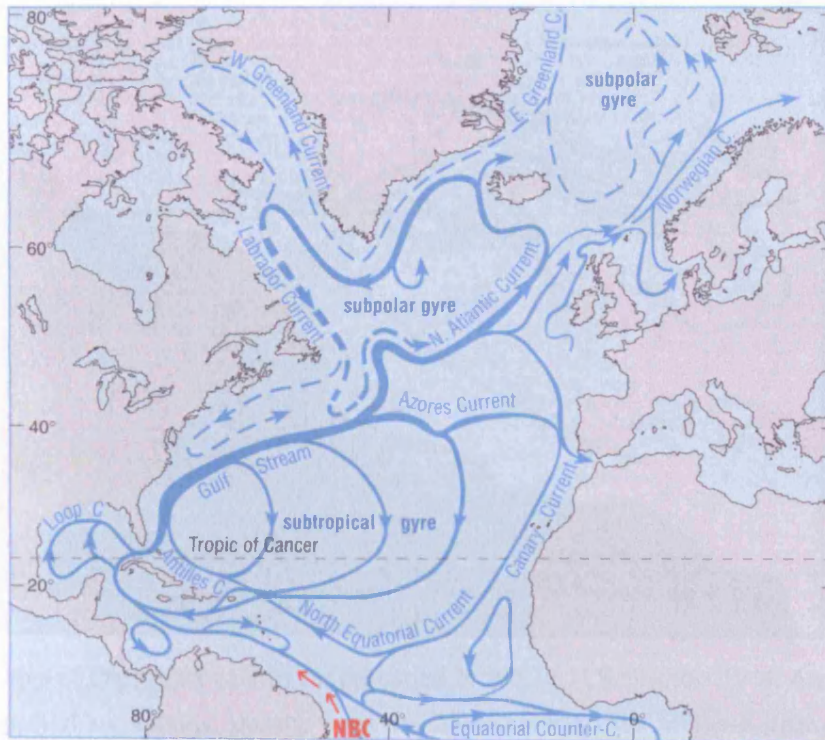


Figure 2.7: Cartoon to illustrate the significance of the North Brazilian Current (NBC) to oceanic circulation in the north Atlantic (modified from Colling, 2001). 'C' denotes 'current'.

The plume of fresh water flowing out from the Amazon is clearly identifiable in satellite imagery of backscattered colour radiance (e.g. Figure 2.8), and in distributions of sea surface salinity (e.g. Figure 2.9). Over the Amazon Fan, the modern-day mixing between waters of the Amazon River and Atlantic Ocean takes place in the ratio 1:5, respectively (Levitus, 1982).

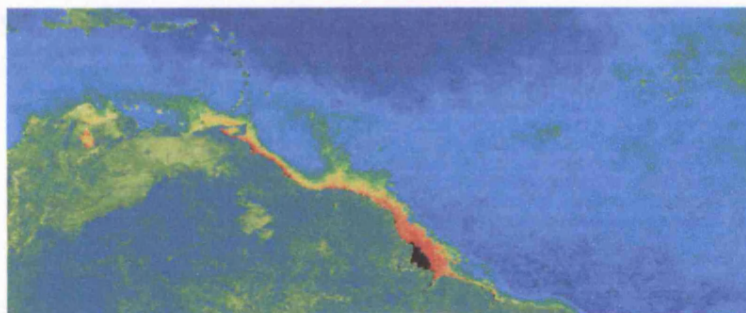


Figure 2.8: SeaWiFS satellite colour reflectance imagery of the Amazon River plume, shown as black and red/yellow/green colours (NASA, 2002).

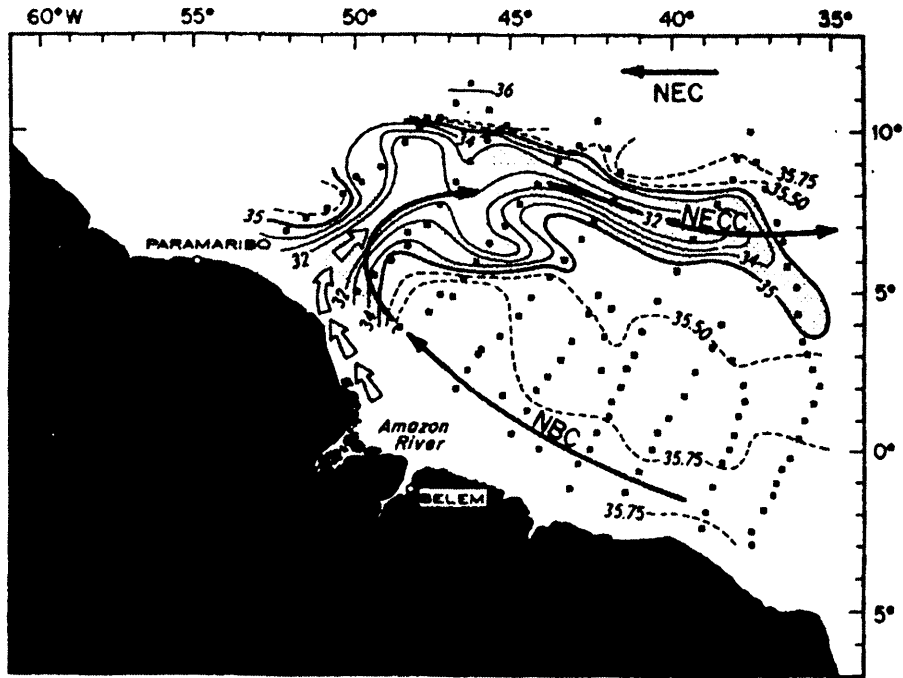


Figure 2.9: Map of sea-surface salinity for the period 24 July to 11 September 1964. Arrows indicate the inferred path of low-salinity Amazon water and major currents (after Müller-Karger *et al.*, 1988).

Lenses of low-salinity surface water resulting from dilution by the Amazon plume may extend up to 100-120 km offshore, occasionally becoming detached and thence becoming entrained by the local ocean currents (Gibbs and Konwar, 1986; Nittrouer and DeMaster, 1986). The patterns of plume dispersal may vary from year to year, as shown in Figure 2.10 (Müller-Karger *et al.*, 1988). During sea level low-stands however, the river would have discharged directly into relatively deep water and mixing of the river plume into the coastal water might have occurred more slowly than at present allowing more extensive freshwater lenses to form (Flood *et al.*, 1995). Variations in the strength of the NBC may also have resulted in locally fresher or saltier surface waters, and evidence for this may be present in the oxygen isotope record (Flood and Piper, 1997).

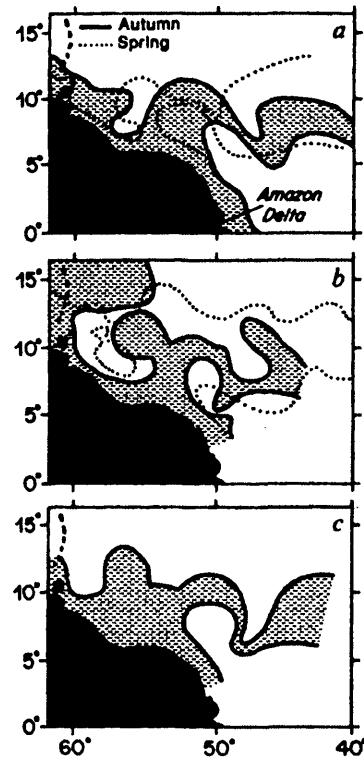


Figure 2.10: Schematic representation of the Amazon River plume as observed in seasonal composites of NASA's Coastal Zone Colour Scanner (CZCS) images for (a) 1979, (b) 1980, and (c) 1981. Shaded areas show plume extent for June-January, broken lines show plume extent for February-May (after Müller-Karger *et al.*, 1988).

Although the size and shape of the discharge plume will be influenced by factors such as wind forces, the structure of the NBC and the seasonal variations in the quantity of river outflow (Didden and Schott, 1993; Fratantoni *et al.*, 1995; Goni and Johns, 2001; Hellweger and Gordon, 2002; Johns *et al.*, 1990; Lenz, 1995), Helwegger and Gordon (2002) calculate that it takes around two months for water discharged by the Amazon River to reach Barbados. The authors also propose that the depth of vertical mixing also increases with distance from the mouth of the river, being 15 m, 30 m and 45 m depth at 900 km, 1800 km and 2600 km distance from the Amazon mouth, respectively.

The cross-equatorial transport of the NBC has extremely important implications for global ocean dynamics and inter-ocean heat transfer (Metcalf, 1968; Metcalf and Stalcup, 1967). Such transport will help to balance the southward interhemispheric transport of cold North Atlantic Deep Water and to close the meridional overturning cell of the global thermohaline circulation (Fine and Molinari, 1988; Gordon, 1986). It also closes the wind-driven equatorial gyre circulation, and feeds a complex system of zonal countercurrents in the region (Johns *et al.*, 1998). Rivers are important variables in oceanography as their

freshwater affects the sea surface salinity and thus buoyancy of the surface layer (Hellweger and Gordon, 2002). Therefore any variation in the discharge and/or transport of Amazon River water has the potential to have far-field implications for ocean circulation and global climate. This is also of significance to reconstructing past regimes, as during glacial times, different surface wind patterns combined with narrower shelves may have meant that ocean circulation patterns of the western equatorial tropical Atlantic could at times have been very different from circulation regime observed in the modern day (Flood and Piper, 1997).

2.3.3 Origins and Structure of the NBC

The origins and structure of the NBC have been a matter of great debate in the past literature and continue to be a subject of ongoing study at the current time. The main components of the NBC system are shown schematically in Figures 2.11 and 2.12, in multi-dimensional and planar view, respectively.

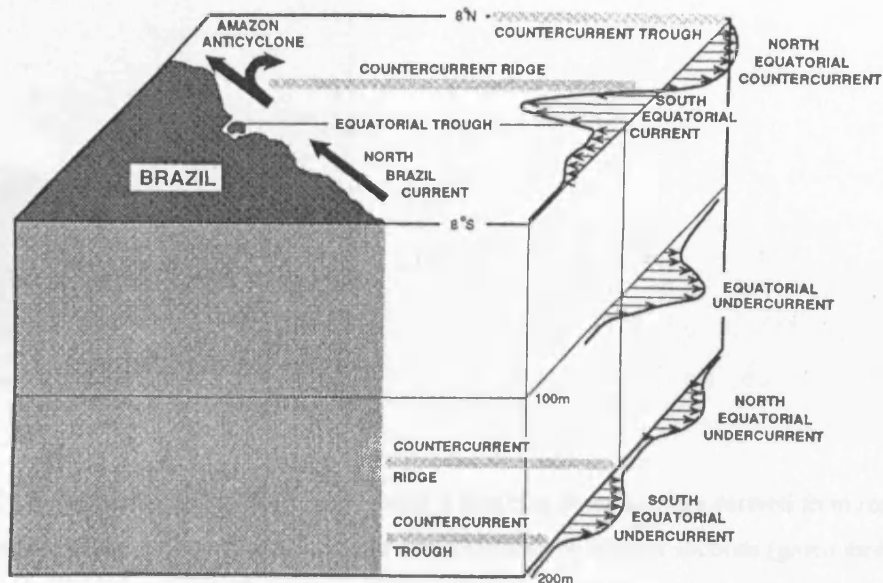


Figure 2.11: A schematic diagram of the modern mean upper ocean circulation pattern of the western tropical Atlantic Ocean (after Wilson *et al.*, 1994).

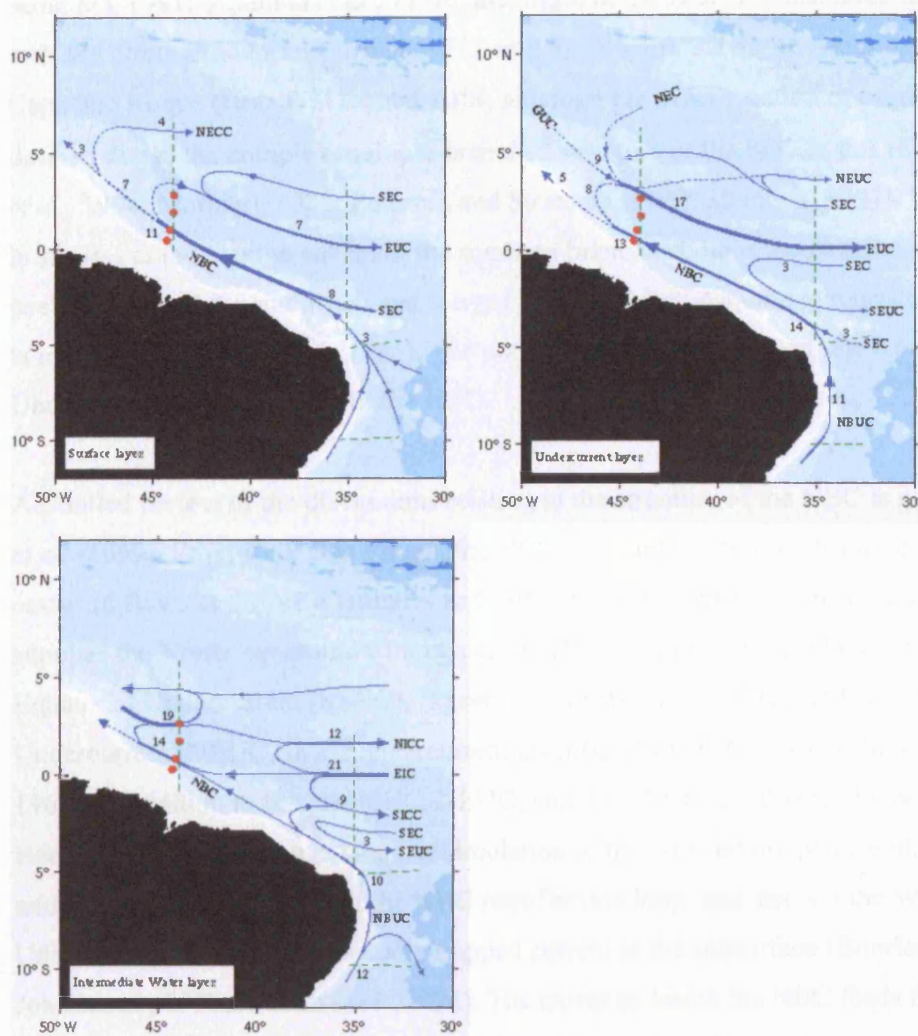


Figure 2.12: Circulation in the Western Tropical Atlantic in density layers derived from repeated sections of water mass properties and current measurements by Meteor sections (green dashed lines) and moored arrays (red dots). The Surface layer reaches from the surface to the 24.5 isopycnal, the Central layer is defined between the 24.5 and 26.8 isopycnals, and the Intermediate layer from 26.8 down to 1000 m depth. Numbers are for the transports (in $Sv = 10^6 \text{ m}^3 \text{ s}^{-1}$) of current branches. Abbreviated as follows: NBC: North Brazilian Current; NBUC: North Brazil Undercurrent; SEC: South Equatorial Current; NEC: North Equatorial Current; GUC: Guyana Undercurrent; NECC: North Equatorial Countercurrent; SECC: South Equatorial Countercurrent; NEUC: North Equatorial Undercurrent; SEUC: South Equatorial Undercurrent; EUC: Equatorial Undercurrent; NICC: Northern Intermediate Countercurrent; SICC: Southern Intermediate Countercurrent; EIC: Equatorial (Intermediate) Undercurrent (modified from <http://www.ifm.uni-kiel.de/fb/fb1/research/woce/woce-ao.html>).

According to a number of publications (e.g. Bischof *et al.*, 2001; Schott *et al.*, 1995; Stramma, 1991; Stramma *et al.*, 1990), the origin of the NBC is considered to be associated with the South Equatorial Current (SEC) as it approaches the South American Coast near to Cape São Roque (Brazil) at around 10°S; although the exact location of origin is poorly defined due to the complex multiple-branched structure of the SEC in this region (da Silveira *et al.*, 1994; Molinari, 1982; Peterson and Stramma, 1990; Stramma, 1991). Where the SEC bifurcates at the continental shelf, the southern branch becomes the Brazil Current, which peels off toward the southwest and merges with the South Atlantic gyre system (da Silveira *et al.*, 1994; Stramma *et al.*, 1995). The northern branch merges with the North Brazil Undercurrent (NBUC) to form the NBC.

A detailed review of the discussions relating to the structure of the NBC is given in Bourlès *et al.* (1999). From Cape São Roque, the NBC is thought to feed both surface and subsurface eastward flows at different latitudes and different depths, where from south to north it supplies the North Equatorial Countercurrent (NECC) in the surface layer; and the South Equatorial Undercurrent (SEUC), Equatorial Undercurrent (EUC), and North Equatorial Undercurrent (NEUC) in the undercurrent layer (Cochrane *et al.*, 1979; Metcalf and Stalcup, 1967). In addition to this, the EUC, NEUC, and the NECC are also fed by Northern Hemisphere waters via a cyclonic recirculation of the NEC taking place within the undercurrent layer to north of the NBC retroflexion loop, and also via the Western Boundary Undercurrent (WBUC), a coastally trapped current at the subsurface (Bourlès *et al.*, 1999; Johns *et al.*, 1990; Wilson *et al.*, 1994). The extent to which the NBC feeds these currents also varies according to the season, which will thus also influence the nature and extent of interhemispheric ocean transport.

2.3.4 Interhemispheric Ocean Transport

Direct interhemispheric ocean transport typically takes place from around February to June (around austral autumn; see Figure 2.13, left) when NBC waters flow directly toward the Northern Hemisphere. Early models suggested this was in the form of a continuous boundary flow from south of the equator toward the Caribbean Sea (Philander and Panakowski, 1986; Picaut *et al.*, 1985). However later studies have suggested that this is actually via a reversed flow of the Northern Equatorial Counter Current (NECC; for details see Wilson *et al.*, 1994) which in turn feeds the northerly Guyana Current flowing into the southern Caribbean Sea (Johns *et al.*, 1998; Metcalf and Stalcup, 1967; Schott *et al.*, 1998).

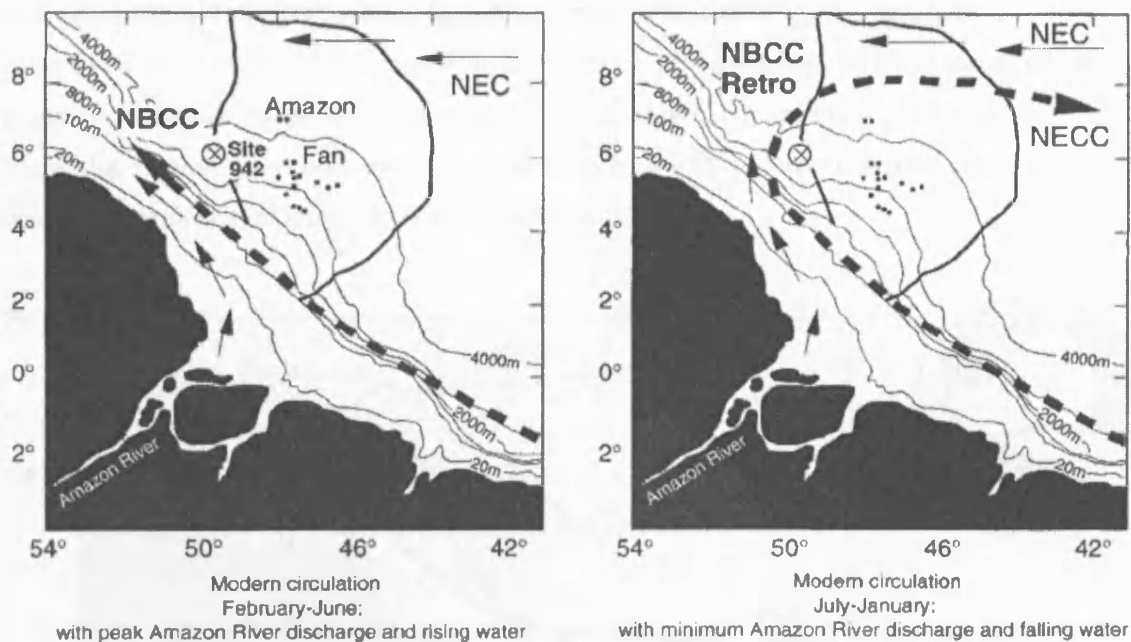


Figure 2.13: A cartoon detailing the main features of the North Brazilian Current (NBCC on figure) for the periods February–June (left) and July–January (modified from Maslin *et al.*, 2000) in relation to ODP Site 942 on the Amazon Fan. NEC = North Equatorial Countercurrent. NECC = North Equatorial Current. Depth contours refer to the relief of the sea floor. Small squares indicate locations of other Sites drilled during ODP Leg 155.

From July to January (austral winter to austral summer), the NBC typically turns (retroreflects) into the eastward-flowing Northern Equatorial Counter Current (NECC) south of the equator (see Figure 2.12, right Flood and Piper, 1997). Inshore of the NBC retroflexion, there may be an enhancement in localised upwelling related to the offshore transport of water (Müller-Karger *et al.*, 1988). This may be associated with a rise in the local seasonal thermocline, as suggested by model reconstructions (Ravelo, unpublished, cited in Greig, 1998). However, the extent of the retroflexion remains uncertain. Where Wilson *et al.* (1994) and Boulès *et al.* (1999) suggest that the NBC retroflexion is total from June to January, Schott *et al.* (1998; 1995) and Johns *et al.* (1998) propose the NBC system continues to have a boundary flowing component through to boreal spring.

Nevertheless, cross-equatorial transport is in fact a year-round phenomenon as during the retroflexion period, the NBC frequently closes in on itself to form numerous anticyclonic ring eddies (see Figure 2.14). These NBC retroflexion rings continue to flow northwestwards across the equator, and represent a significant source of water to the Caribbean Sea (Hellweger and Gordon, 2002; Johns *et al.*, 1998; Johns *et al.*, 1990). On average, NBC rings form 5-6 times per year, propagating at 14 km/day, each having a radius

of approximately 100-200 km (Goni and Johns, 2001; Johns *et al.*, 1990), and have a duration of about 100 days (Bischof *et al.*, 2001). Each ring transports ~ 1 Sv of water, which is approximately one third of the interhemispheric meridional overturning cell (Goni and Johns, 2001). NBC rings may be responsible for up to 3-4 Sv of direct transport across the equatorial tropical gyre boundary (Fratantoni *et al.*, 1995).

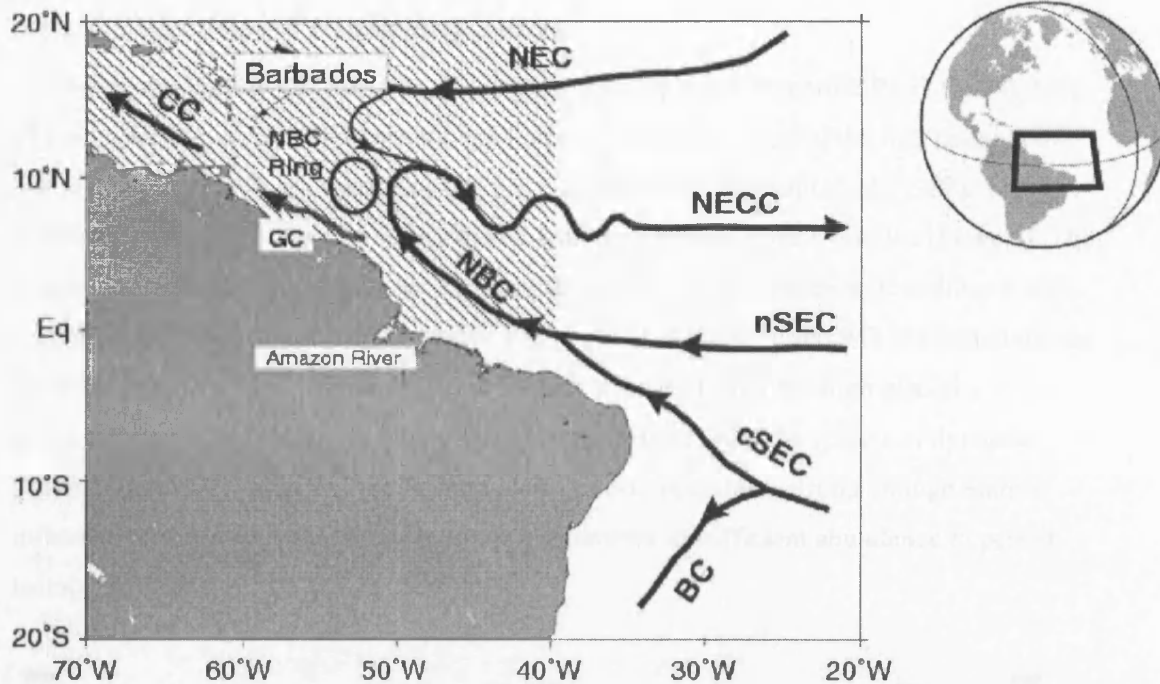


Figure 2.14: A cartoon illustrating the formation of North Brazilian Current Rings during retroflexion periods (after Goni *et al.*, 2003). NBC = North Brazil Current. NEC = North Equatorial Current. NECC = North Equatorial Countercurrent. nSEC/cSEC = northern/central South Equatorial Current. CC = Caribbean Current. BC = Brazilian Current. GC = Guiana Current.

Large spatiotemporal variations in the regional hydrography, coupled with the NBC retroflexion rings make it very difficult to quantify the mean and seasonal transports and water mass-contents of the different currents in this region (Didden and Schott, 1993; Johns *et al.*, 1998; Johns *et al.*, 1990; Schott *et al.*, 1993). Schmitz and McCartney (1993) and Schmitz (1995) estimate the modern overturning cell to comprise between 13 and 17 Sv (c.f. the Gulf Stream, 31 to 150 Sv; Hogg and Johns, 1995). However, Wilson and Johns (1997) estimate that 8 Sv of water of southern origin contribute to the northern Atlantic thermohaline cell through the southern passages of the Caribbean Sea, via the northwestward route along the American coast. Recent studies suggest that after being carried eastward by the NBC retroflexion and then westward in the North Equatorial Current (NEC), waters of South Atlantic origin must then join the Florida Current in the Northern Hemisphere (Mayer and Weisberg, 1993; Wilson and Johns, 1997). Schmitz and Richardson (1991) and Schmitz

(1995) estimate the transport of southern-origin waters in the Florida Current to be 13-14 Sv. However Wilson and Johns (1997) also evoke the possibility that the Florida Current may not act as a vector of South Atlantic water toward the northern high latitudes at all.

2.4 Setting of ODP Site 942 on the Amazon Fan

2.4.1 Site Location and Sedimentary Setting

A detailed description of ODP Site 942 is given by Shipboard Scientific Party (1995). Site 942 is located on a crest of an abandoned levee to the western side of the fan, rising above one or more debris-flow deposits (see Figures 2.1 and 2.14; Damuth *et al.*, 1988). This former channel is proposed to be associated with the Middle Levee Complex (Stage 6). The location of Site 942 was chosen for its potential to accumulate hemipelagic sediment with minimal reworking (Shipboard Scientific Party, 1995). Although Site 942 is situated off the main fan complex itself, it remains close enough to benefit from the high glacial sedimentation rates, yet its location is sufficiently isolated from the effects of dynamic sediment transport higher up the fan structure. It also maintains a strong enough marine influence throughout, so as to accumulate foraminifera in sufficient abundance to permit isotope analysis.

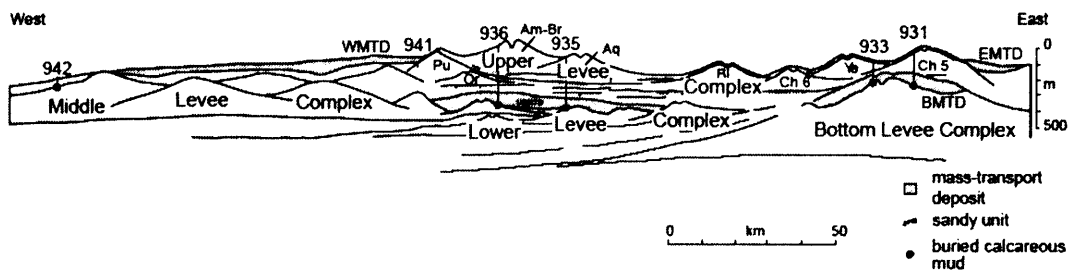


Figure 2.15: The location of ODP Site 942 on the Middle Levee Complex, as shown on a cross-section through the Amazon Fan (modified from Flood and Piper, 1997).

As shown in Figure 2.16 the levee crest and channel appear to be covered with at least 50 m of conformable, acoustically stratified sediment, which suggests that the channel has not been active for some period of time. About 400 m southeast of Site 942 at a depth of about 15 mbsf, the sediment is intercalated with a wedge of debris-flow material, thought to be associated with the Western Debris Flow. This acts to seismically obscure the levee so it cannot be tied to the other channel-levee systems on the central Amazon Fan (Shipboard Scientific Party, 1995), although it has been speculated that the levee of Site 942 is associated with the purple channel system (Flood *et al.*, 1995).

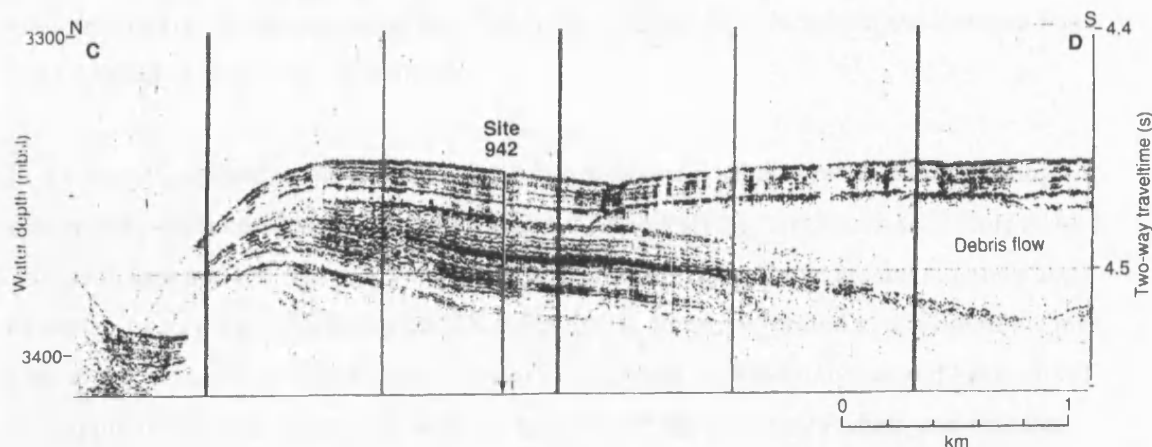


Figure 2.16: 3.5-KHz seismic profile illustrating the sedimentary stratigraphy at Site 942 (after Shipboard Scientific Party, 1995).

2.4.2 Sampling Strategy and Sediment Description

Sediments from Site 942A and 942B were subsampled at the Bremen ODP Core Repository during January 2001 (see Section 2.1). Isotope data presented in this study from 942C are those of Greig (1998), Maslin (2000), and Maslin (2000) measured on material previously subsampled on-ship in 1994. 942A sediment was continuously subsampled every centimetre in one-centimetre thick units (five cubic centimetres [cc]) to a depth of 0.5 metres below sea floor (mbsf). 942B sediment was collected at similar one centimetre resolution for the first ~0.95 mbsf, and then every three centimetres in two-centimetre thick units (20 cc) thereafter to a depth of 15 mbsf. This sampling regime was devised to take account of the switch between relatively faster hemipelagic to relatively slow pelagic sedimentation rate near to the Pleistocene/Holocene boundary (see Chapter 5). This ‘switch’ was clearly evident in the Core lithostratigraphy as a marked transition between two distinct units; from glacial-stage foraminifera-poor, slight-moderately bioturbated, terrigenous clay-rich muds, silts and very fine sands (Unit I), to Holocene hemi-pelagic slightly bioturbated, foraminifera-nannofossil-rich clays (Unit II). A detailed sediment description can be found in Shipboard Scientific Party (1995). Near to the boundary between these two units was a diagenetic iron-rich crust, a feature common across the majority of the Amazon Fan (Shipboard Scientific Party, 1995).

2.4.2a Iron-Rich Crust in 942 Sediments

Between 0.70–0.80 mbsf, an iron-rich crust (hereafter referred to as the ‘Fe-crust’) separates the terrigenous hemipelagic glacial deposits, from the calcium carbonate-rich sediments of the Holocene. This Fe-crust is not unique to Site 942, and has been found to be an extensive occurrence across the Amazon Fan, and adjacent continental rise and abyssal plains of the

western Atlantic. A detailed study and discussion of these deposits within the Amazon Fan can be found in McGeary and Damuth (1973).

In addition to separating the two different lithologies, the crust also marks a sharp change in colour and oxidation state within the sediment. The underlying terrigenous sediments adopt a greyish colour and are reduced, whereas those sediments lying above are tan in colour and oxidised. According to McGeary and Damuth (1973), the crust formed as a result of the postglacial rise in sea level (specifically the post Termination 1a [GS1]) that would have cut off the supply of terrigenous material to the deep water off the continental shelf, and thus the Fan. Decaying organic matter within the deposited sediment of the fan is thought to have reduced the Fe within the terrigenous minerals, which dissolved within the interstitial water, and was then expressed upwards within the sediment column during compaction. Upon reaching the sediment-water interface, the Fe was re-oxidised, and re-precipitated to form an iron-cemented crust within the sediment, since buried by postglacial Holocene pelagic deposition (see Figure 2.17).

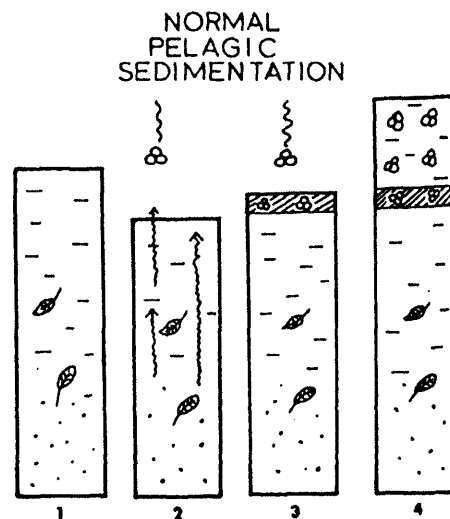


Figure 2.17: A proposed sequence of iron-rich crust formation for environments such as the Amazon Fan (modified from McGeary and Damuth, 1973).

From analysing 19 piston cores taken from the Amazon Fan, McGeary and Damuth (1973) found that although the position of the Fe-crust lay at or near to the Pleistocene-Holocene boundary, its location was not isochronous, and varied by as much as 30 cm above and below the boundary. The authors concluded that the time of the crust formation in any area appeared to be dependant upon the '*remoteness of that area from sources of terrigenous sediment on the South American continent, mainly the Amazon River*' (McGeary and Damuth, 1973 p. 1204), with areas distal from the abyssal plains and the lower continental rise having crusts well below the boundary, whereas close to the mouth of the Amazon and

smaller rivers, the crust lies at or above the boundary. The authors suggested that taking into account local pelagic Holocene sedimentation rates (which in their cores were 3–8 cm kyr⁻¹), the crust always seemed to form within 3000 years of the Pleistocene-Holocene boundary, and in the majority of cases, formed slightly below the boundary in response to the rise in sea level just prior to the onset of the Holocene.

Fe-crusts of a comparable age and chemically similar to those of the western equatorial Atlantic have been found elsewhere in a number of marine sequences, including an area in the northwest Pacific Ocean, east of Japan; the Sierra Leone Basin off western Africa; the Ganges abyssal fan in the Bay of Bengal; the western Mediterranean Sea; the Coral Sea; south of Hawaii; and the Delgada Fan near to the Mendocino Fracture Zone, coastal northern California. Others have been visually identified (although not chemically constrained) in the Mississippi fan in the Gulf of Mexico; the Magdalene River abyssal fan in the Caribbean Sea; a location south of Java in the eastern Indian Ocean; the Blake-Bahama Outer Ridge off southeastern USA; the eastern Mediterranean, and possibly off the coast of Norway (see review in McGeary and Damuth, 1973). It is notable that most of these areas with Fe-crusts have a similar sedimentary regime to the Amazon Fan, and in each case the time of crust formation appears to coincide consistently with the Pleistocene-Holocene transition when terrigenous sedimentation to the deep sea was halted due to post-glacial sea level rise (McGeary and Damuth, 1973).

2.4.2 Hydrographic setting

Of the 17 Sites drilled from the Amazon fan, Site 942 is particularly good for monitoring the modern outflow of the Amazon River. Analyses of surface sediments from across the fan show that 10%-30% of the diatoms are of freshwater origin except at Site 942, where ~75% of the diatoms are freshwater species (Mikkelsen *et al.*, 1997). This higher percentage abundance is likely to reflect the influence of the freshwater plume discharged by the Amazon River, which is either being transported northward by ocean currents, or is breaking away and moving offshore. Based upon this analogy, Site 942 therefore has good potential for monitoring Amazon River outflow in the past.

However, where diatoms are relatively concentrated at the surface, *in situ* dissolution causes a progressive decrease in abundance through the Holocene, to a sustained permanent absence at the transition to the glacial sediments. Therefore the diatom archive cannot be used to identify continental climate-driven variations in river discharge or past changes in surface circulation. Alternatively, the high abundance of freshwater diatoms in the surface sediments

in Site 942 could be the result of a relatively recent northward deflection of the Amazon freshwater plume caused by a more recent change in the prevailing ocean currents (Flood and Piper, 1997; Mikkelsen *et al.*, 1997). It is therefore preferable to 'validate' palaeoclimate data from the Amazon Fan against a variety of other palaeoclimate records from different archives and different geographical locations across northern South America. Through employing such a multi-proxy approach, it should be possible to use records obtained from ODP Site 942 to attempt to decipher past environmental changes for the Amazon Basin.

2.5 References

- Bischof, B., Mariano, A. J., and Ryan, E. J. (2001). The North Brazil Current. HYCOM Consortium for Data Assimilative Modeling; <http://oceancurrents.rsmas.miami.edu/index.html> (accessed 22/10/03).
- Borstad, G. A. (1982). The influence of the meandering Guiana Current and Amazon River discharge on surface salinity near Barbados. *Journal of Marine Research* **40**, 421-434.
- Bourlès, B., Gouriou, Y., and Chuchla, R. (1999). On the circulation in the upper western equatorial Atlantic. *Journal of Geophysical Research* **104**, 21151-21170.
- Bowles, F. A., and Fleischer, P. (1985). Orinoco and Amazon River sediment input to the eastern Caribbean Basin. *Marine Geology* **68**, 53-72.
- Cochrane, J. D., Kelly, F. J., Jr., and Olling, C. R. (1979). Subthermocline countercurrents in the western equatorial Atlantic Ocean. *Journal of Physical Oceanography* **9**, 724-738.
- Colling, A. (2001). "Ocean Circulation." Butterworth Heinemann in association with The Open University, Oxford.
- da Silveira, I. C. A., de Miranda, L. B., and Brown, W. S. (1994). On the origins of the North Brazil Current. *Journal of Geophysical Research* **99**, 22501-22512.
- Damuth, J. E. (1977). Late Quaternary sedimentation in the western equatorial Atlantic. *Geological Society of America Bulletin* **88**, 695-710.
- Damuth, J. E., and Fairbridge, R. W. (1970). Equatorial Atlantic deep-sea arkosic sands and ice-age aridity in tropical South America. *Geological Society of America Bulletin*, 189-206.
- Damuth, J. E., and Flood, R. D. (1984). Morphology, sedimentation processes, and growth pattern on the Amazon deep-sea fan. *Geo-Marine Letters* **3**, 109-117.
- Damuth, J. E., and Flood, R. D. (1985). Amazon Fan, Atlantic Ocean. In "Submarine fans and related turbidite systems." (A. H. Bouma, W. R. Normark, and B. N. E, Eds.), pp. 97-106. Springer-Verlag, New York.
- Damuth, J. E., Flood, R. D., Kowsmann, R. O., Belderson, R. H., and Gorini, M. A. (1988). Anatomy and growth pattern of Amazon deep-sea fan as revealed by long-range
-

side-scan sonar (GLORIA) and high resolution seismic studies. *American Association of Petroleum Geologists Bulletin* **72**, 885-911.

Damuth, J. E., Kowsmann, R. O., Flood, R. D., Belderson, R. H., and Gorini, M. A. (1983a). Age relationships of distributary channels on Amazon deep-sea fan: Implications for fan growth pattern. *Geology* **11**, 470-473.

Damuth, J. E., and Kumar, N. (1975). Amazon Cone: Morphology, sediments, age, and growth pattern. *Geological Society of America Bulletin* **86**, 863-878.

Damuth, J. E., Venkatarathnam, K., Flood, R. D., Kowsmann, R. O., Monteiro, M. C., Gorini, M. A., Palma, J. J. C., and Belderson, R. H. (1983b). Distributary channel meandering and bifurcation patterns on the Amazon deep-sea fan as revealed by long-range side-scan sonar (GLORIA). *Geology* **11**, 94-98.

Dessier, A., and Donguy, J. R. (1993). The sea-surface salinity in the tropical Atlantic between 10°S and 30°N - seasonal and interannual variations (1977-1989). *Deep Sea Research Part I: Oceanographic Research Papers* **41**, 81-100.

Deuser, W. G., Müller-Karger, F. E., and Hemleben, C. (1988). Temporal variations in particle fluxes in the deep subtropical and tropical North Atlantic: Eulerian versus Lagrangian effects. *Journal of Geophysical Research* **93**, 6857-6862.

Didden, N., and Schott, F. A. (1993). Eddies in the North Brazil Current retroflexion region observed by Geosat altimetry. *Journal of Geophysical Research* **98**, 20121-20131.

Droz, L., and Beallaiche, G. (1985). Rhone deep-sea fan: morphostructure and growth pattern. *AAPG Bulletin* **69**, 460-479.

Ealey, P. J. (1969). "Marine Geology of Northern Brazil: A Reconnaissance Survey." Unpublished Ph.D. thesis, University of Illinois, Urbana.

Fairbanks, R. G. (1989). A 17,000 year glacio-eustatic sea level record: influence of glacial melting rates on the Younger Dryas event and deep-ocean circulation. *Nature* **362**, 637-642.

Farre, J. A., McGregor, B. A., Ryan, W. B. F., and Robb, J. M. (1983). Breaching the shelfbreak: passage from youthful to mature phase in submarine canyon evolution. *SEPM Special Publication* **33**, 25-39.

Feeley, M. H., Buffler, R. T., and Bryant, W. R. (1985). Depositional units and growth patterns of the Mississippi Fan. In "Submarine fans and related turbidite systems." (A. H. Bouma, W. R. Normark, and B. N. E, Eds.), pp. 253-257. Springer-Verlag, New York.

Fine, R. A., and Molinari, A. (1988). A continuous deep western boundary current between Abaco (26.5°N) and Barbados (13°N). *Deep Sea Research Part A* **35**, 1411-1450.

Flood, R. D., and Damuth, J. E. (1987). Quantitative characteristics of sinuous distributary channels on the Amazon Deep-Sea Fan. *Geological Society of America Bulletin* **98**, 728-738.

Flood, R. D., Piper, D. J. W., and Shipboard Scientific Party. (1995). Introduction. In "Proceedings of the Ocean Drilling Program, Initial Reports, Vol. 155." (R. D.

Flood, D. J. W. Piper, A. Klaus, and others, Eds.), pp. 5-16, College Station, TX (Ocean Drilling Program).

- Flood, R. D., and Piper, D. W. J. (1997). Amazon Fan sedimentation: the relationship to equatorial climate change, continental denudation, and sea-level fluctuations. *In* "Proceedings of the Ocean Drilling Program, Scientific Results, Vol. 155." (R. D. Flood, D. J. W. Piper, A. Klaus, and L. C. Peterson, Eds.), pp. 653-675, College Station, TX (Ocean Drilling Program).
- Fratantoni, D. M., Johns, W. E., and Townsend, T. L. (1995). Rings of the North Brazil Current: Their structure and behaviour observed from observations and a numerical simulation. *Journal of Geophysical Research* **100**, 10633-10654.
- Froelich, P. N., Atwood, D. K., and Giese, G. S. (1978). Influence of Amazon River discharge on surface salinity and dissolved silicate concentration in the Caribbean Sea. *Deep Sea Research* **25**, 735-744.
- Gibbs, R. J., and Konwar, L. (1986). Coagulation and settling of Amazon River suspended sediments. *Continental Shelf Research* **6**, 127-149.
- Goni, G. J., Garzoli, S. L., and Johns, W. E. (2003). Synoptic study of warm rings in the North Brazil Current retroflection region using altimetry data. *In* "International Union of Geodesy and Geophysics (IUGG) Meeting, Western Boundary Currents Session, July 2003." Sapporo, Japan.
- Goni, G. J., and Johns, W. E. (2001). A census of North Brazil Current Rings observed from TOPEX/POSEIDON Altimetry: 1992-1998. *Geophysical Research Letters* **28**, 1-4.
- Gordon, A. L. (1986). Interocean exchange of thermocline water. *Journal of Geophysical Research* **91**, 5037-5046.
- Greig, S. (1998). Site 942 on the Amazon Fan: stable isotopes and sea surface temperatures. *Unpublished M.Sc. Thesis, Royal Holloway University of London*, 91p.
- Hellweger, F. L., and Gordon, A. L. (2002). Tracing Amazon River water into the Caribbean Sea. *Journal of Marine Research* **60**, 537-549.
- Hogg, N. G., and Johns, W. E. (1995). Western Boundary Currents. U.S. National Report to International Union of Geodesy and Geophysics 1991-1994. *Reviews of Geophysics (supplement)* **33**, 1311-1334.
- Hoorn, C., Guerrero, J., Sarmiento, G. A., and Lorente, M. A. (1995). Andean tectonics as a cause for changing drainage patterns in Miocene Southern South America. *Nature* **23**, 237-240.
- Johns, W. E., Lee, T. N., Beardsley, R. C., Candela, J., Limeburner, R., and Castro, B. (1998). Annual cycle and variability of the North Brazil Current. *Journal of Physical Oceanography* **28**, 103-128.
- Johns, W. E., Lee, T. N., Schott, F. A., Zantopp, R. J., and Evans, R. H. (1990). The North Brazil Current retroflection: Seasonal structure and eddy variability. *Journal of Geophysical Research: D* **95**, 22103-22120.
-

-
- Kelly, P. S., Lwiza, K. M. M., Cowen, R. K., and Goni, G. J. (2000). Low salinity pools at Barbados, West Indies: Their origin, frequency and variability. *Journal of Geophysical Research* **105**, 19699-19708.
- Lenz, S. J. (1995). Seasonal variations in the historical structure of the Amazon plume inferred from historical hydrographic data. *Journal of Geophysical Research* **100**, 2391-2400.
- Levitus, S. (1982). Climatological Atlas of the World Ocean, Professional Paper 13. National Ocean and Atmosphere Administration (NOAA).
- Lovejoy, N. R., Bermingham, E., and Martin, A. P. (1998). Marine incursion into South America. *Nature* **396**, 421-422.
- Manley, P. L., and Flood, R. D. (1988). Cyclic sediment deposition within Amazon Deep-Sea Fan. *The American Association of Petroleum Geologists Bulletin* **72**, 912-925.
- Maslin, M. A., and Burns, S. J. (2000). Reconstruction of the Amazon Basin effective moisture availability over the past 14,000 years. *Science* **290**, 2285-2287.
- Maslin, M. A., Durham, E., Burns, S. J., Platzman, E., Grootes, P., Greig, S. E. J., Nadeau, M. J., Schleicher, M., Pflaumann, U., Lomax, B., and Rimington, N. (2000). Palaeoreconstruction of the Amazon River freshwater and sediment discharge using sediments recovered at site 942 on the Amazon Fan. *Journal of Quaternary Science* **15**, 419-434.
- Maslin, M. A., Mikkelsen, N., Vilela, C., and Haq, B. (1998). Sea-level and gas-hydrate-controlled catastrophic sediment failures of the Amazon Fan. *Geology* **26**, 1107-1110.
- Mayer, D. A., and Weisberg, R. H. (1993). A description of COADS surface meteorological fields and the implied Sverdrup transports for the Atlantic Ocean from 30°S to 60°N. *Journal of Physical Oceanography* **23**, 2201-2221.
- McGeary, D. F. R., and Damuth, J. E. (1973). Postglacial iron-rich crusts in hemipelagic deep-sea sediment. *Geological Society of America Bulletin* **84**, 1201-1211.
- McGuire, W. J., Howarth, R. J., Firth, C. R., Solow, A. R., Pullen, A. D., Saunders, S. J., Stewart, I. S., and Vita-Finzi, C. (1997). Correlation between rate of sea level change and frequency of explosive volcanism in the Mediterranean. *Nature* **389**, 473-476.
- McIver, R. D. (1982). Role of naturally occurring gas hydrates in sediment transport. *American Association of Petroleum Geologists Bulletin* **66**, 789-792.
- Meade, R. H. (1985). Suspended sediment in the Amazon River and its tributaries in Brazil during 1982-1984. In "USGS Open File Report." pp. 85-492.
- Meade, R. H. (1994). Suspended sediment of the modern Amazon and Orinoco Rivers. *Quaternary International* **21**, 29-39.
- Meade, R. H., Dunne, T., Richey, J. E., Santos, U. d. M., and Salati, E. (1985). Storage and remobilization of suspended sediment in the lower Amazon River of Brazil. *Science* **228**, 488-490.
-

-
- Metcalf, W. (1968). Shallow currents along the northeastern coast of South America. *Journal of Marine Research* **26**, 232-243.
- Metcalf, W., and Stalcup, M. C. (1967). Origin of the Atlantic Equatorial Undercurrent. *Journal of Geophysical Research* **72**, 4959-4975.
- Mikkelsen, N., Maslin, M., Giraudeau, J., and Showers, W. (1997). Biostratigraphy and sedimentation rates of the Amazon Fan. In "Proceedings of the Ocean Drilling Program, Scientific Results Vol. 155." (R. D. Flood, D. J. W. Piper, A. Klaus, and L. C. Peterson, Eds.), pp. 577-594, College Station, TX (Ocean Drilling Program).
- Milliman, J. D., Summerhayes, C. P., and Barretto, H. T. (1975). Quaternary sedimentation on the Amazon continental margin: a model. *Geological Society of America Bulletin* **86**, 610-614.
- Mitchum, R. M., Jr. (1985). Seismic stratigraphic expression of submarine fans. *American Association of Petroleum Geologists Memoir* **39**, 117-136.
- Molinari, R. L. (1982). Observations of eastward currents in the tropical South Atlantic Ocean. *Journal of Geophysical Research* **87**, 9707-9714.
- Moore, W. S., Sarmiento, J. L., and Key, R. M. (1986). Tracing the Amazon component of surface Atlantic water using ²²⁸Ra, salinity and silica. *Journal of Geophysical Research* **91**, 2574-2580.
- Mutti, E. (1985). Hecho turbidite system, Spain. In "Submarine fans and related turbidite systems." (A. H. Bouma, W. R. Normark, and B. N. E, Eds.), pp. 205-208. Springer-Verlag, New York.
- Mutti, E., and Zuffa, G. G. (1985). Turbidite systems and their relations to depositional sequences. In "NATO Advances Study Institutes; Series C: Provenance of arenites." pp. 65. D. Reidal Publishing Co., Boston.
- Müller-Karger, F. E., McClain, C. R., and Richardson, P. L. (1988). The dispersal of the Amazon's water. *Nature* **333**, 56-59.
- NASA. (2002). SeaWifs sensor marks five years documenting Earth's dynamic biosphere. *NASA Press Release H02-144, Goddard Space Flight Center July 31, 2002*, http://www.gsfc.nasa.gov/topstory/_20020801seawifs.html.
- Nittrouer, C. A., and DeMaster, D. J. (1986). Sedimentary processes on the Amazon continental shelf: past, present and future research. *Continental Shelf Research* **6**, 5-30.
- Nittrouer, C. A., Kuehl, S. A., DeMaster, D. J., and Kowsmann, R. O. (1986). The deltaic nature of Amazon Shelf sedimentation. *GSA Bulletin* **97**, 444-458.
- Peterson, R. G., and Stramma, L. (1990). Upper level circulation in the South Atlantic Ocean. *Progress in Oceanography* **26**, 1-73.
- Philander, S. G. H., and Panakowski, R. C. (1986). The mass and heat budget in a model of the tropical Atlantic Ocean. *Journal of Geophysical Research* **91**, 14212-14220.
-

-
- Picaut, J., Servain, J., Lecomte, P., Seva, M., Lukas, S., and Rougier, G. (1985). "Climatic Atlas of the Tropical Atlantic, Wind Stress and Sea Surface Temperature 1964-1979." University of Hawaii, Honolulu.
- Richardson, P. L., and Walsh, D. (1986). Mapping climatological and seasonal variations of surface currents in the tropical Atlantic using ship drift data. *Journal of Geophysical Research* **91**, 10537-10550.
- Schlünz, B., Schneider, R. R., Müller, P. J., J. S. W., and Wefer, G. (1999). Terrestrial organic carbon accumulation on the Amazon deep sea fan during the last glacial sea level low stand. *Chemical Geology* **159**, 263-281.
- Schmitz, W. J., Jr. (1995). On the interbasin-scale thermohaline circulation. *Reviews of Geophysics* **33**, 151-173.
- Schmitz, W. J., Jr., and McCartney, M. S. (1993). On the North Atlantic circulation. *Reviews of Geophysics* **31**, 29-49.
- Schmitz, W. J., Jr., and Richardson, P. L. (1991). On the source of the Florida Current. *Deep Sea Research Part A* **38**, Supplement: 379-409.
- Schott, F. A., Fischer, J., Reppin, J., and Send, U. (1993). On mean and seasonal currents and transport at the western boundary of the equatorial Atlantic. *Journal of Geophysical Research* **98**, 14353-14368.
- Schott, F. A., Fischer, J., and Stramma, L. (1998). Transports and pathways of the upper-layer circulation in the western tropical Atlantic. *Journal of Physical Oceanography* **28**, 1904-1928.
- Schott, F. A., Stramma, L., and Fischer, J. (1995). The warm water inflow into the western tropical Atlantic boundary regime, Spring 1994. *Journal of Geophysical Research: Oceans* **100**, 24745-24760.
- Shackleton, N. J. (1987). Oxygen isotopes, ice volume and sea level. *Quaternary Science Reviews* **6**, 183-190.
- Shipboard Scientific Party. (1995). Site 942. In "Proceedings of the Ocean Drilling Program, Initial Reports, Vol. 155." (R. D. Flood, D. J. W. Piper, A. Klaus, and others, Eds.), pp. 537-567, College Station, TX (Ocean Drilling Program).
- Signorini, R. S., Murtugudde, R. G., McClain, C. R., Christian, J. R., Picaut, J., and Busalacchi, A. J. (1999). Biological and physical signatures in the tropical and subtropical Atlantic. *Journal of Geophysical Research* **100**, 18367-18382.
- Steven, D. M., and Brooks, A. L. (1972). Identification of Amazon River water at Barbados, W. Indies, by salinity and silicate measurements. *Marine Biology* **14**, 345-348.
- Stramma, L. (1991). Geostrophic transport of the South Equatorial Current in the Atlantic. *Journal of Marine Research* **49**, 281-294.
- Stramma, L., Fischer, J., and Reppin, J. (1995). The North Brazil Undercurrent. *Deep Sea Research Part I: Oceanographic Research Papers* **41**, 773-795.
- Stramma, L., Ikeda, Y., and Peterson, R. G. (1990). Geostrophic transport in the Brazil Current region north of 20°S. *Deep Sea Research* **37**, 1875-1886.
-

- Weimer, P., and Buffler, R. T. (1989). Seismic definition of fan lobes, Mississippi Fan, Gulf of Mexico. *In "Atlas of Seismic Stratigraphy."* (A. W. Bally, Ed.), pp. 79-87. *Studies in Geology*, No. 27. American Association of petroleum Geologists, Tulsa.
- Wilson, W. D., Johns, E., and Molinari, R. L. (1994). Upper layer circulation in the western tropical North Atlantic Ocean during August 1989. *Journal of Geophysical Research* **99**, 22513-22523.
- Wilson, W. D., and Johns, W. E. (1997). Velocity structure and transport to the Windward Islands Passages. *Deep Sea Research Part I: Oceanographic Research Papers* **44**, 487-520.

3. A REVIEW OF THE MODERN CLIMATOLOGY OF THE AMAZON BASIN AND SURROUNDING REGIONS

3.1 Introduction

Amazon River sediment and water discharge are controlled by continental climate, therefore it is necessary to understand the modern climate setting of the Amazon Basin in order to assist interpretations of changes in the past. This chapter attempts to review the modern climate system over northern South America, with particular emphasis on the factors influencing precipitation over the Amazon Basin.

3.2 The Modern Meteorology of the Amazon Basin

3.2.1 Introduction

The Amazon Basin region is home to the largest tropical rainforest on the planet, containing 30% of the total global biomass (Barry and Chorley, 1995) and up to 60% of the world's plant biodiversity, 90% of all primate species, 40% of all bird species, and 80% of all insects on the planet (Hiscox, 2004). It also represents a major source of heat within the tropics and has been shown to have a significant impact on extratropical circulation by playing host to Earth's largest and most intense land-based convection centre (Marengo *et al.*, 2001). Strong thermal convection over Amazonia can frequently produce rainfall in excess of 40 mm/day over a period of a week, and over shorter periods, even higher average intensities may be experienced. Where 40 mm of rainfall in one day releases sufficient latent heat to warm the troposphere by 10°C, it is clear that sustained convection at this intensity is capable of fuelling Walker Circulation. This becomes significant during ENSO events (see Section 3.2.4): during the high phases (La Niña), air rises over Amazonia, whereas during the low phases (El Niño) the drought over northeast Brazil is intensified (Barry and Chorley, 1995). Changes in the intensity of convective air moving poleward may also modify Hadley Circulation. Due to the conservation of angular momentum, this poleward moving air tends to accelerate and strengthen the westerly jet streams, such that correlations have been found between Amazonian convective activity and the intensity and location of the North American jet stream (Barry and Chorley, 1995). Any changes in the past moisture history of the Amazon Basin could therefore have had potentially very significant impacts on tropical atmospheric circulation.

On a regional scale, the Amazon Basin plays a vital role in the hydrological cycle and water balance over much of South America. Modelling studies (e.g. Lenters and Cook, 1997) have

provided evidence for the relationship between latent heat releases over the Amazon Basin and their impact on upper-tropospheric circulation over South America. During austral summer, increased sensible heating of the elevated Peruvian-Bolivian Altiplano, combined with enhanced latent heat release during frequent convectonal thunderstorms over Amazonia, initiate the development of a persistent upper tropospheric closed anticyclone, the Bolivian High (Lenters and Cook, 1997; Marengo *et al.*, 2001; Vuille, 1999; Zhou and Lau, 1998), analogous to the situation over Tibet (Barry and Chorley, 1995). The formation of the Bolivian High is shown in Figure 3.1. The development of the Bolivian High brings about maximum cloudiness to central Amazonia (Barry and Chorley, 1995) and stormy precipitation typically during afternoon and evening showers (Argollo and Mourguiart, 2000; Garreaud, 1999; Rowe *et al.*, 2002), becoming increasingly sporadic with distance away from the northern part of the basin (Argollo and Mourguiart, 2000). To the east and downstream of the Bolivian High an upper level cold trough sits off the east coast of Brazil; this is associated with descending air masses and is part of the mechanisms that lead to the very low rainfall observed in that region (Barry and Chorley, 1995; Moura and Shukla, 1981).

The development of the Bolivian High also influences atmospheric circulation patterns over Amazonia, where upper tropospheric winds are southerly or southeasterly from December to April, and northwesterly or westerly from May to September. Surface winds (the trade winds) are predominantly northeasterly from September to April, and southeasterly from May to August (Barry and Chorley, 1995; Zhou and Lau, 1998). This should not be confused with the annual average surface wind patterns, as by their strong intensity, the northeasterly trades would appear to dominate year-round.

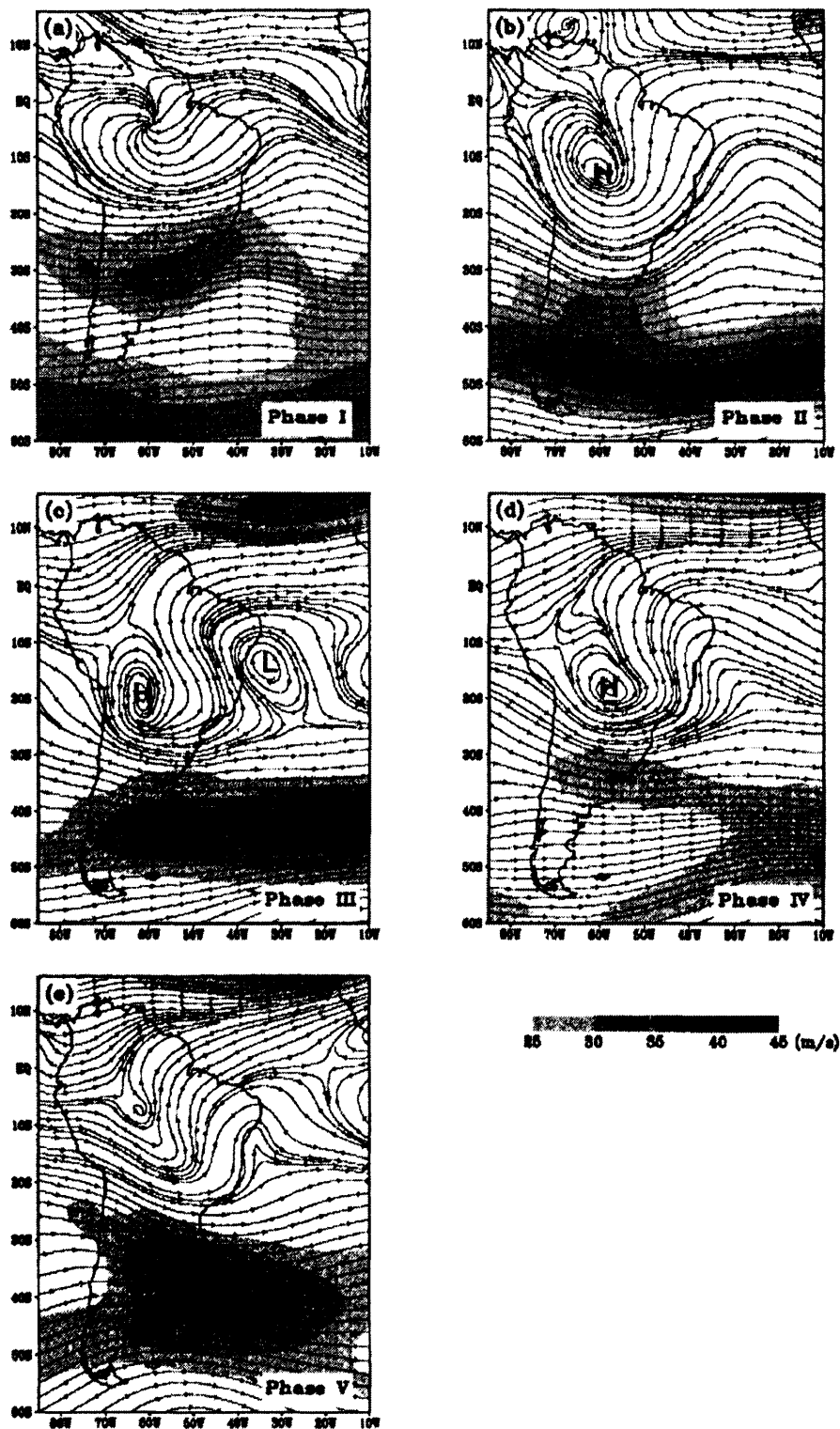


Figure 3.1: Goddard Earth Observing System-I (GEOS-1) assimilation of upper level (200-hPa) circulation composite monitoring the formation and decline of the Bolivian High. (a) October to November; (b) mid-November to December; (c) December to early February (wet season); (d) early February to mid-March; (e) mid-March to end April. H = area of high atmospheric pressure; L = area of low atmospheric pressure (modified from Zhou and Lau, 1998).

Using the re-analysis products of both the data assimilation system (DAS) with version 1 of the Goddard Earth Observing System-1 (GEOS-1) and National Centers for Environmental Prediction (NCEP) models, Zhou and Lau (1998) observed that although the easterly trades prevail in analyses of annual surface wind patterns, there appears to be a seasonal reversal in the surface wind structure during the Southern Hemisphere winter should the annual mean component be removed. During Southern Hemisphere summer the wind anomaly flow originates from the sub-Saharan region, and has the effect of substantially enhancing the easterly trades from tropical North Atlantic. After crossing the equator, the wind anomaly becomes a northwesterly flow along the eastern flanks of the Andes, before turning clockwise around the Gran Chaco atmospheric low pressure system. In Southern Hemisphere winter, this situation is clearly reversed (see Figure 3.2). From this change in prevailing wind direction, Zhou and Lau (1998) propose that the modern climate of South America can be described as a monsoonal system, which they refer to as the South American Summer Monsoon.

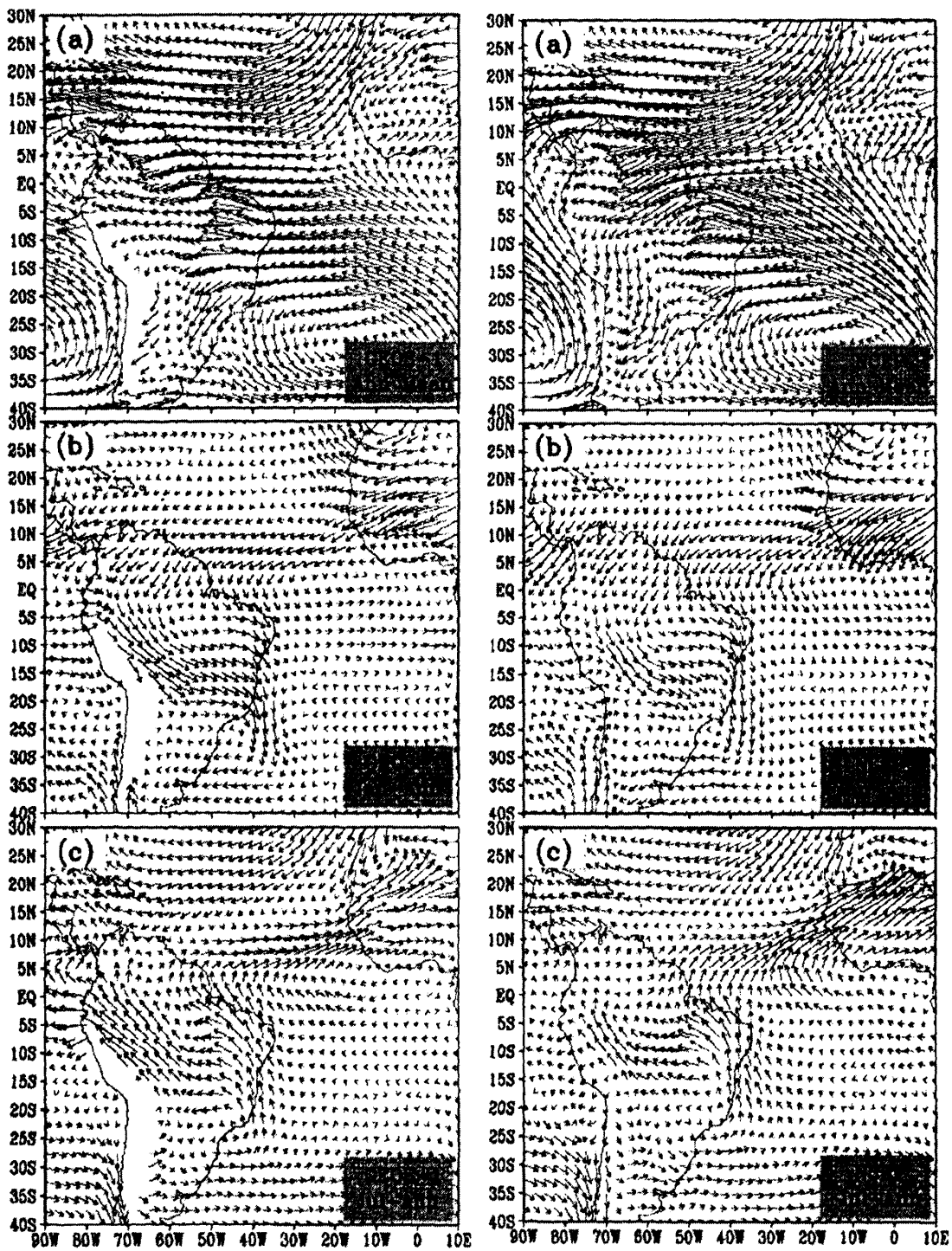


Figure 3.2: GEOS-1 and NCEP re-analysis climatology of lower level (900-hPa) wind ($m s^{-1}$) for (a) annual mean, (b) January minus annual mean, and (c) July minus annual mean (modified from Zhou and Lau, 1998).

Annual rainfall in northern South America varies greatly, from less than 400 mm in northeast Brazil and the Caribbean coast of South America, to levels in excess of 3000 mm in the upper watershed of the Rio Negro (Marengo *et al.*, 2001). Within the Amazon Basin region,

an area occupying $\sim 7,050,000 \text{ km}^2$ (Maslin *et al.*, 2000) three separate centres of abundant rainfall can be identified (Marengo, 1995): northwest Amazonia, central Amazonia (around 5° S), and the area close to the mouth of the Amazon River near Belem, with annual rainfall of more than 3600 mm, 2400 mm and more than 2800 mm, respectively (see Figure 3.3). In northern and central Amazonia, there is no clear dry season; rainfall is abundant throughout the year and at its maximum during austral fall (April-June). In southern Amazonia, there are distinct wet and dry seasons, with annual rainfall peaking during late austral summer/early austral fall (January-March). The extremely intense year-round rainfall localised within narrow strips alongside the eastern side of the Andes is considered to be brought about by upglide condensation and a leeside rain shadow effect (Barry and Chorley, 1995) associated with the easterly winds as they flow from the evapotranspiration-intense Amazon Basin, up and over the cordilleras. The coastal maximum is brought about by nocturnal convergence between the trade winds and the land breeze (Marengo *et al.*, 2001).

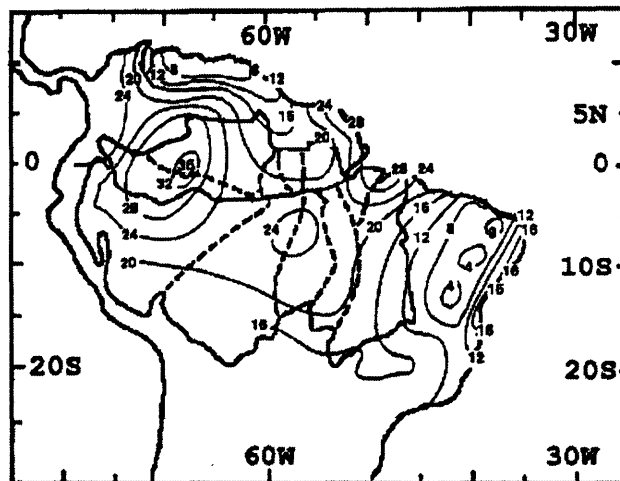


Figure 3.3: Map of the distribution of annual rainfall across the Amazon Basin (modified from Marengo, 1995).

The transition between the dry and the wet seasons in Amazonia is fairly rapid, with the wet season onset typically occurring within a single month; although at times this may occur over a period of just five days. Although there has been little research into the understanding of the wet season onset in Amazonia, it has been found that with the exception of the extreme northwest region, onset progresses in a southeasterly direction, from near mid-September in the north and west to the beginning of October in the southeast (Kousky, 1988; Marengo *et al.*, 2001). Near to the mouth of the Amazon, the onset of the wet season occurs almost at the end of December. North of the equator, rainfall is apparently tied to Northern Hemisphere summer and does not occur until mid-April. As a consequence, the largest cumulative river discharges occur during the early austral winter, shortly after the peak of the

wet season in northern and western Amazonia (See Figure 3.4). The retreat of the wet season progresses in a northwesterly direction, but moves relatively more slowly and more systematically than does the onset (Marengo *et al.*, 2001; Marengo *et al.*, unpublished).

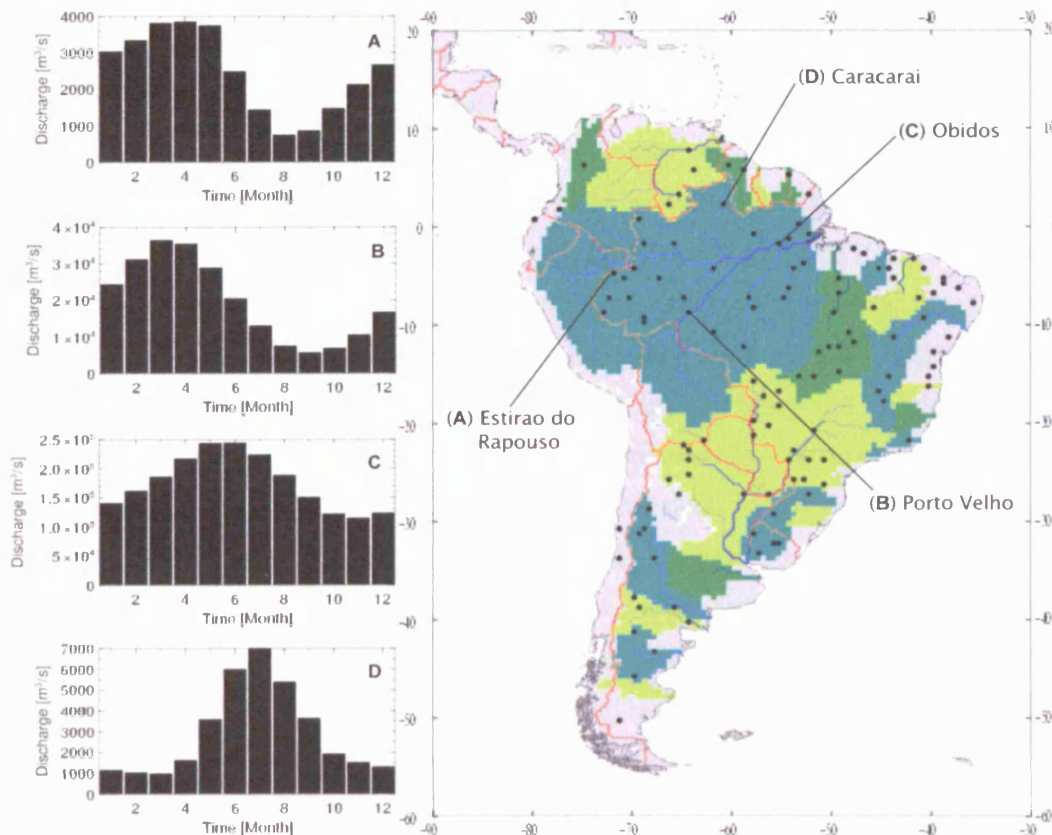


Figure 3.4: Mean monthly river discharges illustrating the onset of the wet season across different parts of the Amazon Basin, measured at (A) Estirao do Raposo, Rio Javari, western Amazonia; (B) Porto Velho, Rio Madeira, southern Amazonia; (C) Obidos, Rio Amazonas, near to the mouth of the Amazon River; (D) Caracarai, Rio Branco, north of the equator. Monthly averages are calculated for the period from January 1928 to March 1996 (modified from Global Runoff Data Centre, 2005).

Veranicos, short drought spells lasting from five to 21 days and typical of tropical regions, occur between November and February during the austral summertime wet season, and have a strong effect on agriculture if they occur near to the beginning of the wet season. Northern Amazonia experiences longer more intense *veranicos* during El Niño years, as compared to short and less intense *veranicos* during La Niña years (*ibid.*).

3.2.2 Temporal Organisation of Rainfall Over the Amazon Basin

Previous studies (e.g. Fu *et al.*, 1999; Marengo, 1995; Rao and Hada, 1990) have shown the temporal aspect of the South American annual rainfall cycle to be controlled largely by the sun through its influence on the meridional displacement of the meteorological equator (the

midpoint along the meridional temperature gradient, and the boundary between the equatorial Hadley cells) and the sea surface temperature (SST) gradient between the Atlantic and Pacific Oceans. These factors may also commonly act as a dominant control over the position of the Inter-tropical Convergence Zone (ITCZ); however there is debate as to whether it actually exists in its characteristic form over the interior of northern South America. Where many researchers (e.g. Argollo and Mourguiart, 2000; Curtis and Hastenrath, 1999; Garcia *et al.*, 1998; Haug *et al.*, 2001; Jennerjahn *et al.*, 2004; Maslin and Burns, 2000; Seltzer *et al.*, 1998) readily attribute the observed/reconstructed climate of South America to be reflecting the changing migratory nature of the ITCZ, an alternative to this paradigm is that due to its unique situation, the Amazon Basin acts as a large land-based convection centre in itself, with the north-south migration of the ITCZ being influential on precipitation only near to the continental east coast. Indeed, Barry and Chorley (1995) note that within Amazonia, the continuously high temperatures (24°-28°C) combined with high evapotranspiration rates cause the region to behave at times as if it were a source of maritime equatorial air. Nevertheless, the seasonal latitudinal changes of the ITCZ/meteorological equator may exert a strong control on the atmospheric pressure cells associated with the South American Summer Monsoon, and therefore on the overall climate of South America. A comparison of the hypothesised position of the ITCZ/meteorological equator and the coeval zones of convection are shown in Figure 3.5.

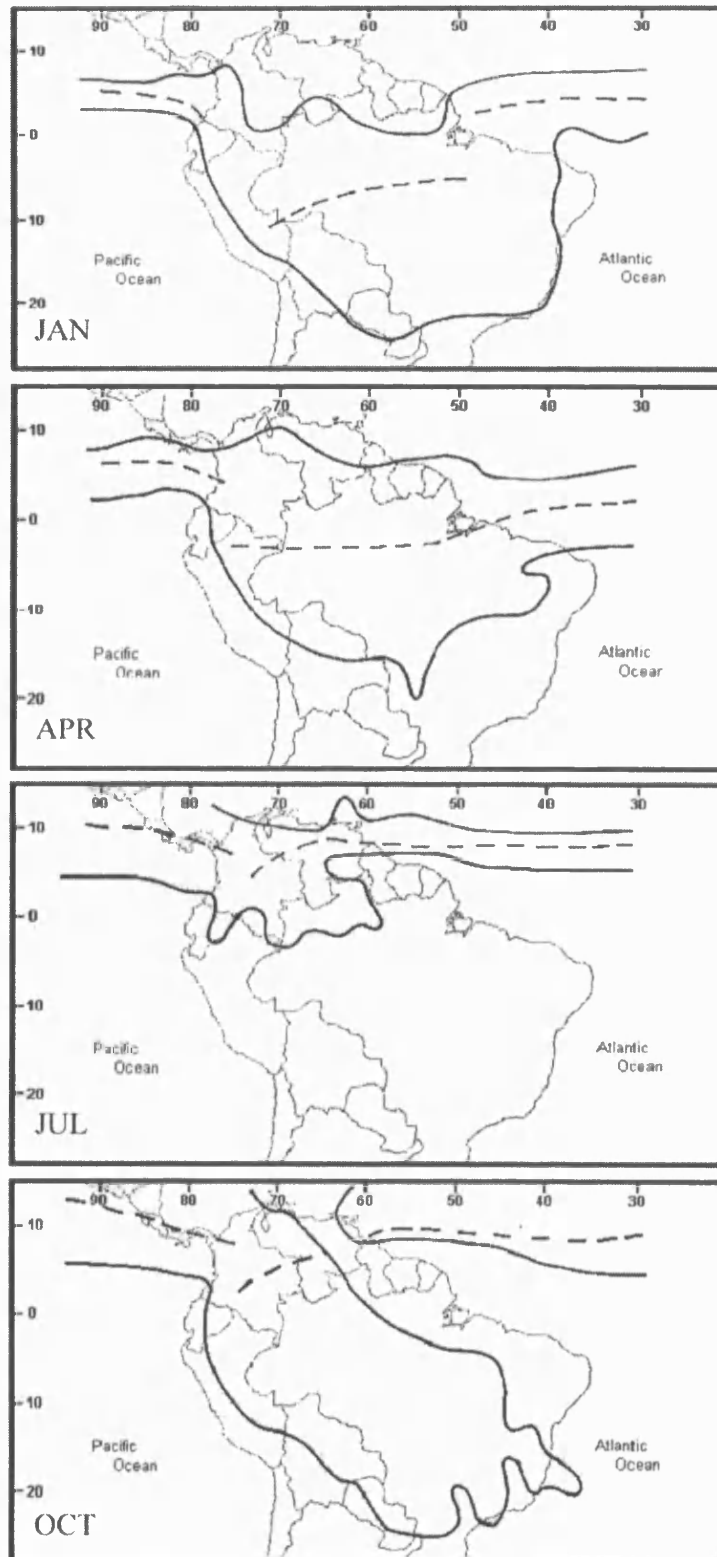


Figure 3.5: A cartoon to show the mean position of the ITCZ/meteorological equator (dashed line) and the coeval zone of atmospheric convection over tropical South America for January, April, July and October (modified from Davison, 1999).

Between July and September/October (austral winter through to early austral spring), the ITCZ swings to its most northerly position, and the South Atlantic subtropical high pressure cell expands westward over the continent causing the low-pressure equatorial trough to fill. Stable easterly mT air from the South Atlantic surface invades Amazonia in a shallow (1000-2000 m), relatively cool and humid layer, separated from the warmer and drier air above by a strong temperature inversion and humidity discontinuity. Although this shallow airflow brings some precipitation in coastal locations, it is particularly arid in drought-prone eastern Brazil at this time, and also in central Amazonia as reflected by inland stations such as Manaus (Barry and Chorley, 1995). After October, the South Atlantic subtropical high pressure cell begins to contract and a continental heat low with strong convection begins to establish over the Gran Chaco region of the continental interior, making the Amazon Basin one of the wettest regions on Earth (Marengo *et al.*, 2001; Vuille, 1999). The temperature inversion rises to 3000-4000 m and may break down altogether bringing about heavy precipitation, especially during the late afternoon or early evening (Barry and Chorley, 1995) giving rise to the October- April rainy season in central and southern Amazonia. However dry conditions may prevail from January-May, during strong ENSO events when the descending branch of Walker Circulation covers most of Amazonia. In comparison, the North Atlantic subtropical high pressure cell is relatively less mobile, but it varies in a more complex manner, having maximum westward extensions in July and February and minima in November and April (Barry and Chorley, 1995; Zhou and Lau, 1998) .

The main vector of moisture toward the Amazon Basin is the humid trade winds blowing in from the tropical North Atlantic (the location of the subtropical high) toward the low-pressure area associated with the meteorological equator. These winds are seasonally influenced by the formation of the Bolivian High, the summertime increase in pressure over the tropical north Atlantic (Barry and Chorley, 1995) and the meridional Atlantic-Pacific SST gradients (Marengo *et al.*, 2001). It has been suggested (Nogues-Paegle and Mo, 1997) that a strong low-level northerly jet east of the Andes enhances this flux of water vapour and heat from the North Atlantic across the Amazon, and into the region of Paraguay and northern Argentina. The trade winds sustain a strong and persistent northeasterly flow from the North Atlantic into the Amazon Basin (Marengo *et al.*, 2001), and accordingly the timing of their transport initiates the onset and intensity of the austral summer wet season (see Section 3.2.1).

Within Amazonia, maximum summer convection is found over the southern region, extending to the southeast. This represents the South Atlantic Convergence Zone (SACZ)

(for details, see Nogues-Paegle and Mo, 1997). During the winter months, these convection bands migrate toward the Northern Hemisphere (Marengo *et al.*, 2001), along with a lesser defined equatorial low-pressure trough (Barry and Chorley, 1995), and in combination with a SST maximum, characterise the circulation and determine the May-September rainy season in northern South America (Marengo *et al.*, 2001). During the winter months (May-September), near-surface surges of cold high-latitude air, known locally as *fraigens*, frequently blow in from the south across southeastern Brazil and the Amazon region, sometimes reaching as far north as the equator. They are capable of modifying the atmospheric structure and climatic conditions considerably as they pass, and may bring severe frosts in the coffee-growing areas of southern Brazil and substantial cooling in the Amazon Basin (Marengo *et al.*, 1997). There were six fraigen events recorded in 1992, nine in 1993, and 14 such events were reported during the winter of 1994 (Marengo *et al.*, 2001).

3.2.3 Spatial Organisation of Rainfall Over the Amazon Basin

Although the timing of the annual rainfall cycle is largely controlled by the sun, rainfall across the different parts of the basin is triggered by different mechanisms. Rainfall in northern Amazonia is particularly influenced by the meridional SST gradient of the tropical North Atlantic which affects deep ITCZ-like convection and moisture transport from the Atlantic (Marengo *et al.*, 2001), occasional incursions of cold fronts from the Southern Hemisphere, and relief effects (Barry and Chorley, 1995) as well as sea-breeze interactions and the inland movement of rain-bringing instability lines originating near the mouth of the Amazon River (Marengo *et al.*, 2001). Such sea-breeze interactions are also particularly influential over eastern Amazonia. These mesoscale lines of instability form near to the coast as a result of converging trade winds and afternoon sea breezes, or due to the interaction of nocturnal land breezes with onshore trade winds. Once formed, they move westward in the general airflow at speeds of about 30 mph (i.e. 50 km hr⁻¹) moving faster in austral summer than in winter, and exhibiting a complex process of convective cell growth, decay, migration and regeneration. Many of these instability lines decay after sunset, only reaching 100 km or so inland, however the more persistent instabilities, some of which may remain active for up to 48 hours, may produce a rainfall maximum about 500 km inland, even reaching as far west as the Andes (Barry and Chorley, 1995). Within central Amazonia, surface warming leads to diurnal deep convection and rainfall, whereas in south/southeast Brazil, often also reaching into western and southern Amazonia, meso- and large-scale convection associated with the summertime penetration of cold fronts (Marengo *et al.*, 2001) may initiate downpours.

3.2.4 The Influence of ENSO on the Precipitation Regime over the Amazon Basin

While the principal moisture source for the Amazon Basin is the tropical Atlantic, there are times when signals from the tropical Pacific can be observed. This arises particularly during intense low phases of ENSO (related to El Niño), such as those of 1925-26, 1982-83 and 1997-98, when anomalously suppressed convection and relatively strong subsidence bring negative rainfall anomalies to the northern and central parts of the Amazon Basin (to date, the drought of 1998 is considered as the most intense of the last 118 years). During high phases of ENSO (La Niña) air rises over Amazonia producing convective rainfall and anomalously wet seasons in northern and central Amazonia, as were observed during La Niña years of 1988-89, and 1995-96 (Marengo *et al.*, 2001). ENSO events exert their strongest impacts in northern Amazonia, where El Niños frequently initiate forest fires, and anomalously low river levels create problems with national infrastructure (e.g. transportation, hydroelectricity generation), while the rainfall regime in southern Amazonia remains relatively unaffected.

3.3 The Modern Meteorology of the Altiplano Region

3.3.1 Introduction

Palaeoclimate records of the Altiplano region have been used to infer past variations in Amazon Basin moisture (e.g. Baker *et al.*, 2001a; Baker *et al.*, 2001b; see Chapter 4), so it is therefore important to consider the modern meteorology of this region also.

3.3.2 The Modern Meteorology of the Altiplano Region

Between 15°S and 22°S the central Andes divides into the eastern and western cordillera, where the intra-montane region is occupied by the Altiplano, a vast tectonic plateau of ~190,000 km² in area (Argollo and Mourguiart, 2000) and 3500-4000 m mean elevation (Vuille, 1999). Extending high up into the middle troposphere, the Altiplano acts as a barrier dividing low level circulation to the west and east of the Central Andes (Rowe *et al.*, 2002; Vuille, 1999). To the west of the continent, moist air is trapped below a very stable inversion at about 900 hPa; the subsiding air masses of the Southeast Pacific Anticyclone bring dry, stable conditions creating some of the world's driest climate along the northern coast of Chile (Vuille, 1999).

Atmospheric moisture received by Lake Titicaca originates from the tropical Atlantic Ocean, and is recycled as it passes over the Amazonian lowlands to the north and east before it is

advected onto the Altiplano. Over 80% of annual precipitation (350-400mm) over the Altiplano falls during the summer months (December-March; Rowe *et al.*, 2002; Vuille, 1999) coinciding with the formation of the upper-level Bolivian High pressure cell (see Section 3.2.1), where the intense solar heating of the high plateau surface destabilises the boundary layer, inducing deep convection which brings maximum cloudiness to the region (Marengo *et al.*, 2001), and ultimately releases the moisture from the humid air blowing in from the Amazon Basin (Garreaud, 1999). The strength and position of this high pressure system are considered to be quite variable (Vuille, 1999), however, modelling studies by Vuille *et al.* (1998) have shown a southward-displaced and strengthened Bolivian High pressure system to be associated with significantly higher precipitation over the southern Altiplano. This indicates that the relationship between upper air circulation and rainfall is sustained despite its latitudinal displacement.

In addition to the locus and intensity of the Bolivian High, the general summer circulation over the Altiplano is also a combined function of the location and magnitude of deep atmospheric convection over the Amazon Basin and equatorial Atlantic Ocean, and sea-surface temperature conditions in the tropical Pacific Ocean (Baker *et al.*, 2001a; Rowe *et al.*, 2002; Vuille, 1999). Consequently, lower level tropospheric circulation is dominated by northerly and northwesterly jet-type flow along the eastern slopes of the central Andes, and by northeasterly trades to the east and north over the Amazon Basin. However, upper level circulation is dominated by a quasi-stationary anti-cyclone north of 35° S, a band of easterly flow near 10° S, and strong cross-equatorial northward flow from 60°-80° W (Rowe *et al.*, 2002). During the winter months, strong zonal winds in the upper troposphere (the Westerlies) and high pressure in the lower troposphere over the region (Rowe *et al.*, 2002) allow only limited sporadic penetration of humid Amazonian air. This leads to areas of isolated, weak-intensity rainfall (Argollo and Mourguiart, 2000), thereby bringing aridity to the Altiplano (Vuille, 1999).

However between May and September, being most frequent during July-August in the Sajama region (Vuille and Baumgartner, 1998), occasional outbreaks of cold air masses from the planetary west wind zone produce considerable amounts of snow; this is especially the case when cold air masses are cut off from the general west wind flow and move over the Altiplano, destabilising the generally warmer atmospheric column above. Taking into account these rare dumps of snow, the low winter precipitation data from the sparse meteorological network in the area should be interpreted with caution as they may represent an underestimation of reality (Vuille and Ammann, 1997). As precipitation episodes over the

Altiplano are driven by convection, the spatial variability in rainfall is high (Vuille, 1999). More locally, the presence of high peaks (> 6000 masl) in the Cordillera Oriental and the orientation of certain valleys give rise to a föhn wind phenomenon that disturbs the rainfall regime of the adjoining region (Argollo and Mourguiart, 2000).

Nevertheless, Vuille (1999) notes that as the precipitation over the Altiplano is episodic in nature, it reveals that although solar heating may be a prerequisite, additional forcing is required for precipitation actually to occur. An alternative mechanism for explaining the nature of precipitation on the Altiplano was recently put forward by Garreaud (1999; 2000) who presented a convincing link between the large scale upper-atmosphere easterly winds over the Altiplano during rainy periods, and the regional easterly flow of moisture from the continental lowlands up and over the Andes towards the Altiplano. His data suggest that the large-scale upper level easterly flow brings about turbulent entrainment of easterly momentum over the Andean ridge, thereby accelerating eastward upslope flow and moisture transport. Conversely, dry periods are related to enhanced westward flow over the Altiplano at all levels, thereby advecting dry air from the Pacific region and suppressing any moist air advection from the east. So, he argues that it is the intensity of easterly moisture transport over the eastern slope of the Andes rather than the degree of moist conditions in the continental interior that is the main factor in determining the modern intraseasonal moisture/rainfall variability on the Altiplano.

Three very large lacustrine basins occupy the vast depression of the Altiplano which has been filling up since the Tertiary (Argollo and Mourguiart, 2000). To the north lies Lake Titicaca (16° S, 69° W) a deep freshwater lake (max. depth 285 m), in fact the largest (8562 km², 903 km³) high altitude (3810 masl) lake in the world, occupying approximately one seventh of the northern Altiplano basin (Argollo and Mourguiart, 2000). The modern lake becomes a closed basin when water level drops below 3804 masl (Rowe *et al.*, 2002), however at present Lake Titicaca drains via the Río Desguadero into the southern altiplano basins of Poopó (2530 km²) and Coipasa and Uyuni (12,000 km²). Lake Poopó, is a very shallow body of water near-central on the Altiplano showing meso- or polyhaline conditions (the lake dried up completely in 1995), and the salars of Coipasa and Uyuni are seasonal hypersaline lakes. This latitudinal distribution of water bodies reflects the pluviometric gradient that exists between the northern and southern parts of the region (Argollo and Mourguiart, 2000). The mean annual precipitation varies from more than 800 mm around Lake Titicaca to less than 200 mm at the southern end of the basin, where the mean evaporation rate over the entire Altiplano region is estimated at more than 1500 mm yr⁻¹

(Grosjean, 1994). This is frequently attributed to the seasonal migrations in the latitudinal position of the ITCZ, which reaches the central Andes during austral summer between the months of November and April, and is at its most southerly position from March-April (Barry and Chorley, 1995).

3.3.3 The Influence of ENSO on the Precipitation Regime over the Altiplano Region

Recent work has focussed on examining the importance of the Bolivian High and its relationship to the phases of the ENSO ocean-atmosphere phenomenon (e.g. Lenters and Cook, 1997; Vuille, 1999). Relatively wet summers (DJF) on the Altiplano have been found to broadly correlate with an intensified and southward-displaced Bolivian High, creating stronger easterly winds that transport humid Amazonian air onto the northern Altiplano. Conversely, dry years are characterised by a weaker easterly flow, which isolates the Altiplano from the Amazonian moisture flux. New evidence based on analysis of meteorological fields during periods of strong oceanic forcing (Rowe *et al.*, 2002), indicates that inter-annual shifts in Altiplano climate modes are primarily forced by SST anomalies in the equatorial Pacific Ocean. Dry summers are coincident with El Niño periods (negative Southern Oscillation Index [SOI] anomalies), whereas wet summers are correlated with La Niña (positive SOI anomalies), suggesting that the oceanic SST structure plays an important role in forcing atmospheric circulation over tropical South America on inter-annual timescales. Forcing mechanisms that control the regional moisture balance on the timescales of centuries to millennia are considered more difficult to characterise, but are probably associated with changes in the seasonal distribution and magnitude of insolation that are brought about by shifts in the Earth's orbital parameters.

3.4 References

- Argollo, J., and Mourguiart, P. (2000). Late Quaternary climate history of the Bolivian Altiplano. *Quaternary International* **72**, 37-51.
- Baker, P. A., Rigsby, C. A., Seltzer, G. O., Fritz, S. C., Lowenstein, T. K., Bacher, N. P., and Veliz, C. (2001a). Tropical climate changes at millennial and orbital timescales on the Bolivian Altiplano. *Nature* **409**, 698-701.
- Baker, P. A., Seltzer, G. O., Fritz, S. C., Dunbar, R. B., Grove, M. J., Tapia, P. M., Cross, S. L., Rowe, H. D., and Broda, J. P. (2001b). The History of South American Tropical Precipitation for the Past 25,000 Years. *Science* **291**, 640-643.
- Barry, R. G., and Chorley, R. J. (1995). Tropical Weather and Climate. In "Atmosphere, Weather and Climate." pp. 224. Routledge, London.

-
- Curtis, S., and Hastenrath, S. (1999). Trends of upper-air circulation and water vapour over equatorial south America and adjacent oceans. *International Journal of Climatology* **19**, 863-876.
- Fu, R., Zhu, B., and Dickinson, R. (1999). How do atmosphere and land surface influence seasonal changes of convection in the tropical Amazon? *Journal of Climate* **12**, 1306-1321.
- Garcia, M., Villalba, F., Araguas-Araguas, L., and Rozanski, K. (1998). The role of atmospheric circulation patterns in controlling the regional distribution of stable isotope contents in precipitation: Preliminary results from two transects in the Ecuadorian Andes. *Isotope techniques in the study of environmental change. Proceedings of a symposium, Vienna, April 1997.. Published by International Atomic Energy Agency, ISBN 9201005989, Editors IAEA*, 127-140.
- Garreaud, R. D. (1999). Multiscale analysis of summertime precipitation over the central Andes. *Monthly Weather Review* **127**, 901-921.
- Garreaud, R. D. (2000). Intraseasonal variability of moisture and rainfall over the South American Altiplano. *Monthly Weather Review* **128**, 3337-3346.
- Global Runoff Data Centre. (2005). Long Term Mean Monthly Discharges and Annual Characteristics of Selected GRDC Stations. <http://grdc.bafg.de>.
- Grosjean, M. (1994). Paleohydrology of the Laguna Lejia (north Chilean Altiplano) and climatic implications for late-glacial times. *Palaeogeography, Palaeoclimatology, Palaeoecology* **109**, 89-100.
- Haug, G. H., Hughen, K. A., Sigman, D. M., Peterson, L. C., and Röhl, U. (2001). Southward Migration of the Intertropical Convergence Zone Through the Holocene. *Science* **293**, 1304-1308.
- Hiscox, J. H.-Y., R. (2004). Tropical Rainforest. In "Microsoft® Encarta® Online Encyclopedia 2004 <http://au.encarta.msn.com>." 1997-2004 Microsoft Corporation. All rights reserved.
- Jennerjahn, T. C., Ittekkot, V., Arz, H. W., Behling, H., Pätzold, J., and Wefer, G. (2004). Asynchronous terrestrial and marine signals of climate change during Heinrich Events. *Science* **306**, 2236-2239.
- Kousky, V. E. (1988). Pentad outgoing longwave radiation climatology for the South American sector. *Revista Brasileira Meteorologia* **3**, 217-231.
- Lenters, J. D., and Cook, K. H. (1997). On the origin of the Bolivian high and related circulation features of the South American climate. *Journal of the Atmospheric Sciences* **54**, 656-677.
- Marengo, J. A. (1995). Interannual variability of deep convection in the tropical South American sector as deduced from ISCCP C2 data. *International Journal of Climatology* **15**, 995-1010.
- Marengo, J. A., Nobre, C. A., and Culf, A. (1997). Climatic impacts of Fraigens in forested and deforested areas of the Amazon Basin. *Journal of Applied Meteorology* **36**, 1553-1566.
-

-
- Marengo, J. A., Nobre, C. A., McClain, M. E., Victoria, R. L., and Richey, J. E. (2001). General Characteristics and Variability of Climate in the Amazon Basin and its Links to the Global Climate System. In "The Biogeochemistry of the Amazon Basin." pp. 17-41. Oxford University Press, Oxford.
- Marengo, J. A., Nobre, C. A., and Sanches, M. B. (unpublished). On the atmospheric water balance and moisture cycling in the Amazon Basin. Characteristics and space-time variability.
- Maslin, M. A., and Burns, S. J. (2000). Reconstruction of the Amazon Basin effective moisture availability over the past 14,000 years. *Science* **290**, 2285-2287.
- Maslin, M. A., Durham, E., Burns, S. J., Platzman, E., Grootes, P., Greig, S. E. J., Nadeau, M. J., Schleicher, M., Pflaumann, U., Lomax, B., and Rimington, N. (2000). Palaeoreconstruction of the Amazon River freshwater and sediment discharge using sediments recovered at site 942 on the Amazon Fan. *Journal of Quaternary Science* **15**, 419-434.
- Moura, A. D., and Shukla, J. (1981). On the dynamics of droughts in Northeast Brazil: Observations, theory and numerical experiments with a general circulation model. *Journal of Atmospheric Science* **38**, 2653-2675.
- Nogues-Paegle, J., and Mo, K. M. (1997). Alternating wet and dry conditions over South America during Summer. *Monthly Weather Review* **125**, 279-291.
- Rao, V. B., and Hada, K. (1990). Characteristics of rainfall over Brazil: Annual variations and connection with the Southern Oscillation. *Theoretical and Applied Climatology* **42**, 81-91.
- Rowe, H. D., Dunbar, R. B., Mucciarone, D. A., Seltzer, G. O., Baker, P. A., and Fritz, S. (2002). Insolation, Moisture Balance and Climate Change on the South American Altiplano Since the Last Glacial Maximum. *Climatic Change* **52**, 175-199.
- Seltzer, G. O., Baker, P., Cross, S., Dunbar, R., and Fritz, S. (1998). High-resolution seismic reflection profiles from Lake Titicaca, Peru-Bolivia: evidence for Holocene aridity in the tropical Andes. *Geology* **26**, 167-170.
- Vuille, M. (1999). Atmospheric Circulation over the Bolivian Altiplano during Dry and Wet Periods and Extreme Phases of the Southern Oscillation. *International Journal of Climatology* **19**, 1579-1600.
- Vuille, M., and Ammann, C. (1997). Regional snowfall patterns in the high arid Andes. *Climate Change* **36**, 413-423.
- Vuille, M., and Baumgartner, M. F. (1998). Monitoring the regional and temporal variability of winter snowfall in the arid Andes using digital NOAA:AVHRR data. *Geocarto International* **13**, 59-67.
- Vuille, M., Hardy, D. R., Braun, C., Keimig, F., and Bradley, R. S. (1998). Atmospheric circulation anomalies associated with 1996:1997 summer precipitation events on Sajama Ice Cap, Bolivia. *Journal of Geophysical Research* **103**, 11191-11204.
- Zhou, J., and Lau, K.-M. (1998). Does a Monsoon Climate Exist Over South America? *Journal of Climate* **11**, 1020-1040.
-

4. A REVIEW OF THE 0 TO 40 KA PALAEOCLIMATE RECONSTRUCTIONS OF TROPICAL AND SUBTROPICAL SOUTH AMERICA

4.1 Introduction to Reconstructions of Palaeoclimate

4.1.1 Introduction

The primary aim of this study is to reconstruct the effective moisture history of the Amazon Basin. It is therefore necessary to review the existing knowledge of past climate change in tropical and subtropical South America. This chapter attempts to critically review the published proxy evidence of climate change in northern South America, with particular focus on the last glacial maximum (LGM) and the last glacial-interglacial transition (LGIT).

Over the recent decades, global climate change from the LGM to the current interglacial has been the subject of rigorous investigation. By contrast, however, relatively few data are available covering these periods from the northern and central parts of South America (Clapperton, 1993). As a consequence, the paucity of proxy records from these regions dictates that comparatively little is known of the past climate history of South America since the LGM, especially as many of the records lack completeness back to this period, and are often highly localised in their spatial representation. Nevertheless, the increasing amount of data that has been emerging over recent years is making it possible to begin constructing a continuous large-scale post-glacial climate history, based upon the integrated records of multiple proxies from different regions.

4.1.2 Limitations to Palaeoclimate Reconstruction

Ongoing limitations continue to inhibit the development of palaeoclimate reconstructions from South America. One of the major restraints is the difficulty in acquiring good chronological control. This is particularly an issue surrounding the LGIT and LGM periods, the precise timing and identification of which remain uncertain in the tropics, particularly for the LGIT. In consequence, inter-comparisons of tropical and extratropical climate change proxies are ambiguous. The chronological placement of the LGIT and LGM are critical when attempting to establish the nature and timing of climatic events in the tropics relative to their analogous counterparts in the higher latitudes. The timing of these climate stages are also essential prerequisites to investigate any potential leads and lags in climate change over geographical space and their associated teleconnections.

A good example is the deglacial climate reversal (DCR) documented within the glacial stage records from the Huascarán and Sajama Andean ice cores (Thompson *et al.*, 2000). Lack of dateable material in the ice cores between 11 and 19 ka has weakened the chronological constraints of the LGM and LGIT. Much debate has focussed on whether the DCR should be correlated to the Younger Dryas (YD) period in NW Europe as shown in Figure 4.1, or whether it should instead be correlated with the Antarctic Cold Reversal (ACR) in the Southern Hemisphere as shown in Figure 4.2. Methane-synchronisation between the central Antarctic Byrd and Vostock records and the Greenland GRIP record suggest the ACR to have preceded the YD by at least ~1.8 kyr, and be in fact synchronous with the Bølling-Allerød warm period in Greenland. This implies that Antarctica was warm during the YD (Blunier *et al.*, 1998; Blunier *et al.*, 1997). However, Steig *et al.* (1998) found the isotopic signal at the coastal Antarctic Taylor Dome site to have changed in parallel with the YD, rather than with the ACR recorded in central Antarctica. It is also possible that Taylor Dome records a regional feature of Antarctic sea surface temperature, possibly related to the YD (Raynaud *et al.*, 2000). The stratigraphy used in the Steig *et al.* (1998) work has also been questioned (Mulvaney *et al.*, 2000). To date, the debate remains ongoing, illustrating the highly complex nature of the global interactions involved, some of which are yet to be fully understood.

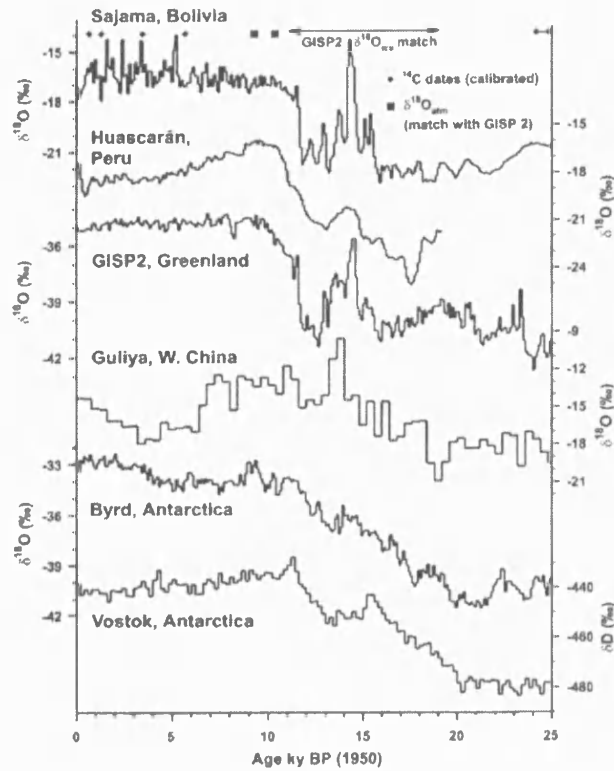


Figure 4.1: Diagram to illustrate the effects of tuning the Sajama and Huascarán Andean ice core records to the sequence of Northern Hemisphere climate change. ¹⁴C cal dates, the δ¹⁸O_{atm} match points, and the time interval over which δ¹⁸O_{ice} was matched to that in the GISP2 core are shown along the top (modified from Thompson *et al.* 2000).

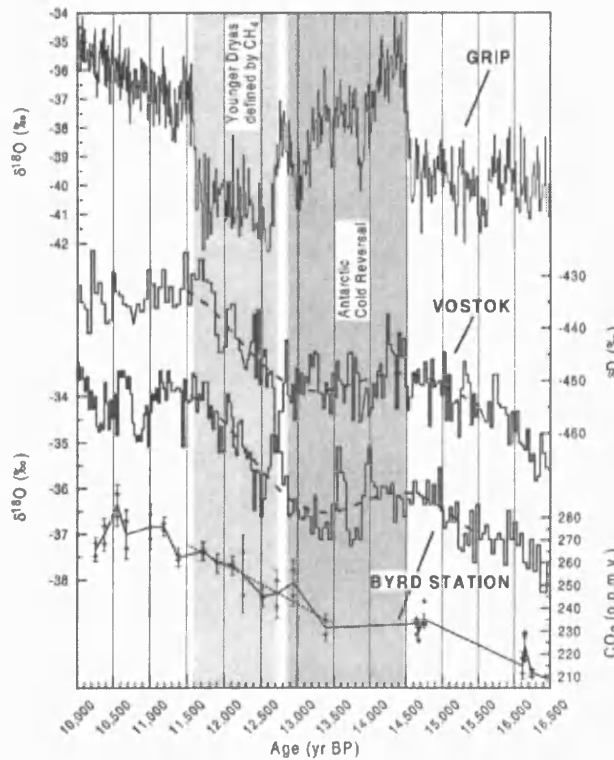


Figure 4.2: Methane-synchronised isotope records of the Greenland GRIP, and Antarctic Vostok and Byrd Station ice cores to show the relative timing of the Antarctic Cold Reversal and the Younger Dryas period (Blunier *et al.*, 1997), together with the increase in atmospheric CO₂ record from Byrd (modified from Raynaud *et al.*, 2000).

Although the Huascarán and Sajama ice caps both sit in the Southern Hemisphere, they each have 11-19 ka age models that have been tuned to a Portuguese marine core and the GISP2 polar ice core, respectively (Thompson, 2000; Thompson *et al.*, 1998; Thompson *et al.*, 2000). This forcible synchronisation of the DCR in the ice core $\delta^{18}\text{O}$ with the YD event has the effect of artificially ascribing a Northern Hemisphere control over the climate at these sites. Should however, the DCR be actually correlated with the ACR instead, this has the overall effect of making the ice core ages between 11 and 19 ka ~ 1.8 kyr relatively older in reality (thus making those dates used in the published age model ~ 1.8 kyr too young). Therefore great caution should be taken when comparing the timing of LGM and LGIT climatic events apparent within the Huascarán and Sajama ice cores with other climate records, on both a regional and global scale.

Care must also be taken to ensure that the event in the record being dated has been correctly identified. A case example is the discussion of possible inter-regional lagtimes surrounding the global sequence of deglaciation after the LGM, as discussed by Seltzer *et al.*, (2002), and Clarke (2002). Lake records from Lakes Titicaca and Junin in tropical South America suggest that the timing of maximum Andean late Pleistocene glaciation was broadly synchronous with the global LGM, 21 Cal ka (Seltzer *et al.*, 2002). However, comparing these data with polar ice core data and the record of glaciation from Owens Lake, California, Seltzer *et al.* (2002) propose that deglacial warming in tropical South America actually preceded the rapid deglacial warming in the northern high latitudes by several thousand years (see Figure 4.3). This prompted the authors to speculate that the warming in the tropics could even have acted as the trigger for the global deglaciation.

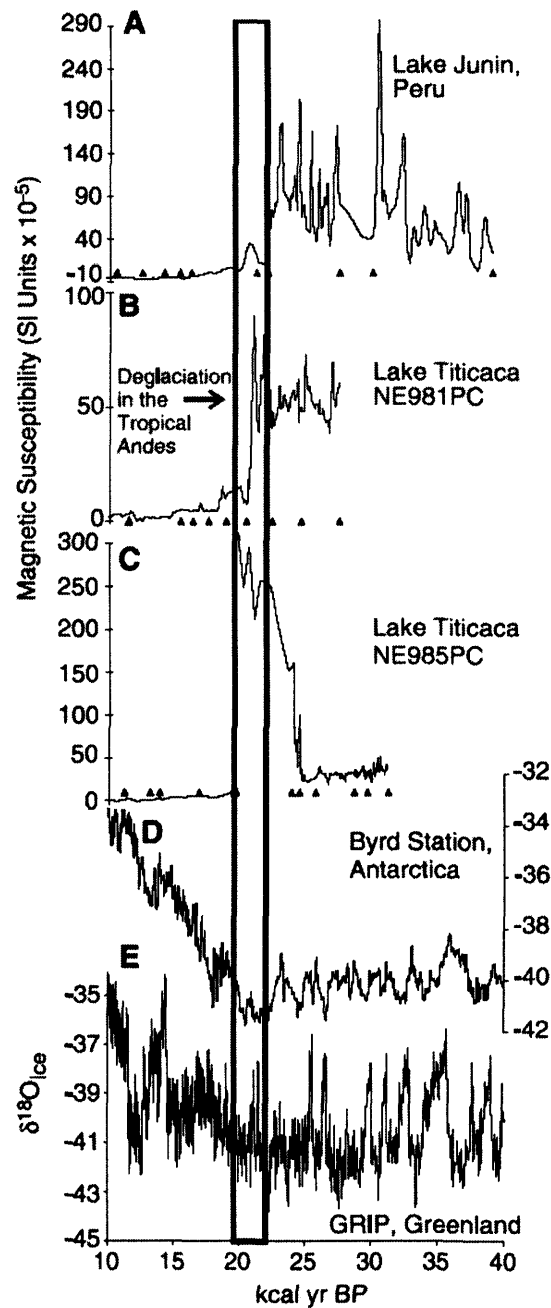


Figure 4.3: Palaeoclimate records from tropical and subtropical South America compared to the polar ice core records, which suggest that deglacial warming in tropical South America preceded the deglacial warming in the northern high latitudes by several thousand years (modified from Seltzer *et al.*, 2002). It should be noted that the GRIP timescale quoted by Seltzer *et al.* (2002) has since been revised to match the GISP2 chronology back to 40 ka (Johnsen *et al.*, 2001) and so is now no longer younger than the GISP2 for ages >15 kyr BP as shown in this figure. Data shown are magnetic susceptibility records from Lake Junin, Peru (A) and Lake Titicaca (B and C); and $\delta^{18}\text{O}_{\text{ice}}$ ice core records from Byrd Station, Antarctica (D) and GRIP, Greenland (E).

However Clark (2002) argued that the Owens Lake data from the Sierra Nevada was inappropriate for comparison with Lakes Titicaca and Junin due to the highly contrasting sedimentary regimes between the lakes of the two regions. At Lakes Junin and Titicaca, nearby LGM glaciers provided the lakes with a constant supply of glaciogenic sediment. Once these glaciers retreated however, moraine-dammed lakes acted as huge sediment traps acting to amplify the deglacial sedimentary signals of the downstream lakes. By contrast, Clark (2002) notes that the retreat of the Sierran glaciers did not produce such sediment trapping and so continued to receive glaciogenic input throughout the time that its watershed was glaciated. Clark (2002) proposes that the tropical South American lake records be instead compared to direct indicators of the timing of ice margin fluctuations.

Indeed several such records from western North America show Northern Hemisphere deglaciation to have occurred simultaneously with that of the tropical Andes. These are shown by black data points and grey shading, respectively, in Figure 4.4. Similar ages of glaciation have also been suggested for sectors of the British, Scandinavian and Laurentide Ice Sheets, coincident with high latitude warming and increased Northern Hemisphere summer insolation (for further details, see 2002 and references cited therein). This therefore supports a high-latitude forcing of the deglaciation. However it should also be noted that these examples of early deglaciation might also have arisen through changes in the local water budgets of the individual regions (Seltzer *et al.*, 2000).

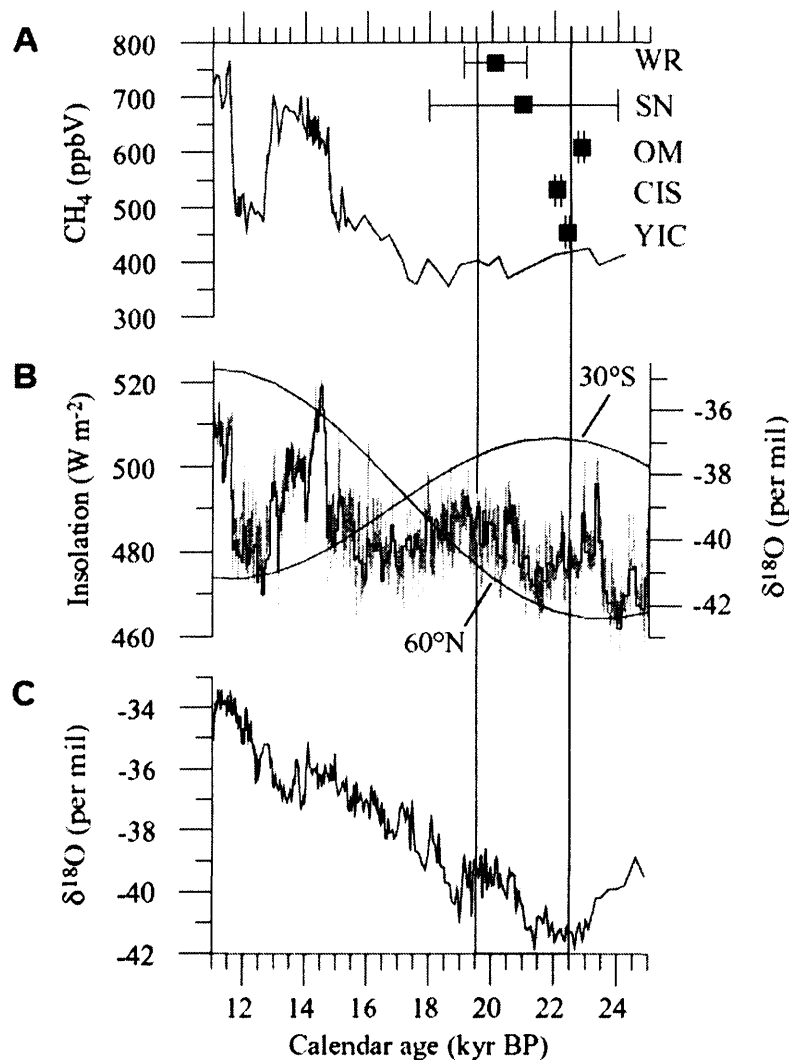


Figure 4.4: Diagram from Clark (2002) to show the synchronicity of deglaciation between the Northern Hemisphere and tropical Andes. The vertical grey box represents the timing of tropical deglaciation established in Seltzer *et al.* (2002). (A) GISP2 record of atmospheric methane. Black markers show the relative ages (with errors) of deglaciation of five glacier systems in western North America (no vertical scale). WR = Wind River Mountains, Wyoming; SN = Sierra Nevada Mountains, California; OM = Olympic Mountains, Washington; CIS = southern margin of the Cordilleran Ice Sheet, Fraser Lowlands, British Columbia; YIC = northern outlet glacier of the Yellowstone Ice Cap, Wyoming. (B) Smooth curves: midmonth insolation at 60°N (June) and 30°S (December). Jagged curves: GISP2 oxygen isotope record, presented at lower and higher-resolutions. (C) Oxygen isotope record from Byrd Station, Antarctica, displayed on the GISP2 timescale. For more details about how this diagram was constructed, please refer to Clark (2002).

Further caveats to South American climate reconstruction have arisen where, in the absence of other evidence, Amazon Basin palaeoclimate has been inferred indirectly from proxies used principally for other variables such as vegetation (e.g. Behling and da Costa, 2001; Behling *et al.*, 1998; e.g. Bush and Colinvaux, 1990; Ledru *et al.*, 2001; Vélez *et al.*, 2003).

Information pertaining to both palaeovegetation and climate has usually been derived from the same set of palaeodata, therefore circular arguments are an inherent problem (Mayle *et al.*, 2004). In recent times however, a growing body of independent climate proxies from a variety of terrestrial and marine archives have enabled more reliable inferences to be made. Nevertheless, vegetation records still remain the most abundant archive of South American palaeoclimate data, but in light of the other records becoming available, the pollen spectra can be further interpreted with greater understanding.

Although it is possible to reconstruct past climate with relative ease for regions such as the Altiplano (Argollo and Mourguiart, 2000; Baker *et al.*, 2001a; Baker *et al.*, 2001b; Rowe *et al.*, 2002; Servant and Servant-Vildary, 2003), it is more difficult to achieve for the Amazon Basin as scarcer published data are currently available – to date, for example, there are only six complete pollen records from Amazonia which extend back to the LGM (Mayle *et al.*, 2004). This arises in part from the fact that many proxy records are discontinuous, either due to sedimentary hiatuses that punctuate the stratigraphic record (e.g. lake desiccation), or due to the effects of processes operating only at specific climate intervals (e.g. speleothem growth during humid periods, sand dune accretion during arid periods). In spite of this, insights into South American palaeoclimate can be inferred from a cumulative variety of sources, which are reviewed in this chapter.

4.2 Palaeotemperature Reconstructions of the Amazon Basin

Information on past temperature changes within the Amazon Basin has been inferred from a variety of sources: CLIMAP (1976; 1981) originally estimated LGM tropical cooling of 2 °C, although this is now commonly considered to be rather conservative (IPCC, 2001); alkenone data (Bard *et al.*, 1997; Wolff *et al.*, 1998) suggest a 3°C LGM cooling of tropical sea-surface temperatures (SST) relative to modern, whereas coral- (Beck *et al.*, 1997; Guilderson *et al.*, 1994; Harris and Mix, 1999) and planktonic foraminifera (Mix *et al.*, 1999) -based tropical SST reconstructions and analyses of noble gas concentrations in Brazilian groundwater (Stute *et al.*, 1995) show a maximum LGM tropical cooling of 5°C; Brazilian palynological data (e.g. Behling, 2002; Behling and Negrelle, 2001; Bush *et al.*, 1990; e.g. Liu and Colinvaux, 1985) suggest a cooling of 3-7°C; kaolinite-bound oxygen ($\delta^{18}\text{O}$) and hydrogen isotopes (δD) in palaeosols from the Colombian Bogotá basin (Mora and Pratt, 2001) suggest an LGM cooling of 5 to 7°C; and high altitude ice core records from the Andes (Thompson *et al.*, 1998; Thompson *et al.*, 1995; Thompson *et al.*, 2000) show temperatures to have been up to 8-12°C lower during the LGM and DCR, although the LGM interpretation has since been reassessed to be more in the region of 3°C, with a similar

cooling also likely for the DCR (for more details see Pierrehumbert 1999). Snowlines (Clapperton, 1993) and treelines (van der Hammen, 1974) are considered to have descended 1000 m or more, and montane vegetation may have expanded to lower elevations (e.g. Bush and Colinvaux, 1990; Bush *et al.*, 1990; Colinvaux *et al.*, 1997; e.g. Colinvaux *et al.*, 1996; Haberle and Maslin, 1999; Liu and Colinvaux, 1985) also suggestive of lower temperatures. Marine pore water and benthic foraminiferal $\delta^{18}\text{O}$ (Schrag *et al.*, 1996) also support an LGM cooling in the tropical regions ($\sim 4^\circ\text{C}$ in tropical deepwaters), although these signals are also likely to be influenced by changes in deep ocean circulation.

However, in a comprehensive synthesis of LGM terrestrial palaeoclimate data, Farrera *et al.* (1999) concluded that tropical cooling was in fact far from spatially uniform, even in the tropical lowland regions and therefore large-scale extrapolated interpretations based upon individual sites should be made with caution. In this case, there remains little empirical palaeoclimate data that provides actual temperature information for the spatial majority of the LGM Amazon Basin, although it is generally assumed that the basin cooled in the region of $\sim 3\text{--}5^\circ\text{C}$ during the most recent cold stages.

At present, a similar synthesis of data for the LGIT has yet to be compiled, although it is assumed that the spatial variability of past temperature within the tropics would be of at least a similar nature to the LGM. Many climate records confirm the existence of a prominent deglacial climate reversal (DCR) in the tropical Andes just before the final warming into the early Holocene, for example Andean ice core $\delta^{18}\text{O}$ (Thompson *et al.*, 1995; Thompson *et al.*, 2000); pollen data from Lagoa do Caçó, northern Brazil (Ledru *et al.*, 2001) and Ecuadorian Amazonia (Bush *et al.*, 1990); climate data from Lake Titicaca (e.g. Baker *et al.*, 2001a; Baker *et al.*, 2001b; Rowe *et al.*, 2002) and the Amazon Fan (Maslin and Burns, 2000; Maslin *et al.*, 2000), although the exact timing and thus interhemispheric synchronicity of this event remains under discussion, however (see Section 4.1.2 above).

By far the most detailed records of trends in low-latitude South American temperature change can be resolved from the Andean ice cores. To date, four significant ice caps have been drilled in the tropical Andes: Huascarán, Quelccaya, Coropuna, and Sajama (in latitudinal order; see Figure 4.5). A number of other cores have been drilled (e.g. Ilimani, Bolivia; Chimborazo, Ecuador; Pucahirca, Copap, Caullaraju and Hualcan, all in Peru) although these have either not been analysed in such great detail, have not been published, or only cover relatively short periods. Records from Quelccaya reach back only as far as the mid-Holocene (Thompson *et al.*, 1985), however the Huascarán and Sajama cores have been

shown to extend back to the ~20 ka and ~25 ka, respectively (Thompson *et al.*, 1998; Thompson *et al.*, 1995; Thompson *et al.*, 2000). Records from Coropuna drilled in 2003 are yet to be assigned a chronology, but may extend back through the Holocene (L. G. Thompson, personal communication 2003). Climate as far back as the last glacial stage (LGS) can therefore be inferred from the Huascarán and Sajama ice core records.



Figure 4.5: A map to show the locations of the ice cores drilled to date in the Tropical Andes.

Huascarán Col ($9^{\circ}07' S$, $77^{\circ}37' W$, elev. 6048 m)

Quelccaya Ice Cap ($13^{\circ}56' S$, $70^{\circ}50' W$, elev. 5670 m)

Coropuna Ice Cap ($15^{\circ}32' S$, $72^{\circ}39' W$, elev. 6450 m)

Nevado Sajama ($18^{\circ}07' S$, $68^{\circ}53' W$, elev. 6642 m)

(<http://researchnews.osu.edu/archive/quelcoropics.htm> [accessed 04.06.04])

Data from the Huascarán (Peru) and Sajama (Bolivia) ice cores are shown in Figures 4.6 and 4.7, respectively, and have been reviewed in detail in a number of publications (e.g. Thompson *et al.*, 1998; e.g. Thompson *et al.*, 1995; Thompson *et al.*, 2000).

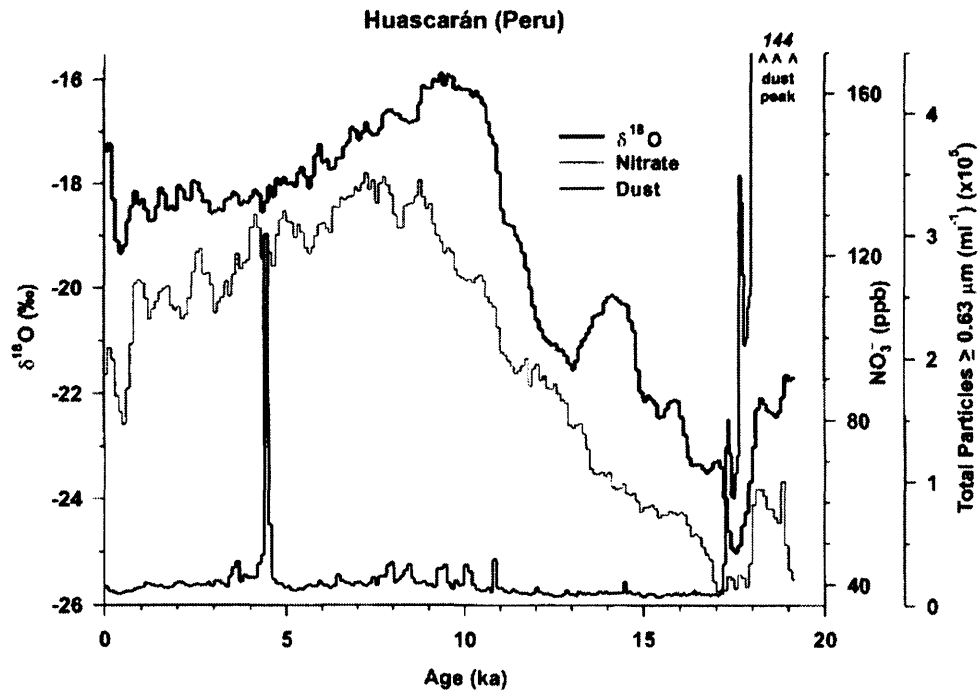


Figure 4.6: $\delta^{18}\text{O}$, nitrate and insoluble dust concentrations from the Huascarán ice core, Peru (modified from Thompson *et al.*, 2000).

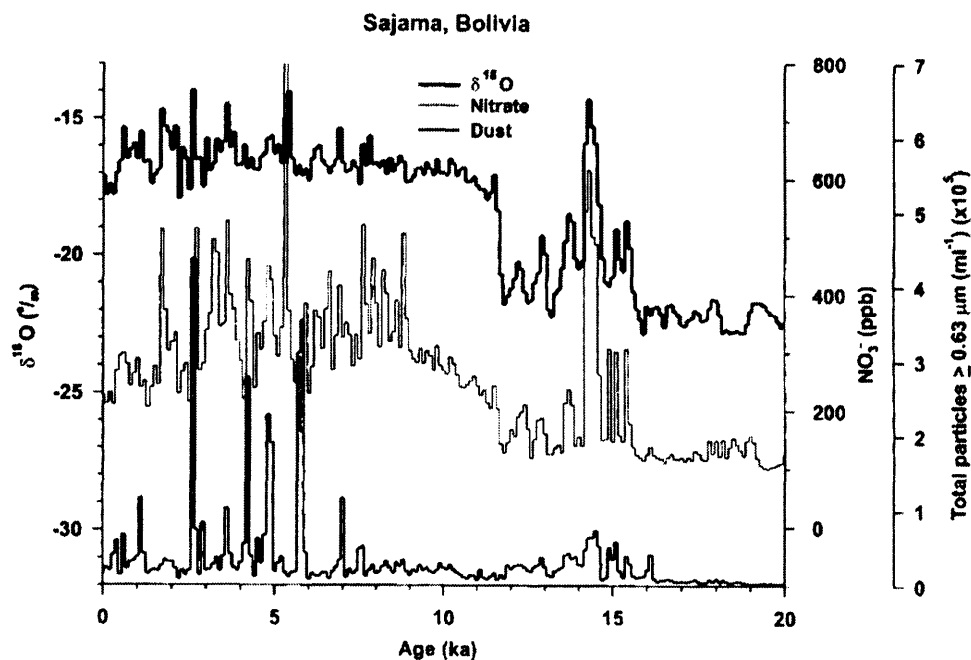


Figure 4.7: $\delta^{18}\text{O}$, nitrate and insoluble dust concentrations from the Sajama ice core, Bolivia (Thompson *et al.*, 2000).

$\delta^{18}\text{O}$ data from the Huascarán ice cap (Thompson *et al.*, 2000; see Figure 4.6) reveal that the isotopically coldest ice was deposited during the LGS, after which there was progressive warming trend, punctuated by the DCR, toward the Holocene. The isotopically warmest ice was laid down during the early Holocene, after which time, the temperature in the Andes has

steadily cooled. Superimposed on this declining Holocene trend were minor centennial-scale oscillations in $\delta^{18}\text{O}$, the coolest time coinciding with the Little Ice Age. During the last ~200 years, $\delta^{18}\text{O}$ has increased markedly, with 20th Century values being the isotopically warmest for the last 6 kyr (Thompson *et al.*, 2000).

Interestingly, in the Sajama record the warming at ~15.5 ka is far more pronounced relative to that in the Huascarán data, and culminates with the isotopically warmest period at ~14.3 ka, rather than in the early Holocene (see Figure 4.7). Thereafter, the DCR is equally obvious in the Sajama record, however the underlying trend in the Holocene data is of slight warming, albeit in an oscillatory fashion.

However, it is important to consider that the $\delta^{18}\text{O}$ signal may not be solely responsive to changes in temperature alone, but may also reflect the isotopic values of precipitation, which may have varied between the different latitudinal locations of Huascarán and Sajama. This may also explain the differences in the isotopic ranges of the two datasets between modern, early Holocene and LGM values shown in Table 4.1 (see also Section 4.3.6a for discussion on ice core climate data interpretation).

	Modern (0–1 ka)	Early Holocene (EH) (6.8–10.0 ka)	Last Glacial Maximum (LGM) (18.0–21.2 ka)	MODERN – LGM (‰)	EH – LGM (‰)
Sajama (Bolivia)	–16.8	–16.7	–22.1	5.4	5.4
Huascarán (Peru)	–18.5	–16.6	–22.9	4.4	6.3
GISP 2 (Greenland)	–35.0	–34.6	–39.7	4.7	5.1
Guliya (W. China)	–14.4	–13.1	–18.5	4.1	5.4
Byrd (Antarctica)	–32.8	–33.9	–40.5	7.6	6.6
Vostok (Antarctica)	–441 (–56.4)	–436 (–55.7)	–472 (–60.2)	3.9	4.5
Vostok (21–24.2 ka)			–479 (–61.1)	4.8	5.4

Table 4.1: A comparison of average $\delta^{18}\text{O}$ values for various time intervals and for different ice cores. Vostock measurements are in δD with comparable $\delta^{18}\text{O}$ values shown in parenthesis (modified from Thompson *et al.*, 2000; see also references therein).

4.3 Palaeomoisture Reconstructions of the Amazon Basin

In comparison to palaeotemperature, palaeoprecipitation is a highly complex variable to reconstruct. As detailed in Chapter 3, precipitation at any given locality in Amazonia is driven by a combination of both tropical and extra tropical factors, which have varying relative influences over different geographical regions of the continent. Therefore past precipitation is likely to have been far from spatially uniform across such a large and diverse watershed as the Amazon Basin.

Potentially, the past moisture history of the Amazon Basin can be reconstructed from a number of proxy variables from a variety of sources. These include records sited both proximal and distal to the Basin, including geomorphological and geological features, lake deposits (sedimentology and palaeoecology), marine sediments, speleothems, and ice cores. However each of these different archives possesses its own set of limitations. For this reason, it becomes practical to review each type of palaeomoisture archive individually.

Colinvaux and De Oliviera (2000) hypothesise that in order for a reconstruction to be valid, the proxy used must meet a set of three ‘validation criteria’:

1. The proxy must have been identified correctly;
2. The proxy must require a climate or environment that is significantly different from the recent past;
3. The proxy must have a proven chronology.

Colinvaux and De Oliviera (2000, p353) also note most importantly that...

“The common denominator in these and other stipulations of Pleistocene aridity in the Amazon is the hypothesis of ice-age aridity itself. The arguments become circular and by semantic trick gain quasi-parsimony. An explanation for a [feature] that relies on Pleistocene aridity is believable: it matters not that no correlation is established or that alternative explanations exist. Thus a false paradigm is born.”

Many inferences of moisture variability, especially those derived from indirect methods, should therefore be regarded speculatively, as they are only suggestive in part, and present no definitive evidence for aridity. Each of the groups of proxy variables reviewed in this chapter will be assessed according to these three validation criteria.

4.3.1 Morphological Observations

Despite the considerable scarcity of LGM records for the Amazon Basin, aridity has been inferred from studies of ancient palaeodune systems, speculations about the ‘origins’ of white sands in soil sequences, buried stonelines, fossil evaporite deposits in river terraces, arkosic sands in buried fan deposits, and sedimentary hiatuses in lake cores, each of which are reviewed against the three validation criteria in Table 4.2.

Morphological proxy cited as evidence for glacial aridity	Site	Validation Criteria			Valid proxy?	Example references
		1) Identified properly?	2) Require climate different from now?	3) Solid chronology?		
Fossil sand dunes (identified in field and from remote sensing data).	Northeast Brazil (Bahia State); Pantanal region of Central Brazil; Ilanos (Orinoco).	×? Questionable, except those of Bahia State.	✓?	× Bahia State system active during Holocene. Difficult to date.	No.	Barreto <i>et al.</i> , 1997; Boggiani and Coimbra, 1995; Clapperton, 1993; Filho <i>et al.</i> , 2002; Klammer, 1982; Latrubesse and Nelson, 2001; Tricart, 1974.
'Aeolian' white sand deposits in soils.	Between Rivers Negro and Branco, northwestern Brazil.	× Not representative of aeolian activity, but probably podsols associated with the low pH of the blackwater system.	×? Site possibly under an edaphic control.	× Difficult to date.	No.	Ab'Saber, 1982; M.L. da Costa, personal communication to K. Suguio, cited in Clapperton, 1993; Colinvaux <i>et al.</i> , 2000.
Buried stone lines.	Near Manaus.	× Are more likely <i>in situ</i> concretions.	×	× Most likely of Tertiary age.	No.	Ab'Saber, 1982; Clapperton, 1993; Irion <i>et al.</i> , 1995.
Evaporite deposits (gypsum and aragonite concretions) in river terraces.	Lower Rio Acre.	× Most likely associated with marine incursion associated with the building of the Andes.	×	× Identification based upon one AMS date of 55 kyr BP. Most likely to be of Miocene age.	No.	Kronberg <i>et al.</i> , 1991; M. Rasaninen, personal communication, cited in Colinvaux and De Oliveira, 2000.
Arkosoic sands (unweathered plagioclase) in submarine delta deposits.	Amazon Fan.	✓	× Could have been weathered from the Andes and carried directly out to sea.	✓ Radiocarbon dated.	No.	Damuth and Fairbridge, 1970; Irion, 1976; Irion <i>et al.</i> , 1995; Meade <i>et al.</i> , 1985; Milliman <i>et al.</i> , 1975.
'Gaps' in sedimentary sequences (see Section 4.3.3).	e.g. Lake Pata.	× Highly dependant upon precision of radiocarbon dating and stratigraphic correlation of dated samples to the boundaries of hypothesised 'gaps'.	× Questionable environmental significance of 'gap' in record.	✓ N.B. only if 'gap' exists!	No.	Colinvaux and De Oliveira, 2000; Ledru <i>et al.</i> , 1998.

Table 4.2: A review of the morphological evidence for palaeomoisture in the Amazon Basin.

With reference to Table 4.2, of all the proxies reviewed, it seems that not one of them fulfils the three validation criteria, so cannot be used individually as direct evidence for past moisture changes in the Amazon Basin. However, these proxy data can provide supplementary evidence to support the inferences made from other archives, and thus provide valuable contributions to composited multiproxy investigations.

4.3.2 Palaeoecological Records

By far the most abundantly studied climate archives in the Amazon Basin are lake sediments, of which it has been estimated that there are at least 100,000 km² of lakes and swamps in the modern Amazon Basin (Flood *et al.*, 1995). However, despite their relative abundance, comparatively few lake records have been studied, with these records often being highly fragmentary and older records being increasingly difficult to source. Therefore LGM records are rather scarce, and highly sought after as a result. Such records commonly have poor chronological control (Colinvaux, 1989), however should enough organic matter be present, and any ¹⁴C reservoir effects be known, it is possible to use radiocarbon dating to assign a chronology.

Past moisture changes have frequently been reconstructed from fossil organic matter (principally pollen assemblages, but also macrofossils and biomarkers) contained within both lake and marine sediments, whereby an ecosystem switch from rainforest to savannah has been implied to represent a transition from moist to arid climates. In addition, the presence/absence of key indicator species of known ecological tolerance can be used to hypothesise about past moisture conditions. Much of this work is also associated with investigating the climatic resilience of the Amazon rainforest through the last glacial cycle.

The ‘Pleistocene Refuge Hypothesis’, first put forward by Haffer (1969), and developed further by Prance (1987) suggests that during glacial stages, the Amazon Basin experienced extreme drying such that, combined with lower temperatures and *p*CO₂ levels, the C₄ pathway of photosynthesis became more efficient for primary production. Consequently, tropical grasses out-competed their C₃ counterparts, thereby restricting the rainforest to isolated pockets within discrete areas of the Amazon Basin. The refuge hypothesis requires an entire biome shift from forest to savannah to be plausible (Colinvaux and De Oliveira, 2000).

The evidence presented to test the Pleistocene Refuge Hypothesis has been discussed and reviewed extensively in the literature (Colinvaux and De Oliveira, 2000; Colinvaux *et al.*, 2000; Hooghiemstra and van der Hammen, 1998; Mayle *et al.*, 2004).

However, rigorous investigation into the LGM Amazon Basin vegetation is somewhat limited by the paucity of available records. To date, there are only very few significant long pollen records that extend back through the LGM, from within the actual Amazon Basin itself, for example: Laguna El Pinal (4°08'N, 70°23'W; Behling and Hooghiemstra, 1999); Laguna Loma Linda (3°18'N, 73°23'W; Behling and Hooghiemstra, 2000); Lake Pata (0°16' N, 66°41' W; Bush *et al.*, 2002; Colinvaux *et al.*, 1996); Caquetà River (0°44'S, 72°04'W; Urrego, 1994; Urrego, 1997); Caçó Lake (2°58'S, 43°25'W; Sifeddine *et al.*, 2003); Carajas (6°20'S, 50°25'W; Absy *et al.*, 1991; Sifeddine *et al.*, 2003); Katira Creek (9°S, 63°W; Absy and van der Hammen, 1976; van der Hammen, 1972; van der Hammen, 1974; van der Hammen and Absy, 1994); Laguna Bella Vista (13°37'S, 61°33'W; Burbridge *et al.*, 2004; Mayle *et al.*, 2000); and Laguna (14°28'S, 61°04'W; Burbridge *et al.*, 2004; Mayle *et al.*, 2000).

Of the studies discussing and supporting the refuge hypothesis however, only records from very marginal sites relative to the modern rainforest, particularly the extreme southwest, can provide substantial evidence for savannah expansion/ migration of forest ecotone boundaries (Colinvaux *et al.*, 2000; Mayle *et al.*, 2004; Mayle *et al.*, 2000). These include Katira Creek in Rondonia (Absy and van der Hammen, 1976; van der Hammen, 1972; van der Hammen, 1974; van der Hammen and Absy, 1994), and the Noel Kempff Mercado National Park (Laguna Bella Vista and Laguna Chaplin; Mayle *et al.*, 2000) in the extreme southwestern edge of the modern forest; and Laguna El Pinal in the Colombian savannahs of the Llanos Orientales (Behling and Hooghiemstra, 1999), and Caçó Lake (Sifeddine *et al.*, 2003) at the opposite end borders of the Basin.

The two records from deeper within the Amazon Basin, from Carajas (often the classic citations in defence of savannah encroachment) and the Caquetà River, have since been reinterpreted as responding to strong local edaphic control (Hooghiemstra and van der Hammen, 1998; Colinvaux and De Oliviera, 2002) and their use as evidence in support of the Pleistocene Refuge Hypothesis is now regarded as controversial.

However interpretations of climate based upon vegetation reconstructions alone must be hedged with caveats due to the potential circular arguments that arise from reconstructing

two separate, yet simultaneously interdependent signals from the same dataset. There is also the flawed frequent assumption that climate is the only important environmental control over species distributions. In reality, vegetation responds to a complex interplay of a range of climatic and environmental factors, both on a local and regional scale; and the sensitivity of vegetation to one particular parameter may vary according to the boundary conditions of another/others. For example, it has been demonstrated by ecophysiological experiments (Cowling and Sage, 1988; Policy *et al.*, 1993), and dynamic vegetation modelling (e.g. Cowling *et al.*, 2001) as well as palaeorecords of stable carbon isotope (Street-Perrott *et al.*, 1997) that temperature and atmospheric CO₂ have an important role to play in controlling plant physiology, and therefore are vital in determining the sensitivity of the rainforest to changes in effective moisture. In light of these new findings, the persistence of forest at a site being taken to imply moist conditions may not therefore represent a fair climatic interpretation of the data.

Vegetation response as a proxy for aridity also carries additional complexities as the vegetation may not necessarily be responding to changes in average annual precipitation *per se* (assuming it to be the principle driver), but rather to critical changes in the length of the annual dry season: Pollen analyses (Bush, 2000; Bush *et al.*, 2002) have suggested that a critical threshold in annual precipitation of 2000 mm yr⁻¹ exists, whereby below this level, forests become more open and fragmented. Therefore, so long as the wet season provides >2000 mm of precipitation, the dry season could be as much as four to five months in duration with as little as 100 mm of rain before there is a noticeable change in the forest structure (Bush *et al.*, 2002). Should the annual dry season exceed four-five months, the rainforest cannot be sustained ecologically. (Maslin, 2004; Sternberg, 2001). Consequently, savannah grasslands will have a competitive advantage and therefore dominate. Depending upon whether these thresholds are breached, it implies that pollen signals could be rather immune to changes in the precipitation regime over a site, as a record showing continuous forest cover need not necessarily preclude that the local climate transitioned from being mildly seasonal, to having a more prolonged or more intense dry season (Bush *et al.*, 2002), and/or indeed that there was a general reduction in precipitation associated with lower lake levels reconstructed (e.g. Bush *et al.*, 2002; Sifeddine *et al.*, 2001).

However, any palaeoecology-based reconstruction is heavily reliant upon the assumption that the environmental ranges of the plant populations are known accurately, not to mention that the climate information has been interpreted correctly from the palaeoecological data. The latter is particularly an issue where deciphering a regional signal of change from a local

signal of change, for example at the Carajas Plateau (Absy *et al.*, 1991; Hooghiemstra and van der Hammen, 1998; van der Hammen and Absy, 1994) where the interpretation of the vegetation signal over the site, previously hypothesised to be climatically controlled, has since been challenged and reinterpreted to be edaphically controlled (Colinvaux *et al.*, 2000).

In terms of meeting the three validation criteria, two are met with relative comfort, whereby the proxy can be identified properly^{1*}, and where possible can be assigned to the late Pleistocene period through radiocarbon dating³. Although identifiable plant populations require a climate significantly different from the recent past², this is only once certain climatic thresholds have been breached, and so therefore the second criterion can really only apply to climatically marginal sites, as those which are insensitive will merely buffer any climate signal. The meeting of this criterion is also strongly dependant upon the accurate interpretation of the palaeoecological data. Nevertheless, the possibility that all three criteria can be met validates the palaeoecological archive as a proxy for reconstructing past moisture in the context of this study.

4.3.3 Inorganic Sedimentary Lake Records

Of the glacial lowland lake sediments that have been recovered from the Amazon Basin, a number of LGM records appear to be highly oxidised implying lower water levels (Colinvaux *et al.*, 1996). A significant number of lowland lakes lack LGM sediments altogether, suggesting that lakes may have completely desiccated during this period (Servant *et al.*, 1993; Sifeddine *et al.*, 2001; van der Hammen, 1974; van der Hammen and Absy, 1994). Indeed, a study of age models in lowland lake studies went as far to suggest that the LGM is represented by a hiatus at *all* known lowland lake sites (Ledru *et al.*, 1998), although the re-dating of a number of these proposed hiatuses has led to this view being challenged (Colinvaux *et al.*, 2000).

A succession of very thin layers of sand and organic matter within LGM sediments from Caco Lake, Maranhao State, northern Brazil (Sifeddine *et al.*, 2003) suggests that the glacial climate of this region was predominantly dry, but interrupted by short humid phases. Conflicting evidence comes from a cluster of lakes (Lakes Pata, Verde and Dragao) on an inselberg in northwestern Brazil (Bush *et al.*, 2002) however, where relatively depleted sedimentary K⁺ concentrations imply the LGM to have been relatively humid (although still

* Numbers refer sequentially to the three validation criteria detailed at the beginning of Section 4.3, and shall be referred to this way hereafter where appropriate.

below modern levels), which is further supported by a complete lack of charcoal in the LGM sediments (M. Bush, unpublished data, cited in Mayle *et al.*, 2004). During the Late Pleistocene, evidence of rapid lake-level rise and forest expansion at Caco Lake suggest the climate became progressively wetter, although the early Holocene was characterised by lower moisture availability and a distinct dry period until 7 Cal ka (Hansen *et al.*, 2003; Sifeddine *et al.*, 2003). This initial dryness is supported by evidence of water level transgression at Lake Silvana, southeastern Brazil shortly before ~ 8 ^{14}C kyr BP (Rodrigues-Filho *et al.*, 2002), and the formation of Lago Calado, near Manaus, central Amazonia ~ 7.7 ^{14}C ka (Behling *et al.*, 2001). Similar moistening throughout the Holocene is also seemingly evident at Lake Pata (Bush *et al.*, 2002). However, inferences about sea-level change from Lago Crispim, northern Brazil (eastern Amazonia) suggest that sea level was higher during the early Holocene, and did not start to regress until ~ 7 ^{14}C ka. This implies that regional water tables could also have been higher about the time of increasing water level at these lakes (Behling and da Costa, 2001). In addition, it is interesting to note that this period is hypothesised to correspond with the onset of the El Niño-Southern Oscillation (ENSO) phenomenon in South America (Martin *et al.*, 1993; Moy *et al.*, 2002; Rodbell *et al.*, 1999).

Outside of the Amazon Basin, authigenic calcite-based oxygen isotope ($\delta^{18}\text{O}$) studies of effective moisture at Lake Junin in the Peruvian high Andes for the last 14 kyr (Seltzer *et al.*, 2000) reveal remarkable correspondence to the $\Delta\delta^{18}\text{O}$ outflow reconstruction from ODP Site 942 on the Amazon Fan (see Figure 4.8, and Section 4.3.4 below; Maslin and Burns, 2000; Maslin *et al.*, 2000). Lake Junin is considered to share the tropical Atlantic as a common moisture source with Amazonia, and assuming that the isotopic change is not related to factors such as changes in either temperature or the $\delta^{18}\text{O}$ of precipitation, the record implies that the climate became progressively drier through the LGIT, reaching maximum aridity during the time corresponding to the YD. Thereafter it became progressively wetter through the Holocene to the modern day.

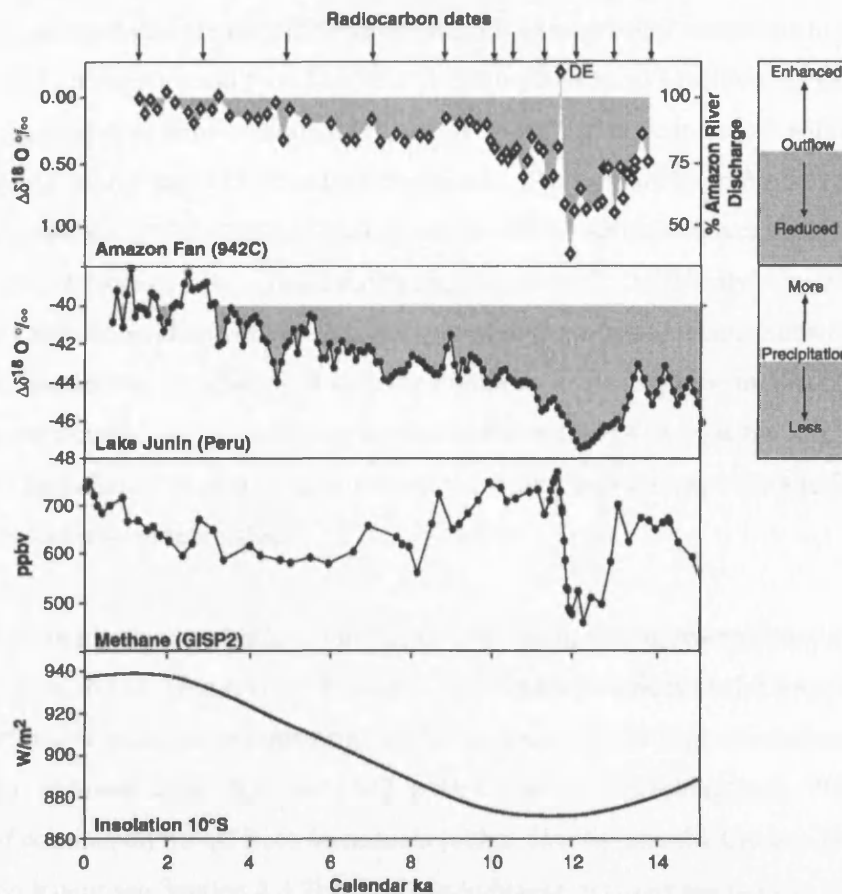


Figure 4.8: A comparison of proxy records for effective moisture in tropical South America from Lake Junin (Peruvian Andes), and ODP Site 942C on the Amazon Fan (modified from Maslin and Burns, 2000). $\Delta\delta^{18}\text{O} = \delta^{18}\text{O}$ measured at ODP Site 942, corrected for global ice volume and sea surface temperature. For details of how $\Delta\delta^{18}\text{O}$ was derived, see Maslin and Burns (2000).

With respect to the validation criteria, whether or not the proxy can be identified correctly¹ is questionable, particularly where attempts have been made to infer past aridity from ‘identified’ sedimentary hiatuses. This also illustrates the difficulties involved with obtaining chronological control³ for lake sediments, which may limit the extent to which the third validation criterion may be met. However, in the contexts where the proxy is more easily measured/identified¹, such as fluctuations in lake level, independent of sea level-related changes in the water table, and $\delta^{18}\text{O}$ records of effective moisture, it is possible to use the records as proxies for past moisture². Furthermore, where a chronology can also be assigned³ to these proxies, all three validation criteria can be satisfied.

4.3.4 Marine Geochemical Records

Using techniques referred to in the previous sections, Amazon Basin aridity has largely been inferred from highly localised and qualitative indicators of effective moisture. However,

Using radiocarbon-dated planktonic foraminifera $\Delta\delta^{18}\text{O}$ to monitor variations in salinity over ODP Site 942 on the Amazon Fan, Maslin and Burns (2000) and Maslin *et al.* (2000) produced the first ever semi-quantified reconstruction of effective moisture within the Amazon Basin for the last 14 Cal ka (see Figure 4.8). The authors hypothesised that during the LGIT, particularly ~12–13.5 Cal ka, the outflow of the Amazon River was reduced to at least 60% of the modern value. This implies significant aridity within the Amazon Basin, notably at a time coincident with the YD prominent in northwest Europe. Such late glacial aridity also happens to correlate well with the rapid rise in atmospheric methane revealed by polar ice core records, providing strong support to the notion of its possible origin in tropical wetlands. Thereafter throughout the Holocene, the Amazon discharge continues a steady progression toward modern values.

What was particularly remarkable about this record was its strong resemblance to a similar $\Delta\delta^{18}\text{O}$ signal from Lake Junin in the Peruvian high Andes (see Section 4.3.3 above), another gauge of effective moisture in equatorial South America, and the high-resolution %Ti and %Fe records obtained from ODP Site 1002 in the Cariaco Basin (Haug *et al.*, 2001), a recorder of continental runoff from Venezuela (either directly into the Cariaco Basin, or via the Orinoco River; see Section 4.3.7b). Such resemblance between the records gives credence to the ODP 942 record as having the potential to monitor past climate over Amazonia, and indeed northern South America for at least the past 14 Cal ka. This thesis attempts to continue and expand upon the record published by Maslin and Burns (2000).

Where reconstructions of South American climate exist from other marine records (e.g. Arz *et al.*, 1998; Arz *et al.*, 1999; Behling *et al.*, 2000; Behling *et al.*, 2002; Harris and Mix, 1999; Rühlemann *et al.*, 2001; Showers and Bevis, 1988), these are of much lower resolution over longer periods, and are also relatively more qualitative.

Assuming the ODP 942 $\Delta\delta^{18}\text{O}$ is purely a record of effective moisture in the Amazon Basin, it is potentially able to fulfill all three of the validation criteria, whereby it can be identified correctly¹, requires a climate that is significantly different from the recent past², and can be assigned a chronology³.

4.3.5 Speleothem Records

To date, very few speleothem records are available which represent the Amazon Basin, most likely arising from the difficulties (geographical and political) in accessing suitable sites in the field. However, speleothems provide highly valued climate records as out of all the

archives available they can potentially yield data at some of the highest available temporal resolution (relative to lake and marine sediments, for example), with chronological control provided by uranium-series dating.

In central west Brazil, a short late Holocene record from João Arruda Cave, Mato Gross do Sul State reveals a trend of increasing rainfall for the last 3.8 kyr, with a higher recurrence of drier events recorded between 3.8-2.5 ka than the later part of the record (Bertaux *et al.*, 2002).

A very long (210 kyr) composite record has recently been published from a number of long speleothems and travertine deposits collected from caves in northern Bahia state, northeastern Brazil (Wang *et al.*, 2004; Wang *et al.*, 2003b; Wang *et al.*, 2003a). This region is presently semiarid, so speleothem deposition does not presently occur, thus delineating any dated subsample as a time when climate must have been wetter than present. Analyses of U-series sample ages reveal that all speleothems grew during glacial periods, implying that in this particular region, the LGM climate of the area was more humid than modern times. Wang *et al.* hypothesise that this can be explained by a southern displacement of the Intertropical Convergence Zone (ITCZ) during glacial times bringing increased rainfall to the region.

This is corroborated by long (116.2 ka) speleothem records collected from southeastern Brazil (Cruz *et al.*, 2005). The authors hypothesise that the $\delta^{18}\text{O}$ signal measured from Botuverá Cave serves as a proxy for shifts in the amount, and source region of precipitation (Amazon Basin versus Atlantic Ocean), and thereby records shifts in atmospheric circulation and convective intensity over South America. Relatively depleted glacial $\delta^{18}\text{O}$ values imply that precipitation was sourced from the Amazon Basin. However, the authors attribute this to a southerly displacement of the Southern Hemisphere Summer Monsoon, rather than to convective rainfall associated with the ITCZ. Nevertheless, both systems are driven by meridional shifts in the meteorological equator (see Chapter 3, Section 3.2.1).

Relatively long Peruvian speleothem records for the last 25 kyr, amongst the first ever studied from the Andes, are also currently being analysed (Vonhof *et al.*, 2003). To date, no published data are currently available, although preliminary $\delta^{18}\text{O}$ data reveal a clear shift to drier conditions at ~ 4 kyr BP, with distinct decadal variation over the last 5 kyr. Nevertheless, this requires replication in other Amazonian speleothem records before firm conclusion can be drawn.

As for the lake and marine geochemical records, speleothem-based climate reconstructions are able to fulfil all three of the validation data in that the proxy used ($\delta^{18}\text{O}$) can be identified properly¹, speleothem records are able to monitor environments significantly different from the recent past², and they can be assigned age models via uranium-series dating³.

4.3.6 Extrapolations of Climate Information From More Distal Regions

Due to the inherent difficulties of reconstructing precipitation in the Amazon Basin, a number of studies have attempted to reconstruct Amazonian palaeoclimate from adjacent regions, including the Altiplano to the south, and the Cariaco Basin to the north.

4.3.6a South of Amazonia: the Altiplano

Attempts have been made to infer Amazonian palaeoclimate from the Altiplano region (e.g. Baker *et al.*, 2001a; Baker *et al.*, 2001b; Thompson *et al.*, 1998; Thompson *et al.*, 2000) where in contrast to the Amazon Basin, climate on the Altiplano is predominantly hypothesised to have been much wetter during the LGM. Evidence from the Altiplano comes in the form of Andean ice core records, and lake records including those from Lake Titicaca and the palaeolake salt flats of Uyuni and Coipasa. However due to the vast geographical distance between the Altiplano and the Amazon Basin, and the complex nature of the South American climate regime, any large-scale extrapolations from such distal and individual sites should be made with caution. This limitation also serves to exceed any of those that arise through evaluation via the three validation criteria, as even if a proxy from these regions were to satisfy all three assessments, it would become obsolete by contextual default if it should not be reflecting the climate of the Amazon Basin. For this reason, the criteria-based evaluation of proxy records from sites distant to the Amazon Basin will not be performed, and any inferences made about Amazon Basin climate from these proxies should be viewed with caution.

i) Ice Core Evidence

Details of the Andean tropical ice cores are given in Section 4.2, with data from the Huascarán and Sajama ice cores shown respectively in Figures 4.6 and 4.7. As discussed previously, difficulties associated with the Sajama age model mean that although the existence of glacial ice can be confirmed, no independent dates can be ascribed to the core between 11.5 – 24 Cal ka. Of the proxy records available from tropical ice cores, some of the

more widely used palaeomoisture archives include insoluble dust, atmospheric nitrate concentrations ($[\text{NO}_3^-]$), and the snow accumulation reconstruction. Pollen records entrapped within the ice can also be used as an indirect proxy for moisture (see Section 4.3.2).

One of the striking features of the Huascarán record is the 200-fold increase in insoluble dust concentrations in the LGS ice relative to the Holocene. This is indicative of a much more turbid LGS atmosphere, implying higher glacial atmospheric aridity and thus lower precipitation. Atmospheric $[\text{NO}_3^-]$, thought to originate from tropical rainforests and forest soils, is also reduced by three to four times in the LGS, and pollen concentrations are virtually negligible supporting a cold, sparsely vegetated environment with low pollen production. Interestingly, insoluble dust and $[\text{NO}_3^-]$ are not suppressed in the Huascarán record during the Younger Dryas period, although the pollen concentrations were still reduced relative to the Holocene (Thompson *et al.*, 2000). It should also be considered, however, that such changes in aerosol concentrations may have arisen equally through changes in the atmospheric circulation regime during the LGS.

Thompson *et al.* (2000) ascribed the lack of LGS dustiness in the Sajama ice core (eight times less than Huascarán) to its proximal location to the Altiplano, where there is evidence for the existence of large regional palaeolakes during the LGS (e.g. Servant and Fontes, 1978; Servant *et al.*, 1995; Sylvestre *et al.*, 1999) implying a moister glacial climate regime over the Altiplano (see Figure 4.9). This is also supported by relatively high glacial snow accumulation at Nevado Sajama, where LGM ice thickness measures an impressive 28 metres. Details of accumulation are shown in Figure 4.10, where glacial stage accumulation is much higher relative to the Holocene, although it should be noted that the periods of maximum accumulation occur either side of the LGM.

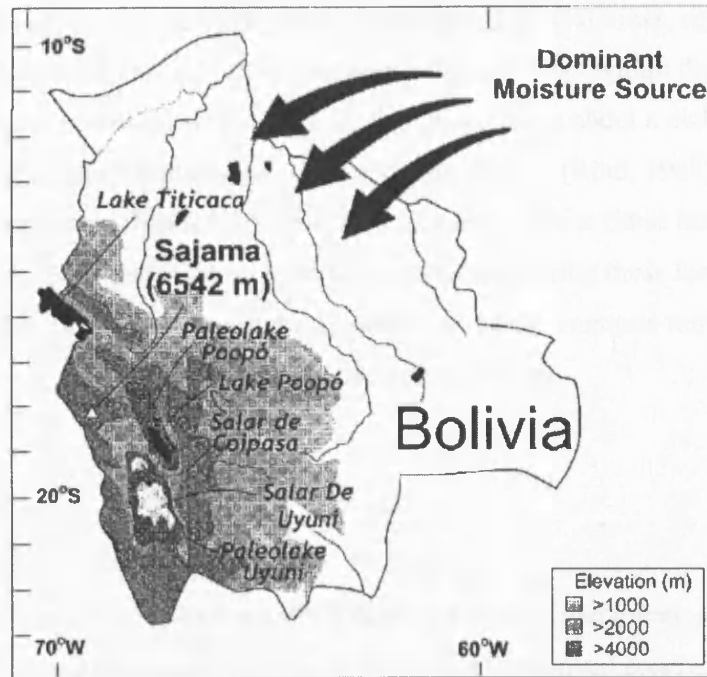


Figure 4.9: The Location of the Sajama ice cap in Bolivia in relation to modern lakes (black) and salt flats (white). Dark grey areas represent the areas covered by palaeolakes during the LGS (modified from Thompson *et al.*, 1998).

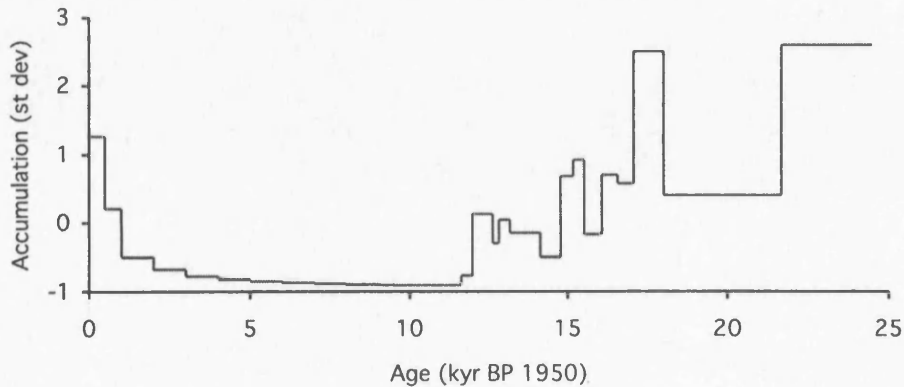


Figure 4.10: Snow accumulation record from the Sajama ice core (modified from Thompson *et al.*, 1998).

Similarities between the $\delta^{18}\text{O}$ data from Huascarán and Sajama (see Table 4.1 and Figures 4.6 and 4.7) have led Thompson *et al.* (2000) to strongly speculate that both ice cores have shared the tropical Atlantic as a common moisture source since the LGS, and this assumption has been frequently held in subsequent interpretations of South American palaeoclimate. However, the interpretation of a drier glacial climate over Huascarán, and a wetter glacial regime over the Sajama presents an inconsistency in this premise, as should they share a moisture supply, they should in theory reflect similar climate signals. Yet in their same

paper, Thompson *et al.* also cite the hypothesis that during glacial times, regardless of mean temperature, a decreased tropical latitudinal temperature gradient within the low to subtropical latitudes may weaken Hadley Circulation and bring about a dichotomy in the climate regimes over the Altiplano and Amazon Basin regions (Rind, 1988). Contrary to what the authors promote therefore, the two ice cores may have at times had independent moisture sources. Thus, great care must be taken when comparing these ice core data to other proxy records from South America as the assumed consistent, common moisture source between the two ice core records remains rather speculative.

ii) Lake Records

Lake Titicaca is considered to be a reliable gauge of Altiplano precipitation. In the present day, it is a virtually closed basin, therefore its water level, chemical composition, and biota are particularly sensitive to changes in modern precipitation (Baker *et al.*, 2001b).

Multiproxy analysis of long sediment cores recovered from the deep portions of Lake Titicaca reveal it to have been a deep, fresh, and continuously overflowing lake from ~26-15 Cal ka (Baker *et al.*, 2001b; Cross *et al.*, 2001; Rowe *et al.*, 2002), implying that the LGM Altiplano was much wetter relative to the present (see Figure 4.11).

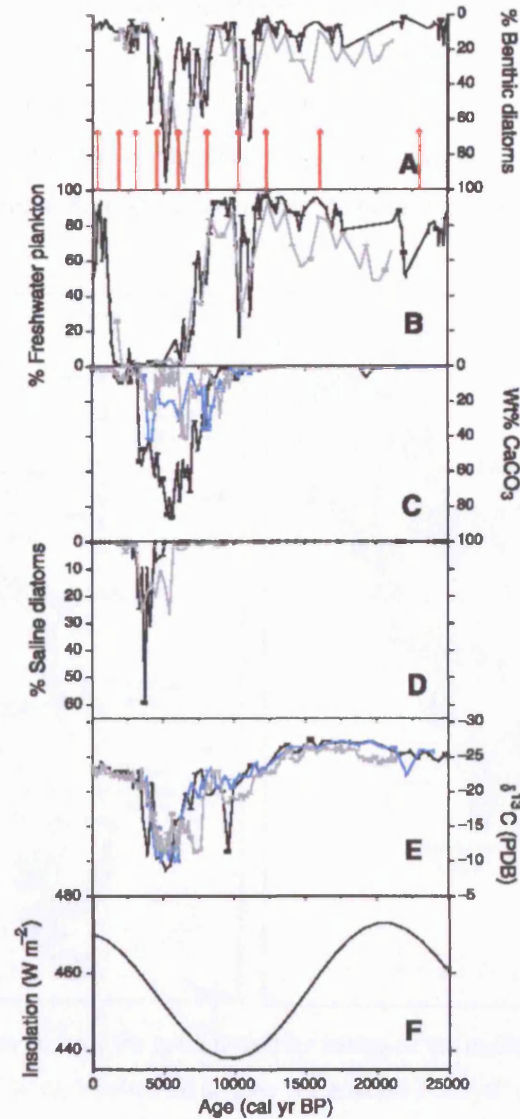


Figure 4.11: Chemical, isotopic, and biotic analyses of sediments from Lake Titicaca, where more elevated data generally signifies higher lake level or fresher water (modified from Baker *et al.*, 2001b). Data are presented from three cores, represented by grey, blue and black curves. (A) relative abundance of benthic diatoms; (B) relative abundance of planktonic freshwater diatoms; (C) weight percentage calcium carbonate; (D) relative abundance of saline diatoms; (E) $\delta^{13}\text{C}$ of total organic carbon; (F) January insolation at 15°S . For more details, see Baker *et al.* (2001b).

This is supported by evidence for the contemporaneous presence of large palaeolakes on the central Altiplano, formed from the overflow of Lake Titicaca, draining via the Rio Desaguadero into the modern southern Altiplano basins of Lake Poopó, and the Salars of Coipasa and Uyuni (Servant and Fontes, 1978). The evidence for the existence of these, and even older, palaeolakes on the Altiplano has been well summarised (e.g. Clapperton, 1993). The youngest, ‘Coipasa’ was a shallow palaeolake, radiocarbon-dated to have existed between 11.5 and 13.4 Cal ka (Servant *et al.*, 1995), coincident with the YD cold event in the

northern high latitudes. The youngest deep palaeolake, 'Tauca' (see Figure 4.12) occupied the southern Altiplano basin from ~13 to ~18 Cal ka (Servant *et al.*, 1995; Sylvestre *et al.*, 1999) and attained a maximum depth of 140m (Bills *et al.*, 1994). The existence of an older deep palaeolake, 'Minchin', has been inferred from two radiocarbon dates of ~30 and ~32 Cal ka from shells within outcropping sediments (Servant and Fontes, 1978).

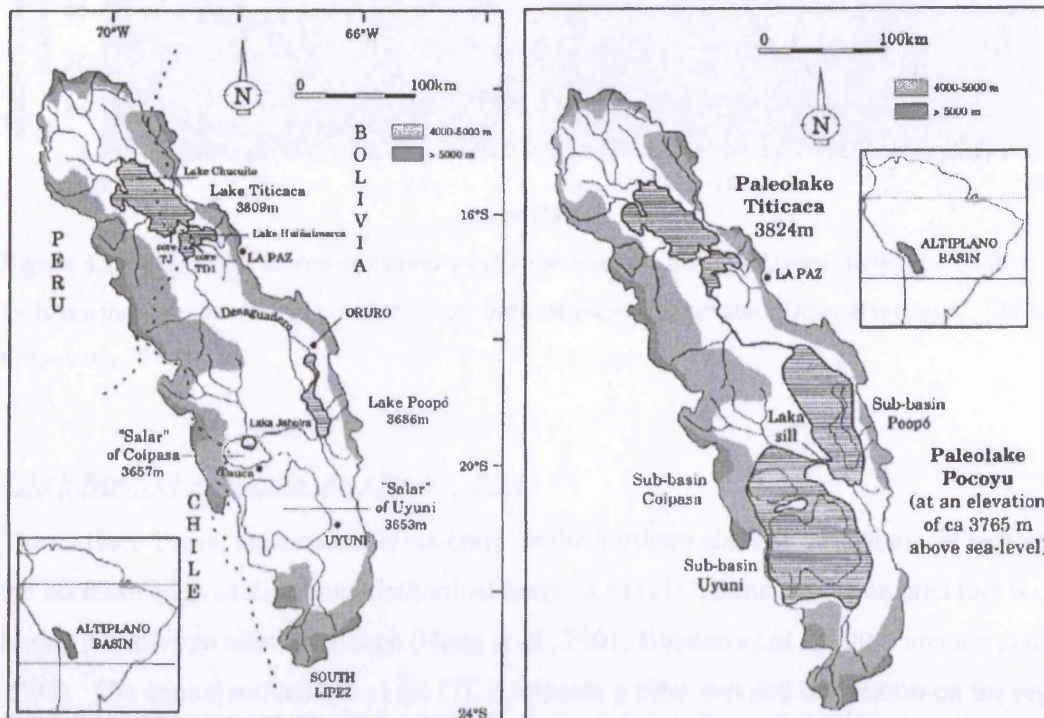


Figure 4.12: Sketch maps to show the main lacustrine basins of the modern Altiplano (left), and the extension of Palaeolake Tauca, labelled on map as "Paleolake Pocoyu" referring to the cumulative basins of Lakes Poopó, Coipasa and Uyuni (Modified from Argollo and Mourguiart, 2000).

However, more recent studies, based on the high-resolution down-core logging of natural gamma (γ)-radiation from deep bore holes drilled from the Salar de Uyuni (Baker *et al.*, 2001a) have suggested that the presence of palaeolake Tauca may have extended as far back as 26 Cal ka (see Figure 4.13). Lacustrine muds have much greater values of natural γ -radiation than do salt deposits, so the proxy serves as a sensitive measure of changing effective moisture through time. Within this record, radiocarbon-dated salt deposits from ~12.9-14.5 Cal ka implying arid conditions coincident with the time of the Bølling-Allerød interstadial (or Antarctic Cold Reversal), are preceded by a continuous sequence of lacustrine muds between ~14.9-26.1 Cal ka, which are thought to be those of Palaeolake Tauca. These dates extend to much older periods than those previously published, although they correspond very well with the lake level data from Lake Titicaca (Baker *et al.*, 2001a). A second major lake sequence is interpolated to have occurred prior to 38.1 Cal ka, with

deeper samples lying beyond the current extent of radiocarbon dating. Baker *et al.* (2001a) attribute this deeper sequence to be that of Lake Minchin, also making it older than previously believed.

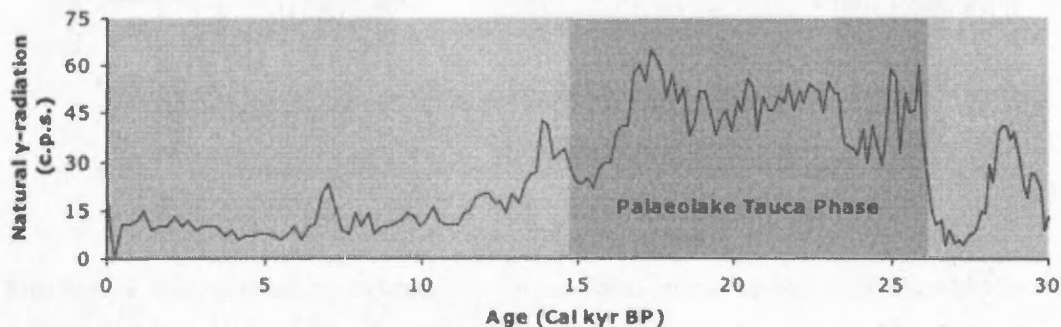


Figure 4.13: Downcore record of natural γ -radiation from the Salar de Uyuni showing effective moisture through time. More positive values indicate increased moisture (after Baker *et al.*, 2001a; Fritz *et al.*, 2004).

4.3.6b North of Amazonia: the Cariaco Basin

The Cariaco Basin, an anoxic marine basin on the northern shelf of Venezuela, is located at the northern edge of the annual latitudinal range of the ITCZ, and is thus an area that is highly sensitive to climate change (Haug *et al.*, 2001; Hughen *et al.*, 2000; Peterson *et al.*, 2000). The annual movement of the ITCZ imposes a clear wet and dry season on the region, with rainfall variations affecting the riverine delivery of terrigenous material to the basin and surrounding shelf (Peterson *et al.*, 2000). Sediments collect in the basin in distinct laminated couplets, with dark-coloured terrigenous grain-rich layers being deposited during the summer/autumn wet season when the ITCZ lies nearly overhead, and light-coloured biogenic-rich layers being deposited during the windy winter/spring dry season, when the ITCZ is located further south and beyond the catchment area of the rivers which drain into the Cariaco Basin (Hastenrath and Greischar, 1993). Changes in the relative abundance of terrigenous material can therefore be hypothesised to reflect latitudinal changes in the northerly limit of the ITCZ through time, and from this, it is in theory possible to extrapolate climate data for the Amazon Basin.

By far the most detailed record published to date from the Cariaco Basin is that of Haug *et al.* (2001). In their 14,000-year high-resolution record, shown in Figure 4.14, the percentage of bulk sedimentary titanium (%Ti) serves as a simple chemical proxy for the input of terrestrially derived material, providing a direct measure of rainfall and runoff from the local watersheds (Hastenrath and Greischar, 1993; Peterson *et al.*, 2000).

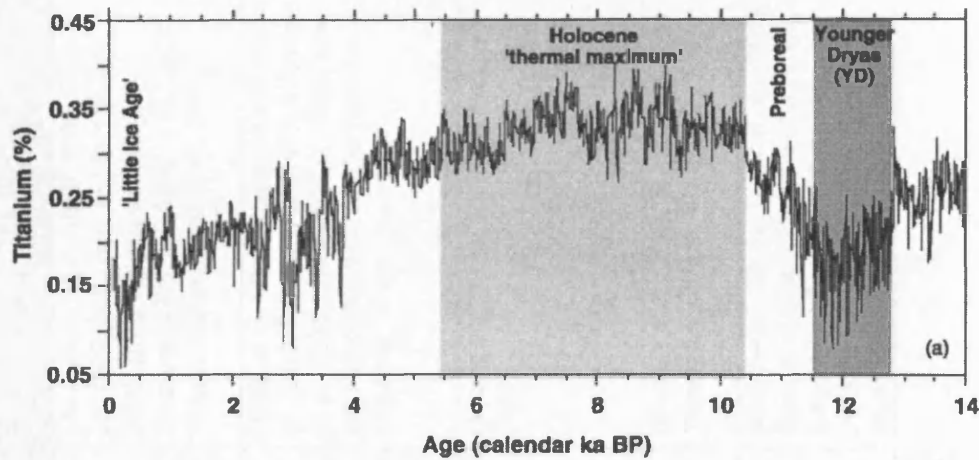


Figure 4.14: Bulk sedimentary Ti content of Cariaco Basin sediments from ODP Site 1002 for the last 14,000 years (three point moving average). Higher Ti content reflects greater terrestrial input from riverine runoff, which is interpreted to reflect greater precipitation over the Cariaco Basin, and a more northerly position of the ITCZ (modified from Haug *et al.*, 2001).

The %Ti record implies the wettest conditions of the last 14 kyr to have occurred from 10.5 to 5.4 ka during the Holocene “thermal maximum”, whereas the most arid climates occurred during the YD period, and the late Holocene. These results also compare well to other proxy records from the Cariaco Basin (see Haug *et al.*, 2001), and also compare well to the inverse Amazon Basin palaeomoisture records from Lake Junin and ODP Site 942 on the Amazon Fan (see Figure 4.8 and Sections 4.3.3 and 4.3.4 above).

4.3.7 Summary of the Palaeomoisture Reconstructions for the Amazon Basin

In addition to the morphological evidence summarised in Table 4.2, the other evidence reviewed in this chapter is summarised in Table 4.3 below.

Proxy cited as evidence for aridity	Site	Validation Criteria			Valid proxy?	Examples of References
		1) Identified properly?	2) Require climate different from now?	3) Solid chronology?		
Palaeoecological records.	Various.	✓	✓? Only applies to climatically marginal sites, and depends upon accurate interpretation of data.	✓? Only when the record can be radiocarbon dated.	Yes.	(Absy <i>et al.</i> , 1991; Bush, 2000; Bush <i>et al.</i> , 2002; Colinvaux and De Oliveira, 2000; Hooghiemstra and van der Hammen, 1998; Sifeddine <i>et al.</i> , 2001; van der Hammen and Absy, 1994).
Inorganic sedimentary lake records.	e.g. Caco Lake, Lake Pata, Lake Silvana, Brazil; Lake Junin, Peru.	✓? Only where the proxy is easily measured (e.g. isotopes).	✓ Does not apply to sites affected to sea level-related changes in the water table.	✓? Only when the record can be radiocarbon dated.	Yes? Is site-dependent.	(Bush <i>et al.</i> , 2002; Rodrigues-Filho <i>et al.</i> , 2002; Servant <i>et al.</i> , 1993; Sifeddine <i>et al.</i> , 2001; Sifeddine <i>et al.</i> , 2003; van der Hammen, 1974; van der Hammen and Absy, 1994).
Marine geochemical records.	ODP Site 942, Amazon Fan.	✓	✓ Assuming the isotopic change is driven by changes in Amazon River outflow.	✓	Yes.	(Maslin and Burns, 2000; Maslin <i>et al.</i> , 2000).
Speleothem records.	Central west, and northeastern Brazil; Peruvian Andes.	✓	✓	✓	Yes.	(Bertaux <i>et al.</i> , 2002; Wang <i>et al.</i> , 2004; Wang <i>et al.</i> , 2003b; Wang <i>et al.</i> , 2003a).
Extrapolations of climate from more distal regions.	e.g. Lake Titicaca; Salar de Uyuni; Salar de Coipasa; Cariaco Basin.	✓	✓	✓.	Questionable due to the distal nature of the records.	(Baker <i>et al.</i> , 2001a; Baker <i>et al.</i> , 2001b; Haug <i>et al.</i> , 2001; Peterson <i>et al.</i> , 2000; Servant and Fontes, 1978; Servant <i>et al.</i> , 1995; Sylvestre <i>et al.</i> , 1999; Thompson <i>et al.</i> , 1998; Thompson <i>et al.</i> , 2000).

Table 4.3: A summary of the proxy evidence for palaeomoisture in the Amazon Basin.

4.4 Summary of Glacial and LGIT Palaeoclimate Records from Tropical and Subtropical South America

In summary, although there remains little empirical palaeoclimate data that provides actual temperature information for the majority of the LGM Amazon Basin, the current published palaeodata suggest that glacial temperatures in the Amazon Basin were suppressed in the region of ~3 to 5°C, and this is likely to also have been the case also for the YD/LGIT period.

Despite the wide variety of clearly identifiable proxy evidence available for the reconstruction of past moisture availability, individual reconstructions are frequently limited by factors such as poor chronological control, and where the proxy may be responding to a number of dynamically interacting variables. However the cumulative multiproxy evidence suggests that cold stage climates were relatively arid for the majority of the Amazon Basin, and northern South America. Opposing scenarios are suggested from cave records in northeastern Brazil (Wang *et al.*, 2004; Wang *et al.*, 2003b; Wang *et al.*, 2003a), and for the Altiplano region (e.g. Baker *et al.*, 2001a; Baker *et al.*, 2001b; e.g. Cross *et al.*, 2001; Rowe *et al.*, 2002), which demonstrates the complex heterogeneous climate system operative over South America. This can be illustrated by comparing the available long continuous records in latitudinal order, which clearly shows a dichotomy in the climate regimes between northern and central South America (see Figure 4.15).

However, perhaps the most major limitation of reconstructing the glacial moisture history of the Amazon Basin is the actual paucity of data itself that extends back through the last glacial stage. Many of these records are also highly fragmented, poorly age-constrained, and qualitative in nature, and the extent to which they may be reflecting a local environmental signal is also questionable. This demonstrates the value of records from the Amazon Fan, as not only are they long, continuous, and can be well-dated, but they have the potential to provide semi-quantitative reconstructions of climate for the area represented by the whole of the Amazon Basin river catchment.

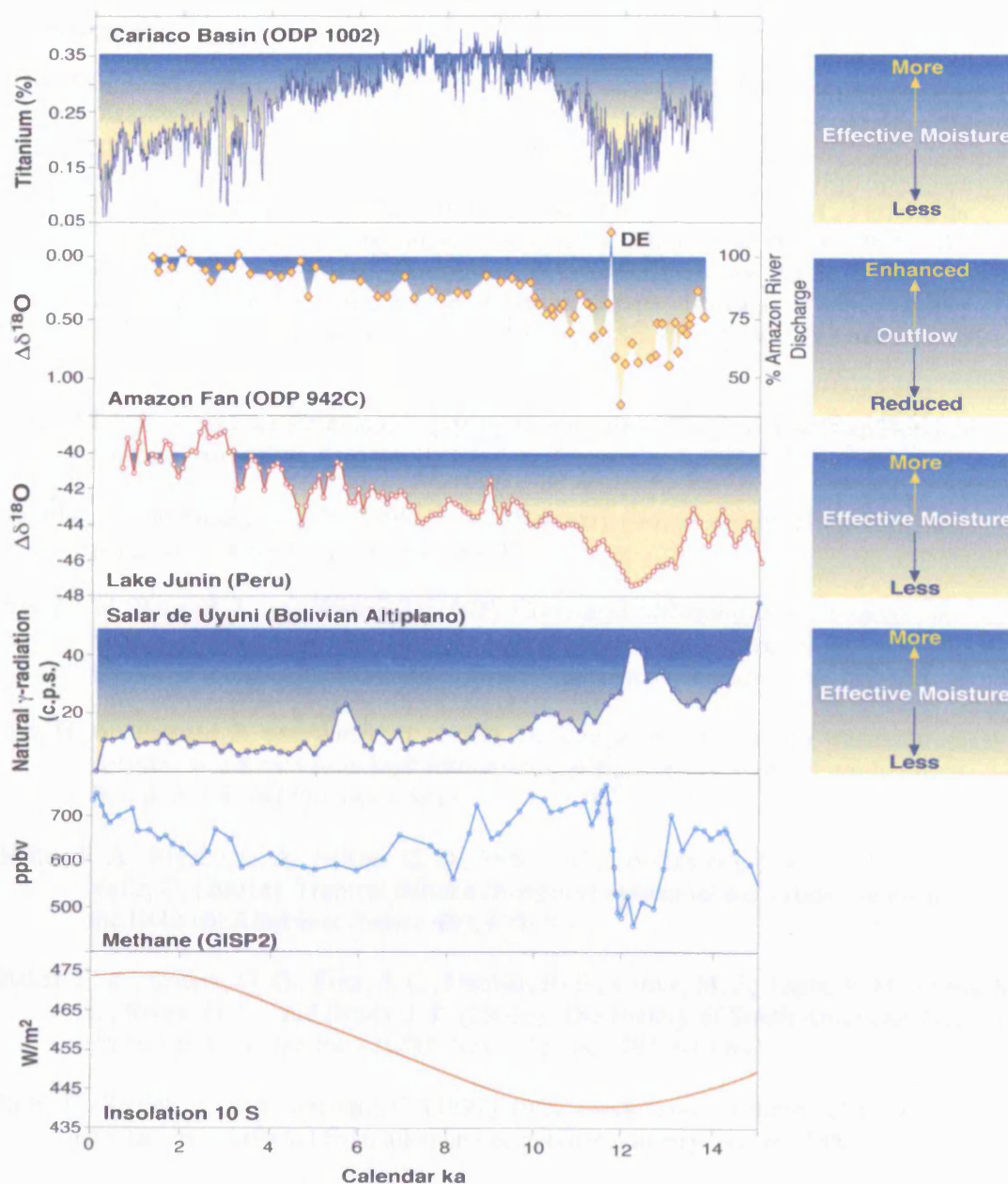


Figure 4.15: A latitudinal comparison of palaeomoisture records from the Cariaco Basin (Haug *et al.*, 2001); ODP Site 942 on the Amazon Fan (Maslin and Burns, 2000; Maslin *et al.*, 2000); Lake Junin in the Peruvian Andes (Seltzer *et al.*, 2000); and the Salar de Uyuni on the Bolivian Altiplano (Baker *et al.*, 2001a). Also shown are the GISP2 methane record (Brook *et al.*, 1996) and solar insolation at 10°S (Berger, 1978a; Berger, 1978b; Berger and Loutre, 1991).

4.5 References

- Ab'Saber, A. N. (1982). The palaeoclimate and palaeoecology of Brazilian Amazonia. *In* "Biological Diversification in the Tropics." (G. T. Prance, Ed.), pp. 41-49. Columbia University Press, New York.
- Absy, M. L., Cleef, A., Fournier, M., Martin, L., Servant, M., Sifeddine, A., Ferreira da Silva, M., Soubies, F., Suguio, K., Turcq, B., and Hammend, V. D. (1991). Mise en évidence de quatre phases d'ouverture de la forêt dans le sud-est de l'Amazonie au cours des 60 000 dernières années. Première comparaison avec d'autres régions tropicales. *Comptes Rendus de l'Académie des Sciences Paris t.312 Serie II*, 673-678.
- Absy, M. L., and van der Hammen, T. (1976). Some paleoecological data from Rondonia, southern part of the Amazon Basin. *Acta Amazonica* **6**, 293-299.
- Argollo, J., and Mourguiart, P. (2000). Late Quaternary climate history of the Bolivian Altiplano. *Quaternary International* **72**, 37-51.
- Arz, H. W., Patzold, J., and Wefer, G. (1998). Correlated Millennial-Scale Changes in Surface Hydrography and Terrigenous Sediment Yield Inferred from Last-Glacial Marine Deposits off Northeastern Brazil. *Quaternary Research* **50**, 157-166.
- Arz, H. W., Patzold, J., and Wefer, G. (1999). The deglacial history of the western tropical Atlantic as inferred from high resolution stable isotope records off northeastern Brazil. *Earth and Planetary Science Letters* **167**, 105-117.
- Baker, P. A., Rigsby, C. A., Seltzer, G. O., Fritz, S. C., Lowenstein, T. K., Bacher, N. P., and Veliz, C. (2001a). Tropical climate changes at millennial and orbital timescales on the Bolivian Altiplano. *Nature* **409**, 698-701.
- Baker, P. A., Seltzer, G. O., Fritz, S. C., Dunbar, R. B., Grove, M. J., Tapia, P. M., Cross, S. L., Rowe, H. D., and Broda, J. P. (2001b). The History of South American Tropical Precipitation for the Past 25,000 Years. *Science* **291**, 640-643.
- Bard, E., Rostek, F., and Sonzogni, C. (1997). Interhemispheric synchrony of the last deglaciation inferred from alkenone palaeothermometry. *Nature* **385**, 707-710.
- Barreto, A. M. F., Tatum, S. H., Suguio, K., Nagatomo, T., and Watanabe, S. (1997). Quaternário Tardio no Sistema de Dunas Fixadas do Médio Rio São Francisco (Bahia) Datado pelo Método da Termoluminescência. *In* "VI Congresso da Associação de Estudos do Quaternário e Reunião sobre o Quaternário da América do Sul." pp. 171-175, Universidade Federal do Paraná, Curitiba, Brazil.
- Beck, J. W., Récy, J., Taylor, F., Edwards, R. L., and Cabioch, G. (1997). Abrupt changes in early Holocene tropical sea surface temperature derived from coral records. *Nature* **385**, 705-707.
- Behling, H. (2002). South and southeast Brazilian grasslands during Late Quaternary times: a synthesis. *Palaeogeography, Palaeoclimatology, Palaeoecology* **177**, 19-27.
- Behling, H., Arz, H. W., Patzold, J., and Wefer, G. (2000). Late Quaternary vegetational and climate dynamics in northeastern Brazil, inferences from marine core GeoB 3104-1. *Quaternary Science Reviews* **19**, 981-994.
-

-
- Behling, H., Arz, H. W., Patzold, J., and Wefer, G. (2002). Late Quaternary vegetational and climate dynamics in southeastern Brazil, inferences from marine cores GeoB 3229-2 and GeoB 3202-1. *Palaeogeography, Palaeoclimatology, Palaeoecology* **179**, 227-243.
- Behling, H., and da Costa, M. L. (2001). Holocene vegetational and coastal environmental changes from the Lago Crispim record in northeastern Para State, eastern Amazonia. *Review of Palaeobotany and Palynology* **114**, 145-155.
- Behling, H., and Hooghiemstra, H. (1999). Environmental history of the Colombian savannas of the Llanos Orientales since the Last Glacial Maximum from lake records El Pinal and Carimagua. *Journal of Paleolimnology* **21**, 461-476.
- Behling, H., and Hooghiemstra, H. (2000). Holocene Amazon rainforest-savanna dynamics and climatic implications: High-resolution pollen record from Laguna Loma Linda in eastern Colombia. *Journal of Quaternary Science* **15**, 687.
- Behling, H., Hooghiemstra, H., and Negret, A. J. (1998). Holocene history of the Choco rain forest from Laguna Piusbi, southern Pacific lowlands of Colombia. *Quaternary Research* **50**, 300-308.
- Behling, H., Keim, G., Irion, G., Junk, W., and Nunes de Mello, J. (2001). Holocene environmental changes in the Central Amazon Basin inferred from Lago Calado (Brazil). *Palaeogeography, Palaeoclimatology, Palaeoecology* **173**, 87-101.
- Behling, H., and Negrelle, R. R. B. (2001). Tropical Rainforest and Climate Dynamic of the Atlantic Lowland, Southern Brazil, during the Late Quaternary. *Quaternary Research* **56**, 383-389.
- Berger, A. (1978a). Long-term variations of caloric insolation resulting from the Earth's orbital elements. *Quaternary Research* **9**, 139-167.
- Berger, A. (1978b). Long-term variations of daily insolation and Quaternary climate changes. *Journal of Atmospheric Science* **35**, 2362-2367.
- Berger, A., and Loutre, M. (1991). Insolation values for the climate of the last 10 million years. *Quaternary Science Reviews* **10**, 297-317.
- Bertaux, J., Sondag, F., Santos, R., Soubies, F., Causse, C., Plagnes, V., Le Cornec, F., and Seidel, A. (2002). Paleoclimatic record of speleothems in a tropical region: study of laminated sequences from a Holocene stalagmite in Central-West Brazil. *Quaternary International* **89**, 3-16.
- Bills, B. G., de Silva, S. L., Currey, D. R., Emenger, R. S., Lillquist, K. D., Donnellan, A., and Worden, B. (1994). Hydro-isostatic deflection and tectonic tilting in the central Andes: Initial results of a GPS survey of Lake Minchin shorelines. *Geophysical Research Letters* **21**, 293-296.
- Blunier, T., Chappellaz, J., Schwander, J., Dällenbach, A., Stauffer, B., Stocker, T., Raynaud, D., Jouzel, J., Clausen, H. B., Hammer, C. U., and Johnsen, S. J. (1998). Asynchrony of Antarctic and Greenland climate change during the last glacial period. *Nature* **384**, 739-743.
- Blunier, T., Schwander, J., Stauffer, B., Stocker, T., Dällenbach, A., Indermühle, A., Tschumi, J., Chappellaz, J., Raynaud, D., and Barnola, J.-M. (1997). Timing of the
-

-
- Antarctic Cold Reversal and the atmospheric CO₂ increase with respect to the Younger Dryas event. *Geophysical Research Letters* **24**, 2683-2686.
- Boggiani, P. C., and Coimbra, A. M. (1995). Quaternary limestone of Pantanal Area. *Anais da Academia Brasileira de Ciências* **67**, 343-349.
- Brook, E. J., Sowers, T. A., and Orchardo, J. (1996). Rapid variations in atmospheric methane concentration during the past 110,000 years. *Science* **273**, 1087-1091.
- Burbridge, R., Mayle, F. E., and Killeen, T. J. (2004). Fifty-thousand-year vegetation and climate history of Noel Kempff Mercado National Park, Bolivian Amazon. *Quaternary Research* **61**, 215-230.
- Bush, M. B. (2000). Deriving response matrices from Central American modern pollen rain. *Quaternary Research* **54**, 132-143.
- Bush, M. B., and Colinvaux, P. A. (1990). A pollen record of a complete glacial cycle from lowland Panama. *Journal of Vegetation Science* **1**, 105-118.
- Bush, M. B., Colinvaux, P. A., Wiemman, M. C., Piperno, D. R., and Liu, K. (1990). Late Pleistocene temperature depression and vegetation change in Ecuadorian Amazonia. *Quaternary Research* **34**, 330-345.
- Bush, M. B., Miller, M. C., Oliveira, P. E. D., and Colinvaux, P. A. (2002). Orbital-forcing signal in sediments of two Amazonian lakes. *Journal of Paleolimnology* **27**, 341-352.
- Clapperton, C. (1993). Nature of Environmental Changes in South America at the Last Glacial Maximum. *Palaeogeography, Palaeoclimatology, Palaeoecology* **101**, 189-208.
- Clark, P. U. (2002). Early Deglaciation in the Tropical Andes. *Science* **298**, 7a.
- CLIMAP Project Members. (1976). The surface of the ice age earth. *Science* **191**, 1131-1137.
- CLIMAP Project Members. (1981). Seasonal reconstruction of the Earth's surface at the Last Glacial Maximum. *Geological Society of America Chart and Map Series* **36**.
- Colinvaux, P. A. (1989). Ice-age Amazon revisited. *Nature* **340**, 188-189.
- Colinvaux, P. A., Bush, M. B., Steinitz-Kannan, M., and Miller, M. C. (1997). Glacial and postglacial pollen records from the Ecuadorian Andes and Amazon. *Quaternary Research* **48**, 69-78.
- Colinvaux, P. A., and De Oliveira, P. E. (2000). Palaeoecology and climate of the amazon basin during the last glacial cycle. *Journal of Quaternary Science* **15**, 347.
- Colinvaux, P. A., De Oliveira, P. E., and Bush, M. B. (2000). Amazonian and neotropical plant communities on glacial time-scales: The failure of the aridity and refuge hypotheses. *Quaternary Science Reviews* **19**, 141-169.
- Colinvaux, P. A., De Oliveira, P. E., Moreno, J. E., Miller, M. C., and Bush, M. B. (1996). A long pollen record from lowland Amazonia: forest and cooling in glacial times. *Science* **274**, 85-88.
-

-
- Cowling, S. A., and Sage, R. F. (1988). Interactive effects of low atmospheric CO₂ and elevated temperature on growth, photosynthesis and respiration. *Phaseolus vulgaris*. *Plant, Cell and Environment* **21**, 427-435.
- Cowling, S. A., Sykes, M. T., and Maslin, M. A. (2001). Paleovegetation simulations of lowland Amazonia and implications for neotropical allopatry and speciation. *Quaternary Research* **55**, 140-149.
- Cross, S. L., Baker, P. A., Seltzer, G. O., Fritz, S. C., and Dunbar, R. B. (2001). Late Quaternary Climate and Hydrology of Tropical South America Inferred from an Isotopic and Chemical Model of Lake Titicaca, Bolivia and Peru. *Quaternary Research* **56**, 1-9.
- Cruz, F. W., Burns, S. J., Karmann, I., Sharp, W. D., Vuille, M., Cardoso, A. O., Ferrari, J. A., Silva Dias, P. L., and Viana Jr, V. (2005). Insolation-driven changes in atmospheric circulation over the past 116,000 years in subtropical Brazil. *Nature* **434**, 63-66.
- Damuth, J. E., and Fairbridge, R. W. (1970). Equatorial Atlantic deep-sea arkosic sands and ice-age aridity in tropical South America. *Geological Society of America Bulletin*, 189-206.
- Farrera, I., Harrison, S. P., Prentice, I. C., Ramstein, G., Guiot, J., Bartlein, P. J., Bonnefille, R., Bush, M., Cramer, W., von Grafenstein, U., Holmgren, K., Hooghiemstra, H., Hope, G., Jolly, D., Lauritzen, S. E., Ono, Y., Pinot, S., Stute, M., and Yu, G. (1999). Tropical climates at the Last Glacial Maximum: a new synthesis of terrestrial palaeoclimate data. I. Vegetation, lake-levels and geochemistry. *Climate Dynamics* **15**, 823-856.
- Filho, A. C., Schwartz, D., Tatumi, S. H., and Rosique, T. (2002). Amazonian Paleodunes Provide Evidence for Drier Climate Phases during the Late Pleistocene-Holocene. *Quaternary Research* **58**, 205.
- Flood, R. D., Piper, D. J. W., and Shipboard Scientific Party. (1995). Introduction. In "Proceedings of the Ocean Drilling Program, Initial Reports, Vol. 155." (R. D. Flood, D. J. W. Piper, A. Klaus, and others, Eds.), pp. 5-16, College Station, TX (Ocean Drilling Program).
- Fritz, S. C., Baker, P. A., Lowenstein, T., Seltzer, G. O., Rigsby, C. A., Dwyer, G., Tapia, P., Arnold, K., Ku, T.-H., and Luo, S. (2004). Hydrologic variation during the last 170,000 years in the southern hemisphere tropics of South America. *Quaternary Research* **61**, 95-104.
- Guilderson, T. P., Fairbanks, R. G., and Rubenstone, J. L. (1994). Tropical temperature variations since 20,000 years ago: modulating interhemispheric climate change. *Science* **263**, 663-665.
- Haberle, S. G., and Maslin, M. A. (1999). Late Quaternary vegetation and climate change in the Amazon Basin based on a 50,000 year pollen record from the Amazon fan, ODP site 932. *Quaternary Research* **51**, 27-38.
- Haffer, J. (1969). Speciation in Amazon Forest Birds. *Science* **165**, 131-137.
- Hansen, B. C. S., Rodbell, D. T., Seltzer, G. O., Leon, B., Young, K. R., and Abbott, M. (2003). Late-glacial and Holocene vegetational history from two sites in the western
-

-
- Cordillera of southwestern Ecuador. *Palaeogeography, Palaeoclimatology, Palaeoecology* **194**, 79.
- Harris, S. E., and Mix, A. C. (1999). Pleistocene precipitation balance in the Amazon Basin recorded in deep sea sediments. *Quaternary Research* **51**, 14-26.
- Hastenrath, S., and Greischar, L. (1993). Circulation mechanisms related to northeast Brazil rainfall anomalies. *Journal of Geophysical Research* **98**, 5093-102.
- Haug, G. H., Hughen, K. A., Sigman, D. M., Peterson, L. C., and Röhl, U. (2001). Southward Migration of the Intertropical Convergence Zone Through the Holocene. *Science* **293**, 1304-1308.
- Hooghiemstra, H., and van der Hammen, T. (1998). Neogene and Quaternary development of the neotropical rain forest: the forest refugia hypothesis, and a literature overview. *Earth-Science Reviews* **44**, 147-183.
- Hughen, K. A., Southon, J. R., Lehman, S. J., and Overpeck, J. T. (2000). Synchronous radiocarbon and climate shifts during the last deglaciation. *Science* **290**, 1951-1954.
- IPCC. (2001). "Third Assessment Report - Climate Change 2001" - the third assessment report of the Intergovernmental Panel on Climate Change (IPCC/WMO/UNEP, Ed.).
- Irion, G. (1976). Quaternary sediments of the upper Amazon lowlands of Brazil. *Biogeografica* **7**, 163-167.
- Irion, G., Muller, J., Nunes de Mello, J., and Junk, W. J. (1995). Quaternary geology of the Amazon lowland. *Geo-Marine Letters* **15**, 172-178.
- Johnsen, S. J., Dahl-Jensen, D., Gundenstrup, N. S., J.P., S., Clausen, H. B., Miller, H., Masson-Delmotte, V., Arny, E., and Sveinbjörnsdóttir, J. W. (2001). Oxygen isotope and palaeotemperature records from six Greenland ice-core stations: Camp Century, Dye-3, GRIP, GISP2, Renland and NorthGRIP. *Journal of Quaternary Science* **16**, 299-307.
- Klammer, G. (1982). Die Paleoste des Pantanal von Mato Grosso und die pleistozene Klimageschichte der brasilianischen Randtropen. *Zeitschrift fuer Geomorphologie N.F.* **26**, 393-416.
- Kronberg, B. I., Benchimol, R. E., and Bird, M. I. (1991). Geochemistry of Acre Subbasin sediments: Window on ice-age Amazonia. *Interciencia* **16**, 138.
- Latrubesse, E. M., and Nelson, B. W. (2001). Evidence for Late Quaternary aeolian activity in the Roraima-Guyana Region. *CATENA* **43**, 63.
- Ledru, M. P., Bertaux, J., Sifeddine, A., and Suguio, K. (1998). Absence of last glacial maximum records in lowland tropical forests. *Quaternary Research* **49**, 233-237.
- Ledru, M. P., Cordeiro, R. C., Landim Dominguez, J. M., Martin, L., Mourguiart, P., Sifeddine, A., and Turcq, B. J. (2001). Late-Glacial cooling in Amazonia inferred from pollen at Lagoa do Caáç, northern Brazil. *Quaternary Research* **55**, 47-56.
- Liu, K., and Colinvaux, P. A. (1985). Forest Changes in the Amazon Basin during the Last Glacial Maximum. *Nature* **318**, 556-557.
-

-
- Martin, L., Fournier, M., Mourguiart, P., Sifeddine, A., Turq, B., Absy, M. L., and Flexor, J. M. (1993). Southern oscillation signal in South American palaeoclimate data of the last 7000 years. *Quaternary Research* **39**, 338-346.
- Maslin, M. (2004). Ecological versus climatic thresholds. *Science* **306**, 2197-2198.
- Maslin, M. A., and Burns, S. J. (2000). Reconstruction of the Amazon Basin effective moisture availability over the past 14,000 years. *Science* **290**, 2285-2287.
- Maslin, M. A., Durham, E., Burns, S. J., Platzman, E., Grootes, P., Greig, S. E. J., Nadeau, M. J., Schleicher, M., Pflaumann, U., Lomax, B., and Rimington, N. (2000). Palaeoreconstruction of the Amazon River freshwater and sediment discharge using sediments recovered at site 942 on the Amazon Fan. *Journal of Quaternary Science* **15**, 419-434.
- Mayle, F. E., Beerling, D. J., Gosling, W. D., and Bush, M. (2004). Responses of Amazonian ecosystems to climatic and atmospheric CO₂ changes since the Last Glacial Maximum. *Philosophical Transactions of the Royal Society* **359**, 499-514.
- Mayle, F. E., Burbridge, R., and Killeen, T. J. (2000). Millennial-Scale Dynamics of Southern Amazonian Rain Forests. *Science* **290**, 2291.
- Meade, R. H., Dunne, T., Richey, J. E., Santos, U. d. M., and Salati, E. (1985). Storage and remobilization of suspended sediment in the lower Amazon River of Brazil. *Science* **228**, 488-490.
- Milliman, J. D., Summerhayes, C. P., and Barretto, H. T. (1975). Quaternary sedimentation on the Amazon continental margin: a model. *Geological Society of America Bulletin* **86**, 610-614.
- Mix, A. C., Morey, A. E., Pisias, N. G., and Hostetler, S. W. (1999). Foraminiferal faunal estimates of paleotemperature: circumventing the no-analogue problem yields cool ice age tropics. *Paleoceanography* **14**, 350-359.
- Mora, G., and Pratt, L. M. (2001). Isotopic evidence for cooler and drier conditions in the tropical Andes during the last glacial stage. *Geology* **29**, 519-522.
- Moy, C. M., Seltzer, G. O., Rodbell, D. T., and Anderson, D. M. (2002). Variability of El Niño/Southern Oscillation activity at millennial timescales during the Holocene epoch. *Nature* **420**, 162-165.
- Mulvaney, R., Rothlisberger, R., Wolff, E. W., Sommer, S., Schwander, J., Hutteli, M. A., and Jouzel, J. (2000). The transition from the last glacial period in inland and near-coastal Antarctica. *Geophysical Research Letters* **27**, 2673-2676.
- Peterson, L. C., Haug, G. H., Hughen, K. A., and Rühl, U. (2000). Rapid Changes in the Hydrologic Cycle of the Tropical Atlantic During the Last Glacial. *Science* **290**, 1947-1951.
- Policy, H. W., Johnson, H. B., Marinot, B. D., and Mayeux, H. S. (1993). Increase in C3 plant water-use efficiency and biomass over Glacial to present CO₂ concentrations. *Nature* **361**, 61-64.
-

-
- Prance, G. T. (1987). Vegetation. In "Biogeography and Quaternary History in Tropical America." (T. C. Whitmore, and G. T. Prance, Eds.), pp. 28-44. Oxford Science Publications, Oxford.
- Raynaud, D., Barnola, J. M., Chappellaz, J., Blunier, T., Indermuhle, A., and Stauffer, B. (2000). The ice record of greenhouse gases: a view in the context of future changes. *Quaternary Science Reviews* **19**, 9-17.
- Rind, D. (1988). Latitudinal temperature gradients and climate change. *Journal of Geophysical Research* **103**, 5943-5971.
- Rodbell, D. T., Seltzer, G. O., Anderson, D. M., Abbott, M. B., Enfield, D. B., and Newman, J. H. (1999). An ~15,000-Year Record of El Nino-Driven Alluviation in Southwestern Ecuador. *Science* **283**, 516-520.
- Rodrigues-Filho, S., Behling, H., Irion, G., and Muller, G. (2002). Evidence for Lake Formation as a Response to an Inferred Holocene Climatic Transition in Brazil. *Quaternary Research* **57**, 131-137.
- Rowe, H. D., Dunbar, R. B., Mucciarone, D. A., Seltzer, G. O., Baker, P. A., and Fritz, S. (2002). Insolation, Moisture Balance and Climate Change on the South American Altiplano Since the Last Glacial Maximum. *Climatic Change* **52**, 175-199.
- Rühlemann, C., Diekmann, B., Mulitza, S., and Frank, M. (2001). Late Quaternary changes of western equatorial Atlantic surface circulation and Amazon lowland climate recorded in Ceara Rice deep-sea sediments. *Paleoceanography* **16**, 293-305.
- Schrag, D. P., Hampt, G., and Murray, D. W. (1996). Pore Fluid Constraints on the Temperature and Oxygen Isotopic Composition of the Glacial Ocean. *Science* **272**, 1930-1932.
- Seltzer, G. O., Rodbell, D. T., Baker, P. A., Fritz, S. C., Tapia, P. M., Rowe, H. D., and Dunbar, R. B. (2002). Early Warming of Tropical South America at the Last Glacial-Interglacial Transition. *Science* **296**, 1685-1686.
- Seltzer, G. O., Rodbell, D. T., and Burns, S. J. (2000). Isotopic evidence for late Quaternary climatic change in tropical South America. *Geology* **28**, 35-38.
- Servant, M., and Fontes, J.-C. (1978). Les lacs quaternaires des hauts plateaux des Andes boliviennes Premières interpretations paleoclimatiques. *Cahiers ORSTOM, Serie Geologie* **10**, 9-23.
- Servant, M., Fournier, M., Argollo, J., Servant-Vildary, S., Sylvestre, F., Wirrmann, D., and Ybert, J. P. (1995). La dernière transition glaciaire/interglaciaire des Andes tropicales sud (Bolivie) d'après l'étude des variations des niveaux lacustres et des fluctuations glaciaires. *Comptes Rendus de l'Académie des Sciences Paris* **320**, 729-736.
- Servant, M., Maley, J., Turcq, B. J., Absy, M. L., Brenac, P., Fournier, M., and Ledru, M. P. (1993). Tropical forest changes during the late quaternary in African and South American lowlands. *Global and Planetary Change* **7**, 25.
- Servant, M., and Servant-Vildary, S. (2003). Holocene precipitation and atmospheric changes inferred from river paleowetlands in the Bolivian Andes. *Palaeogeography, Palaeoclimatology, Palaeoecology* **194**, 187-212.
-

-
- Showers, W. J., and Bevis, M. (1988). Amazon cone isotopic stratigraphy: Evidence for the source of the tropical freshwater spike. *Palaeogeography, Palaeoclimatology, Palaeoecology* **64**, 189-199.
- Sifeddine, A., Martin, L., Trucq, B., Volkmer-Ribeiro, C., Soubies, F., Cordeiro, R. C., and Suguio, K. (2001). Variations of the Amazonian rainforest environment: a sedimentological record covering 30,000 years. *Palaeogeography, Palaeoclimatology, Palaeoecology* **168**, 221-235.
- Sifeddine, A., Spadano Albuquerque, A. L., Ledru, M. P., Trucq, B., Knoppers, B., Martin, L., Zamboni de Mello, W., Passenau, H., Landim Dominguez, J. M., and Campello Cordeiro, R. (2003). A 21000 cal years paleoclimatic record from Caco Lake, northern Brazil: evidence from sedimentary and pollen analyses. *Palaeogeography, Palaeoclimatology, Palaeoecology* **189**, 25-34.
- Steig, E. J., Brook, E. J., White, J. W. C., Sucher, C. M., Bender, M. L., Lehman, S. J., Morse, D. L., Waddington, E. D., and Clow, G. D. (1998). Synchronous Climate Changes in Antarctica and the North Atlantic. *Science* **282**, 92-95.
- Sternberg, L. d. L. (2001). Savanna-forest hysteresis in the tropics. *Global Ecology and Biogeography* **10**, 369-378.
- Street-Perrott, F. A., Huang, Y., Perrott, R. A., Eglington, G., Barker, P., Khelifa, L. B., Harkness, D. D., and Olago, D. O. (1997). Impact of Lower Atmospheric Carbon Dioxide on Tropical Mountain Ecosystems. *Science* **278**, 1422-1426.
- Stute, M., Forster, M., Frischkorn, H., Serejo, A., Clark, J. F., Schlosser, P., Broecker, W. S., and Bonani, G. (1995). Cooling of Tropical Brazil (5°C) during the Last Glacial Maximum. *Science* **269**, 379-383.
- Sylvestre, F., Servant, M., Servant-Vildary, S., Causse, C., Fournier, M., and Ybert, J. P. (1999). Lake-level chronology on the southern Bolivian Altiplano (18°-23°S) during Late-Glacial time and the early Holocene. *Quaternary Research* **51**, 54-66.
- Thompson, L. G. (2000). Ice core evidence for climate change in the Tropics: implications for our future. *Quaternary Science Reviews* **19**, 19-34.
- Thompson, L. G., Davis, M. E., Mosley-Thompson, E., Sowers, T. A., Henderson, K. A., Zagarodnov, V. S., Lin, P. N., Mikhailenko, V. N., Campen, R. K., Bolzan, J. F., Cole-Dai, J., and Francou, B. (1998). A 25,000-Year Tropical Climate History from Bolivian Ice Cores. *Science* **282**, 1858-1863.
- Thompson, L. G., Mosely-Thompson, E., Bolzan, J. F., and Koci, B. R. (1985). A 15000 year record of tropical precipitation recorded in ice cores from the Quelccaya Ice Cap, Peru. *Science* **229**, 971-973.
- Thompson, L. G., Mosley-Thompson, E., Davis, M. E., Lin, P. N., Henderson, K. A., Cole-Dai, J., Bolzan, J. F., and Liu, K. B. (1995). Late Glacial Stage and Holocene Tropical Ice Core Records from Huascaran, Peru. *Science* **269**, 46-50.
- Thompson, L. G., Mosley-Thompson, E., and Henderson, K. A. (2000). Ice-core palaeoclimate records in tropical South America since the Last Glacial Maximum. *Journal of Quaternary Science* **15**, 377-394.
-

-
- Tricart, J. (1974). Existencia de medianos cuaternarios en los Llanos del Orinoco. *Revista del Instituto Geografico Agustin Codazzi* **5**, 69-79.
- Urrego, L. E. (1994). "Los bosques inundables del medio Caquetá (Amazonia Colombiana): Caracterización y successión." Ph.D. Thesis, University of Amsterdam.
- Urrego, L. E. (1997). "Los bosques inundables del medio Caquetá: Caracterización y successión. Estudios en la Amazonia Colombiana/ Studies on the Colombian Amazonia, Vol. 14." Tropenbos-Colombia, Bogotá.
- van der Hammen, T. (1972). Changes in vegetation and climate in the Amazon Basin and surrounding areas during the Pleistocene. *Geologie en Mijnbouw* **51**, 641-643.
- van der Hammen, T. (1974). The Pleistocene changes of vegetation and climate in tropical South America. *Journal of Biogeography* **1**, 3-26.
- van der Hammen, T., and Absy, M. L. (1994). Amazonia during the last glacial. *Palaeogeography, Palaeoclimatology, Palaeoecology* **109**, 247-261.
- Vonhof, H. B., Pittman, L. R., and Kroon, D. (2003). A stable isotope paleoclimate record of late Holocene Amazonian speleothems. *Geophysical Research Abstracts EGS - AGU - EUG Joint Assembly, Nice, France, April 2003* **5**, EAE03-A-05514.
- Vélez, M. I., Hooghiemstra, H., Metcalfe, S., Martinez, I., and Mommersteeg, H. (2003). Pollen- and diatom based environmental history since the Last Glacial Maximum from the Andean core Fuquene-7, Colombia. *Journal of Quaternary Science* **18**, 17-30.
- Wang, X., Auler, A. S., Edwards, R. L., Cheng, H., Cristalli, P. S., Smart, P. L., Richards, D. A., and Shen, C.-C. (2004). Wet periods in northeastern Brazil over the past 210 kyr linked to distant climate anomalies. *Nature* **432**, 740-743.
- Wang, X., Auler, A. S., Edwards, R. L., Cheng, H., Shen, C., Smart, P. L., and Richards, D. A. (2003b). Millennial-Scale ITCZ Variability in the Tropical Atlantic and Dynamics of Amazonian Rain Forest. *Eos Transactions AGU, Fall Meeting Supplement* **84** (46), Abstract PP22A-1195.
- Wang, X., Auler, A. S., Edwards, R. L., Cheng, H., Smart, P. L., and Richards, D. A. (2003a). Millennial-scale changes in paleopluvial phases inferred from speleothem deposits in northeastern Brazil. *XVI INQUA Congress Conference Abstracts*, Paper No. 21-5.
- Wolff, T., Mulitza, S., Arz, H. W., and Wefer, G. (1998). Oxygen isotopes versus CLIMAP (18 ka) temperatures: a comparison from the tropical Atlantic. *Geology* **26**, 675-678.
-

5. ODP SITE 942 COMPOSITE AGE MODEL

5.1 Age Model Construction Using AMS ^{14}C dates

5.1.1 Conversion of AMS Radiocarbon Dates to Calibrated Calendar Years

A total of 41 accelerator mass spectrometry (AMS) radiocarbon (^{14}C) dates were measured on samples from ODP Site 942. Of these dates 36 were used to construct the age model, of which three dates were duplicate measurements of three different samples. For these three samples, the calibrated age used in the model was determined by taking an average of the two dates measured, and so a total of 33 age horizons were used in the model. ^{14}C dates were measured on both multiple- and mono-species foraminiferal samples taken from cores 942B (last glacial stage [LGS]) and 942C (Holocene and LGS), as detailed in Table 5.1. 942C samples were measured at the Leibniz Labor für Alterbestimmung und Isotopenforschung, Kiel University in 1997-98 (Durham, 1997; Greig, 1998; Maslin *et al.*, 2000), and 942B samples were analysed at the Center for Accelerator Mass Spectrometry, Lawrence Livermore National Laboratory (LLNL) in 2002. Each sample measured for $\Delta^{14}\text{C}$ was corrected for isotope fractionation through normalization, using $\delta^{13}\text{C}$ values measured on the same samples.

^{14}C dates up to 20,260 ^{14}C yr BP were converted to calibrated calendar years (Cal yr BP) with the computer programme Calib 4.3 (Stuiver and Reimer, 1993), using the IntCal98 marine calibration curve (Stuiver *et al.*, 1998). For radiocarbon dates older than 20,260 ^{14}C yr BP that are beyond the current capabilities of Calib 4.3, conversion to calendar years was performed using the data presented in Beck *et al.* (2001). This method is not as effective as using statistical software, and produces dates of more questionable precision and accuracy, with noticeably large error margins. However with the data available at present, it is not possible to resolve these calendar dates further. For further discussion, see (Bard *et al.*, 2004; Hughen *et al.*, 2004).

Although a component of the ^{14}C pool above Site 942 may be of terrestrial origin, and thus have a different reservoir effect than the marine ^{14}C component, it is not possible at present to gauge the extent of this pool for each of the individual AMS dates. Therefore the samples were assumed to be 100% marine carbon, and were calibrated using the IntCal98 marine calibration curve (Stuiver *et al.*, 1998).

The maximum and minimum calendar age ranges for each sample were determined in Calib 4.3 by calculating the probability distribution of the sample's true age, as this is considered

to be a more stable estimate of sample age than the intercepts method (Telford *et al.*, 2004). The one-sigma range of the probability distribution was selected as the error term in the radiocarbon ages was fixed at the one-sigma level. Single sample ages were selected by taking the median of the probability distribution. An example of a radiocarbon date converted to a calibrated calendar age is given in Figure 5.1.

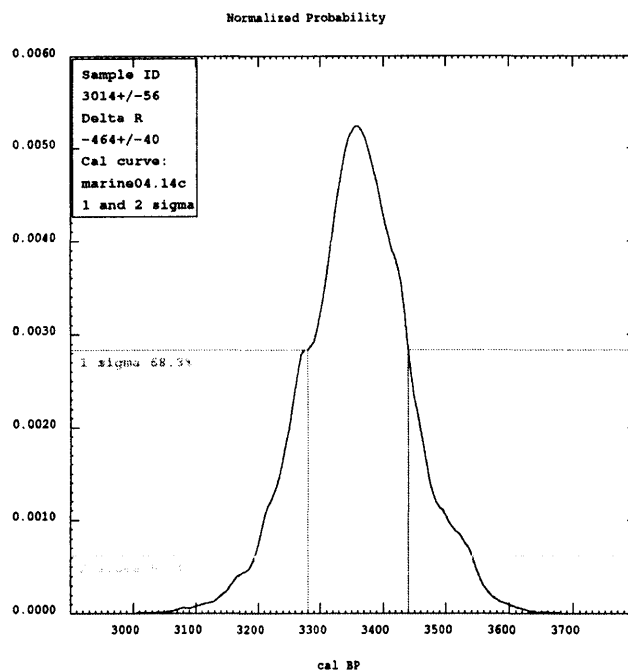


Figure 5.1: An example of a radiocarbon date converted to a calibrated calendar age using the probability distribution method. A radiocarbon age of 3014 ± 56 ^{14}C kyr BP yields a calibrated calendar age range of $\sim 3282 - 3438$ Cal ka at a probability distribution of one sigma.

5.1.2 Accounting for the Marine Reservoir Correction at ODP Site 942

The marine calibration in Calib 4.3 incorporates a time-dependent global ocean radiocarbon reservoir correction of ~ 400 years (Stuiver and Reimer, 1993; Stuiver *et al.*, 2005). However the marine reservoir effect is not constant throughout the global ocean, and may vary considerably over relatively short distances, for example by hundreds of years along the western coast of North America (Reimer and Reimer, 2005, and references therein). To accommodate these local effects, the difference (ΔR) in reservoir age between the local region of interest and the average global ocean reservoir must be determined. Unfortunately at the present time, there is little available information regarding possible local or regional reservoir effects of the tropical Atlantic Ocean in the immediate vicinity of the Amazon Fan. However a possible analogous setting is located further south along the Brazilian coast of Santa Catarina State (Nadal de Masi, 1999). Site #663 (38°E , 16°S) in the Marine Reservoir Correction Database associated with Calib 4.3 (Reimer and Reimer, 2005) is located within a

similar oceanic current setting to the Amazon Fan, so may be exposed to comparable oceanic influences. The abundance of marine shellfish material at archaeological settlements in this region implies that local coastal waters have been highly productive (Eastoe *et al.*, 2002). Marine productivity is also high over the Amazon Fan, in response to the high nutrient loading of the Amazon River discharge plume. High rates of marine productivity are thought to increase the rate of CO₂ drawdown, therefore the local surface water $\Delta^{14}\text{C}$ pool may become relatively more enriched, reducing the local reservoir effects. Furthermore, the discharge of the Amazon River often creates extensive lenses of low-salinity surface water (see Chapter 2, Section 2.3.2), which could inhibit the vertical mixing with deeper waters that contain more 'ancient' carbon. In this way, the local surface water radiocarbon reservoir could be diminished even further. Eastoe *et al.* (2002) compared radiocarbon ages from a number of lagoon and open ocean sites from the coast of Santa Catarina State, Brazil (including Site #663 in the Marine Reservoir Correction Database). The lagoon samples did not appear to differ from those of the open ocean. Some of their data suggested no clear difference between the lagoon samples and the interpreted $\Delta^{14}\text{C}$ of the atmosphere, with the same samples overlapping the range of the open ocean samples. For these reasons, it was decided that Site #663 in the Marine Reservoir Correction Database would be an appropriate analogy to the Amazon Fan, and so radiocarbon ages measured for ODP Site 942 were converted to calibrated radiocarbon years, incorporating a local marine reservoir correction determined by data from this location (Nadal de Masi, 1999; Reimer and Reimer, 2005).

Should the ΔR value assumed in the age model be too great however, it would bias all the calibrated calendar ages presented here toward being too old. For example, when calibrated using a ΔR value of -464 with an uncertainty of 40, 1622 ± 41 ¹⁴C ka is equivalent to ~1590-1730 Cal kyr BP (one sigma). Assuming there were to be no ΔR to be applied, the same date would be equivalent to ~1140-1240 Cal kyr BP (one sigma), i.e. a difference of ~450-490 years. Clearly such a difference in the choice of ΔR will have importance to the interpretation of the data generated by this research, particularly when examining and comparing the duration and timing of climatic events within the Site 942 records. However, although it is possible that the ΔR value selected may be too excessive, there is equally a lack of data to suggest otherwise (Reimer and Reimer, 2005). It should also be considered that the ΔR may have varied through time (see Section 5.2.3), although at present it is difficult to establish if, and by how much this might have been. Until such information about the local marine reservoir can be established, a parsimonious, yet semi-informed approach is therefore to assume that ΔR has been constant throughout the duration of the record, and is that of -464 years, with an uncertainty of 40 years.

5.1.3 Sample Reproducibility

It was unfortunately not possible to measure samples from exactly the same levels in the Cores at both AMS facilities to assess the between-laboratory variation. However the transition between the two datasets at 3.52 to 3.98 mbsf (942B depth scale) does not appear to be anomalous. It is difficult to assess possible between-laboratory variation from the younger samples measured due to variations in sample type which may give rise to fractionation effects, and also due to plateau effects in the radiocarbon production curve. Within-laboratory reproducibility was verified by replicating sample measurements at 7.13 and 7.60 mbsf (942B) for samples measured at LLNL, and 5.50 mbsf (942C) for samples measured at Kiel. Although the sample at 7.60 mbsf implied excellent laboratory reproducibility at LLNL, it was omitted from the final age model due to possible diagenetic alteration/contamination (C. Weyhenmeyer, personal communication 2002). Details of the samples measured are given in Table 5.1.

942B Depth Scale (mbsf)	942C Depth (mbsf)	Site	Hole	AMS Lab	Lab Sample Code	Sample Type	Number of Forams	¹⁴ C age	Error + (1σ)	Error - (1σ)	Cal yr BP (ΔR = -464)	Error +	Error -	Calibration Dataset [#]	Source Reference	Not Used
0.21	0.19	942	C	KIEL	*	<i>G. sacc.</i>	*	1622	41	41	1681	47	93	1	Greig (1998)	
0.37	0.35	942	C	KIEL	*	<i>G. sacc.</i>	1600	3014	56	56	3356	82	74	1	Greig (1998)	
0.52	0.50	942	C	KIEL	*	<i>G. sacc.</i>	1400	5014	56	56	5879	41	122	1	Greig (1998)	
0.63	0.61	942	C	KIEL	*	<i>G. sacc.</i>	1300	6800	50	50	7712	70	54	1	Greig (1998)	
0.74	0.69	942	C	KIEL	*	<i>G. sacc.</i>	1300	8582	90	89	9701	134	229	1	Greig (1998)	
0.82		942	B	LLNL	90540	Mixed	1000	10265	35	35	11993	303	303	1	This study	X
0.85	0.80	942	C	KIEL	*	<i>G. sacc.</i>	1314	9751	95	95	11136	455	293	1	Greig (1998)	
0.89		942	B	LLNL	90541	Mixed	863	10205	30	30	11742	528	244	1	This study	
0.93	0.88	942	C	KIEL	*	Mixed	996	10154	92	94	11885	381	496	1	Greig (1998)	
1.02	0.97	942	C	KIEL	*	<i>P. obiq.</i>	360	9670	60	60	11064	228	228	1	Maslin <i>et al.</i> (2000)	X
1.30	1.25	942	C	KIEL	*	Mixed	*	10890	50	50	12700	375	23	1	Greig (1998)	
1.30	1.25	942	C	KIEL	*	Mixed	*	10800	70	70	12700	248	45	1	Greig (1998)	
1.52	1.47	942	C	KIEL	*	Mixed	1300	4690	40	40	5521	61	61	1	Maslin <i>et al.</i> (2000)	X
1.85	1.80	942	C	KIEL	*	Mixed	500	10510	50	50	12725	83	577	1	Greig (1998)	
2.10	2.04	942	C	KIEL	*	Mixed	900	10690	60	60	12750	147	117	1	Maslin <i>et al.</i> (2000)	
2.93	2.93	942	C	KIEL	*	Mixed	1000	10620	60	60	12800	33	431	1	Maslin <i>et al.</i> (2000)	
3.52	3.54	942	C	KIEL	*	Mixed	1000	11790	70	70	13814	34	360	1	Maslin <i>et al.</i> (2000)	
3.98		942	B	LLNL	90542	Mixed	501	12180	35	35	14116	198	35	1	This study	
4.88		942	B	LLNL	89321	Mixed	604	12430	25	25	14850	412	671	1	This study	
5.28		942	B	LLNL	89322	Mixed	1003	12925	30	30	15526	206	209	1	This study	
5.58		942	B	LLNL	89323	Mixed	1000	13875	30	30	16610	241	232	1	This study	
6.23		942	B	LLNL	89324	Mixed	1000	15190	35	35	18123	347	267	1	This study	
6.58		942	B	LLNL	89325	Mixed	561	16485	35	35	19613	319	307	1	This study	
7.08		942	B	LLNL	90543	Mixed	1003	17840	60	60	21173	341	331	1	This study	

Table 5.1: Continued over page.

942B Depth Scale (mbsf)	942C Depth (mbsf)	Site	Hole	AMS Lab	Lab Sample Code	Sample Type	Number of Forams	¹⁴ C age	Error + (1 σ)	Error - (1 σ)	Cal yr BP (AR = -464)	Error +	Error -	Calibration Dataset [#]	Source Reference	Not Used
7.13		942	B	LLNL	89326	Mixed	1000	18085	50	50	21389	409	267	1	This study	
7.13		942	B	LLNL	90538	Mixed	1000	17970	60	60	21389	278	399	1	This study	
7.20		942	B	LLNL	90544	Mixed	1001	18260	60	60	21656	349	337	1	This study	
7.60		942	B	LLNL	89327	Mixed	1004	17535	35	35	20826	328	327	1	This study	X
7.60		942	B	LLNL	90539	Mixed	1004	17485	50	50	20768	330	330	1	This study	X
7.95		942	B	LLNL	89328	Mixed	1000	20260	60	60	23957	404	417	1	This study	
8.35		942	B	LLNL	89329	Mixed	1006	21470	60	60	25500	700	3700	2	This study	
8.65		942	B	LLNL	89330	Mixed	775	22700	80	80	27350	1750	1750	2	This study	
9.25	4.50	942	C	KIEL	*	Mixed	*	24553	386	368	28600	2100	2100	2	Greig (1998)	
9.35	4.60		C	KIEL	*	*	*	24835	392	374	28800	2100	2100	2	Durham (1997)	
10.13	5.28	942	C	KIEL	*	Mixed	850	26927	620	575	31600	1600	1600	2	Greig (1998)	
10.42	5.50		C	KIEL	*	*	*	27799	572	534	32800	2600	2600	2	Greig (1998)	
10.42	5.50		C	KIEL	*	*	*	27234	433	411	32800	2600	2600	2	Greig (1998)	
10.62	5.70	942	C	KIEL	*	Mixed	850	27910	738	676	33600	1800	3400	2	Greig (1998)	
12.00	7.00	942	C	KIEL	*	Mixed	1274	31753	1155	1010	35950	3050	3050	2	Greig (1998)	
13.27	8.28	942	C	KIEL	*	Mixed	1035	33490	1740	1430	38000	4000	4000	2	Greig (1998)	
14.37	9.30	942	C	KIEL	*	Mixed	1300	39550	2060	1640	42600	1900	1900	2	Greig (1998)	

Table 5.1 continued: Details of samples measured for radiocarbon dating. Asterisks (*) denote where data is unknown. Data in bold indicates B-Core samples; grey shading denotes samples not used to construct age model. 'mbsf' denotes metres below sea floor. [#]Calibration datasets used: (1) Stuiver *et al.*, (1993; version 4.3); (2) Beck *et al.* (2001). '*G. sacc.*' denotes the foraminiferan species *Globigerinoides sacculifer* (sp); '*P. obliq.*' denotes the foraminiferan species *Pulleniatina obliquiloculata*. '1 σ ' denotes one sigma.

5.2 Splicing Together the A-B-C Cores

5.2.1 Splicing of Datasets Using Shipboard Magnetic Susceptibility Records

Individual age-depth models were constructed for each Core, which enabled their respective palaeoenvironmental datasets to be spliced into a composite on the basis of their chronologies (as depth was not constant between each site). This also facilitates the incorporation of further radiocarbon dates, and the splicing of additional related datasets should they arise.

The relative stratigraphic position of each ^{14}C age in each Core was determined by tuning clearly distinguished events in the applicable shipboard down-core magnetic susceptibility (MS) profiles which are assumed to be broadly consistent between the cores which are spaced only 50m apart (see Chapter 2, Section 2.1). The relative depth of the switching between terrestrial and hemi-pelagic fan deposition at the Pleistocene-Holocene boundary was also a useful marker horizon. The depth of the diagenetic iron crust relative to the Pleistocene-Holocene boundary was seen to vary between the three lithostratigraphies and therefore not used as a reference. This is typical of the Amazon Fan where this feature has been found not to be isochronous, even across short distances (McGeary and Damuth, 1973). The maximum vertical displacement required to tune the 942C to 942B MS was ~ 6 cm. No displacement was required to tune the 942A and 942C Cores. The tuning of the C-to-B Cores and the C-to-A Cores are shown in Figures 5.2 and 5.3, respectively.

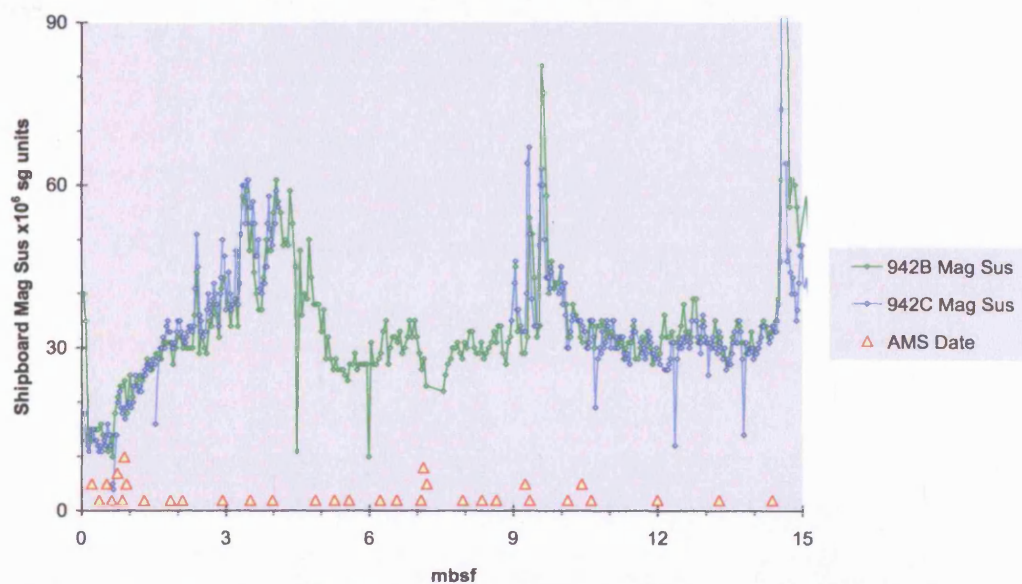


Figure 5.2: Tuning of shipboard magnetic susceptibility curves to transfer AMS dates from 942C onto the 942B depth scale. Maximum lateral displacement of C Core MS = ~ 6 cm. Triangles indicate the relative positions of radiocarbon-dated samples.

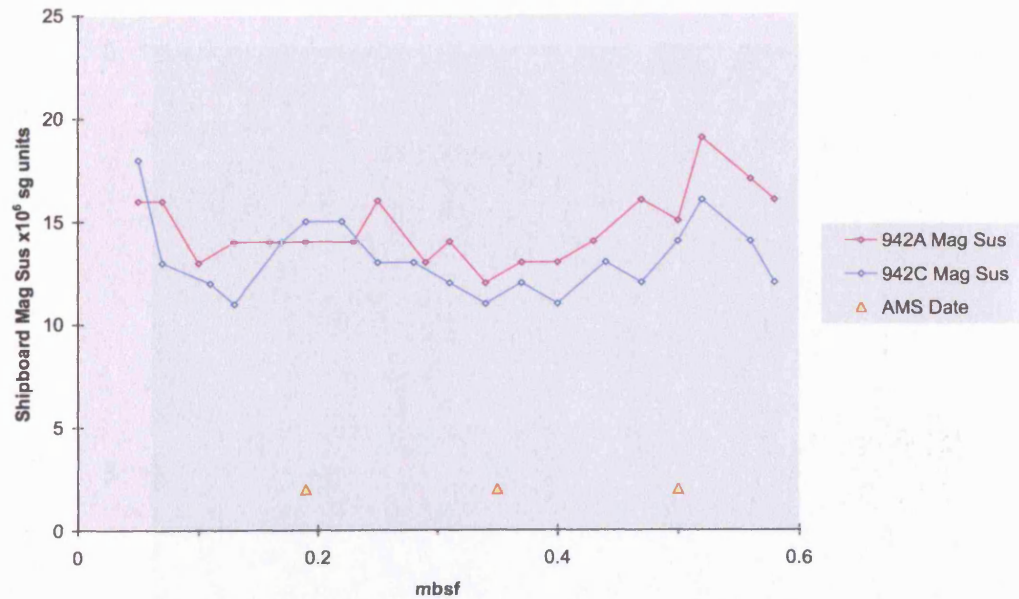


Figure 5.3: Tuning of shipboard magnetic susceptibility curves to transfer AMS dates from 942C onto the 942A depth scale. No lateral displacement of cores. Triangles indicate the relative positions of radiocarbon-dated samples.

5.2.2 Calibrated Age-Depth Plot of ODP 942

A composite age-depth plot of all calibrated AMS dates from the 942 record is shown in Figure 5.4. Figure 5.4a displays the age-depth profile for 0 to 40 Cal kyr BP, and the 0 to 13 Cal kyr BP portion of the profile is shown in greater detail in Figure 5.4b. The depth-scale presented is that of 942B as it represents the longest, most complete sequence of the three Cores.

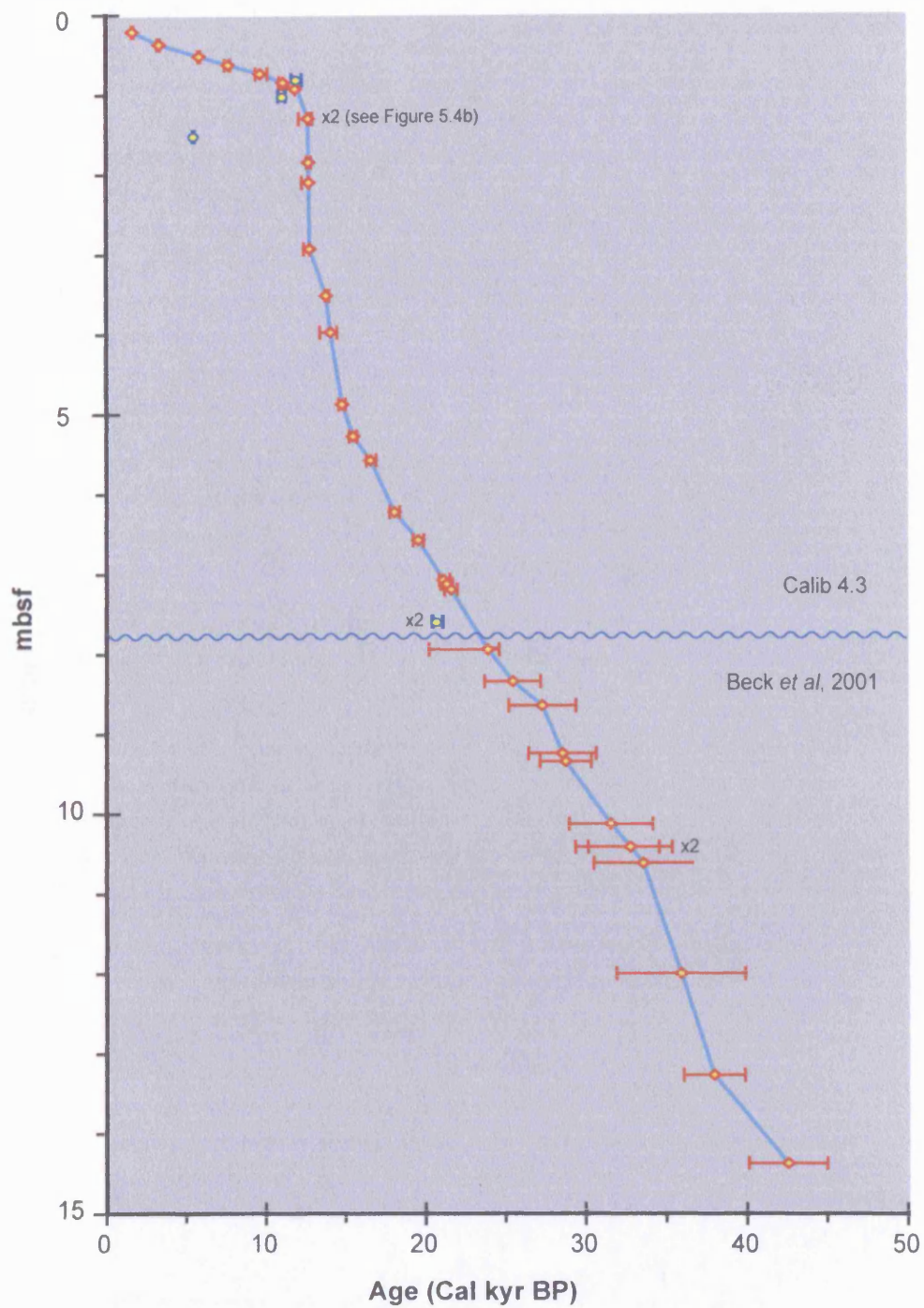


Figure 5.4a: Age-depth plot of calibrated radiocarbon dates from ODP 942 with their respective errors (one sigma). Depth scale is that of Core 942B. Connected diamonds indicate those samples used in age model, unconnected circles indicate those which were excluded. 'x2' indicates replicate samples. Dates above the wavy line were calibrated using Calib 4.3 (Stuiver and Reimer, 1993). Dates below the wavy line were calibrated against the data presented in Beck *et al.* (2000).

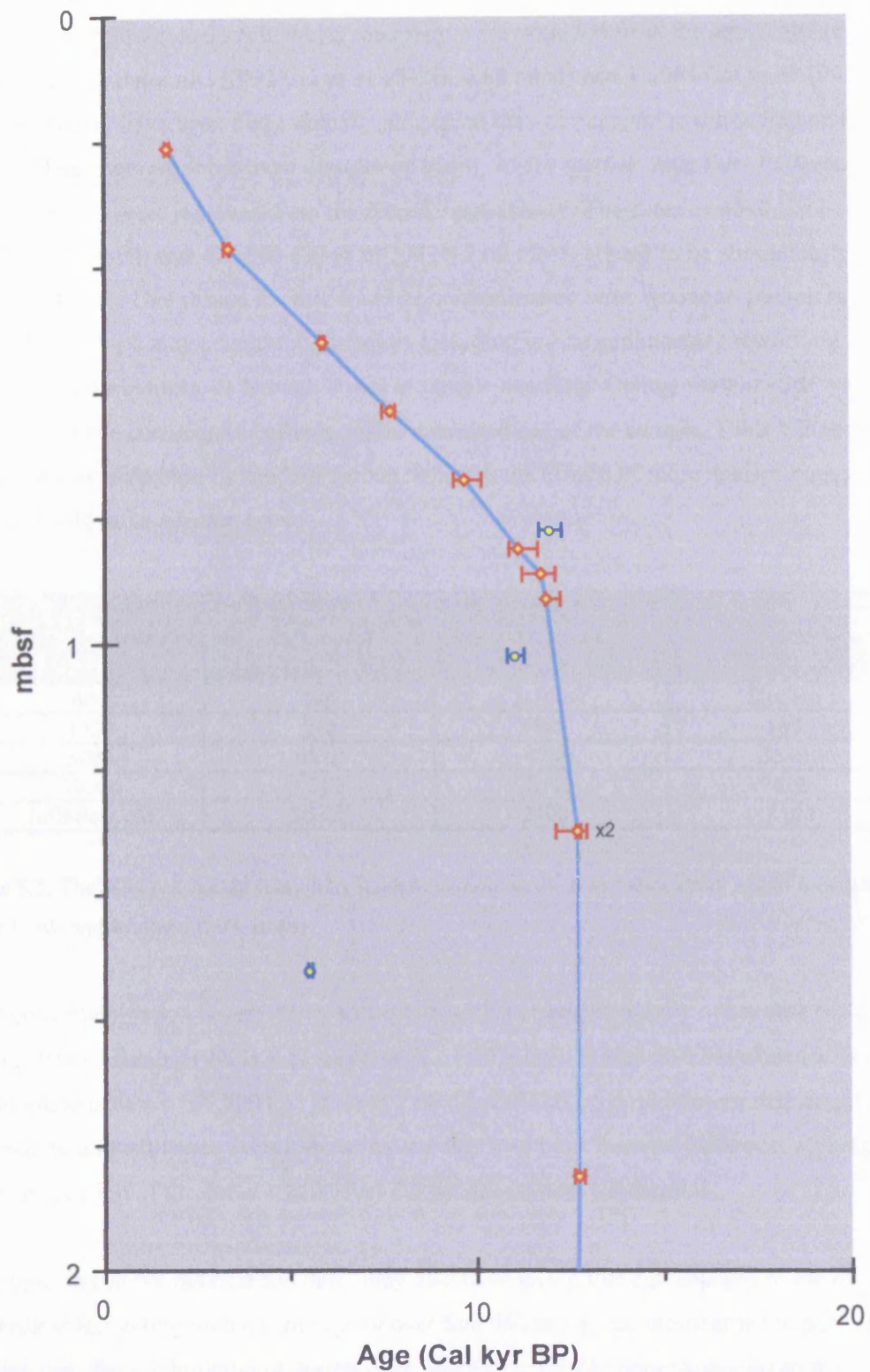


Figure 5.4b: 0-13 Cal kyr BP detail age-depth plot of calibrated radiocarbon dates from ODP 942 with their respective errors (one sigma). Depth scale is that of Core 942B. Connected diamonds indicate those samples used in age model, unconnected circles indicate those which were excluded. 'x2' indicates replicate samples.

As can be seen from Figure 5.4, the majority of the dates are consistently older with depth. Four dates appear anomalous however, and they were excluded from the age model (see also Table 5.1). The dates of 11,993 Cal yr BP (942B, 0.82 mbsf) and 11,064 Cal yr BP (942C 0.97 mbsf) may have been diagenetically altered, as they correspond to the sedimentary iron crust, and an apparent short-lived dissolution event, where species other than *Pulleniatina obliquiloculata* were removed from the record, respectively. The dates of 4690 Cal yr BP (942C, 1.52 mbsf), and ~20,800 Cal yr BP (942B 7.60 mbsf) appear to be anomalously young, however. One reason for this could be contamination with 'younger' carbon (i.e. with higher ^{14}C), which may arise through factors including in-situ sedimentary reworking (e.g. bioturbation, turbidites), or through errors in sample handling. Contamination with 'younger' carbon can have considerable effects on the measured age of the sample. Table 5.2 shows the effects of contamination by modern carbon, whereas the effects of more ancient younger carbon would be to a lesser extent.

True age (years)	Measured age as a result of...		
	1% 'modern' contamination	5% 'modern' contamination	10% 'modern' contamination
600	540	160	Modern
1000	910	545	160
5000	4870	4230	3630
10000	9370	8710	7620
Infinitely old	36600	24000	18400

Table 5.2: The effect of contamination by modern carbon on the true radiocarbon age of a sample (after Lowe and Walker, 1997, p246).

Modern contamination is very likely to explain such a stratigraphically offset date of 4690 Cal yr BP at ~1.5 mbsf (942B 1.52 mbsf; 942C, 1.47 mbsf). It may also have been a factor in the anomalous date of 20,800 Cal yr BP at 7.60 mbsf (942B), a double-measured sample, although to a much lesser extent. Bioturbation may also have been an influence, although visual inspection of the cores at this level did not reveal heavy indication.

Discrepancies in the radiocarbon dates may also have arisen through changes in the overall reservoir effect acting on the carbon pool over Site 942 at a given moment in the past. In the modern day, the mixing ratio of waters over Site 942 is 1:5 (Atlantic:Amazon) so the Amazon River contributes approximately 17% to the total surface water. At the same time, it will also contribute ^{14}C -containing dissolved inorganic carbon (DIC). 80 to 90% of DIC in the Amazon River is bicarbonate (Richey *et al.*, 1991), the form of carbon scavenged by foraminifera to build their tests (Erez, 2003). However, terrestrial ^{14}C is affected by a very

different carbon reservoir to oceanic ^{14}C . Studies have found that the amount of DIC in the Amazon River varies in direct proportion to outflow (e.g. Richey *et al.*, 1991). The effects of variations in river discharge with respect to the contribution of terrestrial ^{14}C to the Site 942 bicarbonate pool will therefore be amplified. For example, should Amazon River outflow be reduced by half, the proportion of freshwater mixed over Site 942 would fall to $\sim 8.5\%$; however the relative amount of terrestrial ^{14}C contributed to the radiocarbon pool would be $< 8.5\%$. Should such a change in the terrestrial bicarbonate input be significant to the overall ^{14}C pool over Site 942, it may therefore influence the local reservoir effect. This would introduce bias to the foraminiferal $\Delta^{14}\text{C}$ measured, and thus affect the calculated radiocarbon age of the sample.

5.3 Sedimentation Rate Over ODP Site 942

5.3.1 The Pleistocene-Holocene Sedimentary Regime Over Site 942

The sedimentation rate for ODP Site 942 is shown in Figure 5.5, and summarised in Table 5.3. The depths indicated are those of 942B, as this is the most stratigraphically complete of the records.

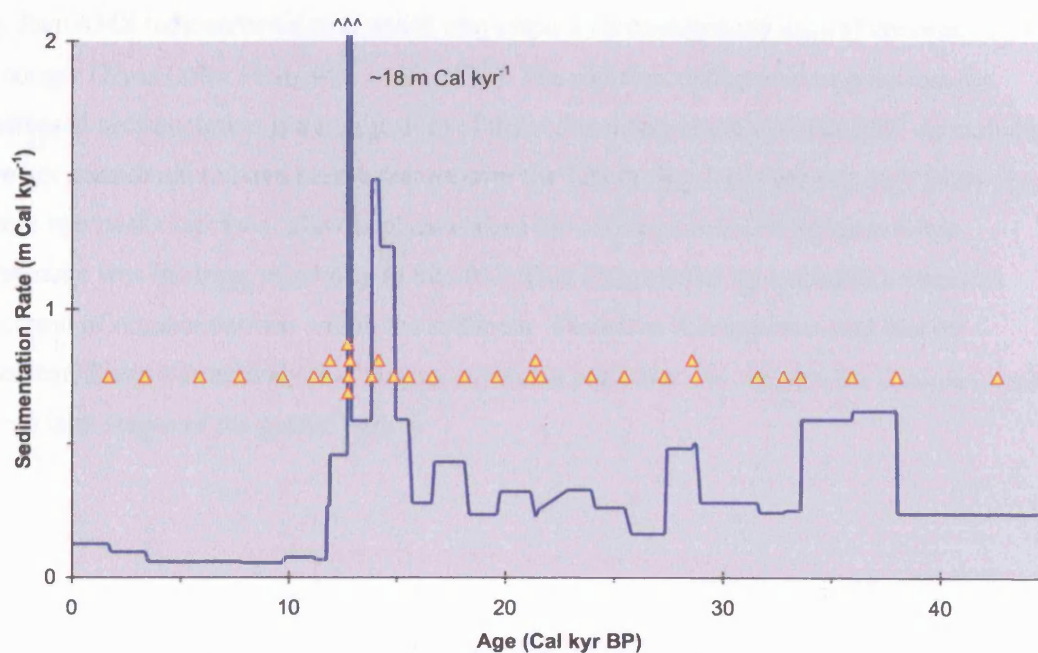


Figure 5.5: Inter-radiocarbon age sedimentation rates for ODP Site 942. Sedimentation rates are in metres per thousand calendar years. Triangles indicate relative stratigraphic position of radiocarbon-dated samples. ‘^^^’ indicates data plotted off the chart (up to $\sim 18\text{m Cal kyr}^{-1}$).

The sedimentation rate as produced by the composite age model can be used to assess the integrity of the dates selected. As shown in Figure 5.4, sedimentation rates at Site 942 vary

throughout the entire record between 0.06 and 18.00 metres per thousand calendar years (m Cal kyr^{-1}). Holocene sedimentation is consistently lower than glacial stage rates, ranging from 0.06 to 0.13 m Cal kyr^{-1} , typical of pelagic environments, indicating that fan deposition was ‘switched off’ throughout this period. Holocene sedimentation rates increase toward modern, especially from ~ 3.3 Cal ka to the present.

Amazon Fan sedimentation was ‘switched on’ during the cold stages, when the terrigenous sediment load of the river is transported directly to the fan (Damuth and Fairbridge, 1970; Damuth and Kumar, 1975). The last glacial maximum is marked by a gradual fall in sedimentation rates from 0.33 to 0.23 m Cal ka^{-1} , although juxtaposed levels are not significantly elevated relative to the rest of the glacial stage.

Maximum cold stage sedimentation took place in approximately four stages: 38 to 33.6 Cal ka; 28.8 to 27.35 Cal ka; 18.12 to 16.61 Cal ka; and 15.53 to 11.74 Cal ka. Sedimentation was particularly high during the latter of these stages, corresponding to the Lateglacial Interstadial and Younger Dryas. Within this period of elevated sedimentation, two discrete peaks of up to ~ 1.5 m kyr^{-1} and even more notably ~ 18.33 m kyr^{-1} arise from 14.85 to 13.81 and 12.8 to 12.7 Cal ka, respectively. As shown in Figure 5.5, this latter peak is constrained by four AMS radiocarbon dates, which also place it chronologically around the onset of the Younger Dryas (after Mangarud *et al.*, 1974). The rigorous dating also implies that the increased sedimentation is a true feature of the sedimentary regime of Site 942. As turbidites are not considered to have been a feature over the Site during these periods, it is likely that these two peaks represent alluvial phases when the active channel of Amazon River discharge was in closer proximity to Site 942. This is supported by a notable coincident increase of organic detritus within the sediment. Therefore it is hypothesised that the Amazon River was actively discharging at least in part, over the western fan complex during these later stages of the glacial period.

942B depth (mbsf)	Cal yr BP	SR (m Cal ka ⁻¹)	942B depth (mbsf)	Cal yr BP	SR (m Cal ka ⁻¹)
0.00	0		5.58	16610	
	↓	0.13		↓	0.43
0.21	1680		6.23	18120	
	↓	0.10		↓	0.23
0.37	3350		6.58	19610	
	↓	0.06		↓	0.32
0.52	5880		7.08	21170	
	↓	0.06		↓	0.23
0.63	7710		7.13	21390	
	↓	0.06		↓	0.26
0.74	9700		7.20	21660	
	↓	0.08		↓	0.33
0.85	11140		7.95	23960	
	↓	0.07		↓	0.26
0.89	11740		8.35	25500	
	↓	0.27		↓	0.16
0.93	11890		8.65	27350	
	↓	0.46		↓	0.48
1.30	12700		9.25	28600	
	↓	18.33		↓	0.50
1.85	12730		9.35	28800	
	↓	12.50		↓	0.28
2.10	12750		10.13	31600	
	↓	16.60		↓	0.24
2.93	12800		10.42	32800	
	↓	0.58		↓	0.25
3.52	13810		10.62	33600	
	↓	1.48		↓	0.59
3.98	14120		12.00	35950	
	↓	1.23		↓	0.62
4.88	14850		13.27	38000	
	↓	0.59		↓	0.24
5.28	15530		14.37	42600	
	↓	0.28		↓	0.24 (inferred)

Table 5.3: Sedimentation rates (m ka⁻¹) calculated between each age horizon for Site 942. Figures in boxes emphasise periods of extreme sediment accumulation. SR = sedimentation rate.

5.3.2 Chronological and Sea-Level Timing of the ‘On/Off Switch’ in Fan Deposition

The extreme transition in sedimentation at the end of the Pleistocene marks the ‘switching off’ of sea-level controlled fan deposition (Milliman *et al.*, 1975) as relative sea level rose into the Holocene, following the melting of glacial ice, starving the fan of its sediment supply (see Chapter 2, Section 2.2.2). According to Milliman *et al.*, (1975), fan deposition was ‘switched on’ when sea level fell to 30 metres below modern. Durham (1997) and Maslin *et al.* (2000) revised this figure to 40 – 50 metres below modern. However, the most recent dating of sediments from ODP Site 942 presented here suggest that this transition apparently took place at ~11.74 Cal ka. According to reconstructions, sea level at this time was nearer to 60 metres below present (see Figure 5.5; Fairbanks, 1989; Shackleton, 1987).

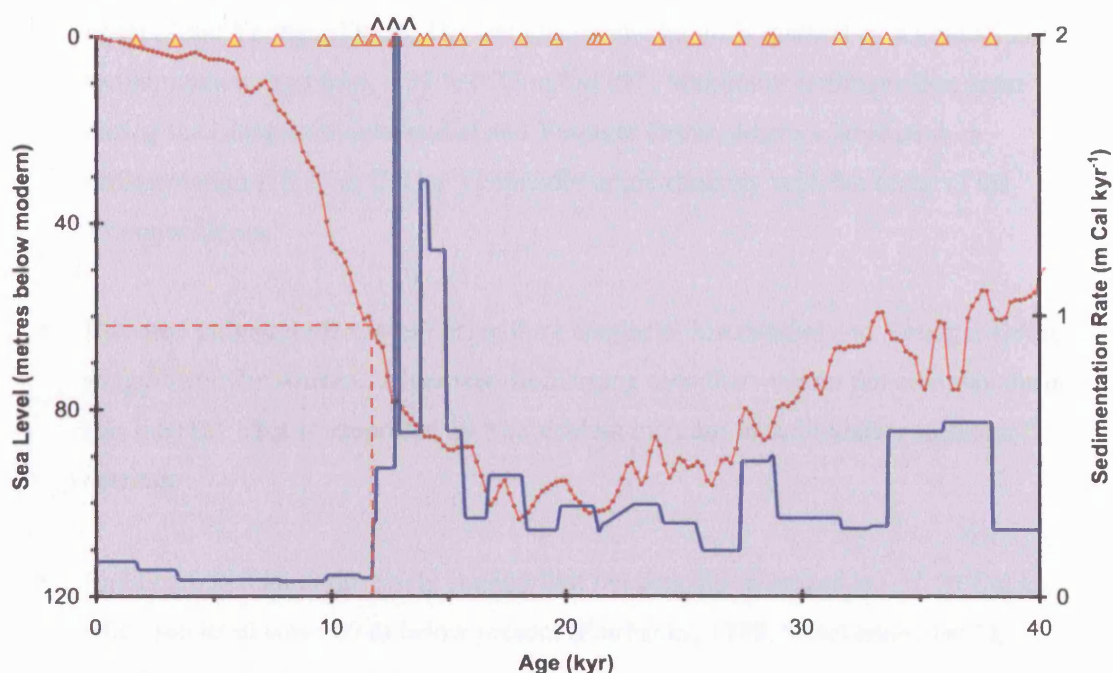


Figure 5.6: Site 942 sedimentation rate plotted alongside the sea level change curve (after Fairbanks, 1989; Shackleton, 1987) illustrating the chronological- and sea level- timing of the ‘on/off switch’ in Amazon Fan sedimentation. ‘^^^’ indicates data plotted off the chart (up to ~18m Cal kyr⁻¹).

5.4 Summary

The key points can be summarised as follows:

- 41 AMS radiocarbon dates were measured on mixed- and mono-species foraminifera samples from ODP Site 942, of which 36 were used to construct the age model (including three replicated samples).
- Although a component of the ¹⁴C pool above Site 942 may be of terrestrial origin, radiocarbon dates were calibrated to Calendar years BP assuming a difference from the global marine reservoir correction (ΔR) of -464 years, with an uncertainty of 40

years. It is also assumed that ΔR was constant throughout the duration of the record. Care must be taken when interpreting the proxy records however, as should ΔR have been over assumed, the calibrated calendar ages assigned to the cores may be too old.

- Date horizons were stratigraphically placed in each of the three cores from Site 942 by tuning the shipboard magnetic susceptibility curves. Separate age models were reconstructed for each core. Isotope datasets for each core were merged on the basis of their chronologies to form composite records for Site 942.
- Sedimentation rates vary from $\sim 0.06 \text{ m ka}^{-1}$ in the Holocene, to $\sim 18.88 \text{ m ka}^{-1}$ at the onset of the Younger Dryas. The last glacial maximum is marked by a gradual fall in sedimentation rates from 0.33 to $0.23 \text{ m Cal ka}^{-1}$. Maximum sedimentation arose during the Lateglacial Interstadial and Younger Dryas, where a large peak in sedimentation ($18.33 \text{ m Cal ka}^{-1}$) coincides approximately with the onset of the Younger Dryas.
- Elevated sedimentation rates during the Lateglacial Interstadial and Younger Dryas suggest that the Amazon River was discharging over the western fan complex during this interval. This is supported by a coincident increase in sedimentary terrestrial detritus.
- Radiocarbon data in this study suggest that fan deposition ceased at $\sim 11.74 \text{ Cal ka}$, when sea level was $\sim 60 \text{ m}$ below present (Fairbanks, 1989; Shackleton, 1987), which is greater than previous estimates.

5.5 References

- Bard, E., Rostek, F., and Ménot-Combes, G. (2004). A Better Radiocarbon Clock. *Science* **303**, 178-179.
- Beck, J. W., Richards, D. A., Edwards, R. L., Silverman, B. W., Smart, P. L., Donahue, D. J., Hererra-Osterheld, S., Burr, G. S., Calsoyas, L., Jull, A. J. T., and Biddulph, D. (2001). Extremely Large Variations of Atmospheric ^{14}C Concentration During the Last Glacial Period. *Science* **292**, 2453-2458.
- Damuth, J. E., and Fairbridge, R. W. (1970). Equatorial Atlantic deep-sea arkosic sands and ice-age aridity in tropical South America. *Geological Society of America Bulletin*, 189-206.

-
- Damuth, J. E., and Kumar, N. (1975). Amazon Cone: Morphology, sediments, age, and growth pattern. *Geological Society of America Bulletin* **86**, 863-878.
- Durham, E. (1997). "Amazon Basin sources of sediment within the Amazon Fan complex." Unpublished MRes thesis, University College London.
- Eastoe, C. J., Fish, S., Dulce Gaspar, M., and Long, A. (2002). Reservoir corrections for marine samples from the south Atlantic coast, Santa Catarina State, Brazil. *Radiocarbon* **44**, 145-148.
- Erez, J. (2003). The source of ions for biomineralisation in foraminifera and their implications for paleoceanographic proxies. *Reviews in Mineralogy and Geochemistry* **54**, 115-149.
- Fairbanks, R. G. (1989). A 17,000 year glacio-eustatic sea level record: influence of glacial melting rates on the Younger Dryas event and deep-ocean circulation. *Nature* **362**, 637-642.
- Greig, S. (1998). Site 942 on the Amazon Fan: stable isotopes and sea surface temperatures. *Unpublished M.Sc. Thesis, Royal Holloway University of London*, 91p.
- Hughen, K., Lehman, S., Southon, J., Overpeck, J., Marchal, O., Herring, C., and Turnbull, J. (2004). ^{14}C activity and global carbon cycle changes over the past 50,000 years. *Science* **303**, 202-207.
- Lowe, J. J., and Walker, M. J. C. (1997). "Reconstructing Quaternary Environments." Longman, Harlow.
- Mangarud, J., Andersen, S. T., Berglund, B. E., and Donner, J. J. (1974). Quaternary stratigraphy of Norden: a proposal for terminology and classification. *Boreas* **3**, 109-127.
- Maslin, M. A., Durham, E., Burns, S. J., Platzman, E., Grootes, P., Greig, S. E. J., Nadeau, M. J., Schleicher, M., Pflaumann, U., Lomax, B., and Rimington, N. (2000). Palaeoreconstruction of the Amazon River freshwater and sediment discharge using sediments recovered at site 942 on the Amazon Fan. *Journal of Quaternary Science* **15**, 419-434.
- McGeary, D. F. R., and Damuth, J. E. (1973). Postglacial iron-rich crusts in hemipelagic deep-sea sediment. *Geological Society of America Bulletin* **84**, 1201-1211.
- Milliman, J. D., Summerhayes, C. P., and Barretto, H. T. (1975). Quaternary sedimentation on the Amazon continental margin: a model. *Geological Society of America Bulletin* **86**, 610-614.
- Nadal de Masi, M. A. (1999). Prehistoric hunter-gatherer mobility on the southern Brazilian coast: Santa Catarina Island. *Unpublished PhD dissertation, Stanford University*, 186 p.
- Reimer, P. J., and Reimer, R. (2005). Marine Reservoir Correction Database, available online <http://radiocarbon.pa.qub.ac.uk/marine/>.
- Richey, J. E., Eneas Salati, R. L. V., and Forsberg, B. R. (1991). The biogeochemistry of a major river system: the Amazon case study. In "Biogeochemistry of Major World
-

- Rivers: SCOPE 42." (E. T. Degens, S. Kempe, and J. E. Richey, Eds.), pp. 57-74. John Wiley and Sons, Chichester.
- Shackleton, N. J. (1987). Oxygen isotopes, ice volume and sea level. *Quaternary Science Reviews* **6**, 183-190.
- Stuiver, M., and Reimer, P. J. (1993). Extended ^{14}C database and revised CALIB radiocarbon calibration program (Version 4.3). *Radiocarbon* **35**, 215-230.
- Stuiver, M., Reimer, P. J., Bard, E., Beck, J. W., Burr, G. S., Hughen, K. A., Kromer, B., McCormac, F. G., van der Plicht, J., and Spurk, M. (1998). INTCAL98 Radiocarbon age calibration 24,000 - 0 Cal BP. *Radiocarbon* **40**, 1041-1083.
- Stuiver, M., Reimer, P. J., and Reimer, R. (2005). "CALIB Manual." available online <http://radiocarbon.pa.qub.ac.uk/calib/manual/>.
- Telford, R. J., Heegaard, E., and Birks, H. J. B. (2004). The intercept is a poor estimate of a calibrated radiocarbon age. *The Holocene* **14**, 296-298.

6: OXYGEN ISOTOPE RECORDS FROM ODP SITE 942 ON THE AMAZON FAN

6.1 Introduction to Reconstructing Amazon River Outflow Using $\delta^{18}\text{O}$ Records

Assuming there has been a continuous Amazon River freshwater influence over Site 942 on the Amazon Fan, variations in past river outflow can be inferred from down-core reconstructions of sea surface salinity (SSS). SSS will fluctuate in response to the varying freshwater outflow of the Amazon River, which is assumed to reflect the coeval effective moisture availability (precipitation-evaporation) in the Amazon Basin. Although diatom concentrations are abundant within the surface sediments of Site 942, down-core assemblage reconstructions of salinity are severely limited due to active dissolution within the deeper levels (see Chapter 2, Section 2.4.2). Consequently, the diatom archive cannot be used to reconstruct a SSS record from Site 942.

It is possible, however, to monitor SSS using oxygen isotopes measured on planktonic foraminifera ($\delta^{18}\text{O}_{\text{plk}}$), which inhabit depths near to the sea surface and will thus isotopically record the influence of the Amazon River freshwater plume (e.g. Maslin and Burns, 2000; Maslin *et al.*, 2000).

As discussed extensively in the literature (see overviews in e.g. Bradley, 1999; Lowe and Walker, 1997; Williams *et al.*, 1998), additional to species-specific vital effects (e.g. associated with a species' depth habitat), $\delta^{18}\text{O}_{\text{plk}}$ is principally a function of the combined isotopic fractionation effects of global ice volume (GIV), sea surface temperature (SST), and sea surface salinity (SSS), i.e.

$$\delta^{18}\text{O}_{\text{plk}} = f(\delta^{18}\text{O}_{\text{GIV}} + \delta^{18}\text{O}_{\text{SST}} + \delta^{18}\text{O}_{\text{SSS}});$$

the latter of which, at surface levels, will be affected by dilution with freshwater. The typical relationship between $\delta^{18}\text{O}$, temperature and salinity in the tropical oceans is illustrated in Figure 6.1.

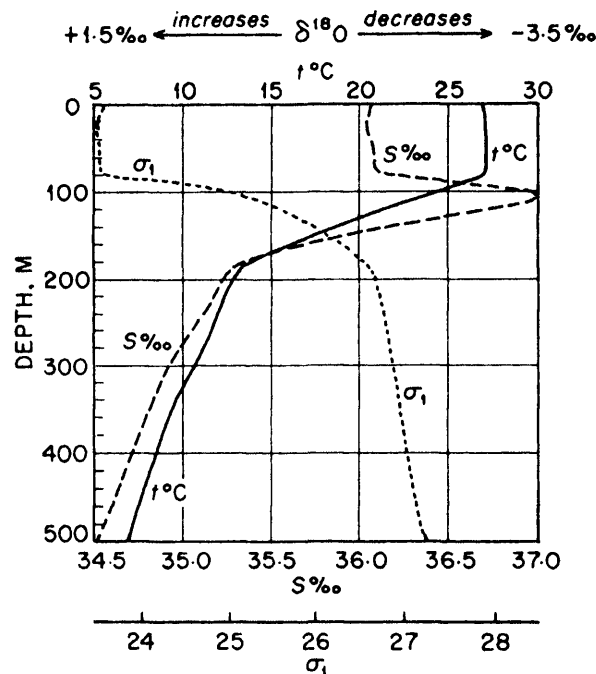


Figure 6.1: A typical vertical temperature ($t^{\circ}\text{C}$), salinity ($S\text{‰}$) and density (σ_1) profile for the tropical oceans (modified from Bradley, 1999).

Freshwater is isotopically more depleted than its oceanic counterpart. Modern Amazon River water has an average $\delta^{18}\text{O}$ value of -5‰ (Grootes, 1993; Thompson *et al.*, 2000), whereas the average tropical Atlantic signal is $+1\text{‰}$ (Arz *et al.*, 1998; Arz *et al.*, 1999; Maslin, 1998). $\delta^{18}\text{O}_{942}$, a planktonic record, will thus register a combination of these two isotopic signals, blended in proportions equivalent to the amount of each water mass mixed over Site 942. Should the volume of Amazon River outflow increase, more isotopically light water will be mixed over the site, and $\delta^{18}\text{O}_{942}$ will consequently become relatively more depleted ($\delta^{18}\text{O}$ values become more negative). Similarly, a decrease in Amazon River outflow will be reflected in $\delta^{18}\text{O}_{942}$ as a relative enrichment ($\delta^{18}\text{O}$ values become more positive). The outflow of the Amazon River can therefore be inferred by isolating the relative shift in surface water $\delta^{18}\text{O}$ brought about by Amazon freshwater-driven changes in surface salinity over Site 942 ($\delta^{18}\text{O}_{\text{Amazon}}$).

Several studies have concluded that water density (a function of temperature and salinity) is of prime importance to individual foraminiferal species, however (e.g. Emiliani, 1954; Emiliani, 1969; Hecht and Savin, 1972). Consequently, the same species may be found in different areas living at different depths, but in water of the same temperature and salinity. As freshwater-driven changes in salinity over Site 942 vary through time, the foraminifera may therefore migrate up and down through the water column to maintain a constant density

environment. Clearly such vertical migrations could result in isotopic signals of freshwater dilution that are considerably less than those changes actually occurring in the water column. $\delta^{18}\text{O}_{\text{plk}}$ -derived estimates of freshwater-driven changes in salinity from ODP Site 942 on the Amazon Fan should thus be considered as potentially conservative.

Maslin and Burns (2000) and Maslin *et al.* (2000) inferred $\delta^{18}\text{O}_{\text{Amazon}}$ by comparing the planktonic $\delta^{18}\text{O}$ record from 942C to that of GeoB-3104-1 (Arz *et al.*, 1999) located off the southeast coast of Brazil; south of the Amazon River mouth, and hence oceanically 'upstream' of the freshwater dilution effects of the Amazon River freshwater plume (see Figure 6.2).



Figure 6.2: Map of South America to show relative locations of ODP Site 942 and GeoB 3104-1. Dark blue arrows represent the direction of surface ocean currents; light blue arrow represents the Amazon River freshwater outflow.

With the same ocean currents thought to be operating over these two core locations, the authors hypothesised that each record would therefore record the same background surface-water marine isotope signal ($\delta^{18}\text{O}_{\text{Atlantic}}$). Consequently, Maslin and Burns (2000) and Maslin *et al.* (2000) proposed that the difference between the isotopic records of the two sites ($\Delta\delta^{18}\text{O}$) would provide a crude reflection of changes in the Amazon River freshwater

influence over Site 942 (i.e. $\delta^{18}\text{O}_{\text{Amazon}}$). The resultant $\Delta\delta^{18}\text{O}_{942\text{C}}$ reconstruction of Amazon River outflow is shown in Figure 6.3, alongside a similarly constructed record of effective moisture from Lake Junin in the Peruvian high Andes (see Maslin and Burns, 2000). The correspondence between these two independent records implies that $\Delta\delta^{18}\text{O}_{942\text{C}}$ is an effective method for reconstructing the past moisture history of the Amazon Basin (see Chapter 4, Section 4.3.4).

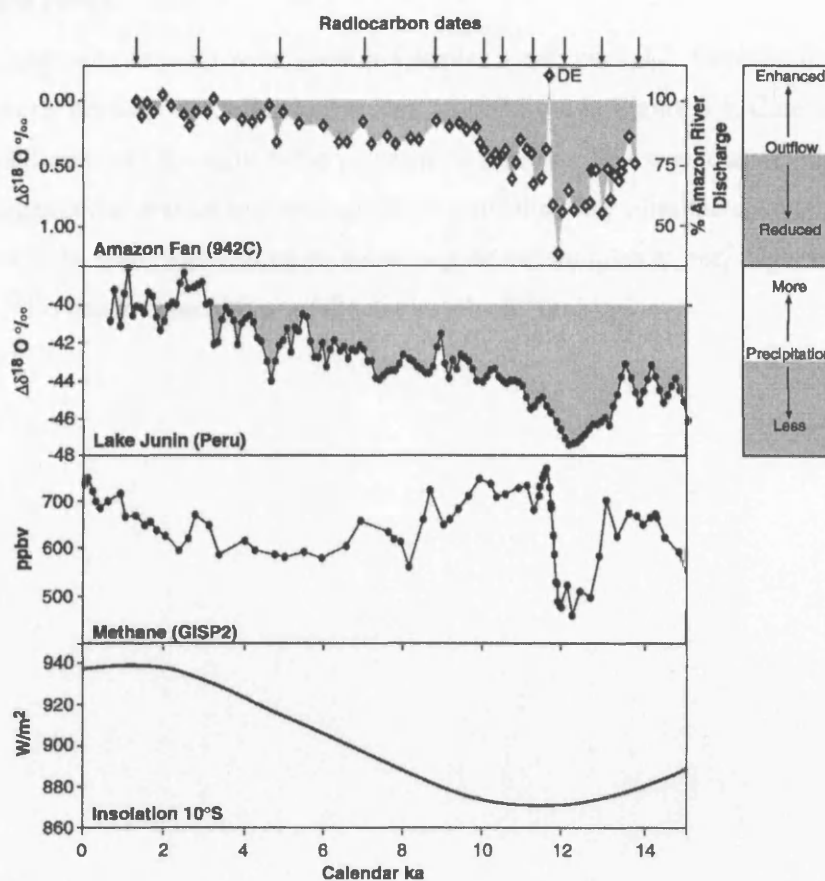


Figure 6.3: From top to bottom: *Neogloboquadrina dutertrei* $\Delta\delta^{18}\text{O}$ data from ODP Site 942C on the Amazon Fan as a proxy for Amazon River discharge; the Peruvian Lake Junin $\Delta\delta^{18}\text{O}$ record of effective moisture; the atmospheric methane record from Greenland Ice Sheet Project 2 (GISP2) in parts per billion by volume (ppbv); and summer insolation changes at 10°S (modified from Maslin and Burns, 2000).

The method employed by Maslin and Burns (2000) and Maslin *et al.* (2000) to isolate the freshwater-driven change in salinity over Site 942 was effectual in the context of the respective studies, as the $\delta^{18}\text{O}_{942\text{C}}$ and $\delta^{18}\text{O}_{\text{GeoB 3104-1}}$ records were of comparable temporal resolution. The present study however, has considerably enhanced the sampling density of $\delta^{18}\text{O}_{942}$ measurements, far in excess of any other records currently available from the study region and surrounds. To use the comparatively low-resolution $\delta^{18}\text{O}_{\text{GeoB 3104-01}}$ as a proxy for $\delta^{18}\text{O}_{\text{Atlantic}}$ would thus compromise the higher resolution of new data presented here. It

becomes necessary therefore, to isolate $\delta^{18}\text{O}_{\text{Amazon}}$ from the composite $\delta^{18}\text{O}_{942}$ record in this study by alternative means.

6.2 $\delta^{18}\text{O}$ Methodology for This Study

6.2.1 Sample Preparation

Details of sediment sampling were given in Chapter 2, section 2.4.2. Samples from 942A and 942B were prepared according to the sequence laid out in Figure 6.4. Care was taken to use only distilled water throughout the preparatory process. This was to avoid any potential residues/diagenetic alteration by chemical dispersants that may alter the chemistry of the foraminifera tests. Care was also taken not to expose the samples to very high temperatures, which may also cause diagenetic modification of the $\delta^{18}\text{O}$ signal.

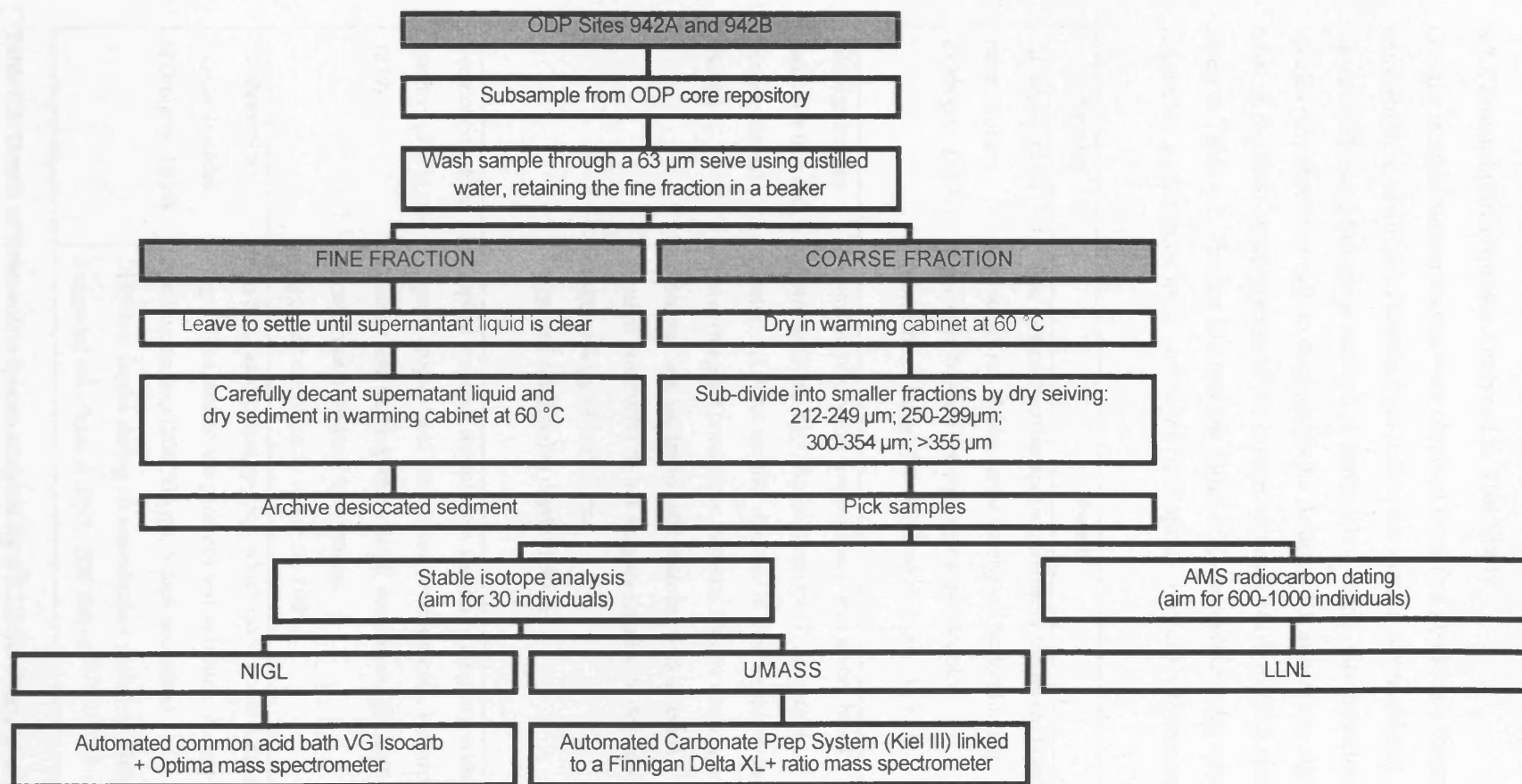


Figure 6.4: Sequence of sample preparation for ODP Site 942 sediments.

6.2.2 Foraminifera Species Analysed in This Study

Oxygen isotope measurements were obtained from five planktonic foraminifera species, representative of different depths from within the surface water column. The depth habitats represented range from near surface, to thermocline levels. Comparative analyses of such species may therefore help to distinguish the Amazon River outflow signal from background noise in the final interpretation of the isotope values. Details of each species measured are given in Table 6.1. The sac and non-sac forms of *G. sacculifer* were counted separately, and referred to in this study as *G. sacculifer (sac)* and *G. sacculifer (non-sac)*, respectively.

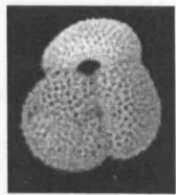
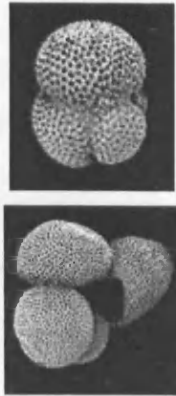


Species	Details	Image
<i>Globigerinoides ruber</i> (white; d'Orbigny, 1839)	Near surface-dwelling species, living in the mixed layer (upper 25 m). White forms belong to the dominating species in tropical and subtropical planktonic foraminifera. Suggested calcification depth: 0-50 m.	
<i>Globigerinoides sacculifer</i> (sac and non sac forms) (Brady)	Abundant in tropical water masses. Has a very broad tolerance for salinity. Some forms of <i>G. sacculifer</i> develop a distinct sac-like chamber in their terminal stage (lower image). Correlations between relative abundances of sac and non-sac forms, and relations with selected physical parameters do not suggest significant differences in the ecology of both forms. Suggested calcification depth: 0-50 m.	
<i>Neogloboquadrina dutertrei</i> (d'Orbigny, 1839)	Tropical seasonal thermocline species, living in a wide range of tropical and subtropical environments. Known to occur near the deep chlorophyll maximum. Thought to calcify at a constant temperature. Suggested calcification depth: 50-100 m.	
<i>Globorotalia truncatulinoides</i> (d'Orbigny, 1839)	A typical subtropical species, which occurs over a broad range of sea surface temperatures and salinities. A deep-dwelling species (200-500 m), which ascends to shallower depths during its reproduction period in winter. Suggested calcification depth: 200-500 m.	

Table 6.1: Details of foraminifera species analysed for $\delta^{18}\text{O}$ (after Anand *et al.*, 2003; Bradley, 1999; Hilbrecht, 1996; Ravelo and Fairbanks, 1992).

6.2.3 Stable Isotope Analysis for This Study

For stable isotope analysis, up to 30 individuals of each species were picked from the 300-354 μm size fraction of the sample, except *G. ruber*, which was picked from the 250-299 μm fraction. Care was taken to avoid broken, dirty-looking/physically altered, and juvenile specimens that could introduce noise to the isotopic signal. Sample analysis was carried out at two facilities according to Table 6.2. In some cases, dilution effects associated with high accumulation rates of terrestrial sediment (e.g. $\sim 1.5 \text{ m Cal ka}^{-1}$ from ~ 13.8 to 14.1 Cal ka) resulted in very low sedimentary foraminifera concentrations. For these samples, fewer individuals were analysed, although no samples of fewer than five individuals were measured. It should be noted however, that variations in sample size may be a significant source of variability in measurement data (Trauth, 1995).

Core	Sample Details	Laboratory
942A	Early Holocene	Stable Isotope Laboratory, Department of Geosciences, University of Massachusetts, Amherst, USA (Finnigan Delta XL + ratio mass spectrometer)
942B	Holocene and last glacial/interglacial transition	Stable Isotope Laboratory, Department of Geosciences, University of Massachusetts, Amherst, USA (Finnigan Delta XL + ratio mass spectrometer)
942B	Last glacial maximum	NERC Isotope Geosciences Laboratory (NIGL), UK (Automated common acid bath VG Isocarb + Optima mass spectrometer)

Table 6.2: Details of $\delta^{18}\text{O}$ sample analyses at different laboratories.

Samples measured at NIGL were manually homogenised by using a mortar and pestle to crush the foraminifera to a powder. Homogenised sub-samples of $60\mu\text{g}$ were loaded into thimbles to be analysed in the mass spectrometer. Samples measured at UMass were homogenised by the Automated Carbonate Prep System (Kiel III) linked to the mass spectrometer. Analytical sample reproducibility errors were $<0.07\text{‰}$ at each facility, based on replicate measurements of within-run laboratory standards, calibrated against standards from the International Atomic Energy Agency National Bureau of Standards. All $\delta^{18}\text{O}$ values were measured in ‰ , and expressed as deviations relative to the Vienna Pee Dee Belemnite standard, where:

$$\delta^{18}\text{O}_{\text{sample}} = \left(\frac{\left(\frac{^{18}\text{O}}{^{16}\text{O}} \right)_{\text{sample}}}{\left(\frac{^{18}\text{O}}{^{16}\text{O}} \right)_{\text{standard}}} - 1 \right) \times 1000\text{‰}$$

The data obtained from each facility were harmonised against each other by comparing the $\delta^{18}\text{O}$ measurements of the laboratory sample standards, and applying a correction factor where appropriate. The harmonisation was also cross-checked by examining inter-laboratory replicate sample data from each of the Cores.

Data from each Core were spliced together using the Core-specific age models (see Chapter 5) as the depth below sea floor will not necessarily be consistent between the cores. The $\delta^{18}\text{O}$ records from 942A and 942B were also spliced to the 942C $\delta^{18}\text{O}$ record from the previous studies (Maslin and Burns, 2000; Maslin *et al.*, 2000), again using the down-core chronologies.

All composited data were normalised to zero against the stratigraphically most recent sample for each species, to express relative isotopic deviation from ‘modern’ (where modern is 1 Cal yr BP or 0.0-0.01 mbsf). This also helps to minimise the between-species ‘vital effects’ associated with individual species of planktonic foraminifera calcifying at different rates of disequilibrium with the surrounding seawater (e.g. Deuser, 1987; Erez and Luz, 1982; Shackleton *et al.*, 1973). However, there is evidence that the vital effect of a species remains constant through time (Duplessy *et al.*, 1970). By normalising all the species to zero at the most recent sample, therefore, the isotopic records from each species become more directly comparable.

6.3 High Resolution $\delta^{18}\text{O}$ Records from ODP Site 942

6.3.1 High Resolution $\delta^{18}\text{O}$ Records

The normalised composite $\delta^{18}\text{O}$ records of the five species measured for Site 942 are shown in Figure 6.5, both against depth (a), and Calendar years BP (b). Species are plotted in relative order of depth habitat, from the shallowest to the deepest.

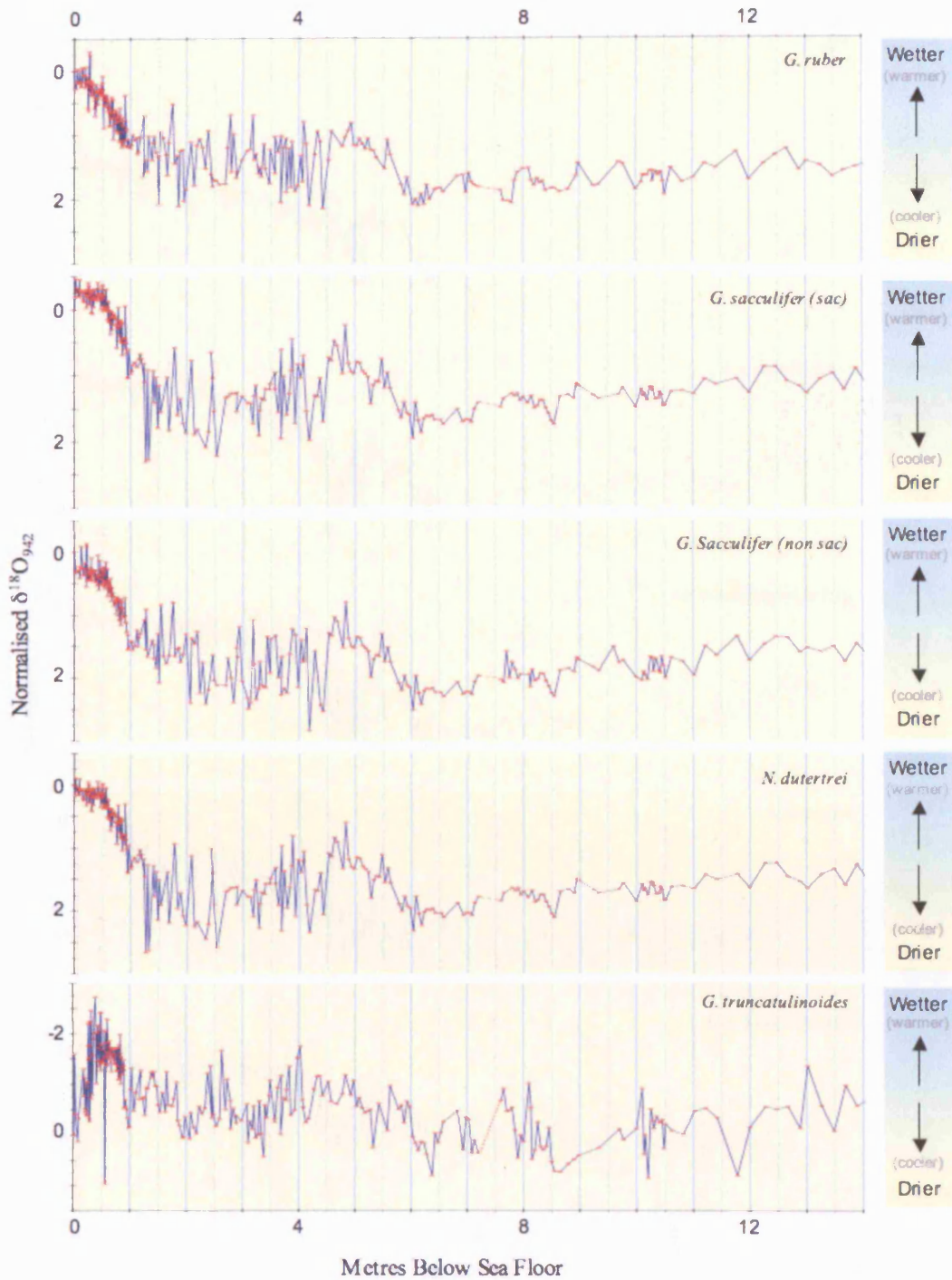


Figure 6.5a: Normalised composite $\delta^{18}O_{942}$ records for each of the five species measured, plotted against metres below sea floor. Markers indicate individual sample levels. All data were normalised against the stratigraphically most recent value to express change relative to modern (where modern = 0.0 to 0.01 mbsf).

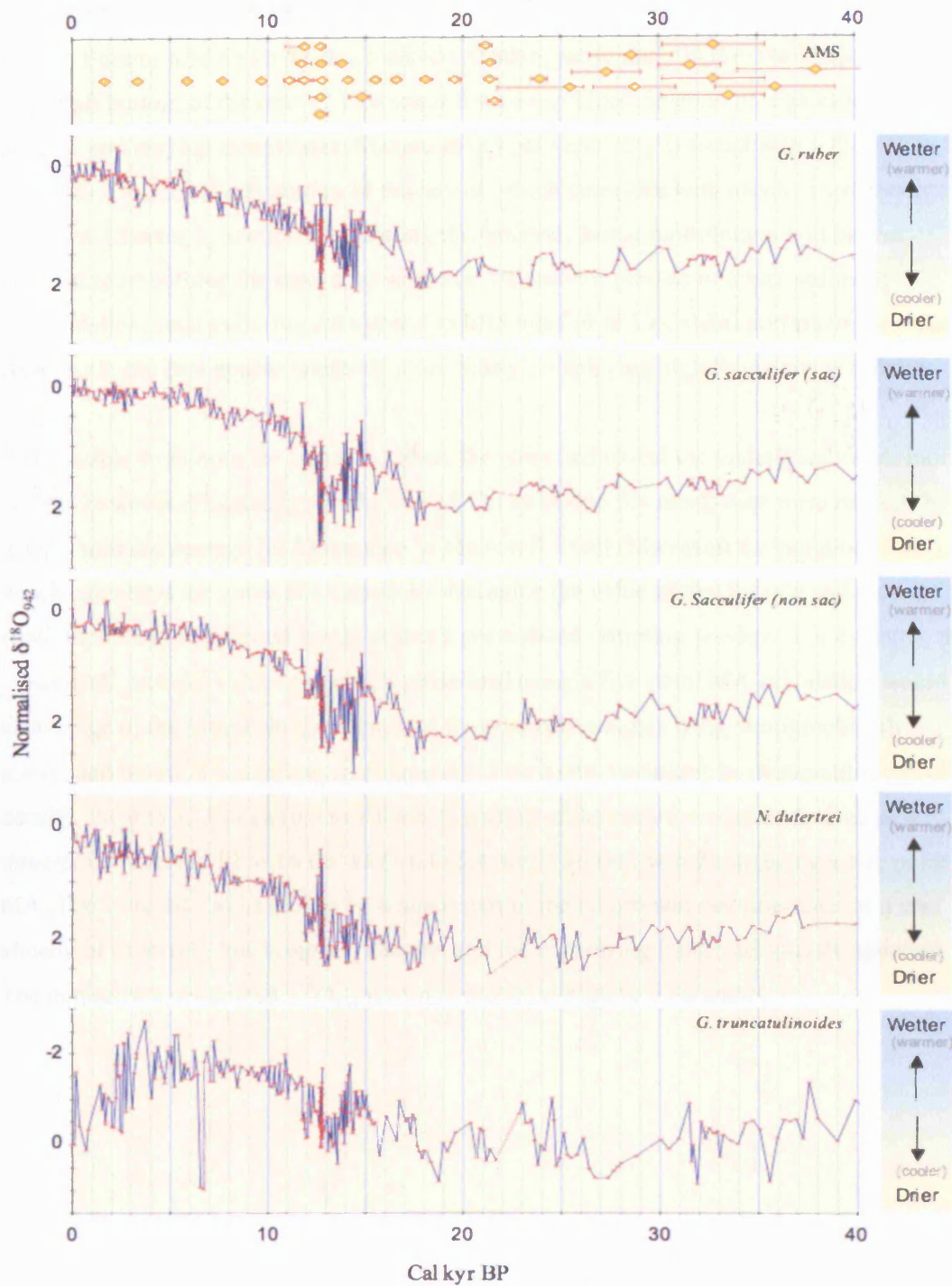


Figure 6.5b: Normalised composite $\delta^{18}O_{942}$ records for each of the five species measured, plotted against calendar years BP. Individual sample levels are indicated by markers. Yellow diamonds indicate the relative stratigraphic placement of AMS radiocarbon dates, with their respective error margins. All data were normalised against the stratigraphically most recent value to express change relative to modern (where modern = 1 Cal yr BP).

6.3.2 Smoothed Isotope Data

Data in Figures 6.5a and b display marked variation, particularly in the 0 to 16 Cal ka (0.0 to 5.4 mbsf) portion of the record. This arises from a combined function of high sampling density, and varying sample size. Maximum sample variability is found within the ~12 to 15 Cal ka (0.9 to 5.28 mbsf) portion of the record, which coincides with elevated sedimentation rates (see Chapter 3, Section 6.3). During this interval, faunal bioturbation will be less efficient at smoothing the record, as would be the case for periods of lower sediment accumulation, such as during the upper 0 to 0.95 mbsf (0 to 10 Cal ka) portion of the record. As a result, the data appear relatively more 'noisy', displaying high frequency variability.

It is possible to smooth the signal to reduce the noise and reveal the underlying trends more clearly, however. Fluctuations in the 0 to 16 Cal ka (0.0 to 5.4 mbsf) data were reduced by using a moving average (MA) function in Microsoft Excel (Microsoft Corporation, 2004), which calculates the value of a sample by averaging the value of that sample and those of the stratigraphically juxtaposed levels, within a pre-defined sampling window. For example, the 'smoothed' isotopic value of a sample calculated using a five point MA calculation would be an average of the sample in question, plus the next two samples lying stratigraphically above, and below (i.e. totalling five samples). Due to the variations in stratigraphic sampling density, the 0 to 12 Cal ka (0.0 to 1.0 mbsf) portion of the record was smoothed using a three-point MA, the 12 to 16 Cal ka (1.0 to 5.4 mbsf) section smoothing using a five point MA. The 16 to 40 Cal ka (5.4 to 13.8 mbsf) part of the record was not smoothed as it was already of relatively low sampling density, and the underlying trend was already apparent. The normalised, smoothed $\delta^{18}\text{O}_{942}$ record is shown in Figures 6.6a and b.

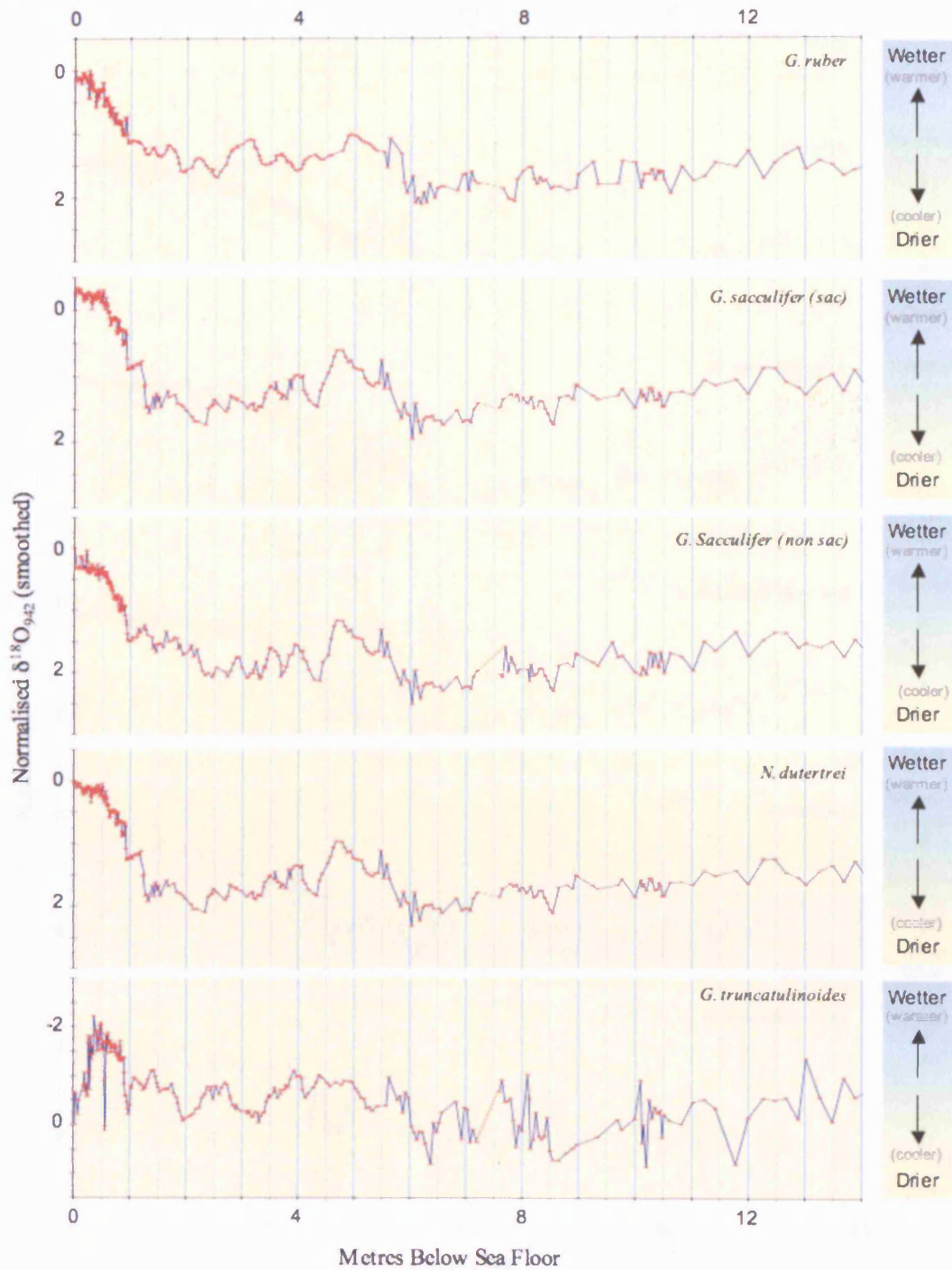


Figure 6.6a: Composite smoothed $\delta^{18}O_{942}$ records for each of the five species measured plotted against metres below sea floor. Individual sample levels are indicated by red dots. All data were normalised against the stratigraphically most recent value to express change relative to modern (where modern = 0.00 to 0.01 mbsf).

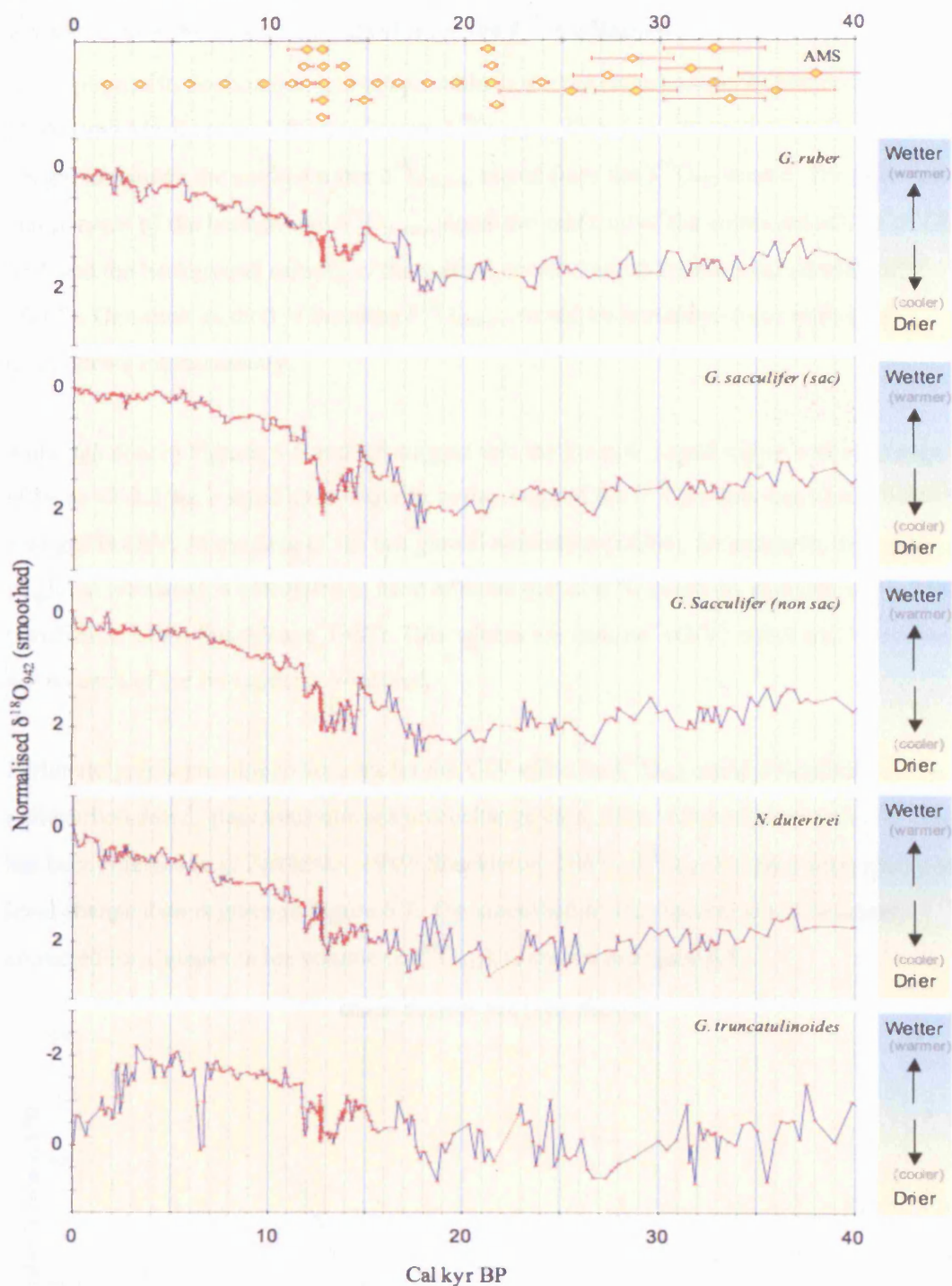


Figure 6.6b: Composite smoothed $\delta^{18}O_{942}$ records for each of the five species measured plotted against Calendar years BP. Individual sample levels are indicated by red dots. Yellow diamonds indicate the relative stratigraphic placement of AMS radiocarbon dates, with their respective error margins. All data were normalised against the stratigraphically most recent value to express change relative to modern (where modern = 1 Cal yr BP).

6.3.4 Isolating the $\delta^{18}\text{O}_{\text{Amazon}}$ Signal from the $\delta^{18}\text{O}_{942}$ Record

As mentioned in Section 6.1, it is not possible to use the same method as Maslin and Burns (2000) and Maslin *et al.* (2000) to isolate $\delta^{18}\text{O}_{\text{Amazon}}$. Therefore alternative methods must be sought to remove the surface water $\delta^{18}\text{O}_{\text{marine}}$ signal from the $\delta^{18}\text{O}_{942}$ record. The principal components of the background $\delta^{18}\text{O}_{\text{marine}}$ signal are made up of the combined effects of GIV, SST and the background salinity of the surface ocean currents (surface ocean salinity, 'SOS'). One such method of isolating $\delta^{18}\text{O}_{\text{Amazon}}$ would be to remove these individual components independently.

Although data in Figures 6.5 and 6.6 suggest that the isotopic signal varies within a range of $\sim 0\text{‰}$ to $\sim 2\text{--}2.5\text{‰}$, a significant majority in the range of the $\delta^{18}\text{O}_{942}$ data can be attributed to changes in GIV. At the time of the last glacial maximum (LGM), for example, the expansion of global ice sheets is calculated to have affected global $\delta^{18}\text{O}$ levels by as much as $+1.25\text{‰}$ (Fairbanks, 1989; Shackleton, 1987). This 'global ice volume' (GIV) effect will be constant across each of the five species measured.

Fortunately, it is possible to account for the GIV effect in $\delta^{18}\text{O}_{942}$ using published, radiocarbon dated, glacio-eustatic sea level change data, from which the associated $\delta^{18}\text{O}_{\text{GIV}}$ has been inferred (e.g. Fairbanks, 1989; Shackleton, 1987). $\delta^{18}\text{O}_{\text{GIV}}$ inferred from global sea level change data is given in Figure 6.7. The smoothed $\delta^{18}\text{O}_{942}$ record, which has been corrected for changes in ice volume ($\Delta\delta^{18}\text{O}_{942}$), is shown in Figure 6.8.

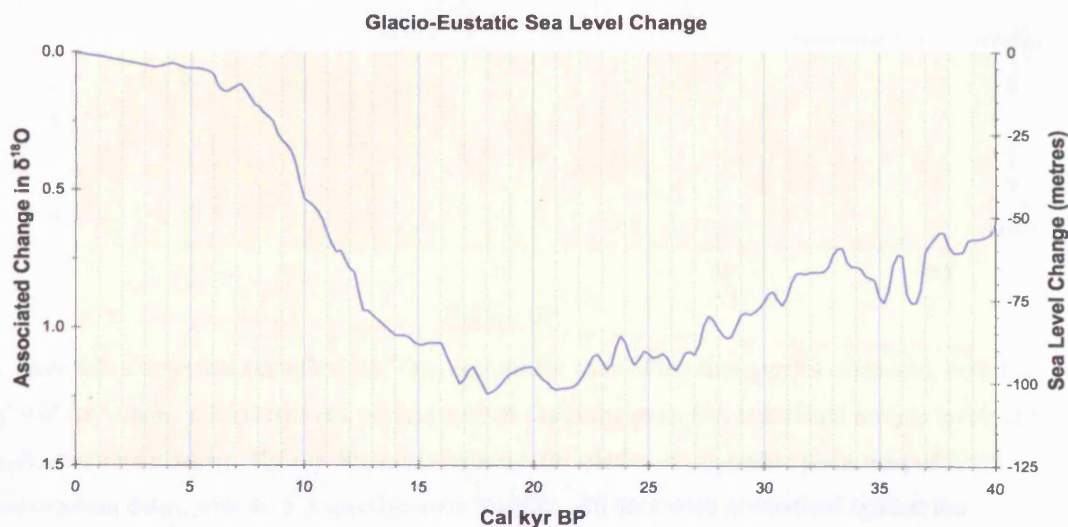


Figure 6.7: Glacio-eustatic sea level change and associated change in $\delta^{18}\text{O}$, as a proxy for the global ice volume effect (after Fairbanks, 1989; Shackleton, 1987).

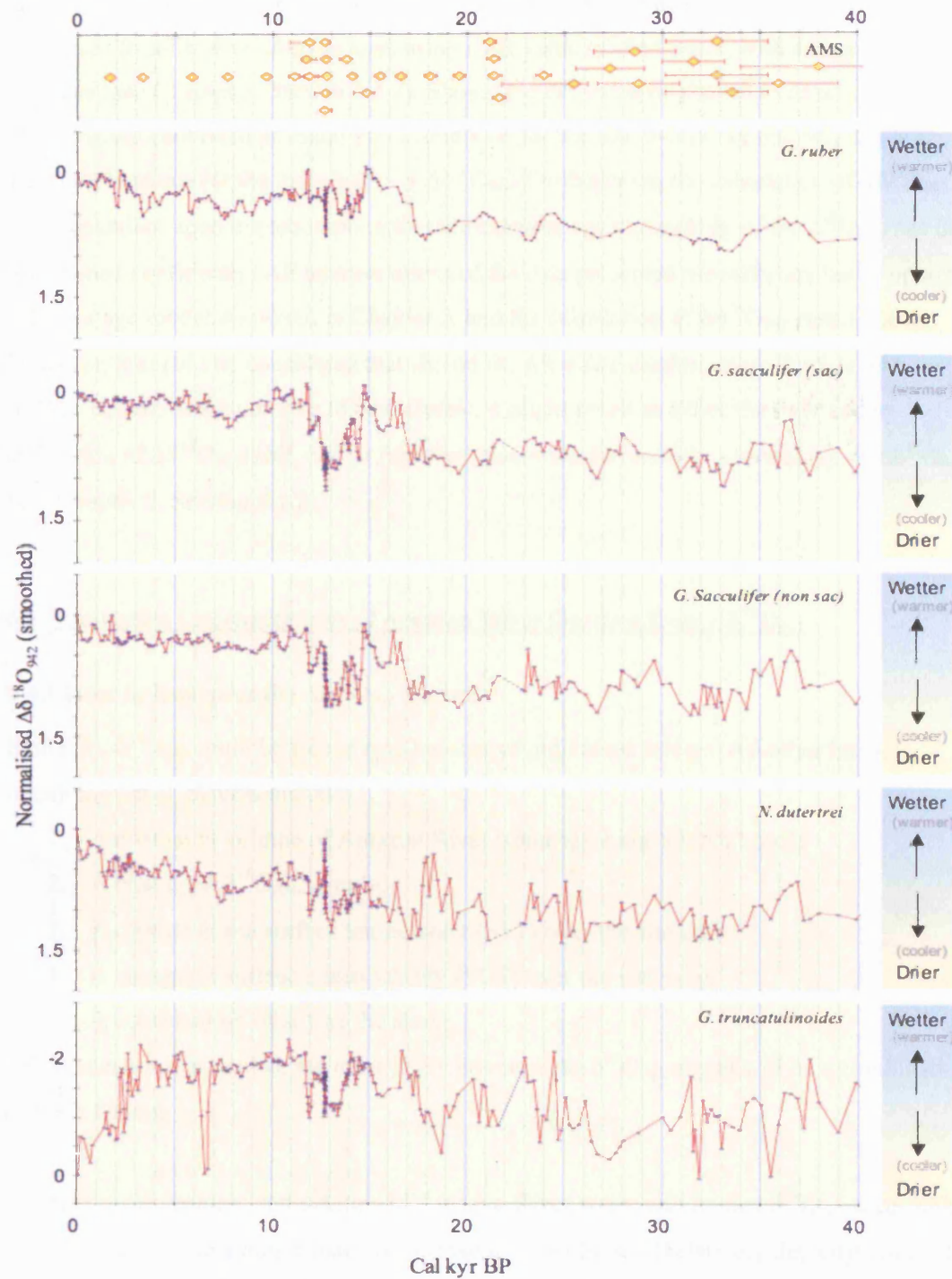


Figure 6.8: Composite smoothed $\Delta\delta^{18}\text{O}_{942}$ records for each of the five species measured, with the global ice volume effect removed, plotted against Calendar years BP. Individual sample levels are indicated with markers. Yellow diamonds indicate the relative stratigraphic placement of AMS radiocarbon dates, with their respective error margins. All data were normalised against the stratigraphically most recent value to express change relative to modern (where modern = 1 Cal yr BP).

It is important to note that the radiocarbon dates used in the Site 942 age model were converted to calibrated calendar ages using a ΔR value of -464 years, with an uncertainty of 40 years (see Chapter 5, Section 5.1.2). Should the ΔR value be proven to be otherwise, thus changing the calibrated calendar years timescale for the Site 942 proxy records, this will have implications for the calculation of $\Delta\delta^{18}\text{O}_{942}$. Furthermore, the calculation of $\Delta\delta^{18}\text{O}_{942}$ is also dependant upon the assumption that the calendar age chronology of the $\delta^{18}\text{O}_{\text{GIV}}$ has been established confidently. All interpretations of the data presented hereafter are based upon the calendar age model discussed in Chapter 5, and the calculation of $\Delta\delta^{18}\text{O}_{942}$ stated above. However, it should be considered that should the ΔR value used in either the Site 942, or $\delta^{18}\text{O}_{\text{GIV}}$ age models be proven to be different, it might result in either the over/under-estimation of $\Delta\delta^{18}\text{O}_{942}$ itself, and/or the over/under-estimation of the chronology of $\Delta\delta^{18}\text{O}_{942}$ (see Chapter 5, Section 5.1.2).

6.4 Qualitative Interpretations of Amazon River Outflow from $\Delta\delta^{18}\text{O}_{942}$

6.4.1 How to Interpret the $\Delta\delta^{18}\text{O}_{942}$ Record

Shifts in $\Delta\delta^{18}\text{O}_{942}$ could be forced by a number of individual drivers. All other factors remaining equal, drivers include:

1. A change in volume of Amazon River water reaching Site 942 only;
2. A change in $\delta^{18}\text{O}_{\text{Amazon}}$ only;
3. A change in sea surface temperature (SST) over the site only;
4. A change in surface ocean salinity (SOS) over the site only;
5. A combination of any of the above.

Of the scenarios presented, the most likely driver of the $\delta^{18}\text{O}_{942}$ signal will be a combination of these factors.

Changes in the isotopic composition of Amazon River water will impact $\delta^{18}\text{O}_{942}$ accordingly. All other factors remaining equal, an increase in the volume of relatively depleted Amazon River water mixed over the Site will force a further depletion in $\delta^{18}\text{O}_{942}$. Conversely, a decrease in the volume of Amazon River water mixed over Site 942 will bring about a relative enrichment in $\delta^{18}\text{O}_{942}$.

SST and background SOS have yet to be accounted for in the $\Delta\delta^{18}\text{O}_{942}$ record, however. For example it is thought that the tropical sea-surface temperatures cooled by up to 5°C during the glacial (e.g. Guilderson *et al.*, 1994), which would represent a surface ocean isotopic

shift of $\sim 1\%$ (Craig, 1965; Epstein *et al.*, 1953). In order to remove accurately the SST effect from the $\Delta\delta^{18}\text{O}_{942}$ signal, a detailed corresponding record of SST is required. Unfortunately, there are no such good quality, high-resolution records available for the hydrographic setting over the Amazon Fan. Although SST records are available for the Amazon Fan region, they either lack integrity, are of too coarse a resolution, or are of questionable precision (e.g. Arz *et al.*, 1998; e.g. Arz *et al.*, 1999; Greig, 1998). Where SST records also exist for the tropical Atlantic (e.g. Billups and Spero, 1996; Hastings *et al.*, 1998; Min *et al.*, 1995; Mix *et al.*, 1999; Niebler *et al.*, 2003; Rühlemann *et al.*, 2001; Wolff *et al.*, 1998), they are considered to be too widely interspaced from which to interpolate/extrapolate stratigraphic records of enough accuracy and/or resolution for the purpose of this study. Furthermore, with the lack of comparable detailed resolution records, it is also very difficult to establish the isotopic effects of natural variation in the salinity of the prevailing ocean currents operational over ODP Site 942. Such variation in SOS may arise from changes in the overall salinity of the water mass (e.g. due to changes in the precipitation-evaporation rates in a source area), or to changes in the precipitation-evaporation regime over the course of the ocean current, which may affect the dilution of the surface waters. Therefore with the data available to date, it is unfortunately not possible to account for down-core variations in SST and SOS in $\Delta\delta^{18}\text{O}_{942}$. However changes in SOS alone are likely to have only a minor impact on the isotopic record relative to other driving factors (Williams *et al.*, 1998, Chapter 7). The majority of the shift in $\Delta\delta^{18}\text{O}_{942}$ therefore, will be a result of changes in the isotopic signal and /or volume of Amazon River outflow, and SST effects over Site 942.

Nevertheless, the hypothesised $\delta^{18}\text{O}_{\text{GIV}}$ derived from glacio-eustatic sea level change records is regarded to be a conservative estimate. In this way some (but not all) of the isotopic effects associated with SST and SOS may inadvertently be accounted for. Therefore, despite the limitations, it should still remain possible to use these $\Delta\delta^{18}\text{O}_{942}$ data to make qualitative assessments of the past variations in Amazon River discharge, albeit to a limited extent. Without actual down-core records of SST however, speculations of past Amazon River outflow should be made with caution, as SST effects may further influence the isotopic record beyond the excess isotopic range accounted for by the conservative estimates of $\delta^{18}\text{O}_{\text{GIV}}$.

6.4.2 General Comparisons Between $\Delta\delta^{18}\text{O}_{942}$ Records of Different Species

Of the data presented in Figures 6.5, 6.6 and 6.8, the isotope signals of *G. ruber*, *G. sacculifer* sp. and *N. dutertrei* all appear to follow similar trends. After correction for ice volume (see Figure 6.8), these four species' records fluctuate within the range of 0‰ to ~1-1.5‰, with the amplitude of variation progressively increasing with depth from the sea surface. This increase in range is most likely to be reflecting isotopic fractionation effects associated with the depth stratification of the species, where gradients of variables such as temperature and salinity will vary. It may also reflect the differing seasonality of the life cycles between the individual species, where calcification of the foraminifera's test is isotopically recording seasonal variation in surface ocean $\delta^{18}\text{O}$.

Although the *G. truncatulinoides* record at times bears certain resemblance to the signals measured on the other species (e.g. between ~11.5 and 14 Cal ka), overall, the signal is very different. The *G. truncatulinoides* record appears to be fractionated to a different order of magnitude than the other four species, with normalised ice-volume-corrected values ranging between 0‰ and 2.25‰. This is a reflection of the much deeper depth-habitat of *G. truncatulinoides* compared to the other species measured (see Table 6.1). At deeper levels, *G. truncatulinoides* is thus relatively more isolated from the isotopic effects of the Amazon Freshwater plume at the ocean surface. The dissimilarity between the *G. truncatulinoides* $\delta^{18}\text{O}$ record and those of its relatively more shallow-dwelling counterparts would imply that the signal could be influenced more strongly by environmental variables, such as thermocline structure, rather than by the dilution effects of Amazon River water. Although the *G. truncatulinoides* record may provide valuable information for reconstructing changes in the past regional vertical ocean structure, it will be difficult to isolate freshwater-driven shifts in surface ocean salinity from its $\delta^{18}\text{O}$ signal.

Consequently, it is therefore more difficult to use $\Delta\delta^{18}\text{O}_{942}$ from *G. truncatulinoides* to monitor the amount of Amazon fresh water mixed over Site 942 compared to other species measured in this study. Furthermore, *G. truncatulinoides* was also relatively less abundant in the sediments, and compared to other species measured, sample sizes were more variable. Variations in sample size can contribute to considerable noise within an isotopic signal (Trauth, 1995), thus the *G. truncatulinoides* $\delta^{18}\text{O}$ record is comparatively less reliable than those of the other species..

Slight dissimilarity is also noted between the *N. dutertrei* records, and those of *G. sacculifer* sp. and *G. ruber*, especially in the glacial-Holocene amplitude, and for the period ~19.5 to

~17.5 Cal ka. Greig (1998) noted that the relative abundance of *N. dutertrei* was greater in glacial sediments compared to the Holocene. *N. dutertrei* is thought to calcify at a constant temperature in the Atlantic Ocean (Ravelo and Fairbanks, 1992), preferentially residing near the thermocline (Hilbrecht, 1996). Increased nutrient supplies at the chlorophyll maximum, coincident with the maximum thermal gradient, lead to marked increases in species abundance when the seasonal thermocline is in the photic zone (Ravelo and Fairbanks, 1992). This implies that the thermocline may have shallowed during the glacial period, allowing cooler, nutrient-rich waters to be nearer the surface, within the photic zone, becoming ecologically more favourable for *N. dutertrei*. Calcification would therefore have taken place at a shallower depth in the water column, where $\delta^{18}\text{O}$ may have been relatively more depleted due to the mixing of Amazon River water in the upper water column. $\delta^{18}\text{O}$ incorporated into the glacial tests of *N. dutertrei* may thus have been more depleted relative to Holocene times, when calcification took place at deeper levels. Care should be taken when attempting to interpret changes in Amazon River outflow from *N. dutertrei* $\delta^{18}\text{O}_{942}$ records, as the signal may also be recording changes in the species' ecological habitat. Nevertheless, information of changes in the thermocline structure may yield useful information for the interpretation of the other $\delta^{18}\text{O}_{942}$ records.

Of the $\Delta\delta^{18}\text{O}_{942}$ records that are considered to be recording variability in Amazon River outflow, the major trend apparent within these species' records is that of a transition between different states within the system. This is illustrated by Figure 6.9, which shows the $\Delta\delta^{18}\text{O}$ record for *G. sacculifer* (sac), where solid horizontal lines indicate a transition between two relatively steady states. From 40 to ~18 Cal ka, isotope data fluctuate around a relatively more enriched mean value (glacial state), whereas from ~12 to 0 Cal ka, isotopic data fluctuate about a mean that is relatively more depleted (Holocene state). A tri-part oscillatory transition arises between these two elements of the system (last glacial-interglacial transition).

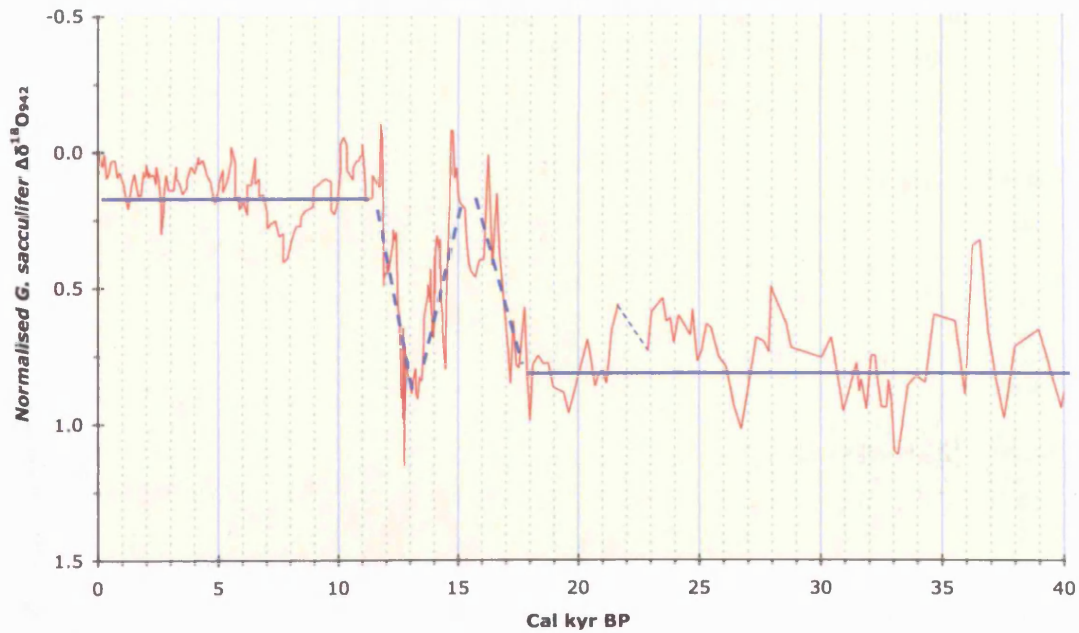


Figure 6.9: Graph of *G. sacculifer* (sac) $\delta^{18}\text{O}$ to illustrate the different system states in the isotopic signal.

The divisions between these system states within the $\Delta\delta^{18}\text{O}_{942}$ record coincide approximately with the defined climatic stages of the late Quaternary (after Blunier *et al.*, 1998; Blunier *et al.*, 1997; Mangerud *et al.*, 1974; ^{14}C ages calibrated using CALIB 5.0.1; Stuiver *et al.*, 2005):

- Last glacial period, Greenland Stadial-2: 40 to ~15 Cal ka (~40 to ~15 ^{14}C ka);
- Lateglacial Interstadial (Bølling/Allerød interstadial event, Greenland Interstadial-1; Northern Hemisphere); Antarctic Cold Reversal (ACR; Southern Hemisphere): ~15 to ~13 Cal ka (~13 to ~11 ^{14}C ka);
- Younger Dryas stadial event, Greenland Stadial-1: ~13 to ~11.5 Cal ka (~11 to ~10 ^{14}C ka);
- Holocene: ~11.5 Cal ka to present (10 ^{14}C ka to present).

The *G. ruber*, *G. sacculifer* sp. and *N. dutertrei* isotope records from ODP Site 942 can be subdivided into these periods, as shown in Figure 6.10, and discussed accordingly. The glacial-Holocene amplitude will also be discussed.

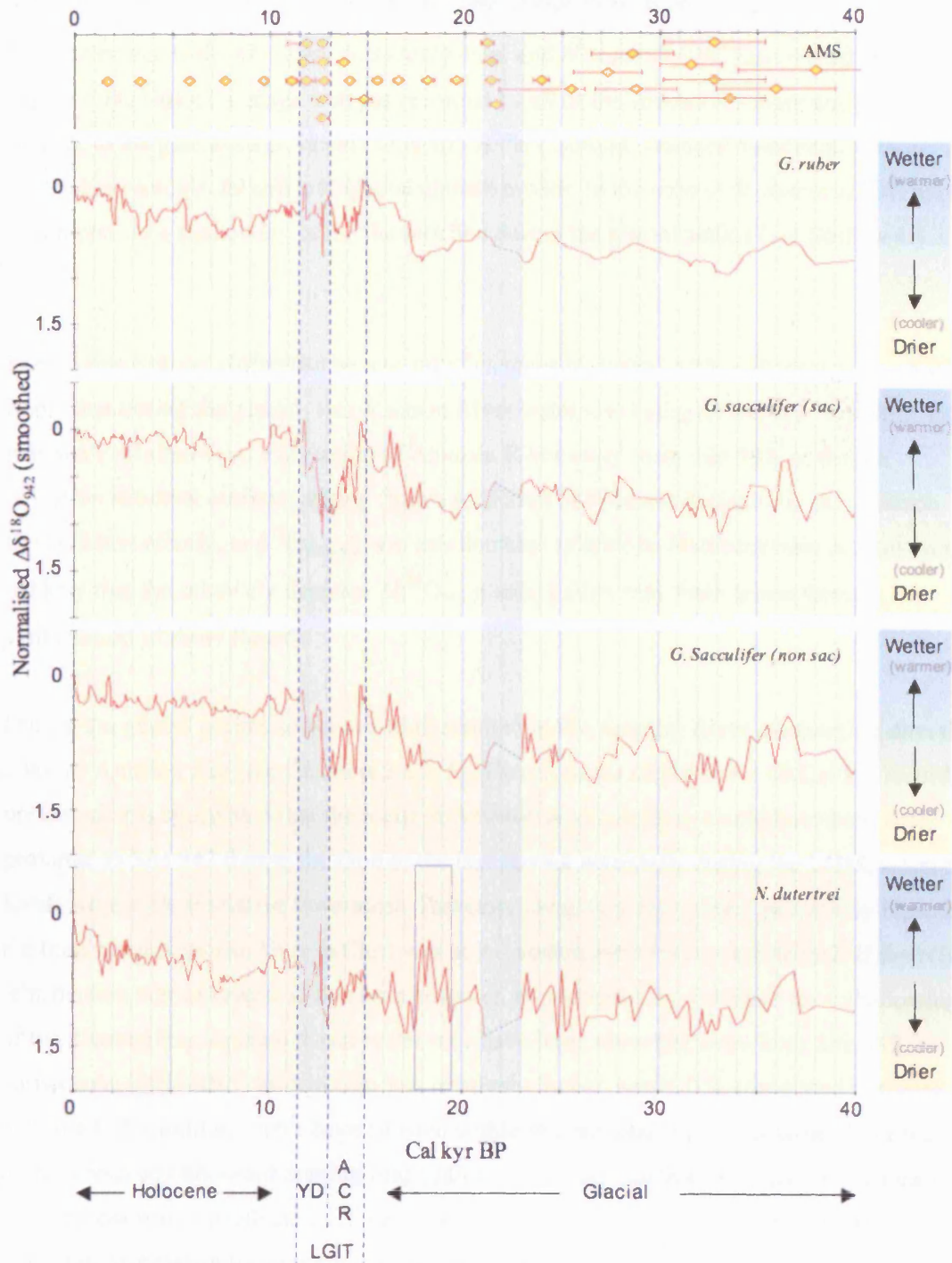


Figure 6.10: Composite smoothed $\Delta\delta^{18}\text{O}$ records for *G. ruber*, *G. sacculifer* sp. and *N. dutertrei*, plotted against Calendar years BP. Individual sample levels markers have been omitted for clarity. Yellow diamonds indicate the relative stratigraphic placement of AMS radiocarbon dates, with their respective error margins. All data were normalised against the stratigraphically most recent value to express change relative to modern (where modern = 1 Cal yr BP). Shading denotes the timeframes approximating to the last glacial maximum (~23 to ~21 Cal ka) and Younger Dryas (~13 to ~11.5 Cal ka). YD= Younger Dryas; ACR= Antarctic Cold Reversal; LGIT= Last Glacial-Interglacial Transition.

6.4.3 Interpretations of the Glacial-Holocene Amplitude in $\Delta\delta^{18}\text{O}_{942}$

With reference to the *G. ruber*, *G. sacculifer* sp. and *N. dutertrei* $\Delta\delta^{18}\text{O}_{942}$ records shown in Figure 6.10, Holocene stage isotopes recorded by all of the species are more depleted relative to the glacial stage values. This may reflect isotopic variance associated with the switch between glacial and interglacial climate modes. In the case of *N. dutertrei*, this may also represent a shallowing of the thermocline during the glacial period (see Section 6.4.2, above).

Should this isotopic difference be a result of changes in Amazon River discharge, it would imply that during the glacial, less Amazon River water was being mixed over Site 942. This may have resulted from a diversion of Amazon River away from Site 942, or from a reduction in actual outflow, arising from a reduction of effective moisture in the Amazon Basin. Alternatively, or $\delta^{18}\text{O}_{\text{Amazon}}$ was less depleted relative to Holocene values. However, it is likely that the relatively depleted $\Delta\delta^{18}\text{O}_{942}$ glacial values may have arisen through a combination of these factors.

During the glacial period, lower sea level resulted in the Amazon River discharging directly onto the Amazon Fan (see Chapters 2 and 5). Therefore out of the entire 40 Cal kyr record presented, it is speculated that the locus of Amazon River outflow would have been most proximal to Site 942 during the time of the last glacial, especially during the LGM, when sea levels were at their relative lowermost. Therefore the glacial record will potentially represent the time when Amazon River outflow was at its greatest influence over Site 942. If the NBC retroflection was enhanced at this time however, as supported by evidence for a shallowing of the thermocline, Amazon River water may have been advected away from Site 942, particularly if the NBC retroflection was relatively further south. It is speculated however, that Site 942 would still have been situated within the influence of the Amazon River plume, as numerous equator-ward moving ring eddies would have continued to have broken away from the eastward retroflection. Nevertheless, there would have been a potential net reduction of Amazon River water transported over Site 942, as the ring eddies are less efficient vectors of water relative to cross-equatorial ocean currents (see Chapter 2, Section 2.3.4).

However, changes in the volume of Amazon River outflow may also have been an important feature of the glacial period. In the modern day, Amazon freshwater mixes with tropical Atlantic water over the Amazon fan in the ratio 1:5 (Amazon:Atlantic; Levitus, 1982). Therefore should less Amazon water be mixed over the Site, the oceanic isotope signal

would become a relatively much more dominant influence, and lead to a relative enrichment in $\Delta\delta^{18}\text{O}_{942}$.

Furthermore, a reduction in Amazon River outflow would imply increased effective aridity in the Amazon Basin. The $\delta^{18}\text{O}$ of precipitation falling within the Amazon Basin could also become relatively enriched due to a reverse ‘amount’ effect, which could bring about an overall enrichment in the $\delta^{18}\text{O}$ of Amazon River water.

It has been estimated that glacial temperatures in the Amazon Basin were up to 5°C cooler than present, (e.g. Colinvaux *et al.*, 1996; Farrera *et al.*, 1999; Liu and Colinvaux, 1985; Stute *et al.*, 1995; see Chapter 4, Section 4.2). Although this would have led to a depletion in $\delta^{18}\text{O}_{\text{Amazon}}$ by ~1‰ (Dansgaard, 1964), should precipitation within the Amazon Basin have decreased, some of this isotopic change may be cancelled out by a reverse ‘amount effect’ (Grootes, 1993; Grootes *et al.*, 1989; Thompson *et al.*, 2000). The amount effect arises due to the initial preferential precipitation of the heavier isotope; therefore $\delta^{18}\text{O}$ will become increasingly depleted during periods of intense rainfall (Grootes *et al.*, 1989). With a reduction in rainfall, a *reverse* amount effect will impact $\delta^{18}\text{O}_{\text{Amazon}}$, whereby the reduced amount of water precipitated will be relatively more enriched in $\delta^{18}\text{O}$. For example, the relationship between monthly averages of rainfall amount and $\delta^{18}\text{O}_{\text{precip}}$ for Manaus, Brazil, indicates that a 50% reduction in precipitation would bring about an associated enrichment in $\delta^{18}\text{O}_{\text{precip}}$ of ~2‰ (International Atomic Energy Agency, 1992; Maslin and Burns, 2000). Therefore, despite cooler temperatures, $\delta^{18}\text{O}_{\text{Amazon}}$ could have become relatively more enriched during glacial times.

Given the scale of the proportion of Amazon River water relative to Atlantic water incorporated into the mixing ratio, the isotopic difference in the glacial $\Delta\delta^{18}\text{O}_{942}$ record could therefore have been driven by increased aridity (decreased effective moisture) in the Amazon Basin. Increased aridity would be marked by a reduction in river discharge, and a possible enrichment in the $\delta^{18}\text{O}$ of Amazon water, should the reverse amount effect have influence the $\delta^{18}\text{O}$ of Amazon Basin precipitation.

The $\Delta\delta^{18}\text{O}_{942}$ records have yet to be corrected for SST, however, which were cooler during the glacial stage. Cooler SSTs will account for some of the glacial enrichment observed in $\Delta\delta^{18}\text{O}_{942}$. The extent of glacial cooling in the western tropical Atlantic remains controversial, with estimates ranging from 0°C to $\geq 5^\circ\text{C}$ (e.g. Billups and Spero, 1996; CLIMAP Project Members, 1981; Dürkoop *et al.*, 1997; Guilderson *et al.*, 1994; Hastings *et al.*, 1998; Min *et*

al., 1995; Mix *et al.*, 1999; Niebler *et al.*, 2003; Rühlemann *et al.*, 2001; Wolff *et al.*, 1998). According to the palaeotemperature estimates of Epstein *et al.* (1953) and Craig (1965), this implies that SST cooling of $\sim 5^{\circ}\text{C}$ could account for up to $\sim +1\text{‰}$ of the glacial stage $\Delta\delta^{18}\text{O}_{942}$, which is a significant majority of the glacial-Holocene amplitude within each individual species' dataset.

Clearly, the SST effect would be of lesser impact with reduced estimations of glacial cooling: The smaller the glacial SST effect in the $\Delta\delta^{18}\text{O}_{942}$ signal, the greater the proportion of the isotopic depletion in $\Delta\delta^{18}\text{O}_{942}$ that must be accounted for by changes in the volume and/or isotopic signature of Amazon River water. Therefore it could be deduced that the colder the glacial SST, the less aridity is required in the Amazon Basin to attain the $\Delta\delta^{18}\text{O}_{942}$ records measured. Conversely, should SST cooling have been relatively minimal, the Amazon Basin must have been much more arid in order to attain the same $\Delta\delta^{18}\text{O}_{942}$ records measured. Down-core estimations of SST are therefore of great importance for deducing past variations in Amazon River outflow, and thus the effective moisture history of the Amazon Basin from $\Delta\delta^{18}\text{O}_{942}$ records. Interpretations of Amazon River outflow and the associated effective moisture history of the Amazon Basin should therefore also consider the isotopic effects of SST that are yet to be removed from the $\Delta\delta^{18}\text{O}_{942}$ signal.

6.4.4 Interpretations of the Glacial Records (40 to ~ 15 Cal kyr)

Unfortunately, the lack of foraminifera-specimens in glacial sediments between ~ 23 and ~ 21.5 Cal ka (~ 7.7 to ~ 7.1 mbsf; ~ 23 to ~ 21 Cal ka; ~ 7.7 to ~ 6.9 mbsf in the *N. dutertrei* record) creates a gap in the isotopic record (marked by hatched lines in the corresponding Figures). This is approximately coincident with the LGM, considered to have occurred at this time in other records from tropical South America (e.g. Baker *et al.*, 2001a; Baker *et al.*, 2001b; Cross *et al.*, 2001; Seltzer *et al.*, 2002). Sediment accumulation rates are not excessively high so as to dilute the marine flux of CaCO_3 during this period (see Chapter 5, Section 6.3.1). Instead, sediment accumulation rates are relatively low (~ 0.26 to ~ 0.33 m/ka⁻¹), comparable with other periods in the record when foraminiferal concentrations were not compromised. Showers and Bevis (1988) also noted a lack of foraminiferal tests in LGM sediments from the three sites they investigated on the Amazon Fan, suggesting it is a fan-wide phenomenon.

The lack of foraminifera in LGM sediments at Site 942 could be explained by a rise of the local lysocline and calcite compensation depth (CCD) at this time. During the sea level low

stand of the LGM, the flux of organic material carried by the Amazon River would have discharged directly onto the fan. As a result, this would have caused an increase in the amount of total organic carbon in the upper ocean, and thus an associated rise in the CCD (Williams *et al.*, 1998). Although no isotope data are available for the LGM exactly, it is speculated that intervening LGM $\delta^{18}\text{O}$ values would be of at least a similar enrichment as those data measured across all species during the glacial period, both prior to and immediately following the LGM.

The GIV-corrected records presented in Figures 6.8 and 6.10 contain varying amounts of noise in the data. The *G. ruber* $\Delta\delta^{18}\text{O}_{942}$ signal is the smoothest for the glacial portion of the record. This is surprising given that it is the shallowest-living of the species measured, and so is most likely to be isotopically affected by the numerous freshwater lenses that break off from the Amazon discharge plume (Flood and Piper, 1997). The degree of noise within the data appears to increase with the depth habitat of the species measured, possibly suggesting an increasingly stronger isotopic response to factors other than freshwater-driven changes in salinity, with depth from the surface. Overall however, the glacial $\Delta\delta^{18}\text{O}_{942}$ records are more depleted relative to Holocene values. The potential relevance of this glacial-Holocene amplitude was discussed in Section 6.4.3, above.

Within the 40 to ~18 Cal ka $\Delta\delta^{18}\text{O}_{942}$ records for *G. ruber*, *G. sacculifer* sp. and *N. dutertrei*, clear oscillation-like fluctuations can be seen, varying within a range of ~0.5‰. Between 40 and ~27 Cal ka, two distinct fluctuations are apparent in all four species records, with a periodicity of ~6 to 7 Cal ka. Between ~27 and 18 Cal ka, two quasi-periodic oscillations are arguably apparent in the *G. ruber* record, but of ~4 to 5 Cal ka duration. The extent to which the same two oscillations, or maybe a single oscillation of longer-duration also feature in each of the two *G. sacculifer* sp. and *N. dutertrei* records is difficult to confirm due to the paucity of samples around the time of the LGM.

According to calculations of the $\delta^{18}\text{O}$ -temperature relationship (Craig, 1965; Epstein *et al.*, 1953), fluctuations within a range of ~0.5‰ could represent variations in SST of ~2 to 2.5°C. However should these variations be attributed to changes in the amount of Amazon River water mixed over the site, it would imply there were alternating periods of enhanced and reduced freshwater input, according to whether $\Delta\delta^{18}\text{O}_{942}$ was relatively depleted or enriched, respectively. Reduced freshwater input may represent a decrease in Amazon River discharge (thus a reduction in the effective moisture availability in the Amazon Basin), or the increased transportation of the Amazon River discharge plume away from Site 942 by

surface ocean currents. Unfortunately, without SST data, it is unclear to what extent these oscillations might be related to the amount of Amazon River water mixed over Site 942.

The timing and nature of these variations in the data may correspond to the ‘Bond Cycles’ of clustered ‘Dansgaard-Oeschger’ events observed in polar ice core records (Bond *et al.*, 1993; Bond and Lotti, 1995; Dansgaard *et al.*, 1993). Heinrich Events (HE), occurring at the culmination of these cycles, were centred around ~38, ~25.6 and ~17 Cal ka (~27.6, ~21.4 and ~14.7 ^{14}C ka, respectively; Maslin, 1995). The most recent HE (H₁) may be coeval with the marked depletion in $\Delta\delta^{18}\text{O}_{942}$ at ~17.5 Cal ka, although low sample resolution and error margins in the 942 age model make it difficult to confirm the relative placement of the other HEs in the $\Delta\delta^{18}\text{O}_{942}$ records.

Between ~19.4 and ~17.9 Cal ka, there is a period of marked depletion (~-0.9‰) in the *N. dutertrei* record, where some of the most depleted values of the entire record are measured. As highlighted on Figure 6.10, this isotopically depleted phase is exclusive to the *N. dutertrei* record. From ~17.9 to ~17.5 Cal ka, there is a marked re-enrichment of comparable magnitude from ~-0.35‰, to near glacial-stage values of ~-1.35‰ (i.e. ~+1‰). Where relative isotopic depletion is a feature of the other records about this time, it is only very minor in comparison, and neither is there a comparative period of enrichment at the terminus of this stage. The *N. dutertrei* signal is clearly being influenced by a factor that is not affecting the other species’ records. The similarity between the other three records from species of shallower depth habitat would imply that the isotopic shift in the *N. dutertrei* record is not related to either SST, or the volume of Amazon River water reaching Site 942. This may represent a change in the ecological habitat of *N. dutertrei* therefore, possibly indicating a shallowing of the thermocline between ~19.4 and ~17.9 Cal ka (see Section 6.4.2).

The interval between ~17.5 to ~15 Cal ka, the end of the glacial stage is marked by a general trend of depletion within the $\Delta\delta^{18}\text{O}_{942}$ records. This period is approximately coincident with the Oldest Dryas period (14.5 to ~13 ^{14}C ka; Bradley, 1999), and also corresponds to a warming trend observed in the δD signal from the Vostock ice core record, prior to the onset of the ACR (Blunier *et al.*, 1998; Blunier *et al.*, 1997). By ~16.25 Cal ka, isotopic values measured on *G. sacculifer* sp. are comparable to those of the Holocene. From this initial peak in the $\Delta\delta^{18}\text{O}_{942}$ trend, records for *N. dutertrei* and *G. sacculifer* sp. enrich briefly for a period of ~500 to 700 Cal yr, respectively. This is approximately coincident with Meltwater Pulse 1a (MWP-1a, midpoint 13 ^{14}C ka; Mix, 1987; Mix and Ruddiman, 1985; or 15 to 15.5

Cal ka; ^{14}C ages calibrated using CALIB 5.0.1; Stuiver et al., 2005). Relatively minor coincident enrichment is noted in the *G. ruber* record, although it is not pronounced enough to punctuate significantly the underlying trend of depletion. Following MWP-1a, $\Delta\delta^{18}\text{O}_{942}$ values continue to show a depleting trend toward the Lateglacial Interstadial.

If the freshwater effects of the Amazon River forced this progressively more negative trend, it would imply that an increasing amount of Amazon water was reaching the site during the Oldest Dryas. However, climatic amelioration about this time is likely to have driven a coincident warming of SST, which could account for a proportion of this isotopic depletion observed in the $\Delta\delta^{18}\text{O}_{942}$ record.

6.4.5 Interpretations of the ~15 to ~13 Cal ka Records

As can be seen clearly in Figure 6.10, in the early stages of the Lateglacial Interstadial, $\Delta\delta^{18}\text{O}_{942}$ measured on *G. ruber* and *G. sacculifer* sp. attain some of the most isotopically depleted values of the last 40 Cal ka. Although there is a coincident negative excursion in the *N. dutertrei* record about this time, measured $\Delta\delta^{18}\text{O}_{942}$ values continue to remain relatively more enriched than those measured for the Holocene. Should the *G. ruber* and *G. sacculifer* sp. records be reflecting freshwater driven changes in salinity over the site, it would imply that the volume of Amazon River water being mixed in the overlying water column was comparable to that of the modern day.

It should also be noted that the relative depletion in the $\Delta\delta^{18}\text{O}_{942}$ record coincides with a marked increase in the sedimentation rate (SR) over the Site, and the appearance of plant matter in the lithostratigraphy (see Chapter 5, Section 5.3.1). This was hypothesised to have arisen from enhanced fan deposition within the vicinity of Site 942 (shown by blue shading in Figure 6.11). An increase in sediment discharge over the western fan complex could imply that the Amazon River freshwater plume was more directly influential over Site 942 at this time, whereby a greater amount of Amazon water was mixed over Site 942 relative to the unit volume discharged. This could therefore have the effect of biasing the isotope signal to more negative values, regardless of the amount of water discharged. However, the extent to which this isotopic depletion represents either a change in the relative influence of the Amazon River freshwater plume and/or a change in the outflow volume remains unclear.

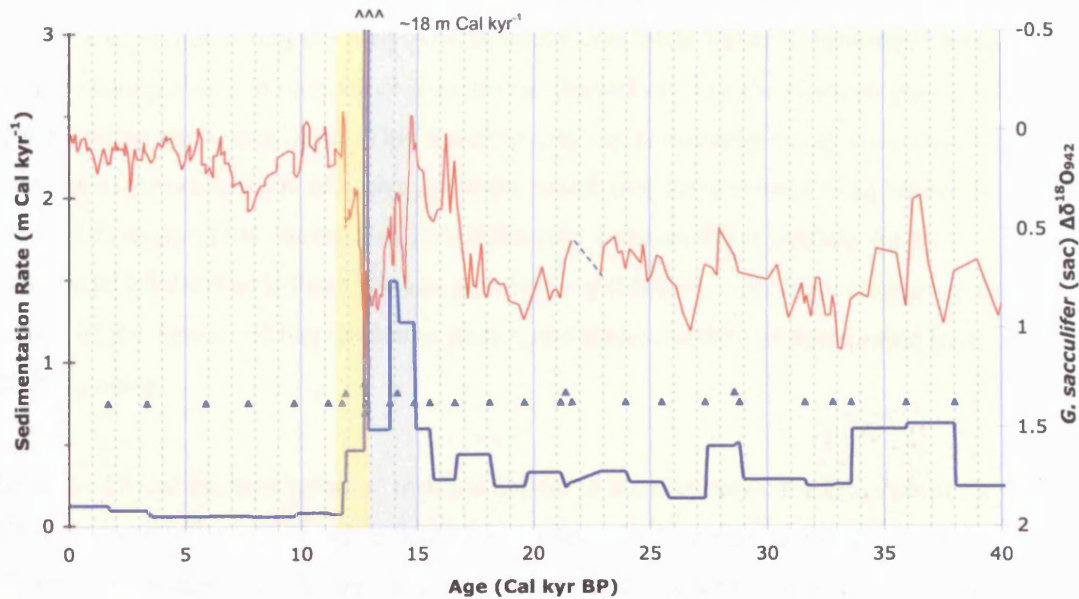


Figure 6.11: A comparison between sedimentation rates and *G. sacculifer* (sac) $\Delta\delta^{18}\text{O}_{942}$ at ODP Site 942. Blue and yellow shading denotes the Lateglacial Interstadial and Younger Dryas periods, respectively.

Thereafter, throughout the Lateglacial Interstadial, $\Delta\delta^{18}\text{O}_{942}$ records for all species oscillate about a more enriching trend toward the Younger Dryas. These oscillations correlate approximately with the three subdivisions defined within the Lateglacial Interstadial (after Mangerud *et al.*, 1974; ^{14}C ages calibrated using CALIB 5.0.1; Stuiver *et al.*, 2005);

- Bølling, ~15 to ~13.9 Cal ka (~13 to ~12 ^{14}C ka);
- Older Dryas, ~13.9 to ~13.7 Cal ka (~12 to ~11.8 ^{14}C ka);
- Allerød, ~13.7 to ~13 Cal ka (~11.8 to ~11 ^{14}C ka).

Although the Lateglacial Interstadial was generally apparent in the Northern Hemisphere as a warm phase, Antarctica may have been experiencing cooler climates at this time, during a stage referred to as the Antarctic Cold Reversal (Blunier *et al.*, 1998; Blunier *et al.*, 1997; see discussion in e.g. Maslin *et al.*, 2001; Sagnotti *et al.*).

Assuming $\Delta\delta^{18}\text{O}_{942}$ is reflecting the amount of isotopically depleted fresh water reaching Site 942, the progressive trend to more positive values implies an overall reduction in the amount of fresh water mixed over the Site. However, the SR also appears to vary with these climatic stages. Although the resolution of changes in SR is relatively low, limited by the down-core stratigraphic frequency of AMS dates measured, SR remains relatively elevated throughout the Bølling and Older Dryas (oscillating directly with $\Delta\delta^{18}\text{O}_{942}$), but then diminishes into the Allerød. The oscillations in $\Delta\delta^{18}\text{O}_{942}$ coupled with variations in SR throughout the Lateglacial Interstadial imply that the isotopic signal was driven at least in part by changes in

the relative influence of the Amazon River freshwater plume. Consequently, the transition in the $\Delta\delta^{18}\text{O}_{942}$ signal during the early Allerød could have been biased to apparently more positive values, due to a coincident reduction in the influence of the Amazon plume relative to the Bølling and Older Dryas. This therefore may not necessarily imply such a marked decrease of Amazon Basin effective moisture, which may have already been relatively reduced throughout the interstadial. Elucidating the Amazon River outflow for the Lateglacial Interstadial is therefore complicated by potentially coincident changes in the regime of the Amazon River discharge plume, and cannot readily be determined from $\Delta\delta^{18}\text{O}_{942}$ alone.

Toward ~13 Cal ka, most species' isotopes appear to be relatively enriched, except for *G. ruber*, for which there is a relative depletion. Unsmoothed isotope data from *G. ruber* (Figure 6.5a) suggest that this relative depletion in the *G. ruber* record is not an artefact of noise in the record. Assuming that the isotopic signals are monitoring the mixing between Amazon and Atlantic water over Site 942, this discrepancy between the species' records could therefore imply that the vertical zone of the mixing was restricted to a shallower depth in the water column at this time.

6.4.6 Interpretations of the ~13 to ~11 Cal ka Records

$\Delta\delta^{18}\text{O}_{942}$ records for the period 13 to 11.5 Cal ka are shown in greater detail in Figure 6.12. As the core material was sampled down-core on a linear basis, a short-lived phase of high sediment accumulation (~12.5 to ~18.3 m ka⁻¹) between ~12.8 and ~12.7 Cal ka has yielded a corresponding isotope record of high temporal resolution. This portion of the record is constrained by five AMS radiocarbon dates. $\Delta\delta^{18}\text{O}_{942}$ records from 13 to 12.5 Cal kyr are also shown in even greater detail in Figure 6.12 (right).

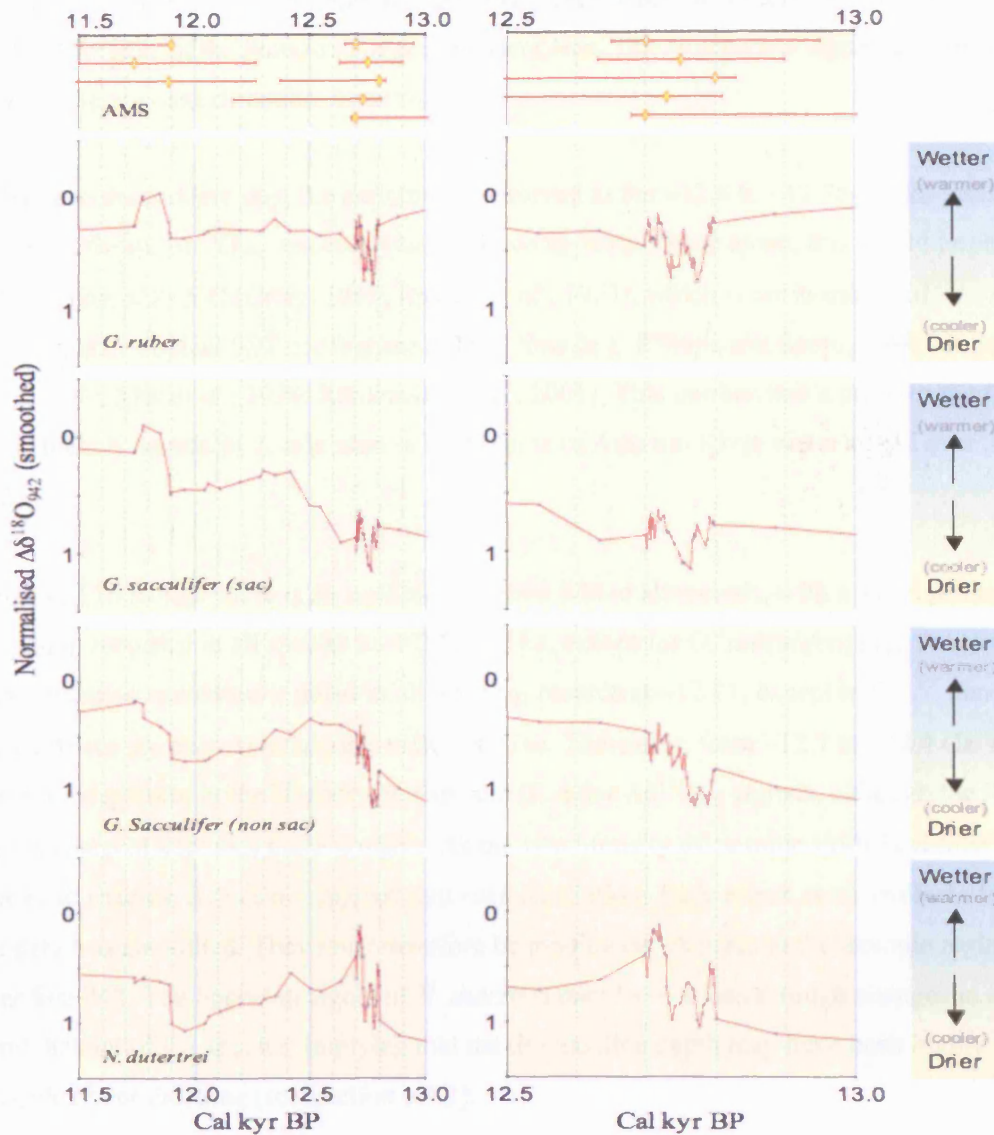


Figure 6.12: 13 to 11.5 Cal ka composite smoothed $\Delta\delta^{18}\text{O}$ records, for *G. ruber*, *G. sacculifer* sp. and *N. dutertrei*. Individual sample levels are shown with markers. The 13–12.5 Cal ka period is shown in more detail on the right. Yellow diamonds indicate the relative stratigraphic placement of AMS radiocarbon dates, with their respective error margins. All data were normalised against the stratigraphically most recent value to express change relative to modern (where modern = 1 Cal yr BP).

In this section of the $\Delta\delta^{18}\text{O}_{942}$ records, there is noticeable sequence in the isotope stratigraphy. From ~13 to ~12.8 Cal ka, the *G. ruber* signal becomes progressively more enriched, whereas the other species' records remain at relatively positive, but with a minor coincident depletion. Between ~12.8 and ~12.76 Cal ka however, *G. ruber* and *G. sacculifer* sp. $\Delta\delta^{18}\text{O}_{942}$ records exhibit a noticeable enrichment, where isotope values are amongst the most positive measured over the last 40 Cal ka. An oscillation is noticeable in the two *G. sacculifer* sp. records, but not so clearly in the *G. ruber* signal. This could perhaps be

attributed to the near-surface depth habitat of *G. ruber*, where it is more exposed to the depleting effects of the Amazon River freshwater lens. The *N. dutertrei* signal appears to trend in the opposite direction, however.

Relative to the modern day, the enrichment observed in the ~12.8 to ~12.76 Cal ka-section of *G. sacculifer* sp. $\Delta\delta^{18}\text{O}_{942}$, exceeds 1‰. If driven by temperature alone, this would imply a SST cooling of $\geq 5^\circ\text{C}$ (Craig, 1965; Epstein *et al.*, 1953), which is far in excess of reconstructed tropical SST cooling around this time (e.g. Billups and Spero, 1996; Dürkoop *et al.*, 1997; Mix *et al.*, 1999; Rühlemann *et al.*, 2001). This implies that a proportion of the enrichment is caused by a reduction in the volume of Amazon River water mixed over Site 942.

From ~12.76 to 12.7 there is an isotopic depletion within all records, with a small positive excursion recorded in all species at ~12.73 Cal ka, except for *G. sacculifer* (sac). A second minor positive excursion is noted in all $\Delta\delta^{18}\text{O}_{942}$ records at ~12.71, except in the *N. dutertrei* signal where the excursion appears to be negative. Thereafter, from ~12.7 to ~12.4 Cal ka, there is a depletion in the *G. sacculifer* sp. and *G. ruber* $\Delta\delta^{18}\text{O}_{942}$ signals, although the *N. dutertrei* signal becomes more positive. As the synchronicity of isotopic shifts is similar across all species, it does not suggest that such oscillations have arisen as an artefact of how the data was smoothed. They must therefore be monitoring changes in the isotopic regime over Site 942. The opposing signal of *N. dutertrei* may have arisen through changes in the depth habitat of the species, implying that the thermocline depth may have been highly variable about this time (see Section 6.4.2).

Overall, should the *G. ruber* and *G. sacculifer* sp. $\Delta\delta^{18}\text{O}_{942}$ be monitoring the outflow of the Amazon River, the relatively enriched $\Delta\delta^{18}\text{O}$ values of from ~12.8 to ~12.7 Cal ka would imply that the river was considerably reduced in volume relative to the modern day. This would imply a reduction in the effective moisture of the Amazon Basin. Sedimentation rates over Site 942 can support such a hypothesis. As shown in Figure 6.11, the sedimentation rate peaks sharply between 13 and 12.7 Cal ka, where accumulation at Site 942 reached levels as high as $\sim 18\text{m Cal ka}^{-1}$. This sedimentation peak is constrained by four AMS radiocarbon dates. Should the Amazon River discharge have been diminishing throughout this time, as suggested by the $\Delta\delta^{18}\text{O}_{942}$ record, the river would have had increasingly less energy available to transport its load. It would consequently have deposited sediment either in the floodplain, or relatively further inland on the exposed Amazon delta. This sedimentary regime could potentially have been enhanced during the annual dry season. The onset of the wet season,

and thus enhanced discharge (although still relatively reduced), could have subsequently debouched large volumes of this sediment, and have transported it out to the Atlantic, suspended in the Amazon freshwater plume. In this way, it is possible to account for a reduced freshwater discharge signal, yet a record of enhanced sediment supply over Site 942. Episodic periods of deposition/debauchment have been observed within the Amazon floodplain, where they are related to alternating periods of drought and flood associated with ENSO variability (e.g. Aalto *et al.*, 2003). Enhanced sedimentation over Site 942 at this time may also imply that the hydrographic setting was such that the Amazon River plume was discharging over the western fan complex, or that ocean currents were steering the trajectory of the plume toward Site 942.

The Younger Dryas (YD) stadial, as inferred from Northern Hemisphere records, is marked on Figure 6.11 as a band of yellow shading. The YD chronozone is defined as the period between 11 and 10 ¹⁴C ka (Mangerud *et al.*, 1974), which when calibrated, places it around 13 to 11.5 Cal ka (Stuiver *et al.*, 2005). Assuming records at Site 942 are monitoring the outflow of the Amazon River, the marked peak in sedimentation coupled with a positive excursion in the $\Delta\delta^{18}\text{O}_{942}$ across all species suggests the onset of a brief period of pronounced aridity at ~12.8 Cal ka; which may coincide with the cooling associated with the onset of the YD in northwest Europe.

However, Maslin and Burns (2000) suggested that the YD featured at a later stage in Amazon Fan record, between ~12.4 and ~11.9 Cal ka (see Figure 6.2). This positive excursion is clearly identifiable in all of the enhanced resolution species' records of this study, but is less pronounced in the *G. ruber* signal. This may represent a shallowing of the freshwater-mixed layer, although *G. ruber* $\Delta\delta^{18}\text{O}_{942}$ values are still relatively enriched at this time, suggestive of lesser depletion by fresh water. While this positive oscillation in the $\Delta\delta^{18}\text{O}_{942}$ records at ~12.4 to ~11.9 Cal ka falls within the timeframe ascribed to the YD stadial, the longer, higher resolution, and more chronologically constrained data presented in this study suggest that it was not the most isotopically enriched stage within this period.

The end of this 'within-YD' oscillation at ~11.78 Cal ka, is marked by an obvious negative excursion in the *G. ruber* and *G. sacculifer* sp. records. Isotope values measured for this stage are amongst the most negative of the entire record. This excursion is not apparent in the *N. dutertrei* record, however, suggesting it impacted the isotopic signal relatively higher up in the water column (or there was a change in the ecological habitat of *N. dutertrei*). Assuming $\Delta\delta^{18}\text{O}_{942}$ was not recording a short-lived warming of SST, it may reflect the

depleting influence of the Amazon River outflow, either by an increase in the volume of freshwater reaching the site, or even a depletion of the $\delta^{18}\text{O}$ value of Amazon River water itself. It is interesting to note, however, that this also appears to be the time corresponding to when terrestrial sedimentation ceased at Site 942, and fan accumulation switched 'off' (see Figure 6.11).

6.4.7 Interpretations of the Holocene Records (~11 Cal ka to Present)

Throughout the Holocene, the isotope signals for all species fluctuate about relatively more depleted values relative to the glacial period. This may be related to changes in the amount of Amazon River freshwater mixing over Site 942, or to glacial-interglacial changes in SST, or a combination of the two (see Section 6.4.3).

Across all species records shown in Figure 6.10, a slight positive excursion in $\Delta\delta^{18}\text{O}_{942}$ between ~10.8 and ~10.6 Cal ka coincides approximately with Meltwater Pulse 1b (MWP-1b, midpoint 9.5 ^{14}C ka; Mix, 1987; Mix and Ruddiman, 1985; or ~10.8 to ~10.6 Cal ka; ^{14}C ages calibrated using CALIB 5.0.1; Stuiver et al., 2005). Thereafter, between the early- and mid-Holocene, records take on a slightly concave (positive) trend. This period is broadly simultaneous with the Holocene 'thermal maximum' (HTM), associated with wetter conditions in Africa (COHMAP Members, 1988; deMenocal *et al.*, 2000a; deMenocal *et al.*, 2000b). If $\Delta\delta^{18}\text{O}_{942}$ were monitoring the outflow of the Amazon River at this time, it would imply that there was a decrease in Amazon Basin effective moisture (i.e. increased aridity) coeval with a humid phase in Africa. From the HTM to the present, $\Delta\delta^{18}\text{O}_{942}$ values become progressively depleted, which may reflect a progressive increase in effective moisture in the Amazon Basin from the mid-Holocene to the modern day. SSTs are also likely to have varied throughout this time, however, and may thus account for some of the trend observed in the $\Delta\delta^{18}\text{O}_{942}$.

It should also be noted that $\Delta\delta^{18}\text{O}_{942}$ values appear to oscillate throughout the Holocene. Although more noticeable in the *G. ruber* and *G. sacculifer* (sac) records, all species' records appear to 'pulse' about a quasi-periodic cyclicality of ~1500 to 2000 years, particularly after ~7 to 7.5 Cal ka, approximately coincident with the proposed onset of increased ENSO activity in northern South America (Martin *et al.*, 1993; Moy *et al.*, 2002; Rodbell *et al.*, 1999). Much attention has been focussed recently on quasi-cyclic 'Dansgaard-Oeschger'-like trends in Holocene concentrations of drift-ice deposits in the North Atlantic, identified by Bond *et al.* (2001). These trends were purported to relate to variations in the surface winds

and surface hydrography of the subpolar North Atlantic region, associated with millennial-scale changes in solar output. Evidence upon which this hypothesis is based remains controversial, however (see discussion in Maslin *et al.*, 2003). Upon comparison, assuming a robust chronology for each dataset, the records of $\Delta\delta^{18}\text{O}_{942}$ and drift-ice deposit concentrations do not appear to directly co-vary, although some similarity is noted from ~ 2.6 Cal ka to present (see Figure 6.13). An equivalent magnitude of change in drift-ice debris concentrations between the early and late Holocene is not noted in the $\Delta\delta^{18}\text{O}_{942}$ record, however.

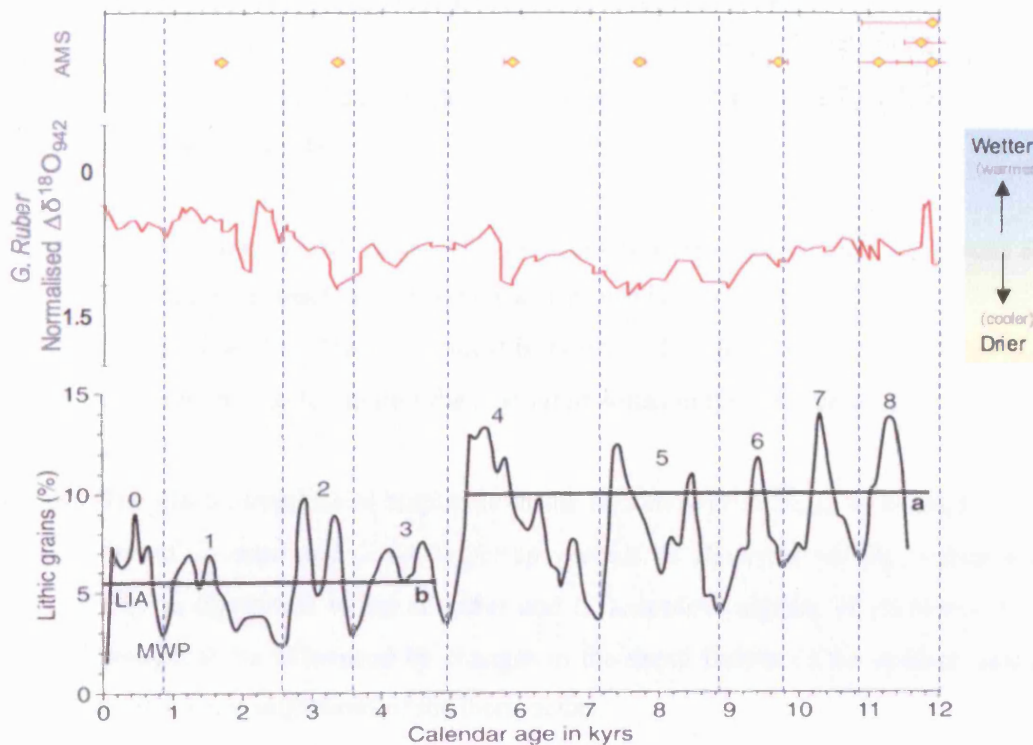


Figure 6.13: a comparison between *G. ruber* $\Delta\delta^{18}\text{O}_{942}$ and the Bond *et al.* (2001) stacked record of drift-ice deposits expressed as a percentage of ice-rafted lithic grains in the 63 to 150 μm size range (modified from Maslin *et al.*, 2003).

6.5 Summary of the Qualitative Interpretations of the $\Delta\delta^{18}\text{O}_{942}$ records

The key points can be summarised as follows:

- $\delta^{18}\text{O}$ was measured on five foraminifera species representative of water column depths ranging from the surface, to the thermocline and sub-thermocline: *G. ruber*; *G. sacculifer* (sac); *G. sacculifer* (non sac); *N. dutertrei*; and *G. truncatulinoides*.
- $\delta^{18}\text{O}_{942}$ values were ‘corrected’ for global ice volume effects by using $\delta^{18}\text{O}_{\text{GIV}}$ inferred from sea level change curves (Fairbanks, 1989; Shackleton, 1987). $\Delta\delta^{18}\text{O}_{942}$

data were normalised against the stratigraphically most recent sample to express isotopic shifts relative to modern, and minimise the vital effects between the species. The calculation of $\Delta\delta^{18}\text{O}_{942}$ is based upon the assumption that the calendar age chronologies of $\delta^{18}\text{O}_{942}$ and $\delta^{18}\text{O}_{\text{GIV}}$ have been established correctly.

- It was not possible to incorporate a correction for SST effects into $\Delta\delta^{18}\text{O}_{942}$ due to the paucity of reliable, comparably high-resolution SST estimates from the region. However, SST estimates are essential to isolate the shift in $\delta^{18}\text{O}_{942}$ associated with freshwater-driven changes in salinity over the Amazon Fan.
- A lack of foraminifera in LGM sediments is ascribed to a temporary rise in the lysocline and CCD.
- A deep depth-habitat, combined with the effects associated with small sample size measurements mask the Amazon water-driven isotopic changes in the *G. truncatulinoides* $\delta^{18}\text{O}_{942}$ records. It is therefore difficult to use $\Delta\delta^{18}\text{O}_{942}$ from *G. truncatulinoides* to monitor the amount of Amazon fresh water mixed over Site 942.
- The glacial-interglacial amplitude in the *N. dutertrei* $\Delta\delta^{18}\text{O}_{942}$ is markedly less than that of *G. ruber* and *G. sacculifer* sp. records. *N. dutertrei* $\Delta\delta^{18}\text{O}_{942}$ values also covary in opposition to the *G. ruber* and *G. sacculifer* signals. *N. dutertrei* $\delta^{18}\text{O}_{942}$ is thought to be influenced by changes in the depth habitat of the species, associated with vertical migrations of the thermocline.
- Relatively enriched glacial $\Delta\delta^{18}\text{O}_{942}$ values may imply reduced mixing of Amazon freshwater over Site 942. If this were reflective of Amazon River discharge, it would suggest a reduction of effective moisture (precipitation-evaporation) in the Amazon Basin. However, the isotopic enrichment may also have been driven by cooler SSTs, or increased transport of Amazon River water away from Site 942 by surface ocean currents.
- Quasi-periodic oscillations in the glacial $\Delta\delta^{18}\text{O}_{942}$ records may be related to Bond Cycles and Heinrich Events, however large errors associated with the radiocarbon dates make this difficult to confirm. Without SST records, it is also difficult to determine to what extent these 'oscillations' are driven by Amazon freshwater mixed over Site 942.

-
- There is a notable depletion in all species' $\Delta\delta^{18}\text{O}_{942}$ records at ~ 17.5 Cal ka, coincident with the onset of the Oldest Dryas, and a period of warming in Antarctica.
 - The Lateglacial Interstadial/ACR is a period marked by increasing enrichment in $\Delta\delta^{18}\text{O}_{942}$ values. Should this be driven by changes in Amazon River outflow, it would imply that the Amazon Basin had relatively low levels of effective moisture at this time. Enhanced sedimentation rates coincident with this period also imply that the Amazon River plume was discharging directly over the Western Fan Complex, and therefore more proximal to Site 942.
 - A sharp positive excursion arises in all isotope records at ~ 12.8 to ~ 12.76 Cal ka, coincident with a sharp peak in sedimentation rates ($\sim 18 \text{ m ka}^{-1}$). This is hypothesised to mark a period of very reduced Amazon River discharge, where sediments deposited inland during the dry season are debauched during the wet season and transported in the plume toward Site 942. These features in the isotopic and sediment stratigraphy of 942 may be coeval with rapid cooling associated with the onset of the Younger Dryas in northwest Europe.
 - Based upon the shorter, lower-resolution $\Delta\delta^{18}\text{O}_{942\text{C}}$ record, Maslin *et al.* (2000) and Maslin and Burns (2000) hypothesised that the positive isotopic oscillation between ~ 12.5 and 12 Cal ka was equivalent to the YD. This, however, is not the isotopically most depleted portion of the record. The timing of this oscillation coincides with a warming phase in Antarctica (e.g. Blunier *et al.*, 1998; Blunier *et al.*, 1997).
 - A negative excursion at ~ 11.78 Cal ka coincides with cessation of terrestrial deposition at Site 942. This may therefore reflect changes in fan-related hydrography, rather than a meltwater discharge from the Andes, as suggested by Maslin *et al.* (2000) and Maslin and Burns (2000).
 - MWP-1a and MWP-1b are apparent in the $\Delta\delta^{18}\text{O}_{942}$ records as positive excursions from ~ 15.5 to ~ 15 Cal ka, and ~ 10.8 to ~ 10.6 Cal ka, respectively.
 - Overall, Holocene $\Delta\delta^{18}\text{O}_{942}$ values are depleted relative to the glacial, and become relatively more depleted to the present day. This may be representative of a
-

progressive increase in the amount of Amazon water mixed over Site 942, however warmer SSTs may also account for a portion of the depletion in the signal.

- $\Delta\delta^{18}\text{O}_{942}$ displays a relative enrichment during the Holocene ‘thermal maximum’. Should $\Delta\delta^{18}\text{O}_{942}$ serve as a proxy for effective moisture in the Amazon Basin, it would imply that there was increased aridity in the Amazon Basin, coincident with a relatively humid phase in Africa (COHMAP Members, 1988; deMenocal *et al.*, 2000a; deMenocal *et al.*, 2000b).
- Quasi-periodic oscillations in Holocene $\Delta\delta^{18}\text{O}_{942}$ data, particularly after ~ 7 Cal ka appear to be relatively dissimilar to the ‘Dansgaard-Oeschger’-type cycles observed within stacked records of drift-ice debris in the North Atlantic, although some covariance is noted for the last ~ 2.6 Cal kyr. However, the trend may be related to the onset of ENSO activity over South America (Moy *et al.*, 2002; Rodbell *et al.*, 1999).

6.6 References

- Aalto, R., Maurice-Bourgoin, L., Dunne, T., Montgomery, D. R., Nittrouer, C. A., and Guyot, J. L. (2003). Episodic sediment accumulation on Amazonian flood plains influenced by El Niño/Southern Oscillation. *Nature* **245**, 493-497.
- Anand, P., Elderfield, H., and Conte, M. H. (2003). Calibration of Mg/Ca thermometry in planktonic foraminifera from a sediment trap time series. *Paleoceanography* **18**, 1050-1065.
- Arz, H. W., Patzold, J., and Wefer, G. (1998). Correlated Millennial-Scale Changes in Surface Hydrography and Terrigenous Sediment Yield Inferred from Last-Glacial Marine Deposits off Northeastern Brazil. *Quaternary Research* **50**, 157-166.
- Arz, H. W., Patzold, J., and Wefer, G. (1999). The deglacial history of the western tropical Atlantic as inferred from high resolution stable isotope records off northeastern Brazil. *Earth and Planetary Science Letters* **167**, 105-117.
- Baker, P. A., Rigsby, C. A., Seltzer, G. O., Fritz, S. C., Lowenstein, T. K., Bacher, N. P., and Veliz, C. (2001a). Tropical climate changes at millennial and orbital timescales on the Bolivian Altiplano. *Nature* **409**, 698-701.
- Baker, P. A., Seltzer, G. O., Fritz, S. C., Dunbar, R. B., Grove, M. J., Tapia, P. M., Cross, S. L., Rowe, H. D., and Broda, J. P. (2001b). The History of South American Tropical Precipitation for the Past 25,000 Years. *Science* **291**, 640-643.
- Billups, K., and Spero, H. J. (1996). Reconstructing the stable isotope geochemistry and paleotemperatures of the equatorial Atlantic during the last 150,000 years: Results from individual foraminifera. *Paleoceanography* **11**, 217-238.

-
- Blunier, T., Chappellaz, J., Schwander, J., Dällenbach, A., Stauffer, B., Stocker, T., Raynaud, D., Jouzel, J., Clausen, H. B., Hammer, C. U., and Johnsen, S. J. (1998). Asynchrony of Antarctic and Greenland climate change during the last glacial period. *Nature* **384**, 739-743.
- Blunier, T., Schwander, J., Stauffer, B., Stocker, T., Dällenbach, A., Indermühle, A., Tschumi, J., Chappellaz, J., Raynaud, D., and Barnola, J.-M. (1997). Timing of the Antarctic Cold Reversal and the atmospheric CO₂ increase with respect to the Younger Dryas event. *Geophysical Research Letters* **24**, 2683-2686.
- Bond, G., Kromer, B., Beer, J., Muscheler, R., Evans, M. N., Showers, W. J., Hoffmann, S., Lotti-Bond, R., Hajdas, I., and Bonani, G. (2001). Persistent Solar Influence on North Atlantic Climate During the Holocene. *Science* **294**, 2130-2136.
- Bond, G. C., Broecker, W., Johnsen, S., McManus, J., Labeyrie, L., Jouzel, J., and Bonani, G. (1993). Correlations between climate records from North Atlantic sediments and Greenland ice. *Nature* **365**, 143-147.
- Bond, G. C., and Lotti, R. (1995). Iceberg discharge into the North Atlantic on millennial time scales during the Last Glaciation. *Science* **267**, 1005-1010.
- Bradley, R. S. (1999). "Paleoclimatology: Reconstructing Climates of the Quaternary." Harcourt Academic Press, San Deigo.
- CLIMAP Project Members. (1981). Seasonal reconstruction of the Earth's surface at the Last Glacial Maximum. *Geological Society of America Chart and Map Series* 36.
- COHMAP Members. (1988). Climatic changes of the last 18000 years; observations and model simulations. *Science* **241**, 1043-1052.
- Colinvaux, P. A., De Oliveira, P. E., Moreno, J. E., Miller, M. C., and Bush, M. B. (1996). A long pollen record from lowland Amazonia: forest and cooling in glacial times. *Science* **274**, 85-88.
- Craig, H. (1965). The measurement of oxygen isotope paleotemperature. In "Proceedings of the Spoleto conference on Stable Isotopes in Oceanographic Studies and Paleotemperatures." pp. 3-24. Consiglio Nazionale delle Richerche Geologia Nucleare, Pisa.
- Cross, S. L., Baker, P. A., Seltzer, G. O., Fritz, S. C., and Dunbar, R. B. (2001). Late Quaternary Climate and Hydrology of Tropical South America Inferred from an Isotopic and Chemical Model of Lake Titicaca, Bolivia and Peru. *Quaternary Research* **56**, 1-9.
- Dansgaard, W. (1964). Stable Isotopes of Precipitation. *Tellus* **16**, 436-469.
- Dansgaard, W., Johnson, S. J., Clausen, H. B., Dahl-Jensen, D., Gundenstrup, N. S., Hammer, C. U., Hvidberg, C. S., Seffensen, J. P., and Sveinbjörnsdóttir. (1993). Evidence for general instability of past climate from 250-kyr ice-core record. *Nature* **364**, 218-220.
- deMenocal, P., Oritz, J., Guilderson, T., and Sartnthein, M. (2000a). Coherent high- and low-latitude climate variability during the Holocene Warm period. *Science* **288**, 2198-2202.
-

-
- deMenocal, P., Ortiz, J., Guilderson, T. P., Adkins, J., Sarnthein, M., Baker, L., and Yarusinsky, M. (2000b). Abrupt onset and termination of the African Humid Period; rapid climate responses to gradual insolation forcing. *Quaternary Science Reviews* **19**, 347-361.
- Deuser, W. G. (1987). Seasonal variation in isotopic composition and deep water fluxes of the tests of perennially abundant planktonic foraminifera of the Sargasso Sea: Results of sediment trap collections and their paleoceanographic implications. *Journal of Foraminiferal Research* **19**, 268-293.
- Duplessy, J.-C., Lalou, C., and Vinot, A. C. (1970). Differential isotopic fractionation in benthic foraminifera and paleotemperatures re-assessed. *Science* **168**, 250-251.
- Dürkoop, A., Hale, W., Mulitza, S., Pätzold, J., and Wefer, G. (1997). Late Quaternary variations of sea surface salinity and temperature in the western tropical Atlantic: Evidence from $\delta^{18}\text{O}$ of Globigerinoides sacculifer. *Paleoceanography* **12**, 764-772.
- Emiliani, C. (1954). Depth habitats of some species of pelagic foraminifera as indicated by oxygen isotope ratios. *American Journal of Science* **252**, 149-158.
- Emiliani, C. (1969). A new micropaleontology. *Micropaleontology* **15**, 265-300.
- Epstein, S., Buchsbaum, R., Lowenstam, H. A., and Urey, H. C. (1953). Revised carbonate-water isotopic temperature scale. *Geological Society of America Bulletin* **64**, 1315-1326.
- Erez, J., and Luz, B. (1982). Temperature control of oxygen-isotope fractionation of cultured planktonic foraminifera. *Nature* **297**, 220-222.
- Fairbanks, R. G. (1989). A 17,000 year glacio-eustatic sea level record: influence of glacial melting rates on the Younger Dryas event and deep-ocean circulation. *Nature* **362**, 637-642.
- Farrera, I., Harrison, S. P., Prentice, I. C., Ramstein, G., Guiot, J., Bartlein, P. J., Bonnefille, R., Bush, M., Cramer, W., von Grafenstein, U., Holmgren, K., Hooghiemstra, H., Hope, G., Jolly, D., Lauritzen, S. E., Ono, Y., Pinot, S., Stute, M., and Yu, G. (1999). Tropical climates at the Last Glacial Maximum: a new synthesis of terrestrial palaeoclimate data. I. Vegetation, lake-levels and geochemistry. *Climate Dynamics* **15**, 823-856.
- Flood, R. D., and Piper, D. W. J. (1997). Amazon Fan sedimentation: the relationship to equatorial climate change, continental denudation, and sea-level fluctuations. In "Proceedings of the Ocean Drilling Program, Scientific Results, Vol. 155." (R. D. Flood, D. J. W. Piper, A. Klaus, and L. C. Peterson, Eds.), pp. 653-675, College Station, TX (Ocean Drilling Program).
- Greig, S. (1998). "Site 942 on the Amazon Fan: stable isotopes and sea surface temperatures." Unpublished MSc thesis, Royal Holloway University of London.
- Grootes, P. M. (1993). Interpreting continental oxygen isotope records. In "Climate Change in Continental Isotopic Records, Vol. 78." (P. K. Swart, K. C. Lohmann, J. McKenzie, and S. Savin, Eds.), pp. 37-46. AGU, Washington.
-

-
- Grootes, P. M., Stuiver, M., Thompson, L. G., and Mosley-Thompson, E. (1989). Oxygen Isotope Changes in Tropical Ice, Quelccaya, Peru. *Journal of Geophysical Research* **94**, 1187-1194.
- Guilderson, T. P., Fairbanks, R. G., and Rubenstone, J. L. (1994). Tropical temperature variations since 20,000 years ago: modulating interhemispheric climate change. *Science* **263**, 663-665.
- Hastings, D. W., Russell, A. D., and Emerson, S. R. (1998). Foraminiferal magnesium in *Globoquadrina sacculifer* as a paleotemperature proxy. *Paleoceanography* **13**, 161-169.
- Hecht, A. D., and Savin, S. M. (1972). Phenotypic variation and oxygen isotope ratios in recent planktonic foraminifera. *Journal of Foraminiferal Research* **2**, 55-67.
- Hilbrecht, H. (1996). "Extant planktic foraminifera and the physical environment in the Atlantic and Indian Oceans - Mitteilungen aus dem Geologischen Institut der Eidgen. Technischen Hochschule und der Universität Zürich, Neue Folge. No. 300." Zürich.
- International Atomic Energy Agency. (1992). "Statistical Treatment of Data on Environmental Isotopes in Precipitation, Technical Reports Series No. 331." IAEA, Vienna.
- Levitus, S. (1982). Climatological Atlas of the World Ocean, Professional Paper 13. National Ocean and Atmosphere Administration (NOAA).
- Liu, K., and Colinvaux, P. A. (1985). Forest Changes in the Amazon Basin during the Last Glacial Maximum. *Nature* **318**, 556-557.
- Lowe, J. J., and Walker, M. J. C. (1997). "Reconstructing Quaternary Environments." Longman, Harlow.
- Mangerud, J., Andersen, S. T., Berglund, B. E., and Donner, J. J. (1974). Quaternary stratigraphy of Norden: a proposal for terminology and classification. *Boreas* **3**, 109-127.
- Martin, L., Fournier, M., Mourguiart, P., Sifeddine, A., Turq, B., Absy, M. L., and Flexor, J. M. (1993). Southern oscillation signal in South American palaeoclimate data of the last 7000 years. *Quaternary Research* **39**, 338-346.
- Maslin, M., Pike, J., Stickley, C., and Ettwein, V. (2003). Evidence of Holocene Climate Variability in Marine Sediments. In "Global Change In The Holocene." (A. Mackay, R. Battarbee, J. Birks, and F. Oldfield, Eds.), pp. 185-209. Arnold, London.
- Maslin, M. A. (1995). "A Study of the Palaeoceanography of the N.E. Atlantic in the Late Pleistocene." PhD thesis, University of Cambridge.
- Maslin, M. A. (1998). Equatorial Western Atlantic Ocean circulation changes linked to the Heinrich Events: deep-sea sediment evidence from the Amazon Fan. In "Geological Evolution of the Ocean Basins: Results from the Ocean Drilling Program." (A. Cramp, C. J. McLeod, S. Lee, and E. J. W. Jones, Eds.), pp. 111-127. Geological Society of America, Special Publications 131.
-

-
- Maslin, M. A., and Burns, S. J. (2000). Reconstruction of the Amazon Basin effective moisture availability over the past 14,000 years. *Science* **290**, 2285-2287.
- Maslin, M. A., Durham, E., Burns, S. J., Platzman, E., Grootes, P., Greig, S. E. J., Nadeau, M. J., Schleicher, M., Pflaumann, U., Lomax, B., and Rimington, N. (2000). Palaeoreconstruction of the Amazon River freshwater and sediment discharge using sediments recovered at site 942 on the Amazon Fan. *Journal of Quaternary Science* **15**, 419-434.
- Maslin, M. A., Seidov, D., and Lowe, J. (2001). Synthesis of the Nature and Causes of Rapid Climate Transitions During the Quaternary. In "The Oceans and Rapid Climate Change: Past, Present and Future." (D. Seidov, B. J. Haupt, and M. Maslin, Eds.), pp. 9-50. American Geophysical Union, Washington DC.
- Microsoft Corporation. (2004). Microsoft® Excel 2004 for Mac®.
- Min, G., Edwards, R. L., Taylor, F. W., Recy, J., Gallup, C. D., and Beck, J. W. (1995). Annual cycles of U/Ca in coral skeletons and U/Ca thermometry. *Geochimica et Cosmochimica Acta* **59**, 2025-2042.
- Mix, A. C. (1987). The oxygen isotope record of glaciation. In "The Geology of North America, Volume K-3: North America and Adjacent Oceans During the Last Deglaciation." (W. F. Ruddiman, and H. E. Wright Jr., Eds.), pp. 111-135. Geological Society of America, Boulder, CO.
- Mix, A. C., Morey, A. E., Pisias, N. G., and Hostetler, S. W. (1999). Foraminiferal faunal estimates of paleotemperature: circumventing the no-analogue problem yields cool ice age tropics. *Paleoceanography* **14**, 350-359.
- Mix, A. C., and Ruddiman, W. F. (1985). Structure and timing of the last deglaciation; oxygen isotope evidence. *Quaternary Science Reviews* **4**, 59-108.
- Moy, C. M., Seltzer, G. O., Rodbell, D. T., and Anderson, D. M. (2002). Variability of El Nino/Southern Oscillation activity at millennial timescales during the Holocene epoch. *Nature* **420**, 162-165.
- Niebler, H.-S., Arz, H. W., Donner, B., Mulitza, S., Pätzold, J., and Wefer, G. (2003). Sea surface temperatures in the equatorial and South Atlantic Ocean during the Last Glacial Maximum (23-19 ka). *Paleoceanography* **18**, 14.1-14.12.
- Ravelo, A. C., and Fairbanks, R. G. (1992). Oxygen isotopic composition of multiple species of planktonic foraminifera: Recorders of the modern photic zone temperature gradient. *Paleoceanography* **9**, 943-972.
- Rodbell, D. T., Seltzer, G. O., Anderson, D. M., Abbott, M. B., Enfield, D. B., and Newman, J. H. (1999). An ~15,000-Year Record of El Nino-Driven Alluviation in Southwestern Ecuador. *Science* **283**, 516-520.
- Rühlemann, C., Diekmann, B., Mulitza, S., and Frank, M. (2001). Late Quaternary changes of western equatorial Atlantic surface circulation and Amazon lowland climate recorded in Ceara Rice deep-sea sediments. *Paleoceanography* **16**, 293-305.
- Sagnotti, L., Macri, P., Camerlenghi, A., and Rebesco, M. (2001). Environmental magnetism of Antarctic Late Pleistocene sediments and interhemispheric correlation of climatic events. *Earth and Planetary Science Letters* **192**, 65.
-

-
- Seltzer, G. O., Rodbell, D. T., Baker, P. A., Fritz, S. C., Tapia, P. M., Rowe, H. D., and Dunbar, R. B. (2002). Early Warming of Tropical South America at the Last Glacial-Interglacial Transition. *Science* **296**, 1685-1686.
- Shackleton, N. J. (1987). Oxygen isotopes, ice volume and sea level. *Quaternary Science Reviews* **6**, 183-190.
- Shackleton, N. J., Wiseman, J. D. H., and Buckley, H. A. (1973). Non-equilibrium isotopic fractionation between sea-water and planktonic foraminiferal tests. *Nature* **242**, 177-179.
- Showers, W. J., and Bevis, M. (1988). Amazon cone isotopic stratigraphy: Evidence for the source of the tropical freshwater spike. *Palaeogeography, Palaeoclimatology, Palaeoecology* **64**, 189-199.
- Stuiver, M., Reimer, P. J., and Reimer, R. W. (2005). CALIB 5.0. <http://radiocarbon.pa.qub.ac.uk/calib/calib.html>.
- Stute, M., Forster, M., Frischkorn, H., Serejo, A., Clark, J. F., Schlosser, P., Broecker, W. S., and Bonani, G. (1995). Cooling of Tropical Brazil (5°C) during the Last Glacial Maximum. *Science* **269**, 379-383.
- Thompson, L. G., Mosley-Thompson, E., and Henderson, K. A. (2000). Ice-core palaeoclimate records in tropical South America since the Last Glacial Maximum. *Journal of Quaternary Science* **15**, 377-394.
- Trauth, M. H. (1995). "Bioturbate Signalverzerrung hochauflösender palaoozeanographischer Zeitreihen (Bioturbation signal distortion of high resolution time-series)." PhD Thesis, Universität Kiel (Geologische und Paleontologische Institute).
- Williams, M., Dunkerley, D., De Deckker, P., Kershaw, P., and Chappell, J. (1998). "Quaternary Environments." Arnold, London.
- Wolff, T., Mulitza, S., Arz, H. W., and Wefer, G. (1998). Oxygen isotopes versus CLIMAP (18 ka) temperatures: a comparison from the tropical Atlantic. *Geology* **26**, 675-678.

7: SEMI-QUANTITATIVE RECONSTRUCTION OF PAST CHANGES IN AMAZON RIVER OUTFLOW

7.1 Introduction

At the present time, Amazon and Atlantic waters mix over ODP Site 942 in the ratio 1:5 (Levitus, 1982). The average isotopic signal of the Amazon water is -5‰ (Grootes, 1993; Thompson *et al.*, 2000), whereas the average tropical Atlantic signal is $+1\text{‰}$ (Arz *et al.*, 1998; Arz *et al.*, 1999; Maslin, 1998). Consequently, $\delta^{18}\text{O}_{942}$ will be comprised of a combination of these two isotopic signals, blended in proportion to the mixing ratio over the Site 942. The modern freshwater-mixing scenario over Site 942 can therefore be expressed as:

$$\delta^{18}\text{O}_{942} = (1 \times \delta^{18}\text{O}_{\text{Amazon}}) + (5 \times \delta^{18}\text{O}_{\text{Atlantic}})$$

$$\text{i.e. } \delta^{18}\text{O}_{942} = (1 \times -5\text{‰}) + (5 \times +1\text{‰}) = 0\text{‰}$$

Clearly, the freshwater mixing ratio will change should the relative proportions of each water mass vary at a given time. However, providing the $\delta^{18}\text{O}_{\text{Amazon}}$ and $\delta^{18}\text{O}_{\text{Atlantic}}$ are known variables (or can be realistically assumed), it should be possible to infer the relative proportions of each water mass mixed from the resulting $\delta^{18}\text{O}_{942}$. Should the amount of freshwater mixed over Site 942 be directly proportional to the outflow of the Amazon River, it should therefore be possible to estimate past variations in freshwater discharge, relative to the modern day. This semi-quantified estimation should also serve as a proxy for effective moisture in the Amazon Basin. However, such quantitative estimations should also be viewed with caution due to the assumptions made in the model, as discussed throughout this chapter.

7.2 Quantifying the Isotopic Fractionation Effects

When attempting to semi-quantify past changes in the outflow of the Amazon River, Maslin *et al.*, (2000) and Maslin and Burns (2000) utilised the down-core $\Delta\delta^{18}\text{O}_{942\text{C}}$ record calculated from $\delta^{18}\text{O}_{942\text{C}} - \delta^{18}\text{O}_{\text{GeoB 3104-1}}$ to serve as a proxy for $\delta^{18}\text{O}_{\text{Amazon}}$ (see Chapter 6, Section 6.1). However, in using this method to remove the combined ‘marine’ isotopic effects of GIV, SST and background surface ocean salinity (SOS) from the record, it was assumed that the relative fractionation effects of these variables would be manifested in equal proportions over the two sites at any given time period, regardless of the non-‘marine’-fractionated continental freshwater isotopic inputs at Site 942. The only impact on both the

freshwater and the Atlantic components of $\delta^{18}\text{O}_{942}$ signal should be SST effects, as fractionation would have occurred after the freshwater mixing has taken place.

Figure 7.1 illustrates the estimated modern hydrographic scenario in the surface waters over Site 942. Under the modern mixing scenario, the Atlantic Ocean contributes approximately 5/6 of the surface water over Site 942, and the Amazon River approximately 1/6 (Levitus, 1982). Assuming a constant mixing ratio, it would imply that a change in $\delta^{18}\text{O}_{\text{Atlantic}}$ will impact only 83% (5/6) of the total $\delta^{18}\text{O}_{942}$. At GeoB 3104-1 however, a change in $\delta^{18}\text{O}_{\text{Atlantic}}$ would impact the entire $\delta^{18}\text{O}_{\text{GeoB 3104-1}}$ value, as the signal is assumed to be 100% marine. Therefore the fractionation effects associated with each component of the water mass at Site 942 will only influence $\delta^{18}\text{O}_{942}$ in direct proportion to the amount of each component mixed. This is of significance when accounting for past GIV fractionation effects impacting $\delta^{18}\text{O}_{\text{Atlantic}}$, which constitute relatively large shifts in $\delta^{18}\text{O}$ (e.g. $\sim 1.2\text{‰}$ during the LGM; Fairbanks, 1989; Shackleton, 1987; see Chapter 6, Section 6.3.4, and Figure 6.7). As the GIV effects would not have been constant between the two sites, the method employed by Maslin *et al.* (2000) and Maslin and Burns over-compensates for the GIV effects impacting $\Delta\delta^{18}\text{O}_{942}$. The isolation of the freshwater-driven shift in $\delta^{18}\text{O}$ is therefore not as straightforward as previously assumed.

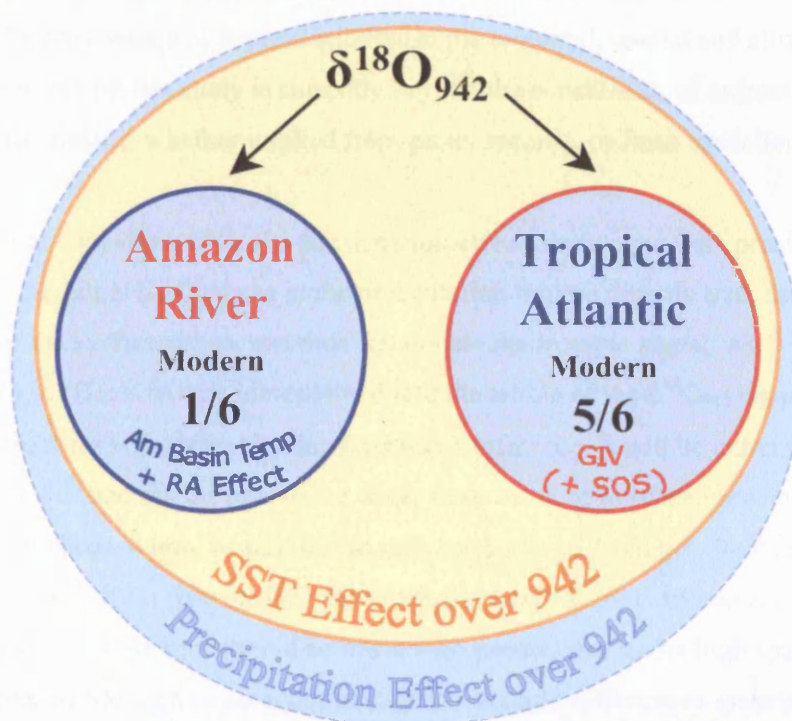


Figure 7.1: Factors influencing the tropical Atlantic and Amazon River components of the $\delta^{18}\text{O}_{942}$ signal, as well as those influencing the overall $\delta^{18}\text{O}_{942}$ ('RA Effect' = Reverse Amount Effect; 'GIV' = Global Ice Volume; 'SOS' = Surface Ocean Salinity; 'SST' = Sea Surface Temperature).

Similarly, any factors affecting the freshwater component of the isotopic signal will only influence $\delta^{18}\text{O}_{942}$ in direct proportion to the amount of Amazon River water mixed in the water column. With reference to Figure 7.1, The freshwater component of the $\delta^{18}\text{O}_{942}$ signal ($\delta^{18}\text{O}_{\text{Amazon}}$) will be influenced by factors fractionating the $\delta^{18}\text{O}$ of precipitation, including Amazon Basin temperature (Dansgaard, 1964), and a reverse ‘amount’ effect (see Section 6.4.3; Grootes, 1993; Grootes *et al.*, 1989; Thompson *et al.*, 2000). Amazon Basin palaeotemperature data can be obtained from published records (see Chapter 4, Section 4.2) and the associated fractionation effects can be calculated using $\delta^{18}\text{O}$ -temperature equations (e.g. Craig, 1965; Epstein *et al.*, 1953). The relationship between monthly averages of rainfall amount and $\delta^{18}\text{O}_{\text{precip}}$ for Manaus, Brazil, indicates that a 50% reduction in precipitation would bring about an associated enrichment in $\delta^{18}\text{O}_{\text{precip}}$ of $\sim 2\text{‰}$ (International Atomic Energy Agency, 1992; Maslin and Burns, 2000). It should therefore be possible to account for the reverse amount effect in $\delta^{18}\text{O}_{\text{Amazon}}$ through an iterative process.

Other factors influencing $\delta^{18}\text{O}_{\text{Amazon}}$ will be the initial isotopic signature of precipitation, which will be influenced by factors such as the source location of the water vapour (Vuille *et al.*, 2003a; Vuille *et al.*, 2003b), the altitude of droplet formation (Dansgaard, 1964), and the extent of recycling of precipitation across the Amazon Basin (Salati *et al.*, 1979). However, identifying the provenance of the precipitation at the temporal, spatial and altitudinal resolution required by this study is currently beyond the capabilities of current available palaeo-reconstructions; whether implied from proxy records, or from modelling experiments.

A final factor to consider will be the fractionation effects associated with precipitation directly over the Site 942. Changes in the precipitation regime directly over the site will alter the salinity of the surface ocean, and thus fractionate the isotopic signal. As for SST effects, the precipitation effects will be incorporated into the whole of the $\delta^{18}\text{O}_{942}$ signal. However at Site 942 where there is a strong riverine freshwater influence, it will be extremely difficult to distinguish the dilution effects of riverine water from those of overhead precipitation. For individual time slices, it may be possible to infer such effects from proximal records sufficiently isolated from riverine influence (e.g. the Ceara Rise; Dürkoop *et al.*, 1997). However, such extrapolations should be made with caution due to the high spatial variability of precipitation within a given area, not to mention isotopic differences associated with the different hydrographies at each location.

Such distinctions between the different isotopic fractionation effects of the freshwater and marine water masses of Site 942 are of relatively lesser importance when making qualitative

assessments of Amazon River outflow. Nevertheless, they become of increasingly greater significance when formulating a mathematical model to semi-quantify Amazon River outflow from the varying freshwater and marine components of the $\delta^{18}\text{O}_{942}$ record. However, a new mathematical Amazon River outflow model can be developed which attempts to account for the relative proportions of different isotopic fractionation effects in $\delta^{18}\text{O}_{942}$.

7.3 Construction of the Amazon River Outflow Model

The past outflow of the Amazon River, expressed as a percentage relative to modern flow (where modern = 100%), can be quantified using the algebraic equation detailed below, variables of which are defined in Table 7.1.

Part 1: calculating $\Delta\delta^{18}\text{O}_{942(t-kyr)}$

$$\Delta\delta^{18}\text{O}_{942(t-kyr)} = \left(\delta^{18}\text{O}_{Amazon(t-kyr)} \times \frac{1}{x} \right) + \left(\delta^{18}\text{O}_{Atlantic(t-kyr)} \times \frac{(x-1)}{x} \right)$$

i.e. for 'modern' (assumed 100% outflow)

$$\Delta\delta^{18}\text{O}_{942(t)} = \left(\delta^{18}\text{O}_{Amazon(t)} \times \frac{1}{x} \right) + \left(\delta^{18}\text{O}_{Atlantic(t)} \times \frac{(x-1)}{x} \right)$$

$$\Delta\delta^{18}\text{O}_{942(t)} = \left(\delta^{18}\text{O}_{Amazon(t)} \times \frac{1}{6} \right) + \left(\delta^{18}\text{O}_{Atlantic(t)} \times \frac{(6-1)}{6} \right)$$

$$\Delta\delta^{18}\text{O}_{942(t)} = \left(-5\text{‰} \times \frac{1}{6} \right) + \left(1\text{‰} \times \frac{5}{6} \right)$$

$$\Delta\delta^{18}\text{O}_{942(t)} = 0\text{‰}$$

Part 2: Calculating percentage change in outflow relative to modern

$$\% \text{ change in outflow}_{(t-kyr)} = \left(\frac{\text{'change' in } \Delta\delta^{18}\text{O}_{942}}{\text{'original' } \Delta\delta^{18}\text{O}_{942}} \right) \times 100$$

i.e.:

$$\% \text{ change in outflow}_{(t-kyr)} = \left(\frac{\Delta\delta^{18}\text{O}_{942 \text{ 0:6 mixing } (t-kyr)} - \Delta\delta^{18}\text{O}_{942(t-kyr)}}{\Delta\delta^{18}\text{O}_{942 \text{ 0:6 mixing } (t-kyr)} - \Delta\delta^{18}\text{O}_{942 \text{ 1:5 mixing } (t-kyr)}} \right) \times 100$$

Variable Name	Description
$\Delta\delta^{18}\text{O}_{t\text{-kyr}}$	$\Delta\delta^{18}\text{O}$ at time t-kyr
$\Delta\delta^{18}\text{O}_{1:5\ t\text{-kyr}}$	$\Delta\delta^{18}\text{O}$ of 1:5 (Amazon:Atlantic) mixing over 942 at time period in question (i.e. equivalent of ‘modern’ 100% outflow)
$\Delta\delta^{18}\text{O}_{0:6\ t\text{-kyr}}$	$\Delta\delta^{18}\text{O}$ of 0:6 (Amazon:Atlantic) mixing over 942 at time period in question (i.e. $\delta^{18}\text{O}_{\text{Atlantic}}$)
$\delta^{18}\text{O}_{\text{Atlantic}\ t\text{-kyr}}$	$\delta^{18}\text{O}$ of the Atlantic at the time period in question
$\delta^{18}\text{O}_{\text{Amazon}\ t\text{-kyr}}$	$\delta^{18}\text{O}$ of the Amazon River water at the time period in question
t-kyr	Time period in question
x:y	Mixing ratio of waters over Site 942, Amazon:Atlantic

Table 7.1: Definition of variables used in the Amazon River outflow model.

The integrity of the model was validated against a series of hypothetical scenarios where all input and calculated variables were already known. Given that the isotopic boundary conditions will differ under previous climate regimes, it is first necessary to calculate the $\Delta\delta^{18}\text{O}$ value representative of 100% river outflow for the new time period investigated. This ‘100% outflow’ would represent modern-day outflow within the context of the different isotopic regimes being reconstructed. Modelled outflow can then be calculated relative to ‘100% outflow’, and expressed as a percentage of ‘modern flow’.

7.4 Variables Used in the Refined Outflow Model

Until there are reconstructions of sufficient resolution for variables such as local SST and Amazon Basin temperature, continuous down-core semi-quantitative reconstructions of past Amazon River outflow are not possible. However, data exists for the LGM, and the YD to allow these time-slices to be modelled (see Chapter 4, Section 4.2). It is speculated that similar climatic conditions would have prevailed during the Antarctic Cold Reversal (ACR), although this is uncertain. Nevertheless, it is still possible to attempt to reconstruct the ACR using these assumed climatic variables.

Published climate variable data for the LGM and YD reconstructions and their relative isotopic effects are summarised in Table 7.2. These data were used to ‘adjust’ the relevant isotopic input variables accordingly (i.e. normalised $\delta^{18}\text{O}_{942}$, modern $\delta^{18}\text{O}_{\text{Amazon}}$, and modern $\delta^{18}\text{O}_{\text{Atlantic}}$). The extent of glacial cooling in the western tropical Atlantic in the region of the Amazon Fan has been a subject of long-standing debate in the literature, however, with considerable variation in the published estimations. Therefore it was necessary to run the

model under a variety of SST scenarios to investigate the relative effects of different SST cooling estimates on modelled Amazon River outflow. All calculations were based on the modern mixing ratio of 1:5 (Amazon:Atlantic) and modern isotopic signatures of -5‰ and +1‰ for the Amazon and Atlantic, respectively (see above). Temperature fractionation effects were calculated using the equations of e.g. Craig (1965), and Epstein (1953). The reverse amount (RA) effect on $\delta^{18}\text{O}_{\text{Amazon}}$ was determined by initially running the model with no RA effect. The model output was used to derive the RA effect by an iterative process, which was input back into the model, and output values were re-calculated.

Climatic Variable	Isotopic Effect on $\delta^{18}\text{O}_{942}/\delta^{18}\text{O}_{\text{Atlantic}}/\delta^{18}\text{O}_{\text{Amazon}}$	References
GIV Effect	YD: +0.94 ‰ ACR: +0.99 ‰ LGM: +1.20 ‰	(Fairbanks, 1989; Shackleton, 1987)
SST	0 to 2°C cooling = +0 to +0.46 ‰	(e.g. Billups and Spero, 1996; CLIMAP Project Members, 1981; Dürkoop <i>et al.</i> , 1997).
	2 to 4°C cooling = +0.46 to +0.92 ‰	(e.g. Arz <i>et al.</i> , 1998; Arz <i>et al.</i> , 1999; Hastings <i>et al.</i> , 1998; Min <i>et al.</i> , 1995; Mix <i>et al.</i> , 1999; Niebler <i>et al.</i> , 2003; Rühlemann <i>et al.</i> , 2001; Wolff <i>et al.</i> , 1998).
	4 to 5 °C cooling = +0.92 to +1.15 ‰	(e.g. Guilderson <i>et al.</i> , 1994).
Amazon Basin Temperature Effect	4 to 5°C cooling = -1‰	(e.g. Colinvaux <i>et al.</i> , 1996; Dansgaard, 1964; Farrera <i>et al.</i> , 1999; Liu and Colinvaux, 1985; Pierrehumbert, 1999; Rind and Peteet, 1985; also see Chapter 3 Stute <i>et al.</i> , 1995)
Reverse Amount Effect (derived through an iterative process)	Variable, based on reduction of 50% modern precipitation = ~+2‰	(e.g. Grootes, 1993; International Atomic Energy Agency, 1992; Maslin and Burns, 2000; Thompson <i>et al.</i> , 2000)

Table 7.2: Published palaeoclimate variables and their associated isotopic fractionation effects.

The *G. sacculifer* sp. $\delta^{18}\text{O}_{942}$ records were selected for the outflow calculation. The *G. sacculifer* sp. records appear to be sufficiently isolated from the numerous freshwater lenses that formed at the surface, and the depth habitat of the species is thought to have remained relatively consistent throughout the downcore record, relatively unaffected by changes in the depth of the thermocline. The two records measured on this species also compare well to

each other, confirming that variations in the isotope signals are relatively unaffected by noise. $\delta^{18}\text{O}_{942}$ data used in the model calculations were based on average values for the time periods represented. This also helps to address the chronological issues arising from the choice of marine reservoir correction used to calibrate the radiocarbon dates in the age model for Site 942 (see Chapter 5, Section 5.1.2).

Although no isotope data exists for the actual LGM, $\delta^{18}\text{O}_{942}$ values used in the model were inferred averages for the time period 21 to 22 Cal ka. YD $\delta^{18}\text{O}_{942}$ values selected represent average values during the isotopically most enriched stage from ~12.9 to 12.7. ACR $\delta^{18}\text{O}_{942}$ values selected represent the isotopically enriched period from ~13 to ~13.5 Cal ka. Model calculations were performed using Microsoft Excel 2005 for Apple Macintosh (Microsoft Corporation, 2004).

7.5 Amazon River Outflow Model Results

The input variables and model output for *G. sacculifer* (sac) and *G. sacculifer* (non sac) are summarised in Tables 7.3 and 7.4, respectively. Model results for both species are summarised in Table 7.5.

	Time period	Cal kyr BP	Normalised $\delta^{18}\text{O}_{942}$	Amazon Basin Temperature Effect (‰)	Calculated Amazon Basin RA Effect (‰)	SST Scenario	SST Effect (‰)	GIV Effect (‰)	% Outflow Relative to Modern	% Change in Outflow
No RA effect	YD	12.9-12.7	1.85	1.00	-	-2°C	0.46	0.94	42	-58
	YD	12.9-12.7	1.85	1.00	-	-3°C	0.69	0.94	59	-41
	YD	12.9-12.7	1.85	1.00	-	-4°C	0.92	0.94	76	-24
	YD	12.9-12.7	1.85	1.00	-	-5°C	1.15	0.94	94	-6
With RA effect	YD	12.9-12.7	1.85	1.00	2.79	-2°C	0.46	0.94	59	-41
	YD	12.9-12.7	1.85	1.00	2.10	-3°C	0.69	0.94	74	-26
	YD	12.9-12.7	1.85	1.00	1.40	-4°C	0.92	0.94	87	-13
	YD	12.9-12.7	1.85	1.00	0.71	-5°C	1.15	0.94	97	-3
No RA effect	ACR	13-13.5	1.82	1.00	-	-2°C	0.46	0.99	47	-53
	ACR	13-13.5	1.82	1.00	-	-3°C	0.69	0.99	65	-35
	ACR	13-13.5	1.82	1.00	-	-4°C	0.92	0.99	82	-18
	ACR	13-13.5	1.82	1.00	-	-5°C	1.15	0.99	99	-1
With RA effect	ACR	13-13.5	1.82	1.00	2.71	-2°C	0.46	0.99	64	-36
	ACR	13-13.5	1.82	1.00	2.02	-3°C	0.69	0.99	79	-21
	ACR	13-13.5	1.82	1.00	1.33	-4°C	0.92	0.99	90	-10
	ACR	13-13.5	1.82	1.00	0.64	-5°C	1.15	0.99	100	0
No RA effect	LGM	21-22	1.80	1.00	-	-2°C	0.46	1.20	63	-37
	LGM	21-22	1.80	1.00	-	-3°C	0.69	1.20	80	-20
	LGM	21-22	1.80	1.00	-	-4°C	0.92	1.20	97	-3
	LGM	21-22	1.80	1.00	-	-5°C	1.15	1.20	113	13
With RA effect	LGM	21-22	1.80	1.00	2.07	-2°C	0.46	1.20	77	-23
	LGM	21-22	1.80	1.00	1.40	-3°C	0.69	1.20	88	-12
	LGM	21-22	1.80	1.00	0.72	-4°C	0.92	1.20	98	-2
	LGM	21-22	1.80	1.00	0.05	-5°C	1.15	1.20	106	+6

Table 7.3: Amazon River outflow model input variable, and output data for *G. sacculifer* (sac).

Time period	Cal kyr BP	SST Scenario	<i>G. sacculifer</i> (sac)		<i>G. sacculifer</i> (non sac)		Average	
			% Outflow Relative to Modern	% Change in Outflow	% Outflow Relative to Modern	% Change in Outflow	% Outflow Relative to Modern	% Change in Outflow
YD	12.9-12.7	-2°C	59	-41	47	-53	53	-47
YD	12.9-12.7	-3°C	74	-26	65	-35	69	-31
YD	12.9-12.7	-4°C	87	-13	79	-21	83	-17
YD	12.9-12.7	-5°C	97	-3	90	-10	94	-6
ACR	13-13.5	-2°C	64	-36	49	-51	57	-43
ACR	13-13.5	-3°C	79	-21	66	-34	72	-28
ACR	13-13.5	-4°C	90	-10	80	-20	85	-15
ACR	13-13.5	-5°C	100	0	91	-9	95	-5
LGM	21-22	-2°C	77	-23	65	-35	71	-29
LGM	21-22	-3°C	88	-12	78	-22	83	-17
LGM	21-22	-4°C	98	-2	90	-10	94	-6
LGM	21-22	-5°C	106	+6	99	-1	103	+3

Table 7.5: Summary of Amazon River outflow model output for *G. sacculifer* (both sac forms).

With reference to Table 7.5, the model produces similar statistics for each of the *G. sacculifer* species, although *G. sacculifer* (sac) reconstructions are more conservative, associated with the relatively more depleted $\delta^{18}\text{O}_{942}$ input data. The model output suggests that the extent of SST cooling in the tropical Atlantic is a crucial variable in the calculation of the Amazon River outflow model. The greater the extent of SST cooling, the smaller the modelled change in Amazon River outflow. However, this does not imply that tropical Atlantic SST is forcing Amazon River outflow, as the ‘relationship’ is an artefact of the isotopic balance between the fractionation effects comprising $\delta^{18}\text{O}_{942}$.

Should LGM SSTs have cooled by 5°C, as suggested by Guilderson *et al.* (1994), the model output suggests that there was little change in Amazon River outflow, possibly even an increase. This implies that the Amazon Basin was potentially as humid as the modern day, if not slightly more. However, this is in conflict with sedimentary palaeoclimate reconstructions, which suggest that the Amazon Basin was relatively more arid during glacial times (see Chapter 4).

The majority of glacial tropical Atlantic SST reconstructions have centred around a more conservative cooling of between 2 and 3(-4)°C. Similar cooling was hypothesised from GeoB 3104-1 records (Arz *et al.*, 1998; Arz *et al.*, 1999), and is further supported by the coarse resolution SIMMAX SST reconstruction at Site 942 (Greig, 1998). Glacial SST cooling of 2-3°C yields an approximate 20 to 30% reduction in Amazon River outflow, relative to modern flow (averaged from both species). Should YD SSTs have cooled by a similar amount during the YD, Amazon River outflow is reconstructed to have reduced by approximately 20 to 50 %. This implies that the Amazon Basin was relatively more arid during the hypothesised YD (~12.9 to ~12.7 Cal ka) than during the LGM.

Lack of tropical Atlantic SST data and reconstructions of temperature within the Amazon Basin during the ACR makes it difficult to assess the modelled change in Amazon River outflow for these time periods. However, should continental and sea surface temperatures have been cooler, Amazon River outflow would have been reduced. More data is clearly required to enable reconstructions for the time period corresponding to the ACR.

Interestingly, if the refined model is run with $\delta^{18}\text{O}_{942}$ values corresponding to the section of the record assumed by Maslin *et al.* (2000) and Maslin and Burns (2000) to represent the YD (~12.4 to ~12 Cal ka), the predicted reduction in Amazon River outflow relative to modern is 10 to 21% (with a SST cooling of 2 to 3°C). This is considerably less than the 40 to 50% reduction initially hypothesised by Maslin *et al.* (2000) and Maslin and Burns (2000) for this time period, and therefore implies that effective moisture in the Amazon Basin was less depleted in the later stages of the YD, relative to the onset. Furthermore, this prediction was computed around a brief period of isotopically more enriched values, so the model predictions should be regarded as conservative.

The input variables and model output for *G. sacculifer* (sac) and *G. sacculifer* (non sac) for the period ~12.4 to ~12 Cal ka are summarised in Tables 7.6 and 7.7, respectively. Model results for both species are summarised in Table 7.8.

	No RA effect			With RA effect		
Time period	"YD"	"YD"	"YD"	"YD"	"YD"	"YD"
Cal kyr BP	12.4-12	12.4-12	12.4-12	12.4-12	12.4-12	12.4-12
Normalised $\delta^{18}\text{O}_{942}$	1.21	1.21	1.21	1.21	1.21	1.21
Amazon Basin Temperature Effect (‰)	1.00	1.00	1.00	1.00	1.00	1.00
Calculated Amazon Basin RA Effect (‰)	-	-	-	0.90	0.19	-0.52
SST Scenario	-2°C	-3°C	-4°C	-2°C	-3°C	-4°C
SST Effect (‰)	0.46	0.69	0.92	0.46	0.69	0.92
GIV Effect (‰)	0.75	0.75	0.75	0.75	0.75	0.75
% Outflow Relative to Modern	77	95	113	88	98	106
% Change in Outflow	-23	-5	13	-12	-2	6
	31					13

Table 7.6: Amazon River outflow model input variable, and output data for *G. sacculifer* (sac), for the time period 12.4 to 12 Cal ka.

	No RA effect			With RA effect		
Time period	"YD"	"YD"	"YD"	"YD"	"YD"	"YD"
Cal kyr BP	12.4-12	12.4-12	12.4-12	12.4-12	12.4-12	12.4-12
Normalised $\delta^{18}\text{O}_{942}$	1.46	1.46	1.46	1.46	1.46	1.46
Amazon Basin Temperature Effect (‰)	1.00	1.00	1.00	1.68	0.97	0.25
Calculated Amazon Basin RA Effect (‰)	-	-	-	0.90	0.19	-0.52
SST Scenario	-2°C	-3°C	-4°C	-2°C	-3°C	-4°C
SST Effect (‰)	0.46	0.69	0.92	0.46	0.69	0.92
GIV Effect (‰)	0.75	0.75	0.75	0.75	0.75	0.75
% Outflow Relative to Modern	58	76	94	74	87	97
% Change in Outflow	-42	-24	-6	-26	-13	-3
	+11					105

Table 7.7: Amazon River outflow model input variable, and output data for *G. sacculifer* (non sac), for the time period 12.4 to 12 Cal ka.

Time period	Cal kyr BP	SST Scenario	<i>G. sacculifer</i> (sac)		<i>G. sacculifer</i> (non sac)		Average	
			% Outflow Relative to Modern	% Change in Outflow	% Outflow Relative to Modern	% Change in Outflow	% Outflow Relative to Modern	% Change in Outflow
"YD"	12.4-12	-2°C	88	-12	74	-26	81	-19
"YD"	12.4-12	-3°C	98	-2	87	-13	92	-8
"YD"	12.4-12	-4°C	106	6	97	-3	101	1
"YD"	12.4-12	-5°C	113	13	105	+5	109	9

Table 7.8: Summary of Amazon River outflow model output for *G. sacculifer* (both sac forms), for the time period 12.4 to 12 Cal ka.

7.6 Limitations of the Amazon River Outflow Model

Despite the fact that it has been able to reconstruct past changes in Amazon River outflow, the model is based on a number of assumptions that may not reflect reality. For example, as the model is based on the modern-day freshwater mixing ratio, it assumes that the amount of freshwater mixed over Site 942 has always varied in direct proportion to the Amazon River discharge. The model is therefore unable to account for changes in the mixing ratio brought about by other factors such as variations in surface circulation, or in the trajectory of the Amazon River freshwater plume. The model also assumes that the isotopic value of precipitation has not changed independently of the Amazon Basin temperature, and reverse amount effects. The isotopic value of precipitation may have varied in the past due to changes in water vapour source, for example (Vuille *et al.*, 2003a; Vuille *et al.*, 2003b). The model is also highly dependant upon the quality of the input variables, as demonstrated by the range of modelled Amazon River outflow arising under different SST regimes. However, further refinement of the model to improve the resolution of the Amazon River outflow reconstruction is limited by the palaeodata currently available.

7.7 Summary

The key findings can be summarised as follows:

- The extent of SST cooling in the tropical Atlantic is a crucial variable in the refined Amazon River outflow model. The greater the extent of SST cooling, the smaller the modelled change in Amazon River outflow.
- Model predictions assuming a SST cooling of $\sim 5^{\circ}\text{C}$ imply that Amazon River outflow was greater than modern levels. This is in conflict to glacial stage proxy-based palaeoclimate reconstructions from the Amazon Basin.
- Assuming a SST cooling of 2 to 3°C , the Amazon River outflow is predicted to have reduced by ~ 30 to $\sim 50\%$ at the speculated YD onset, and by ~ 20 to $\sim 30\%$ during the LGM. Should SST have been similar at the time of the ACR, outflow is predicted to have reduced by ~ 15 to $\sim 45\%$. However, these semi-quantified reconstructions are limited by the assumptions used in the model.
- If the model is run for the time period assumed by Maslin *et al.* (2000) and Maslin and Burns (2000) to represent the YD (~ 12.4 to ~ 12 Cal ka), outflow is predicted to have reduced by ~ 10 to 20% . Not only is this considerably less than previous predictions, but it also implies that the Amazon Basin was relatively humid in the YD relative to the LGM, although still more arid relative to the present day. Furthermore, outflow was calculated about a positive excursion in the $\Delta\delta^{18}\text{O}_{942}$ record, therefore the model predictions for this period should be regarded as conservative.

7.8 References

- Arz, H. W., Patzold, J., and Wefer, G. (1998). Correlated Millennial-Scale Changes in Surface Hydrography and Terrigenous Sediment Yield Inferred from Last-Glacial Marine Deposits off Northeastern Brazil. *Quaternary Research* **50**, 157-166.
- Arz, H. W., Patzold, J., and Wefer, G. (1999). The deglacial history of the western tropical Atlantic as inferred from high resolution stable isotope records off northeastern Brazil. *Earth and Planetary Science Letters* **167**, 105-117.
- Billups, K., and Spero, H. J. (1996). Reconstructing the stable isotope geochemistry and paleotemperatures of the equatorial Atlantic during the last 150,000 years: Results from individual foraminifera. *Paleoceanography* **11**, 217-238.

-
- CLIMAP Project Members. (1981). Seasonal reconstruction of the Earth's surface at the Last Glacial Maximum. *Geological Society of America Chart and Map Series 36*.
- Colinvaux, P. A., De Oliveira, P. E., Moreno, J. E., Miller, M. C., and Bush, M. B. (1996). A long pollen record from lowland Amazonia: forest and cooling in glacial times. *Science* **274**, 85-88.
- Craig, H. (1965). The measurement of oxygen isotope paleotemperature. In "Proceedings of the Spoleto conference on Stable Isotopes in Oceanographic Studies and Paleotemperatures." pp. 3-24. Consiglio Nazionale delle Ricerche Geologia Nucleare, Pisa.
- Dansgaard, W. (1964). Stable Isotopes of Precipitation. *Tellus* **16**, 436-469.
- Dürkoop, A., Hale, W., Mulitza, S., Pätzold, J., and Wefer, G. (1997). Late Quaternary variations of sea surface salinity and temperature in the western tropical Atlantic: Evidence from $\delta^{18}\text{O}$ of Globigerinoides sacculifer. *Paleoceanography* **12**, 764-772.
- Epstein, S., Buchsbaum, R., Lowenstam, H. A., and Urey, H. C. (1953). Revised carbonate-water isotopic temperature scale. *Geological Society of America Bulletin* **64**, 1315-1326.
- Fairbanks, R. G. (1989). A 17,000 year glacio-eustatic sea level record: influence of glacial melting rates on the Younger Dryas event and deep-ocean circulation. *Nature* **362**, 637-642.
- Farrera, I., Harrison, S. P., Prentice, I. C., Ramstein, G., Guiot, J., Bartlein, P. J., Bonnefille, R., Bush, M., Cramer, W., von Grafenstein, U., Holmgren, K., Hooghiemstra, H., Hope, G., Jolly, D., Lauritzen, S. E., Ono, Y., Pinot, S., Stute, M., and Yu, G. (1999). Tropical climates at the Last Glacial Maximum: a new synthesis of terrestrial palaeoclimate data. I. Vegetation, lake-levels and geochemistry. *Climate Dynamics* **15**, 823-856.
- Greig, S. (1998). "Site 942 on the Amazon Fan: stable isotopes and sea surface temperatures." Unpublished MSc thesis, Royal Holloway University of London.
- Grootes, P. M. (1993). Interpreting continental oxygen isotope records. In "Climate Change in Continental Isotopic Records, Vol. 78." (P. K. Swart, K. C. Lohmann, J. McKenzie, and S. Savin, Eds.), pp. 37-46. AGU, Washington.
- Grootes, P. M., Stuiver, M., Thompson, L. G., and Mosley-Thompson, E. (1989). Oxygen Isotope Changes in Tropical Ice, Quelccaya, Peru. *Journal of Geophysical Research* **94**, 1187-1194.
- Guilderson, T. P., Fairbanks, R. G., and Rubenstone, J. L. (1994). Tropical temperature variations since 20,000 years ago: modulating interhemispheric climate change. *Science* **263**, 663-665.
- Hastings, D. W., Russell, A. D., and Emerson, S. R. (1998). Foraminiferal magnesium in Globigerinoides sacculifer as a paleotemperature proxy. *Paleoceanography* **13**, 161-169.
- International Atomic Energy Agency. (1992). "Statistical Treatment of Data on Environmental Isotopes in Precipitation, Technical Reports Series No. 331." IAEA, Vienna.
-

-
- Levitus, S. (1982). Climatological Atlas of the World Ocean, Professional Paper 13. National Ocean and Atmosphere Administration (NOAA).
- Liu, K., and Colinvaux, P. A. (1985). Forest Changes in the Amazon Basin during the Last Glacial Maximum. *Nature* **318**, 556-557.
- Maslin, M. A. (1998). Equatorial Western Atlantic Ocean circulation changes linked to the Heinrich Events: deep-sea sediment evidence from the Amazon Fan. In "Geological Evolution of the Coean Basins: Results from the Ocean Drilling Program." (A. Cramp, C. J. McLeod, S. Lee, and E. J. W. Jones, Eds.), pp. 111-127. Geological Society of America, Special Publications 131.
- Maslin, M. A., and Burns, S. J. (2000). Reconstruction of the Amazon Basin effective moisture availability over the past 14,000 years. *Science* **290**, 2285-2287.
- Maslin, M. A., Durham, E., Burns, S. J., Platzman, E., Grootes, P., Greig, S. E. J., Nadeau, M. J., Schleicher, M., Pflaumann, U., Lomax, B., and Rimington, N. (2000). Palaeoreconstruction of the Amazon River freshwater and sediment discharge using sediments recovered at site 942 on the Amazon Fan. *Journal of Quaternary Science* **15**, 419-434.
- Microsoft Corporation. (2004). Microsoft® Excel 2004 for Mac®.
- Min, G., Edwards, R. L., Taylor, F. W., Recy, J., Gallup, C. D., and Beck, J. W. (1995). Annual cycles of U/Ca in coral skeletons and U/Ca thermometry. *Geochimica et Cosmochimica Acta* **59**, 2025-2042.
- Mix, A. C., Morey, A. E., Pisias, N. G., and Hostetler, S. W. (1999). Foraminiferal faunal estimates of paleotemperature: circumventing the no-analogue problem yields cool ice age tropics. *Paleoceanography* **14**, 350-359.
- Niebler, H.-S., Arz, H. W., Donner, B., Mulitza, S., Pätzold, J., and Wefer, G. (2003). Sea surface temperatures in the equatorial and South Atlantic Ocean during the Last Glacial Maximum (23-19 ka). *Paleoceanography* **18**, 14.1-14.12.
- Pierrehumbert, R. T. (1999). Huascanan $\delta^{18}\text{O}$ as an indicator of tropical climate during the Last Glacial Maximum. *Geophysical Research Letters* **26**, 1345-1348.
- Rind, D., and Peteet, D. (1985). Terrestrial conditions at the Last Glacial Maximum and CLIMAP sea-surface temperature estimates: Are they consistent? *Quaternary Research* **24**, 1-22.
- Rühlemann, C., Diekmann, B., Mulitza, S., and Frank, M. (2001). Late Quaternary changes of western equatorial Atlantic surface circulation and Amazon lowland climate recorded in Ceara Rice deep-sea sediments. *Paleoceanography* **16**, 293-305.
- Salati, E., Dall'olio, A., Matsui, E., and Gat, J. R. (1979). Recycling of water in the Amazon Basin: An isotopic study. *Water Resources Research* **15**, 1250-1258.
- Shackleton, N. J. (1987). Oxygen isotopes, ice volume and sea level. *Quaternary Science Reviews* **6**, 183-190.
- Stute, M., Forster, M., Frischkorn, H., Serejo, A., Clark, J. F., Schlosser, P., Broecker, W. S., and Bonani, G. (1995). Cooling of Tropical Brazil (5°C) during the Last Glacial Maximum. *Science* **269**, 379-383.
-

-
- Thompson, L. G., Mosley-Thompson, E., and Henderson, K. A. (2000). Ice-core palaeoclimate records in tropical South America since the Last Glacial Maximum. *Journal of Quaternary Science* **15**, 377-394.
- Vuille, M., Bradley, R. S., Healy, R., Werner, M., Hardy, D. R., Thompson, L. G., and Keimig, F. (2003a). Modeling $\delta^{18}\text{O}$ in precipitation over the tropical Americas: 2. Simulation of the stable isotope signal in Andean ice cores. *Journal of Geophysical Research* **108**, 4175, doi:10.1029/2001JD002039.
- Vuille, M., Bradley, R. S., Werner, M., Healy, R., and Keimig, F. (2003b). Modeling $\delta^{18}\text{O}$ in precipitation over the tropical Americas: 1. Interannual variability and climatic controls. *Journal of Geophysical Research* **108**, 4174, doi:10.1029/2001JD002038.
- Wolff, T., Mulitza, S., Arz, H. W., and Wefer, G. (1998). Oxygen isotopes versus CLIMAP (18 ka) temperatures: a comparison from the tropical Atlantic. *Geology* **26**, 675-678.

8: SYNTHESIS AND DISCUSSION

8.1 Introduction

Data measured in this study have provided a continuous, chronologically constrained high-resolution record of Amazon Basin palaeoclimate for the last 40 Cal ka. It is hypothesised that the $\Delta\delta^{18}\text{O}_{942}$ record is monitoring past changes in the mixing ratio of riverine and marine waters over Site 942 on the Amazon Fan. Should it be assumed that the proportion of fresh water mixed over the site varies in direct proportion to the outflow of the Amazon River, $\Delta\delta^{18}\text{O}_{942}$ can thus serve as a proxy for the effective moisture history of the Amazon Basin (where effective moisture is equal to precipitation minus evaporation). However, the extent to which the effective moisture history of the Amazon Basin is representative of the past precipitation regime is less certain.

For example, Cowling (2004) hypothesises that the amount of water discharged by the Amazon River will be more a reflection of the intensity at which precipitation is recycled eco-physiologically by the Amazon Rainforest, rather than the actual amount of rainfall that has fallen. Cowling (2004) suggests that the recycling of precipitation is largely controlled by the canopy density of the forest (related to rainforest productivity), where the leaf area index (LAI) will determine the amount of water transpired, and the surface area available for rainfall interception, both of which will return the water to the atmosphere (Costa and Foley, 1997). Cowling (2004) tested this hypothesis by calculating a series of mass balance equations, incorporating the effects of modelled past variations in Amazon rainforest canopy density, for the 'Younger Dryas' scenario proposed by Maslin *et al.* (2000) and Maslin and Burns (2000). It was concluded that by incorporating biospheric recycling into the equation, the calculations of the reduction in Amazon River outflow by Maslin *et al.* (2000) and Maslin and Burns (2000) were considerably overestimated by up to 50%. However, the refined Amazon River outflow model of this study proposes that for this same period, river discharge was reduced by just 10 to 21%, relative to modern (with a SST cooling of 2 to 3°C; see Chapter 7; Section 7.5), which is comparable to the independently calculated estimations of Cowling (2004). Therefore the $\Delta\delta^{18}\text{O}_{942}$ records may provide an indication of past changes in Amazon River outflow after all. Where past variations in LAI may have been influential to the past outflow of the Amazon River, such information cannot easily be derived from the palaeoecological record. Past changes in LAI must therefore be derived from model simulations, which may not necessarily reflect reality should the model be too simplistic (P. Cox, personal communication, 2002).

Should $\Delta\delta^{18}\text{O}_{942}$ be monitoring Amazon Basin effective moisture and river outflow, the signal it records will be an average of the entire drainage basin. The Amazon Basin occupies $\sim 7\,050\,000\text{ km}^2$ (Franzinelli and Potter, 1983), and is comprised of a series of sub-basins which feed the main river in varying relative proportions. As discussed in Chapter 3, precipitation at any given locality in Amazonia is driven by a combination of both tropical- and extra-tropical factors. Therefore rainfall is unlikely to be spatially uniform across such a large, diverse area as the Amazon Basin, so the effective moisture is also likely to vary across the watershed. In this way, variations in effective moisture between the different sub-basins may introduce a regional bias to the overall Amazon River discharge signal. However, without an abundance of continuous, well-dated palaeoclimate reconstructions from sufficiently representative quadrats within the Amazon Basin, a possible regional bias in Amazon River outflow inferred from $\Delta\delta^{18}\text{O}_{942}$ will be difficult to determine. As discussed in Chapter 4, palaeoclimate records from the Amazon Basin are relatively sparse, particularly for the glacial period, and are frequently discontinuous, or are representative of discrete time-slices. Records often also lack good chronological control. The majority of palaeoclimate data from within the Amazon Basin is derived from the palaeoecological record, although it is often difficult to determine whether the data are monitoring a local *versus* a regional signal of change. In addition, where palaeoclimate information has been derived indirectly through palynological reconstructions, circular arguments present an inherent limitation. However, non-ecological palaeoclimate evidence may provide useful information for the interpretation of the $\Delta\delta^{18}\text{O}_{942}$ record (see following Sections).

Furthermore $\Delta\delta^{18}\text{O}_{942}$ from the Amazon Fan can also be compared to other large-scale palaeoclimate reconstructions from tropical South America, which indicate more regional signals of change. Comparison between these data, records of solar insolation and polar ice core records may yield significant insights into the causal mechanisms of tropical climate variability. This chapter will attempt to synthesise the current available palaeoclimate information inferred for tropical South America, and examine the $\Delta\delta^{18}\text{O}$ record from Site 942 on the Amazon Fan in the context of the dynamic workings of the tropical palaeoclimate system that are currently hypothesised.

8.2 Comparison of $\Delta\delta^{18}\text{O}_{942}$ to Other Proxy Records From Tropical and Subtropical South America

8.2.1 Comparison to Proxy Records From Within the Amazon Basin

Relatively enriched $\Delta\delta^{18}\text{O}_{942}$ records from the Amazon Fan imply an overall reduction in Amazon River discharge during the last glacial relative to the Holocene and present day.

This suggests that effective moisture in the Amazon Basin was reduced, indicating a relatively drier glacial climate. This is supported by inorganic sedimentary lake records from within the Amazon Basin which imply lower water levels, or even complete desiccation during the last glacial maximum (LGM; e.g. Colinvaux *et al.*, 1996; Ledru *et al.*, 1998; Servant *et al.*, 1993; Sifeddine *et al.*, 2001; Sifeddine *et al.*, 2003; van der Hammen, 1974; van der Hammen and Absy, 1994). Lake evidence from northwestern Brazil indicates that the glacial climate of this region was relatively humid however, although lake levels were still below modern levels (Bush *et al.*, 2002). Various morphological proxies of glacial aridity in the Amazon Basin have also been presented, although they are of questionable integrity (see Chapter 3, Table 4.2).

$\Delta\delta^{18}\text{O}_{942}$ evidence of increasing Amazon Basin effective moisture through the Holocene is supported by the formation of lakes in central and eastern Amazonia (Behling and da Costa, 2001; Behling *et al.*, 2001). Despite the paucity of proxy evidence from within the Amazon Basin, the majority supports the effective moisture history inferred from $\Delta\delta^{18}\text{O}_{942}$ records from the Amazon Fan.

8.2.3 Comparison to Large-Scale Proxy Records from Tropical and Subtropical South America

Much longer, more continuous records exist from outside the Amazon Basin, and are shown stacked in approximate latitudinal order in Figure 8.1, alongside the $\Delta\delta^{18}\text{O}_{942}$ record from the Amazon Fan, and calculated summer insolation at 10°S (Berger, 1978a; Berger, 1978b; Berger and Loutre, 1991). Details of these proxy records are given in Table 8.1.

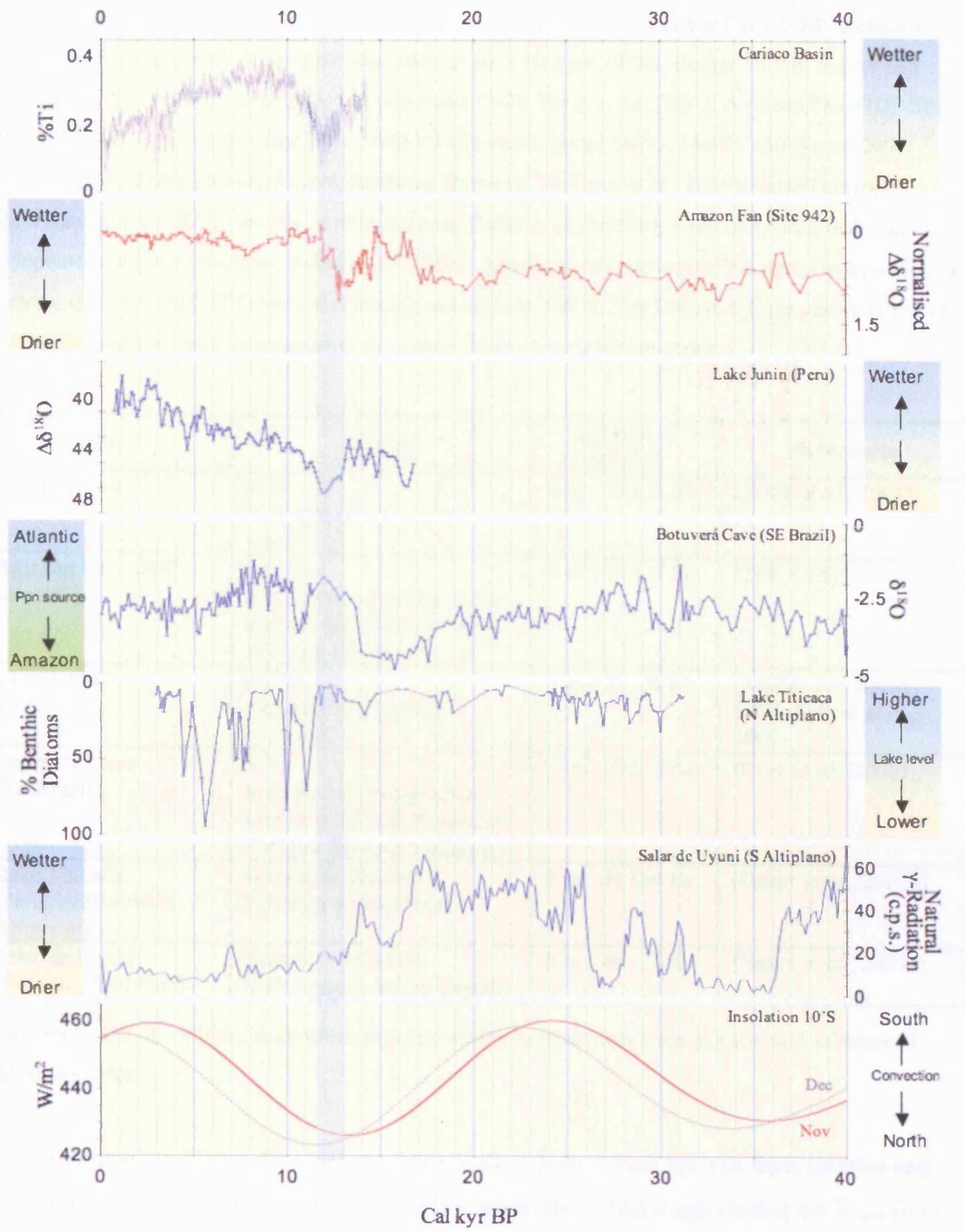


Figure 8.1: Caption on next page.

←**Figure 8.1 (previous page):** Long, continuous regional-scale proxy records from tropical and subtropical South America, stacked in approximate latitudinal order against Cal kyr BP, alongside calculated November and December insolation at 10°S (Berger 1978a; Berger 1978b; Berger and Loutre, 1991). From top to bottom: Cariaco Basin (%Ti; Haug *et al.*, 2001); Amazon Fan, ODP Site 942 ($\Delta\delta^{18}\text{O}_{942}$ *G. sacculifer* (sac); this study); Lake Junin, Peru ($\Delta\delta^{18}\text{O}$; Maslin and Burns, 2000; Seltzer *et al.*, 2000); Botuverá Cave, southeast Brazil ($\delta^{18}\text{O}$; Cruz *et al.*, 2005); Lake Titicaca, Peruvian/Bolivian Altiplano (% benthic diatoms; Baker *et al.*, 2001b); Salar de Uyuni, Bolivian Altiplano (natural γ -radiation; Baker *et al.*, 2001a). Shaded area denotes the Younger Dryas period as determined by GISP2 $\delta^{18}\text{O}$ records (Grootes and Stuiver, 1997). The Botuverá Cave record (Cruz *et al.* 2005) monitors relative changes in the source area of precipitation (ppn).

Site	Proxy	Length of Record	References
Cariaco Basin	%Ti Indicator of continental runoff	0 to ~14 Cal ka	(Haug <i>et al.</i> , 2001)
Amazon Fan (ODP Site 942)	$\Delta\delta^{18}\text{O}_{942}$ Indicator of Amazon River outflow and Amazon Basin effective moisture	0 to ~40 Cal ka	(This study)
Lake Junin (Peru)	$\Delta\delta^{18}\text{O}$ Indicator of effective moisture	0 to ~17 Cal ka	(Maslin and Burns, 2000; Seltzer <i>et al.</i> , 2000)
Botuverá Cave (SE Brazil)	$\delta^{18}\text{O}$ Indicator of precipitation source and South American Summer Monsoon intensity	0 to >40 Cal ka	(Cruz <i>et al.</i> , 2005)
Lake Titicaca (Peruvian/Bolivian Altiplano)	% Benthic diatoms Indicator of lake level	0 to ~31 Cal ka	(Baker <i>et al.</i> , 2001b)
Salar de Uyuni (Bolivian Altiplano)	Natural γ -radiation Indicator of wet/dry climate	0 to >40 Cal ka	(Baker <i>et al.</i> , 2001a)

Table 8.1: Details of long, continuous regional-scale proxy records from tropical and subtropical South America.

With reference to Figure 8.1, the long large-scale palaeoclimate records from tropical and subtropical South America correspond well to each other. This suggests that $\Delta\delta^{18}\text{O}_{942}$ from the Amazon Fan is recording a regional signal of change that is likely to be forced by the climate system operating over South America throughout the duration of the record (40 Cal kyr). However, palaeomoisture records from the Altiplano appear to trend in opposite directions to those further north: when the Amazon Basin is relatively more arid, the Altiplano appears to be relatively wet, and vice versa. The Botuverá Cave speleothem record (Cruz *et al.*, 2005), which monitors changes in the source area of precipitation, implies that periods of relatively increased aridity in the Amazon Basin coincide with a more Atlantic-sourced precipitation source over the cave location. When $\Delta\delta^{18}\text{O}_{942}$ is relatively more

depleted however, over-cave precipitation is advected southeastwards from the relatively more humid Amazon Basin.

Trends in the data appear to follow precessional-driven insolation at 10°S. A close adherence to precessional insolation was also found within long (170 ka) lake sequences (Bush *et al.*, 2002), and speleothem records (Wang *et al.*, 2004; Wang *et al.*, 2003b; Wang *et al.*, 2003a) from northeastern Brazil. The records presented in Figure 8.1 bear particular resemblance to 10°S insolation values calculated between November and December, which is coincident with the formation of the Bolivian High over the Altiplano region (Lenters and Cook, 1997; Marengo *et al.*, 2001; Vuille, 1999). This marks the development of the South American summer monsoon (SASM) system over tropical South America, and is associated with intense convection over the Amazon Basin at the boundaries of the Hadley cell at the meteorological equator (Zhou and Lau, 1998; see Chapter 3, Section 3.2.1).

8.3 Interpretation of Climate From Large-Scale Proxy Records from Tropical and Subtropical South America

Maxima in solar insolation during Southern Hemisphere summer result in a maximum southward displacement of the SASM, and consequently intensified convective activity over the Amazon Basin. It is hypothesised that convective activity will become further intensified with a coincident progressive increase in solar radiation over the Altiplano, strengthening the formation of the Bolivian High. The Holocene records displayed in Figure 8.1 support this interpretation. $\Delta\delta^{18}\text{O}_{942}$ records from the Amazon Fan imply a gradual increase in Amazon Basin effective moisture throughout the Holocene, coincident with an insolation-driven southward displacement of the SASM. $\Delta\delta^{18}\text{O}$ data from Lake Junin also suggest a coincident increase in effective moisture (Maslin and Burns, 2000; Seltzer *et al.*, 2000). Furthermore, evidence from Lake Titicaca (Baker *et al.*, 2001b) and snow accumulation at Nevado Sajama (Thompson *et al.*, 1998; see Chapter 4, Figure 4.10) also imply a steady increase in available moisture sourced from the Amazon Basin throughout the Holocene. The Botuverá Cave Holocene record also indicates a relative increase in the amount of Amazon Basin-sourced moisture throughout the Holocene (Cruz *et al.*, 2005). Further evidence for the intensification of Amazon Basin convective activity throughout the Holocene comes from the Cariaco Basin. Precipitation over the Cariaco Basin is strongly influenced by the mean latitudinal position of the Intertropical Convergence Zone (ITCZ; Haug *et al.*, 2001). The %Ti record, a measure of continental runoff, displays a strong correlation to solar insolation, and is hypothesised to record the gradual insolation-driven southward shift of the ITCZ through the Holocene. Insolation-driven changes in the latitude and intensity of the SASM

and Hadley cell convection therefore present a plausible hypothesis for the observed variation in the climate reconstructions from tropical and subtropical South America.

In addition to solar insolation, the long-term mean location and latitudinal boundaries of convective activity associated with the SASM and the Hadley cells will also be determined by the latitudinal position of the meteorological equator. During the cold stages, steeper temperature gradients between the pole and the tropics in the Northern Hemisphere would have maintained the meteorological equator to a position south of that dictated by insolation forcing alone. Therefore at the time of the LGM, although insolation would have forced a mean position approximately equivalent to that of the late Holocene, cold Greenland temperatures would have forced the meteorological equator further south. In this way, the northerly boundary of convective activity over the Amazon Basin would have been restricted to a relatively more southerly position. Evidence suggests that the wind systems became more zonal at this time, as cooler temperatures would have weakened Hadley cell intensity (e.g. Lorenz *et al.*, 1996). This is supported by the relatively more depleted *N. dutertrei* $\Delta\delta^{18}\text{O}_{942}$ in this study, and also by assemblage abundance records (Greig, 1998), which imply a shallowing of the thermocline during the glacial, possibly forced by increased wind stress. A more southerly restricted zone of convection activity coupled with weaker Hadley cell and SASM intensity would have reduced the amount of convective precipitation over the Amazon Basin relative to today. This is confirmed by $\Delta\delta^{18}\text{O}_{942}$ records from the Amazon Fan, which propose a reduction in glacial river outflow relative to modern, despite similar insolation forcing. Data from the Altiplano, however, imply that conditions were wetter during the glacial stage. Nevertheless, modelling studies suggest that in response to the more zonal wind system, there was an increased eastward penetration of South Atlantic and/or Pacific Ocean-sourced moisture toward the Altiplano (Hostetler and Mix, 1999).

A shaded area on Figure 8.1 suggests the portion of the palaeoclimate records corresponding to the Younger Dryas (YD) period, as defined by GISP2 $\delta^{18}\text{O}$ records (Grootes and Stuiver, 1997), and based upon the Site 942 calendar age model discussed in Chapter 5. During the YD, insolation forcing would have placed the meteorological equator in a southerly position over tropical South America. Furthermore, the onset of the YD would have further steepened meridional temperature gradients in the northern hemisphere, which would have further enhanced the southward forcing of convective activity. In this way, it is hypothesised that the spatial extent of the convection activity over the Amazon Basin was reduced. Cooler temperatures would also have weakened Hadley cell intensity. It is predicted that together, this would have had the effect of weakening the convection associated with the SASM,

thereby reducing effective moisture in the Amazon Basin to levels even less than those of the LGM. This is confirmed by the positive excursion in the $\Delta\delta^{18}\text{O}_{942}$ data from the Amazon Fan. The results of the Amazon River outflow model also corroborate the hypothesis of a greater reduction in Amazon Basin effective moisture relative to the LGM. Furthermore, data from Botuverá Cave support a weakening of the SASM and relatively more arid Amazon Basin, as the $\delta^{18}\text{O}$ implies a shift toward a more Atlantic precipitation source. Data from Lake Junin and the Cariaco Basin also imply a relative decrease in effective moisture over tropical South America at this time (Haug *et al.*, 2001; Maslin *et al.*, 2000; Seltzer *et al.*, 2000). As predicted from a southerly-displaced SASM, and weakened Hadley cell intensity, data from the Altiplano suggests a relative increase in moisture coincident with the YD (Baker *et al.*, 2001a; Baker *et al.*, 2001b).

8.3 Comparison of $\Delta\delta^{18}\text{O}_{942}$ Records With Polar Ice Cores: Possible Inter-Hemispheric Drivers for Tropical South American Palaeoclimate

Following the onset of the YD, $\delta^{18}\text{O}$ in the Greenland ice core records (e.g. Grootes and Stuiver, 1997) imply a minor amelioration in temperature. However, $\Delta\delta^{18}\text{O}_{942}$ values from the Amazon Fan become significantly more depleted. Should $\Delta\delta^{18}\text{O}_{942}$ be monitoring effective moisture, this would imply that the Amazon Basin was becoming increasingly wetter through the YD. Such a trend would also be apparent even if the calendar age scale of the Site 942 records was found to be biased toward older ages, as a result of the ΔR value used in the calibration of the radiocarbon dates (see Chapter 5). Furthermore, superimposed on this depleting trend is a marked positive excursion in the $\Delta\delta^{18}\text{O}$ record between ~ 12.4 and ~ 11.9 Cal ca. It is speculated that the temperature changes observed in the Greenland ice core record cannot be inferred to have forced the magnitude of change observed in $\Delta\delta^{18}\text{O}$ on the Amazon Fan. However, it has been hypothesised that Northern and Southern Hemisphere climate were out of phase at this time (e.g. Blunier *et al.*, 1998; Blunier *et al.*, 1997; Broecker, 1998). Figure 8.2 displays the same palaeoclimate proxies shown in Figure 8.1, but also compares the polar ice core records.

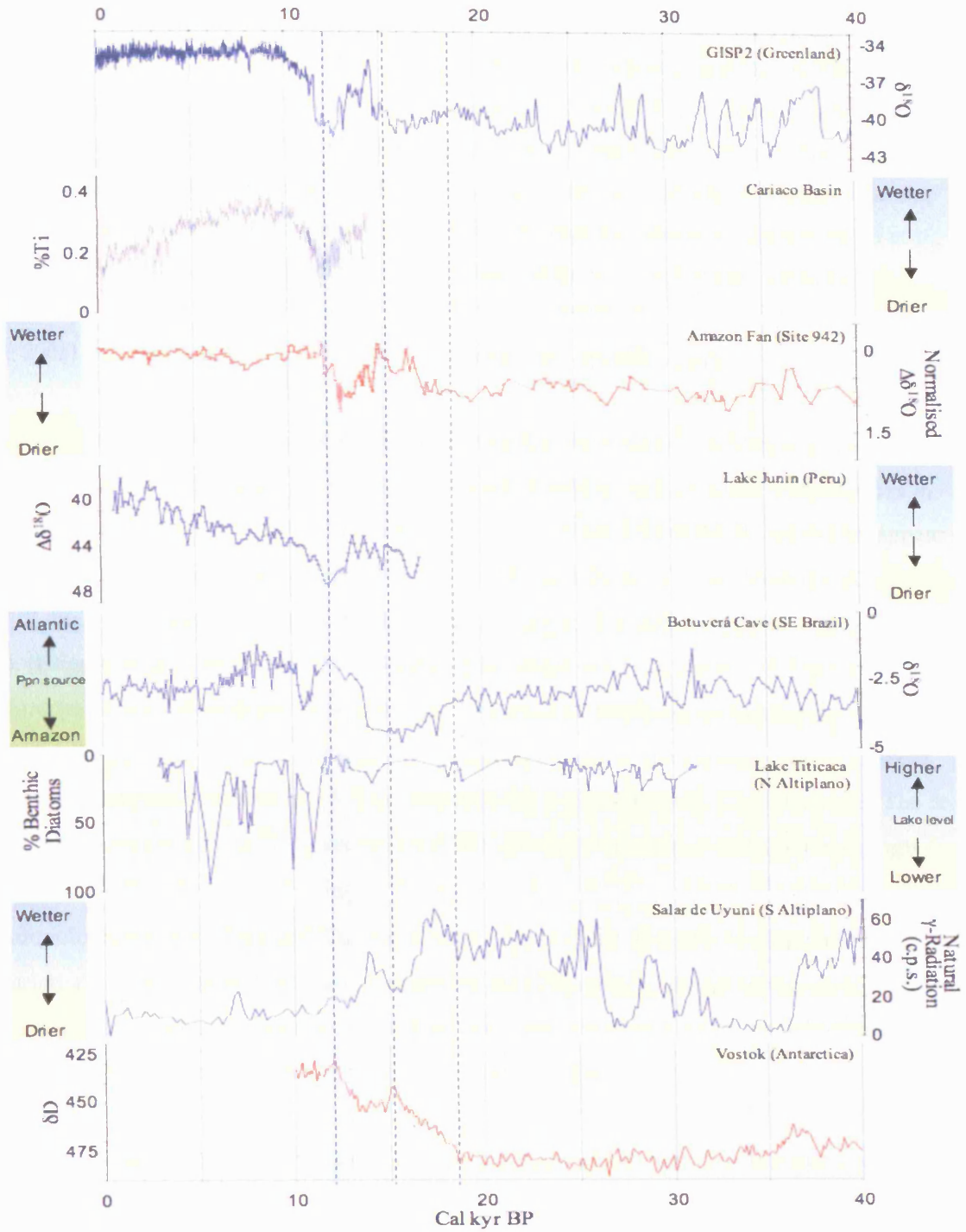


Figure 8.2: Caption on next page.

← **Figure 8.2 (previous page):** Long, continuous regional-scale proxy records from tropical and subtropical South America, stacked in approximate latitudinal order against Cal kyr BP, alongside polar ice core data. From top to bottom: GISP2 ice core ($\delta^{18}\text{O}$; Grootes and Stuiver, 1997); Cariaco Basin (%Ti; Haug et al., 2001); Amazon Fan, ODP Site 942 ($\Delta\delta^{18}\text{O}_{942}$ G. sacculifer (sac); this study); Lake Junin, Peru ($\Delta\delta^{18}\text{O}$; Maslin and Burns, 2000; Seltzer et al., 2000); Botuverá Cave, southeast Brazil ($\delta^{18}\text{O}$; Cruz et al., 2005); Lake Titicaca, Peruvian/Bolivian Altiplano (% benthic diatoms; Baker et al., 2001b); Salar de Uyuni, Bolivian Altiplano (natural γ -radiation; Baker et al., 2001a); Vostok ice core (δD ; Blunier, 1998). Shaded area denotes the Younger Dryas period as determined by GISP2 $\delta^{18}\text{O}$ records (Grootes and Stuiver, 1997). The Botuverá Cave record (Cruz et al. 2005) monitors relative changes in the source area of precipitation (ppn).

Data presented in Figure 8.2 clearly demonstrate that the positive excursion in the $\Delta\delta^{18}\text{O}_{942}$ record between ~ 12.4 and 11.9 Cal ka is coincident with a peak in warm temperatures in Antarctica. Furthermore, other trends in the $\Delta\delta^{18}\text{O}_{942}$ record from the Amazon Fan appear to co-vary with the Antarctic temperature record. Marked features in the Vostok δD record are hi-lighted on Figure 8.2 with dotted lines. According to the ice core chronology of Blunier et al. (Blunier *et al.*, 1997), periods of warming in Antarctica (e.g. from ~ 18.5 to ~ 15 Cal ka) correspond to relative depletions in the $\Delta\delta^{18}\text{O}_{942}$ record, implying an increase in Amazon Basin effective moisture. An episode of increasing aridity in the Amazon Basin inferred from a relative enrichment in $\Delta\delta^{18}\text{O}_{942}$ corresponds to the Antarctic Cold Reversal. The co-variance between the $\Delta\delta^{18}\text{O}_{942}$ record from the Amazon Fan, and Vostok δD is strongly suggestive of an Antarctic forcing of the Amazon Fan $\Delta\delta^{18}\text{O}_{942}$ signal. Even if the chronological scale of the $\Delta\delta^{18}\text{O}_{942}$ were to be adjusted, for example to compensate for variations in the marine radiocarbon reservoir (see Chapter 5), the co-variation with the Antarctic temperature record would still be apparent, regardless of whether the time scale of Site 942 was shifted to slightly younger, or slightly older.

It is hypothesised that this tropical-Antarctic teleconnection may arise through the impact of Antarctic temperature changes on the latitudinal position of the meteorological equator. Antarctic temperatures will thus influence limits of the southerly penetration of the SASM and Hadley cell into the Amazon Basin. Throughout the YD therefore, steep temperature gradients in the Northern Hemisphere would displace the meteorological equator to a more southerly position than that dictated by insolation. However, increasingly warmer temperatures in Antarctica would reduce the temperature gradient in the Southern Hemisphere, and enhance this southward forcing. It is speculated that the net result would be a deeper penetration of the SASM into the Amazon Basin, and a coincident increase in

Amazon Basin effective moisture. The higher resolution $\Delta\delta^{18}\text{O}_{942}$ data from the Amazon Fan presented in this study support such a hypothesis.

An Antarctic climate forcing over tropical South America has implications for the interpretation of the Sajama and Huascarán tropical ice core records. As their chronologies between 12 and 19 ka have been tuned to GISP2 and a Portuguese marine core, respectively, their signals will be inherently biased toward a Northern Hemisphere signal (Thompson, 2000; Thompson *et al.*, 1998; Thompson *et al.*, 1995; Thompson *et al.*, 2000). In this respect, the deglacial climate reversal observed in the $\delta^{18}\text{O}$ signal may represent the Antarctic Cold Reversal. The re-tuning of these age models to an Antarctic forcing may reconcile the difference observed between the Huascarán and Lake Junin $\delta^{18}\text{O}$ records between ~ 11 and ~ 14 ka which forces more positive values in the $\Delta\delta^{18}\text{O}$ calculation, used as proxy for effective moisture in the Lake Junin catchment (see Figure 8.3; Seltzer *et al.*, 2000).

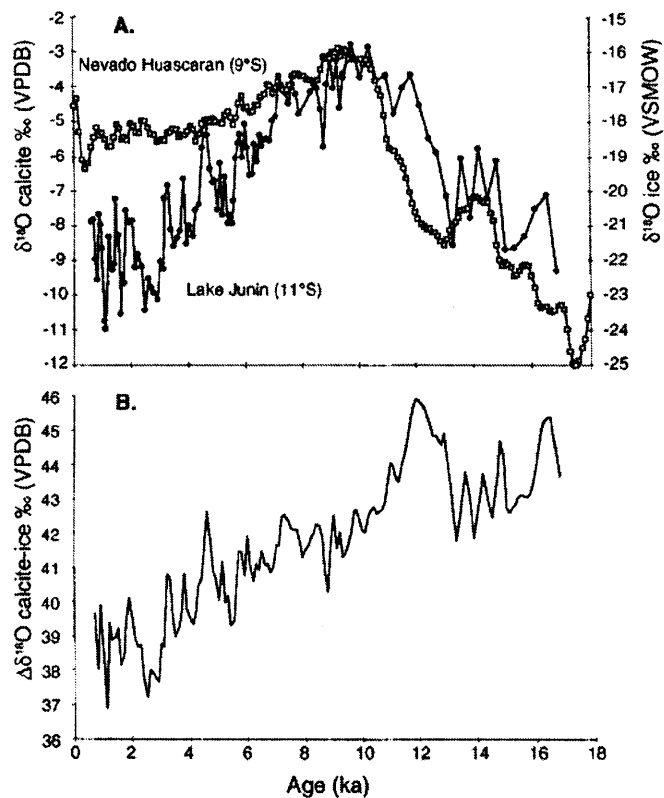


Figure 8.3: A comparison between $\delta^{18}\text{O}$ records from the Huascarán ice core (A), and Lake Junin (B; Peru). Chronological bias to the Northern Hemisphere in the Huascarán age model may account for the noticeable dissimilarity between the isotopic records from ~ 11 to ~ 14 ka, which results in relatively more enriched $\Delta\delta^{18}\text{O}$ values around this time (B), where $\Delta\delta^{18}\text{O}$ represents the difference between the two records (modified from Seltzer *et al.*, 2000).

8.4 Comparison of Tropical South American Palaeoclimate Records for the Onset of the Younger Dryas

It was hypothesised in Chapter 6 that the large increase in sedimentation rate coincident with a marked enrichment in $\Delta\delta^{18}\text{O}_{942}$ between ~ 12.8 and ~ 12.7 Cal ka was representative of the onset of the YD. Figure 8.4 details the same palaeoclimate records as in Figure 8.2, but in greater detail for the period between ~ 15 and ~ 10 Cal ka. Shading indicates the period of enhanced sedimentation over Site 942, the timing of which is constrained by four AMS radiocarbon dates (see Chapter 5, Section 5.3.1, Figure 5.5, Tables 5.1 and 5.3). However the exact timing of this ‘event’ in calendar years is dependant upon the marine radiocarbon reservoir correction applied during the calibration exercise (see Chapter 5, Section 5.1.2).

Figure 8.4 (next page): ~ 10 to ~ 15 ka detail. Long, continuous regional-scale proxy records from tropical and subtropical South America, stacked in approximate latitudinal order against Cal kyr BP, alongside polar ice core data. From top to bottom: GISP2 ice core ($\delta^{18}\text{O}$; Grootes and Stuiver, 1997); Cariaco Basin (%Ti; Haug *et al.*, 2001); Amazon Fan, ODP Site 942 ($\Delta\delta^{18}\text{O}_{942}$ *G. sacculifer* (sac); this study); Lake Junin, Peru ($\Delta\delta^{18}\text{O}$; Maslin and Burns, 2000; Seltzer *et al.*, 2000); Botuverá Cave, southeast Brazil ($\delta^{18}\text{O}$; Cruz *et al.*, 2005); Lake Titicaca, Peruvian/Bolivian Altiplano (% benthic diatoms; Baker *et al.*, 2001b); Salar de Uyuni, Bolivian Altiplano (natural γ -radiation; Baker *et al.*, 2001a); Vostok ice core (δD ; Blunier, 1998). Shaded area indicates the time of rapid sediment accumulation on the Amazon Fan (~ 18 m Cal ka^{-1}). The Botuverá Cave record (Cruz *et al.* 2005) monitors relative changes in the source area of precipitation (ppn). →

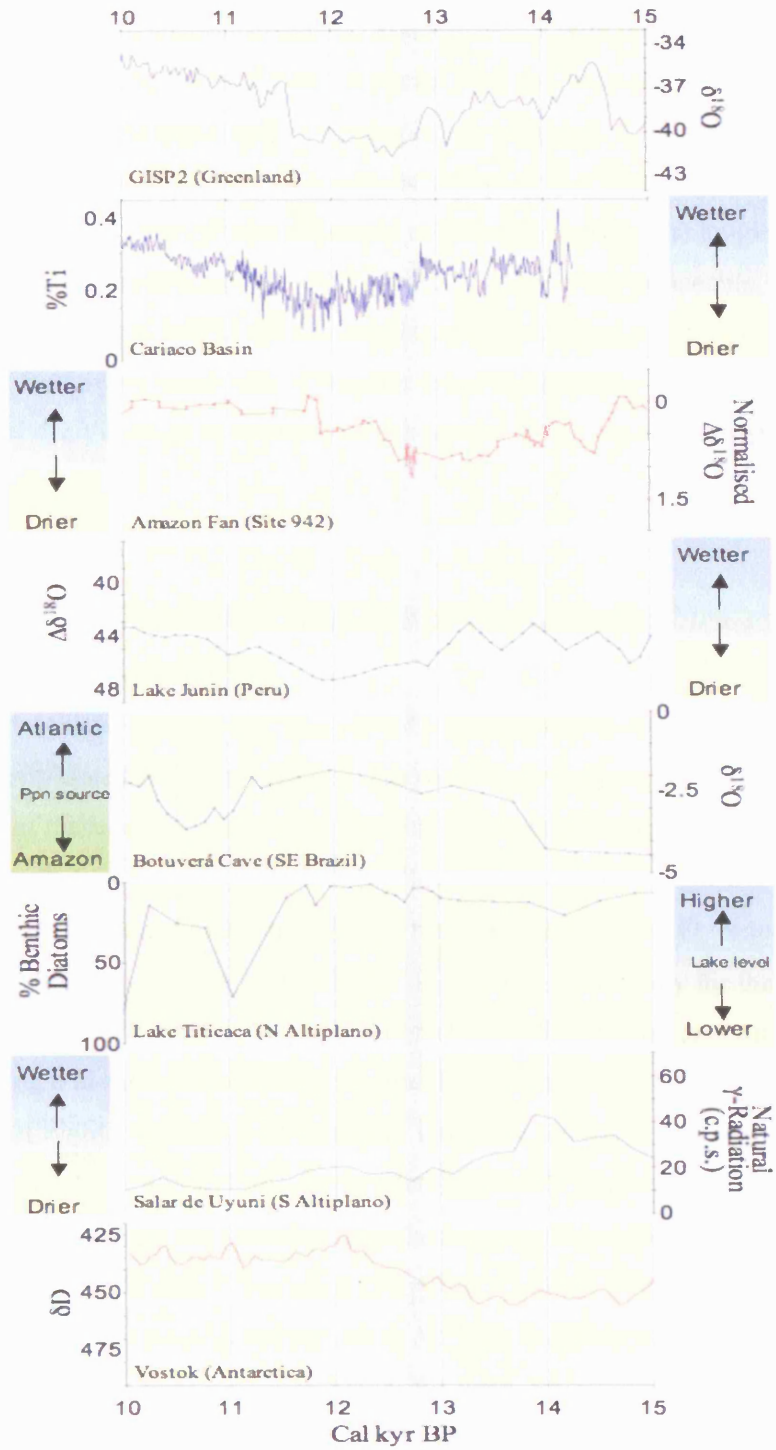


Figure 8.4: Caption on previous page.

With reference to Figure 8.4, assuming each of the datasets have reliable age models, the timing of enhanced sedimentation at Site 942 compares well with the depletion in GISP2 $\delta^{18}\text{O}$, which supports the hypothesis that it is coeval with the onset of the YD in the Northern Hemisphere (assuming the associated chronologies are accurate). Aside from the Cariaco Basin data, other palaeoclimate data shown are of relatively low temporal resolution. However, assuming each record has a relatively reliable chronology, the majority of signals imply some form of excursion around ~ 12.8 to ~ 12.7 Cal ka. Most noticeable, is the relatively rapid decrease in %Ti in the Cariaco Basin record (Haug *et al.*, 2001). Evidence of such possible synchronous excursions within the data may therefore purport to the manifestation of the YD onset in tropical and subtropical South American palaeoclimate records.

8.5 Comparison of the Holocene $\Delta\delta^{18}\text{O}_{942}$ Amazon Basin Effective Moisture Record with Records of ENSO Variability

Quasi-periodic oscillations in the $\Delta\delta^{18}\text{O}_{942}$ records, particularly those measured on *G. ruber*, imply that the outflow of the Amazon River was variable throughout the Holocene. The apparent onset of these ‘cycles’ may coincide with the onset of increased ENSO frequency over tropical South America (Moy *et al.*, 2002; Rodbell *et al.*, 1999). Figure 8.5 compares the $\Delta\delta^{18}\text{O}_{942}$ record measured on *G. ruber* to the reconstruction of ENSO frequency from Laguna Pallcacocha in the southern Ecuadorian Andes. The chronology for the Laguna Pallcacocha record was derived indirectly through stratigraphic tuning to another core, and through assuming a bi-modal sedimentary regime during which accumulation was constant for each mode of ENSO, regardless of intensity. Therefore the age model may contain errors (C.M. Moy, personal communication). Consequently, the $\Delta\delta^{18}\text{O}_{942}$ record may vary in phase with ENSO variability. This is a plausible hypothesis given that sufficient heat is released over Amazonia to drive Walker Circulation (Barry and Chorley, 1995). However at present, it is unclear as to whether positive excursions in $\Delta\delta^{18}\text{O}_{942}$ coincide with enhanced or reduced ENSO frequency. The tie lines placed on Figure 8.5 were determined on the observation that isotopically more depleted values in the late Holocene were coincident with an apparent reduction in ENSO frequency.

In the modern day, ENSO exerts its strongest impact over northern Amazonia, where low phases (El Niño) are associated with anomalously low river levels. Should the $\Delta\delta^{18}\text{O}_{942}$ record be monitoring variation in ENSO frequency, it therefore presents the possibility of a

biasing in the record toward Northern Amazonia. However, past variations in the meteorological equator may have shifted this biasing to elsewhere within the Amazon Basin.

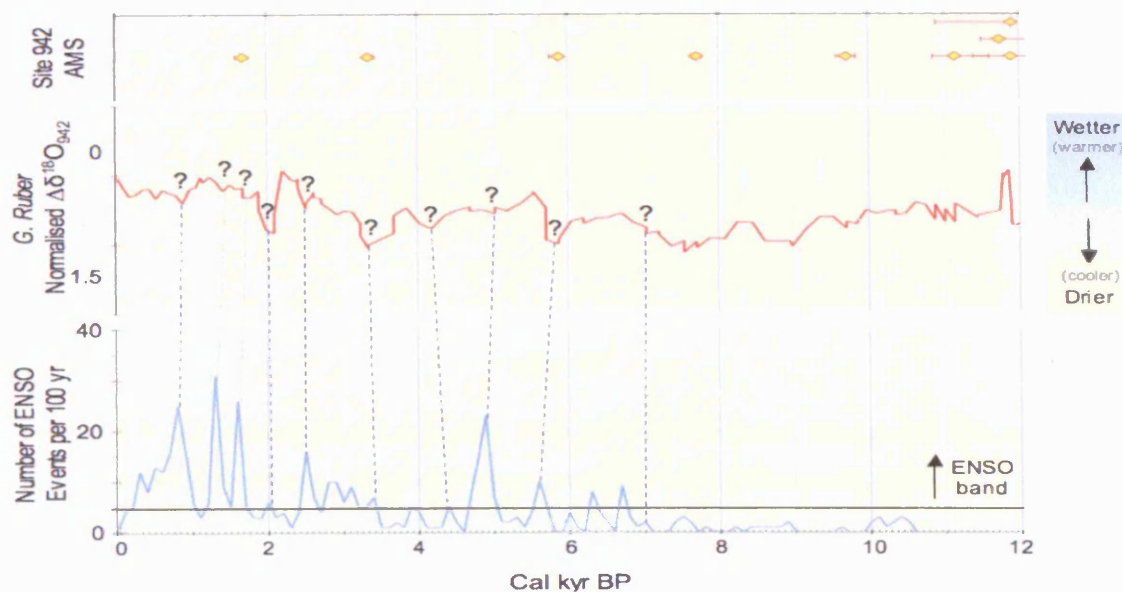


Figure 8.5: A comparison of the *G. ruber* $\Delta\delta^{18}\text{O}_{942}$ record of effective moisture in the Amazon Basin against the reconstruction of ENSO frequency from Laguna Pallcacocha in the southern Ecuadorian Andes (after Moy *et al.*, 2002).

8.6 Comparison of the $\Delta\delta^{18}\text{O}_{942}$ Amazon Basin Effective Moisture Record with Records of Atmospheric Methane

A record of past variations the effective moisture history of the Amazon Basin provides an opportunity to assess the extent to which the tropics might contribute to atmospheric methane concentrations. Figure 8.6 shows a comparison of the *G. sacculifer* $\Delta\delta^{18}\text{O}_{942}$ Amazon Basin effective moisture record and the GISP2 global atmospheric methane record (Brook *et al.*, 1996). Shading indicates the timing of the YD, as defined by GISP2 $\delta^{18}\text{O}$ (Grootes and Stuiver, 1997). The higher-resolution and more chronologically constrained Amazon Basin effective moisture record from the Amazon Fan implies that there is little relationship with global methane during the YD or glacial stages, even if the age model for Site 942 were found to be biased to too old/young by up to 400 years (see Chapter 5, Section 5.1.2). Throughout the Holocene however, both records appear to co-vary. This may imply that the tropical contribution of atmospheric methane is relatively more significant when summer insolation is at maxima over tropical South America, and thus convection over the Amazon Basin would be intensified.

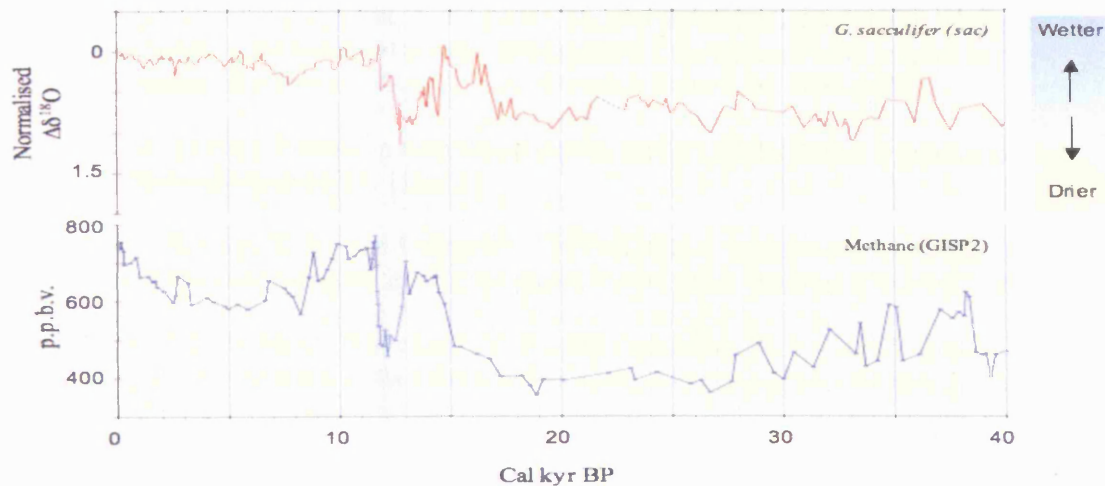


Figure 8.6. A comparison of the *G. sacculifer* (sac) $\Delta\delta^{18}\text{O}_{942}$ record from the Amazon Fan as a proxy for tropical humidity, and the GISP2 atmospheric methane record (Brook *et al.*, 1996).

8. References

- Baker, P. A., Rigsby, C. A., Seltzer, G. O., Fritz, S. C., Lowenstein, T. K., Bacher, N. P., and Veliz, C. (2001a). Tropical climate changes at millennial and orbital timescales on the Bolivian Altiplano. *Nature* **409**, 698-701.
- Baker, P. A., Seltzer, G. O., Fritz, S. C., Dunbar, R. B., Grove, M. J., Tapia, P. M., Cross, S. L., Rowe, H. D., and Broda, J. P. (2001b). The History of South American Tropical Precipitation for the Past 25,000 Years. *Science* **291**, 640-643.
- Barry, R. G., and Chorley, R. J. (1995). Tropical Weather and Climate. In "Atmosphere, Weather and Climate." pp. 224. Routledge, London.
- Behling, H., and da Costa, M. L. (2001). Holocene vegetational and coastal environmental changes from the Lago Crispim record in northeastern Para State, eastern Amazonia. *Review of Palaeobotany and Palynology* **114**, 145-155.
- Behling, H., Keim, G., Irion, G., Junk, W., and Nunes de Mello, J. (2001). Holocene environmental changes in the Central Amazon Basin inferred from Lago Calado (Brazil). *Palaeogeography, Palaeoclimatology, Palaeoecology* **173**, 87-101.
- Berger, A. (1978a). Long-term variations of caloric insolation resulting from the Earth's orbital elements. *Quaternary Research* **9**, 139-167.
- Berger, A. (1978b). Long-term variations of daily insolation and Quaternary climate changes. *Journal of Atmospheric Science* **35**, 2362-2367.
- Berger, A., and Loutre, M. (1991). Insolation values for the climate of the last 10 million years. *Quaternary Science Reviews* **10**, 297-317.
- Blunier, T., Chappellaz, J., Schwander, J., Dällenbach, A., Stauffer, B., Stocker, T., Raynaud, D., Jouzel, J., Clausen, H. B., Hammer, C. U., and Johnsen, S. J. (1998). Asynchrony of Antarctic and Greenland climate change during the last glacial period. *Nature* **384**, 739-743.

-
- Blunier, T., Schwander, J., Stauffer, B., Stocker, T., Dällenbach, A., Indermühle, A., Tschumi, J., Chappellaz, J., Raynaud, D., and Barnola, J.-M. (1997). Timing of the Antarctic Cold Reversal and the atmospheric CO₂ increase with respect to the Younger Dryas event. *Geophysical Research Letters* **24**, 2683-2686.
- Broecker, W. (1998). Paleocan circulation during the last deglaciation: a bipolar seesaw? *Paleoceanography* **13**, 119-121.
- Brook, E. J., Sowers, T. A., and Orchardo, J. (1996). Rapid variations in atmospheric methane concentration during the past 110,000 years. *Science* **273**, 1087-1091.
- Bush, M. B., Miller, M. C., Oliveira, P. E. D., and Colinvaux, P. A. (2002). Orbital-forcing signal in sediments of two Amazonian lakes. *Journal of Paleolimnology* **27**, 341-352.
- Colinvaux, P. A., De Oliveira, P. E., Moreno, J. E., Miller, M. C., and Bush, M. B. (1996). A long pollen record from lowland Amazonia: forest and cooling in glacial times. *Science* **274**, 85-88.
- Costa, M. H., and Foley, J. A. (1997). Water balance of the Amazon Basin: dependence on vegetation cover and canopy conductance. *Journal of Geophysical Research D: Atmospheres* **102**, 23973-23989.
- Cowling, S. A. (2004). Tropical forest structure: a missing dimension to Pleistocene landscapes. *Journal of Quaternary Science* **19**, 733-743.
- Cruz, F. W., Burns, S. J., Karmann, I., Sharp, W. D., Vuille, M., Cardoso, A. O., Ferrari, J. A., Silva Dias, P. L., and Viana Jr, V. (2005). Insolation-driven changes in atmospheric circulation over the past 116,000 years in subtropical Brazil. *Nature* **434**, 63-66.
- Franzinelli, E., and Potter, P. (1983). Petrology, chemistry and texture of Amazon River sands. Amazon River system. *Journal of Geology* **91**, 23-39.
- Greig, S. (1998). Site 942 on the Amazon Fan: stable isotopes and sea surface temperatures. *Unpublished M.Sc. Thesis, Royal Holloway University of London*, 91p.
- Grootes, P. M., and Stuiver, M. (1997). Oxygen 18/16 variability in Greenland snow and ice with 10³ to 10⁵-year time resolution. *Journal of Geophysical Research* **102**, 26455-26470.
- Haug, G. H., Hughen, K. A., Sigman, D. M., Peterson, L. C., and Röhl, U. (2001). Southward Migration of the Intertropical Convergence Zone Through the Holocene. *Science* **293**, 1304-1308.
- Hostetler, S. W., and Mix, A. (1999). Reassessment of ice-age cooling of the tropical ocean and atmosphere. *Nature* **399**, 673-676.
- Ledru, M. P., Bertaux, J., Sifeddine, A., and Suguio, K. (1998). Absence of last glacial maximum records in lowland tropical forests. *Quaternary Research* **49**, 233-237.
- Lenters, J. D., and Cook, K. H. (1997). On the origin of the Bolivian high and related circulation features of the South American climate. *Journal of the Atmospheric Sciences* **54**, 656-677.
-

-
- Lorenz, S., Grieger, B., Helbig, P., and Herterich, K. (1996). Investigating the sensitivity of the Atmospheric General Circulation Model ECHAM 3 to paleoclimatic boundary conditions. *Geologische Rundschau* **85**, 513-524.
- Marengo, J. A., Nobre, C. A., McClain, M. E., Victoria, R. L., and Richey, J. E. (2001). General Characteristics and Variability of Climate in the Amazon Basin and its Links to the Global Climate System. In "The Biogeochemistry of the Amazon Basin." pp. 17-41. Oxford University Press, Oxford.
- Maslin, M. A., and Burns, S. J. (2000). Reconstruction of the Amazon Basin effective moisture availability over the past 14,000 years. *Science* **290**, 2285-2287.
- Maslin, M. A., Durham, E., Burns, S. J., Platzman, E., Grootes, P., Greig, S. E. J., Nadeau, M. J., Schleicher, M., Pflaumann, U., Lomax, B., and Rimington, N. (2000). Palaeoreconstruction of the Amazon River freshwater and sediment discharge using sediments recovered at site 942 on the Amazon Fan. *Journal of Quaternary Science* **15**, 419-434.
- Moy, C. M., Seltzer, G. O., Rodbell, D. T., and Anderson, D. M. (2002). Variability of El Niño/Southern Oscillation activity at millennial timescales during the Holocene epoch. *Nature* **420**, 162-165.
- Rodbell, D. T., Seltzer, G. O., Anderson, D. M., Abbott, M. B., Enfield, D. B., and Newman, J. H. (1999). An ~15,000-Year Record of El Niño-Driven Alluviation in Southwestern Ecuador. *Science* **283**, 516-520.
- Seltzer, G. O., Rodbell, D. T., and Burns, S. J. (2000). Isotopic evidence for late Quaternary climatic change in tropical South America. *Geology* **28**, 35-38.
- Servant, M., Maley, J., Turcq, B. J., Absy, M. L., Brenac, P., Fournier, M., and Ledru, M. P. (1993). Tropical forest changes during the late quaternary in African and South American lowlands. *Global and Planetary Change* **7**, 25.
- Sifeddine, A., Martin, L., Trucq, B., Volkmer-Ribeiro, C., Soubies, F., Cordeiro, R. C., and Suguio, K. (2001). Variations of the Amazonian rainforest environment: a sedimentological record covering 30,000 years. *Palaeogeography, Palaeoclimatology, Palaeoecology* **168**, 221-235.
- Sifeddine, A., Spadano Albuquerque, A. L., Ledru, M. P., Trucq, B., Knoppers, B., Martin, L., Zamboni de Mello, W., Passenau, H., Landim Dominguez, J. M., and Campello Cordeiro, R. (2003). A 21000 cal years paleoclimatic record from Caco Lake, northern Brazil: evidence from sedimentary and pollen analyses. *Palaeogeography, Palaeoclimatology, Palaeoecology* **189**, 25-34.
- Thompson, L. G. (2000). Ice core evidence for climate change in the Tropics: implications for our future. *Quaternary Science Reviews* **19**, 19-34.
- Thompson, L. G., Davis, M. E., Mosley-Thompson, E., Sowers, T. A., Henderson, K. A., Zagorodnov, V. S., Lin, P. N., Mikhalenko, V. N., Campen, R. K., Bolzan, J. F., Cole-Dai, J., and Francou, B. (1998). A 25,000-Year Tropical Climate History from Bolivian Ice Cores. *Science* **282**, 1858-1863.
- Thompson, L. G., Mosley-Thompson, E., Davis, M. E., Lin, P. N., Henderson, K. A., Cole-Dai, J., Bolzan, J. F., and Liu, K. B. (1995). Late Glacial Stage and Holocene Tropical Ice Core Records from Huascarán, Peru. *Science* **269**, 46-50.
-

-
- Thompson, L. G., Mosley-Thompson, E., and Henderson, K. A. (2000). Ice-core palaeoclimate records in tropical South America since the Last Glacial Maximum. *Journal of Quaternary Science* **15**, 377-394.
- van der Hammen, T. (1974). The Pleistocene changes of vegetation and climate in tropical South America. *Journal of Biogeography* **1**, 3-26.
- van der Hammen, T., and Absy, M. L. (1994). Amazonia during the last glacial. *Palaeogeography, Palaeoclimatology, Palaeoecology* **109**, 247-261.
- Vuille, M. (1999). Atmospheric Circulation over the Bolivian Altiplano during Dry and Wet Periods and Extreme Phases of the Southern Oscillation. *International Journal of Climatology* **19**, 1579-1600.
- Wang, X., Auler, A. S., Edwards, R. L., Cheng, H., Cristalli, P. S., Smart, P. L., Richards, D. A., and Shen, C.-C. (2004). Wet periods in northeastern Brazil over the past 210 kyr linked to distant climate anomalies. *Nature* **432**, 740-743.
- Wang, X., Auler, A. S., Edwards, R. L., Cheng, H., Shen, C., Smart, P. L., and Richards, D. A. (2003b). Millennial-Scale ITCZ Variability in the Tropical Atlantic and Dynamics of Amazonian Rain Forest. *Eos Transactions AGU, Fall Meeting Supplement* **84 (46)**, Abstract PP22A-1195.
- Wang, X., Auler, A. S., Edwards, R. L., Cheng, H., Smart, P. L., and Richards, D. A. (2003a). Millennial-scale changes in paleopluvial phases inferred from speleothem deposits in northeastern Brazil. *XVI INQUA Congress Conference Abstracts*, Paper No. 21-5.
- Zhou, J., and Lau, K.-M. (1998). Does a Monsoon Climate Exist Over South America? *Journal of Climate* **11**, 1020-1040.
-

9. CONCLUSIONS AND RECOMMENDATIONS FOR FURTHER WORK

9.1 Conclusions

This research has contributed an insight into the palaeoclimatology of the Amazon Basin over the last 40 kyr. The principal aim of this research was to use marine sediments drilled from ODP Site 942 to reconstruct a record of continental palaeoclimate for the Amazon Basin. Assuming the isotope records from Site 942 have monitored a signal of Amazon River discharge, these data were used as a proxy to imply the effective moisture history of the Amazon Basin. Data presented in this thesis have extended and further developed the earlier published records from Site 942 (Maslin and Burns, 2000; Maslin *et al.*, 2000). An enhanced age model for the Site has produced a highly constrained record of tropical climate change throughout the last glacial-interglacial transition (LGIT). Furthermore, the improved chronological constraints on the sediment stratigraphy have provided insights into the depositional regime of the Amazon Fan.

The principal findings of this research are as follows.

1. Down-core $\Delta\delta^{18}\text{O}$ records from Site 942 imply the Amazon Basin was relatively more arid throughout the last glacial, relative to the modern day. Reduced effective moisture levels are also implied for the Younger Dryas (YD), although the high-resolution data presented in this study suggest that the Amazon Basin was becoming increasingly more humid post-onset. This is in contradiction to previously published hypotheses (Maslin and Burns, 2000; Maslin *et al.*, 2000).
2. The 0-40 Cal ka $\Delta\delta^{18}\text{O}_{942}$ record produced in this study compares well to other long-term records of past climate change from tropical and subtropical South America. Analogous trends between these records demonstrate a particular correspondence to precessionally driven changes in solar insolation at 10°S. There is a particular accordance to November-December insolation forcing. This timing is coincident with the modern-day development of the Bolivian High pressure cell, which initiates the onset of the South American summer monsoon (SASM) system over the Amazon Basin. $\Delta\delta^{18}\text{O}_{942}$ records may therefore be monitoring a record of insolation-forced variations in the intensity of the SASM over tropical South America. A gradual insolation-forced enhancement of the SASM can account for the progressively increased levels of effective moisture implied from the early Holocene

to the modern day. However, it is hypothesised that variations in the tropical temperature gradients will govern the northern and southern limits of convection over tropical South America. Therefore the $\Delta\delta^{18}\text{O}_{942}$ records may be monitoring the combined effects of both the *intensity* and the *extent* of the SASM.

3. Trends in the effective moisture reconstruction compare well to records of past temperature variation in Antarctica (Blunier *et al.*, 1998; Blunier *et al.*, 1997). It is hypothesised that tropical temperature gradients in the Southern Hemisphere govern the southern extent of the SASM over tropical South America. This can help to explain the proposed relatively more arid conditions in the Amazon Basin reconstructed for the LGM, despite a similar increased summer insolation forcing to the late Holocene (which would dictate an enhancement in the SASM). During the LGM, steeper temperature gradients in the Southern Hemisphere would have restricted the southerly penetration of the SASM into South America, bringing more arid conditions to the Amazon Basin, relative to the late Holocene.
4. A rigorous sampling strategy through the LGIT has yielded a detailed record spanning the timeframe coincident with the Younger Dryas period in the Northern Hemisphere. Moreover, this section of the record is well constrained by densely spaced AMS radiocarbon ages. The significantly enhanced resolution of the $\Delta\delta^{18}\text{O}$ records from Site 942 have demonstrated that the positive excursion between ~ 12.4 and ~ 11.9 Cal ka was not the most isotopically enriched portion of the record, as previously assumed (Maslin and Burns, 2000; Maslin *et al.*, 2000). Assuming the improved chronology devised in this research is correct, it has determined that timing of the most enriched isotopic values within this section of the record is not coincident with the onset of the YD. Instead, it represents a within-YD oscillation in the $\Delta\delta^{18}\text{O}_{942}$ record, following a period of warming in the southern high latitudes. It is hypothesised that this brief warming phase in Antarctica (asynchronous to temperatures inferred from Greenland) permitted a more southerly penetration of the SASM, and thus moisture, into the Amazon Basin at this time.
5. A period of marked enrichment, and a coincident surge in sediment accumulation imply extreme aridity in the Amazon Basin between ~ 12.8 and ~ 12.7 Cal ka. This period is constrained by four AMS radiocarbon ages, and corresponds well to the timing of the onset of the YD, as determined by $\delta^{18}\text{O}$ records from the GISP2 ice core (Grootes and Stuiver, 1997), and a calendar age chronology for Site 942

assuming a constant ΔR value of -464 ± 40 . Model predictions suggest the Amazon River outflow at this time was less than that predicted for the LGM (30 to 50% reduction compared to 20 to 30% reduction, respectively). It is hypothesised that steeper tropical temperature gradients at the onset of the YD, coupled with summer insolation minima, would have weakened, and reduced the extent of the SASM over the Amazon Basin. The subsequent climatic amelioration in Antarctica, coupled with increasing summer insolation on the Altiplano can provide a plausible explanation for the overall trend of increasing Amazon Basin effective moisture levels reconstructed thereafter, throughout the YD. It is proposed therefore, that the $\Delta\delta^{18}\text{O}_{942}$ data produced in this thesis provide evidence for the existence of northern and southern high latitude-tropical teleconnections at the time of the YD.

6. The 'YD onset' in the $\Delta\delta^{18}\text{O}_{942}$ stratigraphy (as determined by the calendar age chronology) may also be manifested in the other large-scale palaeoclimate records from tropical and subtropical South America. However, except for the Cariaco Basin record (Haug *et al.*, 2001), relatively low data resolution makes this difficult to confirm at present.
7. Similarities between the Holocene $\Delta\delta^{18}\text{O}_{942}$ signal and proxy records of ENSO frequency (Moy *et al.*, 2002) are suggestive of a possible relationship. This is plausible given that precipitation across the Amazon Basin is strongly influenced by modern day ENSO activity. However, the relationship between trends in $\Delta\delta^{18}\text{O}_{942}$ and ENSO frequency remains unclear, as it is difficult to determine the nature of the phasing between the two records.
8. The improved chronology and sample resolution of this study has produced a more detailed record of the LGIT. As a consequence, it has enabled the hypothesised relationship between the extent of tropical wetlands and atmospheric methane records to be examined in more detail. However, the more tightly constrained $\Delta\delta^{18}\text{O}$ records for the LGIT do not imply a phased relationship between changes in tropical South American moisture and global atmospheric methane, regardless of a shift of ± 400 years in the calendar chronology at Site 942.
9. The accumulation of sediments on the Amazon Fan takes place only during periods of low sea level, when the continental shelf is exposed, and the Amazon River extends out to the shelf break. During sea level high-stands, the edge of the

continental shelf is flooded, and sedimentary deposition is focussed relatively further inland (Damuth and Fairbridge, 1970; Damuth and Kumar, 1975). Consequently, the switch between these two depositional states is marked in the stratigraphic record by a transition from predominantly terrigenous, to predominantly hemipelagic sediment. High-resolution dating about the lithostratigraphic boundary of these two sediment-types suggest that deposition of terrestrial sediment ceased on the fan ~11.74 Cal ka. According to records of sea level change (Fairbanks, 1989; Shackleton, 1987), and assuming the Site 942 age chronology is reliable, data produced in this study imply that fan sedimentation was switched 'on' only when sea levels were lower than ~60m below present. This is up to 30m lower than previous suggestions (Maslin *et al.*, 2000; Milliman *et al.*, 1975).

9.2 Recommendations for Further Work

In addition to contributing to a more detailed understanding of tropical South American palaeoclimate, this research has highlighted the requirement for necessary further investigation. Not only is this intended to develop specifically the record produced from the Amazon Fan, but it may also enhance the interpretation of other existing palaeoclimate records both from the tropical and extra-tropical regions. From the data presented in this thesis, further research is recommended as follows.

1. This study attempted to provide a quantified record of past changes in Amazon River outflow. However, the lack of good quality sea surface temperature (SST) records for the Amazon Fan inhibited a down-core reconstruction. The modelling work demonstrated the significance of SST estimates to the approximation of Amazon River outflow, using isotopic balancing models. Cooler SST estimates imply that less of the isotopic shift in $\Delta\delta^{18}\text{O}_{942}$ signal must be forced by freshwater-driven changes in salinity. SST is a critical variable to the inference of the Amazon Basin moisture history from the $\Delta\delta^{18}\text{O}_{942}$ records in this study. Detailed SST profiles will also enable the Amazon River outflow model to be applied down-core, producing a continuous semi-quantitative reconstruction of Amazon River outflow that can be compared to other large-scale palaeoclimate records. Therefore it is recommended that estimations of downcore sea surface temperature be obtained for the Amazon Fan region.

-
2. The $\Delta\delta^{18}\text{O}_{942}$ records produced in this study are assumed to record changes in the relative proportions of Amazon River and tropical Atlantic Ocean water mixed over Site 942. It is assumed that the proportion of Amazon River water 'entering' the $\Delta\delta^{18}\text{O}_{942}$ signal will vary directly with the amount of water discharged. However, the mixing ratio over the site may also be influenced by local hydrographic factors, such as changes in the retroflexion regime of the North Brazil Current (NBC). Moreover, changes in the vertical hydrography of the site (e.g. thermocline depth) may also influence the extent to which the Amazon Outflow signal is being isotopically recorded. Detailed reconstructions of the hydrographic regime specific to Site 942 would therefore provide valuable interpretations of the continental palaeoclimate record produced in this study. Furthermore, the NBC is the only known modern surface water current to cross the equator, and acts as an extremely important vector of heat and salinity between the two hemispheres (Johns *et al.*, 1998; Metcalf and Stalcup, 1967; Richardson and Walsh, 1986). Therefore, variations in the outflow of the Amazon River may have implications for climate change further afield, (e.g. the Caribbean). Reconstructions of the palaeoceanography, specifically the NBC retroflexion, will thus provide valuable additional information to assess the extent to which the effects of climate change in tropical South America may be transferred around the world.

 3. The identification of an apparent Antarctic forcing on the climate of the Amazon Basin presents an exciting direction for tropical palaeoclimate research. It therefore suggests that existing records may have to be re-examined, particularly those which have chronologies tied to Northern Hemisphere records, such as the Andean Ice cores (e.g. Thompson, 2000; Thompson *et al.*, 2000). In order to compare these records to the $\Delta\delta^{18}\text{O}_{942}$ data from this study, it is recommended that their respective age models be re-tuned to a Southern Hemisphere forcing.

 4. The possible discovery of the onset of the YD in the $\Delta\delta^{18}\text{O}_{942}$ data is also significant, as it may enable the determination of possible leads and lags between tropical climate change and that which occurs in the northern and southern high latitudes. It is recommended that this proposed YD onset 'event' be sought in other large-scale proxy records from South America, and where possible, improve the resolution of the data about this period.
-

5. The tentative relationship between inferred Amazon River outflow and ENSO frequency may imply that there is a regional bias in the $\Delta\delta^{18}\text{O}_{942}$ signal. Global climate model reconstructions of river drainage may be able to provide further insight to the interpretation of the $\Delta\delta^{18}\text{O}_{942}$ record.
6. To further investigate the timing of climatic events identified from the Site 942 records, it is necessary to establish the extent of the local difference in radiocarbon reservoir age (ΔR) between the Amazon Fan region of the western tropical Atlantic, and the average global reservoir. It would also be extremely valuable to determine the extent to which ΔR might have varied in the past. Such information would allow the proxy records obtained from the Amazon Fan to be compared to other global climate records with greater confidence.

9.3 References

- Blunier, T., Chappellaz, J., Schwander, J., Dällenbach, A., Stauffer, B., Stocker, T., Raynaud, D., Jouzel, J., Clausen, H. B., Hammer, C. U., and Johnsen, S. J. (1998). Asynchrony of Antarctic and Greenland climate change during the last glacial period. *Nature* **384**, 739-743.
- Blunier, T., Schwander, J., Stauffer, B., Stocker, T., Dällenbach, A., Indermühle, A., Tschumi, J., Chappellaz, J., Raynaud, D., and Barnola, J.-M. (1997). Timing of the Antarctic Cold Reversal and the atmospheric CO_2 increase with respect to the Younger Dryas event. *Geophysical Research Letters* **24**, 2683-2686.
- Damuth, J. E., and Fairbridge, R. W. (1970). Equatorial Atlantic deep-sea arkosic sands and ice-age aridity in tropical South America. *Geological Society of America Bulletin*, 189-206.
- Damuth, J. E., and Kumar, N. (1975). Amazon Cone: Morphology, sediments, age, and growth pattern. *Geological Society of America Bulletin* **86**, 863-878.
- Fairbanks, R. G. (1989). A 17,000 year glacio-eustatic sea level record: influence of glacial melting rates on the Younger Dryas event and deep-ocean circulation. *Nature* **362**, 637-642.
- Grootes, P. M., and Stuiver, M. (1997). Oxygen 18/16 variability in Greenland snow and ice with 10^3 to 10^5 -year time resolution. *Journal of Geophysical Research* **102**, 26455-26470.
- Haug, G. H., Hughen, K. A., Sigman, D. M., Peterson, L. C., and Röhl, U. (2001). Southward Migration of the Intertropical Convergence Zone Through the Holocene. *Science* **293**, 1304-1308.
- Johns, W. E., Lee, T. N., Beardsley, R. C., Candela, J., Limeburner, R., and Castro, B. (1998). Annual cycle and variability of the North Brazil Current. *Journal of Physical Oceanography* **28**, 103-128.

-
- Maslin, M. A., and Burns, S. J. (2000). Reconstruction of the Amazon Basin effective moisture availability over the past 14,000 years. *Science* **290**, 2285-2287.
- Maslin, M. A., Durham, E., Burns, S. J., Platzman, E., Grootes, P., Greig, S. E. J., Nadeau, M. J., Schleicher, M., Pflaumann, U., Lomax, B., and Rimington, N. (2000). Palaeoreconstruction of the Amazon River freshwater and sediment discharge using sediments recovered at site 942 on the Amazon Fan. *Journal of Quaternary Science* **15**, 419-434.
- Metcalf, W., and Stalcup, M. C. (1967). Origin of the Atlantic Equatorial Undercurrent. *Journal of Geophysical Research* **72**, 4959-4975.
- Milliman, J. D., Summerhayes, C. P., and Barretto, H. T. (1975). Quaternary sedimentation on the Amazon continental margin: a model. *Geological Society of America Bulletin* **86**, 610-614.
- Moy, C. M., Seltzer, G. O., Rodbell, D. T., and Anderson, D. M. (2002). Variability of El Nino/Southern Oscillation activity at millennial timescales during the Holocene epoch. *Nature* **420**, 162-165.
- Richardson, P. L., and Walsh, D. (1986). Mapping climatological and seasonal variations of surface currents in the tropical Atlantic using ship drift data. *Journal of Geophysical Research* **91**, 10537-10550.
- Shackleton, N. J. (1987). Oxygen isotopes, ice volume and sea level. *Quaternary Science Reviews* **6**, 183-190.
- Thompson, L. G. (2000). Ice core evidence for climate change in the Tropics: implications for our future. *Quaternary Science Reviews* **19**, 19-34.
- Thompson, L. G., Mosley-Thompson, E., and Henderson, K. A. (2000). Ice-core palaeoclimate records in tropical South America since the Last Glacial Maximum. *Journal of Quaternary Science* **15**, 377-394.

APPENDIX: ISOTOPE DATA
Appendix 1: *G. ruber*

Cal yr BP	Depth (mbsf)	<i>G. ruber</i> $\delta^{18}\text{O}$	<i>G. ruber</i> $\delta^{18}\text{O}$ (normalised)	Smoothed <i>G. ruber</i> $\delta^{18}\text{O}$ (normalised)	$\delta^{18}\text{O}$ (GIV effect)	<i>G. ruber</i> $\Delta\delta^{18}\text{O}$ ($\delta^{18}\text{O}$ - GIV effect)	<i>G. ruber</i> $\Delta\delta^{18}\text{O}$ (normalised)	Smoothed <i>G. ruber</i> $\Delta\delta^{18}\text{O}$ (normalised)
1.00	0.00	-2.04	0.00	0	0.00	-2.04	0.00	0
177.84	0.02	-1.77	0.27	0.15	0.00	-1.77	0.27	0.15
266.26	0.04	-1.85	0.19	0.14	0.00	-1.86	0.18	0.14
354.68	0.05	-2.08	-0.04	0.11	0.01	-2.08	-0.04	0.10
443.11	0.07	-1.88	0.16	0.10	0.01	-1.89	0.16	0.09
531.53	0.08	-1.87	0.17	0.17	0.01	-1.88	0.17	0.17
619.95	0.09	-1.86	0.19	0.11	0.01	-1.87	0.17	0.10
708.37	0.10	-2.06	-0.02	0.14	0.01	-2.07	-0.03	0.12
796.79	0.11	-1.80	0.24	0.15	0.01	-1.81	0.23	0.14
885.21	0.12	-1.81	0.24	0.21	0.01	-1.82	0.22	0.20
973.63	0.13	-1.88	0.16	0.11	0.01	-1.89	0.15	0.10
1062.05	0.14	-2.10	-0.06	0.10	0.01	-2.11	-0.07	0.08
1120.00	0.14	-1.86	0.18	0.03	0.02	-1.88	0.16	0.01
1150.47	0.15	-2.09	-0.05	0.06	0.02	-2.10	-0.06	0.05
1238.89	0.16	-1.98	0.06	0.03	0.02	-2.00	0.04	0.01
1327.32	0.17	-1.98	0.06	0.07	0.02	-2.00	0.05	0.05
1415.74	0.18	-1.97	0.07	0.13	0.02	-1.99	0.05	0.11
1504.16	0.19	-1.79	0.26	0.09	0.02	-1.81	0.23	0.06
1592.58	0.20	-2.11	-0.07	0.12	0.02	-2.13	-0.09	0.10
1679.00	0.21	-1.87	0.17	0.11	0.02	-1.89	0.15	0.09
1681.00	0.21	-1.82	0.22	0.19	0.02	-1.84	0.20	0.16
1785.38	0.22	-1.88	0.16	0.19	0.03	-1.91	0.13	0.16
1887.75	0.23	-1.87	0.17	0.14	0.03	-1.89	0.15	0.11
1889.75	0.23	-1.96	0.08	0.28	0.03	-1.99	0.05	0.25
1994.13	0.24	-1.47	0.58	0.42	0.03	-1.50	0.55	0.39
2097.50	0.25	-1.42	0.62	0.45	0.03	-1.45	0.59	0.42
2098.50	0.25	-1.90	0.15	0.31	0.03	-1.93	0.11	0.27
2202.88	0.26	-1.89	0.15	0.00	0.03	-1.92	0.12	-0.03
2306.25	0.27	-2.34	-0.30	0.05	0.04	-2.38	-0.34	0.02
2307.25	0.27	-1.73	0.31	0.06	0.04	-1.76	0.28	0.03
2409.63	0.28	-1.86	0.18	0.08	0.04	-1.90	0.14	0.04
2410.63	0.28	-2.29	-0.25	0.06	0.04	-2.33	-0.29	0.02
2411.63	0.28	-1.79	0.25	0.12	0.04	-1.83	0.21	0.09
2515.00	0.29	-1.67	0.37	0.28	0.04	-1.71	0.34	0.24
2516.00	0.29	-1.84	0.21	0.24	0.04	-1.87	0.17	0.20
2618.38	0.30	-1.90	0.15	0.17	0.04	-1.94	0.10	0.13

Cal yr BP	Depth (mbsf)	G. ruber $\delta^{18}\text{O}$	G. ruber $\delta^{18}\text{O}$ (normalised)	Smoothed G. ruber $\delta^{18}\text{O}$ (normalised)	$\delta^{18}\text{O}$ (GIV effect)	G. ruber $\Delta\delta^{18}\text{O}$ ($\delta^{18}\text{O}$ - GIV effect)	G. ruber $\Delta\delta^{18}\text{O}$ (normalised)	Smoothed G. ruber $\Delta\delta^{18}\text{O}$ (normalised)
2619.38	0.30	-1.87	0.17	0.16	0.04	-1.91	0.13	0.12
2620.38	0.30	-1.88	0.16	0.20	0.04	-1.92	0.12	0.16
2723.75	0.31	-1.78	0.27	0.21	0.04	-1.82	0.22	0.17
2724.75	0.31	-1.84	0.20	0.24	0.04	-1.88	0.16	0.20
2828.13	0.32	-1.77	0.27	0.28	0.04	-1.82	0.23	0.24
2932.50	0.33	-1.66	0.38	0.33	0.05	-1.71	0.33	0.28
3035.88	0.34	-1.71	0.33	0.30	0.05	-1.75	0.29	0.26
3141.25	0.35	-1.84	0.20	0.32	0.05	-1.89	0.15	0.27
3244.63	0.36	-1.63	0.41	0.40	0.05	-1.68	0.36	0.35
3245.63	0.36	-1.46	0.58	0.48	0.05	-1.51	0.53	0.43
3349.00	0.37	-1.58	0.46	0.58	0.05	-1.64	0.40	0.53
3350.00	0.37	-1.34	0.70	0.56	0.05	-1.40	0.64	0.50
3686.33	0.39	-1.53	0.51	0.47	0.05	-1.58	0.46	0.42
3687.33	0.39	-1.84	0.20	0.34	0.05	-1.89	0.15	0.29
3855.00	0.40	-1.73	0.31	0.28	0.05	-1.78	0.26	0.24
4024.67	0.41	-1.70	0.34	0.39	0.04	-1.74	0.30	0.35
4192.33	0.42	-1.52	0.52	0.43	0.04	-1.56	0.48	0.39
4193.33	0.42	-1.62	0.43	0.43	0.04	-1.66	0.39	0.38
4362.00	0.43	-1.71	0.33	0.34	0.04	-1.75	0.29	0.30
4530.67	0.44	-1.78	0.26	0.30	0.05	-1.83	0.21	0.25
4698.33	0.45	-1.73	0.32	0.28	0.06	-1.78	0.26	0.23
4699.33	0.45	-1.77	0.27	0.32	0.06	-1.82	0.22	0.26
4868.00	0.46	-1.68	0.36	0.31	0.06	-1.74	0.30	0.25
5035.67	0.47	-1.75	0.29	0.34	0.06	-1.81	0.23	0.28
5036.67	0.47	-1.68	0.36	0.29	0.06	-1.74	0.30	0.23
5204.33	0.48	-1.83	0.22	0.32	0.06	-1.88	0.16	0.26
5205.33	0.48	-1.65	0.39	0.31	0.06	-1.71	0.33	0.25
5374.00	0.49	-1.71	0.33	0.27	0.06	-1.77	0.27	0.21
5541.67	0.50	-1.96	0.08	0.20	0.06	-2.02	0.02	0.14
5542.67	0.50	-1.86	0.18	0.18	0.06	-1.92	0.12	0.12
5710.33	0.51	-1.75	0.29	0.30	0.07	-1.82	0.22	0.24
5711.33	0.51	-1.60	0.44	0.54	0.07	-1.67	0.37	0.47
5879.00	0.52	-1.15	0.89	0.57	0.07	-1.23	0.81	0.50
5880.00	0.52	-1.65	0.39	0.55	0.07	-1.73	0.31	0.47
6046.36	0.53	-1.68	0.36	0.43	0.09	-1.77	0.27	0.33
6211.73	0.54	-1.50	0.54	0.43	0.12	-1.62	0.42	0.31
6212.73	0.54	-1.67	0.38	0.48	0.13	-1.79	0.25	0.35

Cal yr BP	Depth (mbsf)	G. ruber $\delta^{18}\text{O}$	G. ruber $\delta^{18}\text{O}$ (normalised)	Smoothed G. ruber $\delta^{18}\text{O}$ (normalised)	$\delta^{18}\text{O}$ (GIV effect)	G. ruber $\Delta\delta^{18}\text{O}$ ($\delta^{18}\text{O}$ - GIV effect)	G. ruber $\Delta\delta^{18}\text{O}$ (normalised)	Smoothed G. ruber $\Delta\delta^{18}\text{O}$ (normalised)
6379.09	0.55	-1.51	0.53	0.45	0.14	-1.65	0.39	0.31
6545.45	0.56	-1.60	0.44	0.45	0.14	-1.74	0.30	0.31
6711.82	0.57	-1.67	0.37	0.42	0.14	-1.80	0.24	0.28
6878.18	0.58	-1.61	0.43	0.47	0.13	-1.74	0.30	0.34
7043.55	0.59	-1.42	0.62	0.50	0.12	-1.54	0.50	0.38
7044.55	0.59	-1.58	0.46	0.55	0.12	-1.70	0.34	0.43
7209.91	0.60	-1.48	0.56	0.53	0.12	-1.60	0.44	0.41
7210.91	0.60	-1.48	0.56	0.56	0.12	-1.60	0.44	0.43
7377.27	0.61	-1.49	0.55	0.65	0.14	-1.63	0.41	0.52
7542.64	0.62	-1.18	0.86	0.63	0.16	-1.34	0.70	0.48
7543.64	0.62	-1.57	0.47	0.73	0.16	-1.72	0.32	0.56
7709.00	0.63	-1.19	0.85	0.66	0.18	-1.37	0.67	0.48
7710.00	0.63	-1.40	0.64	0.71	0.18	-1.58	0.46	0.53
7890.91	0.64	-1.39	0.65	0.65	0.19	-1.59	0.45	0.46
8071.82	0.65	-1.38	0.66	0.67	0.21	-1.59	0.45	0.47
8206.50	0.65	-1.33	0.71	0.59	0.22	-1.55	0.49	0.38
8252.73	0.66	-1.64	0.41	0.57	0.22	-1.86	0.18	0.34
8433.64	0.67	-1.45	0.59	0.58	0.24	-1.69	0.35	0.35
8455.25	0.66	-1.30	0.74	0.59	0.24	-1.54	0.50	0.35
8614.55	0.68	-1.60	0.44	0.75	0.25	-1.85	0.19	0.48
8952.75	0.69	-0.98	1.06	0.78	0.32	-1.29	0.75	0.48
8976.36	0.70	-1.22	0.82	0.84	0.32	-1.54	0.51	0.52
9157.27	0.71	-1.41	0.64	0.73	0.33	-1.74	0.30	0.40
9338.18	0.72	-1.31	0.73	0.66	0.35	-1.66	0.38	0.31
9450.25	0.73	-1.43	0.61	0.68	0.37	-1.80	0.24	0.31
9519.09	0.73	-1.35	0.69	0.70	0.38	-1.73	0.31	0.30
9699.00	0.74	-1.24	0.80	0.81	0.44	-1.68	0.36	0.39
9700.00	0.74	-1.11	0.93	0.79	0.44	-1.55	0.49	0.34
9830.91	0.75	-1.40	0.64	0.84	0.48	-1.88	0.16	0.35
9961.82	0.76	-1.10	0.94	0.77	0.52	-1.63	0.41	0.25
10091.73	0.77	-1.31	0.73	0.82	0.54	-1.85	0.19	0.28
10092.73	0.77	-1.26	0.78	0.82	0.54	-1.80	0.24	0.28
10223.64	0.78	-1.08	0.97	0.81	0.55	-1.62	0.42	0.26
10353.55	0.79	-1.35	0.69	0.81	0.56	-1.91	0.13	0.26
10354.55	0.79	-1.26	0.78	0.85	0.56	-1.82	0.22	0.29
10485.45	0.80	-0.96	1.08	0.85	0.57	-1.53	0.51	0.28
10615.36	0.81	-1.35	0.69	0.78	0.58	-1.94	0.10	0.20

Cal yr BP	Depth (mbsf)	G. ruber $\delta^{18}\text{O}$	G. ruber $\delta^{18}\text{O}$ (normalised)	Smoothed G. ruber $\delta^{18}\text{O}$ (normalised)	$\delta^{18}\text{O}$ (GIV effect)	G. ruber $\Delta\delta^{18}\text{O}$ ($\delta^{18}\text{O}$ - GIV effect)	G. ruber $\Delta\delta^{18}\text{O}$ (normalised)	Smoothed G. ruber $\Delta\delta^{18}\text{O}$ (normalised)
10616.36	0.81	-1.47	0.57	0.79	0.58	-2.05	-0.01	0.20
10747.27	0.82	-0.93	1.11	0.82	0.60	-1.54	0.50	0.22
10877.18	0.83	-1.26	0.78	0.94	0.63	-1.89	0.15	0.32
10878.18	0.83	-1.10	0.94	0.85	0.63	-1.73	0.32	0.21
11008.09	0.84	-1.21	0.83	0.99	0.66	-1.87	0.17	0.34
11009.09	0.84	-0.85	1.19	0.91	0.66	-1.51	0.53	0.25
11139.00	0.85	-1.32	0.72	1.02	0.69	-2.00	0.04	0.34
11140.00	0.85	-0.90	1.14	0.91	0.69	-1.58	0.46	0.21
11439.00	0.87	-1.19	0.85	1.02	0.73	-1.92	0.12	0.31
11440.00	0.87	-0.97	1.07	1.03	0.73	-1.70	0.34	0.29
11739.00	0.89	-0.88	1.16	1.00	0.75	-1.63	0.41	0.26
11740.00	0.89	-1.27	0.77	1.00	0.75	-2.02	0.02	0.25
11776.50	0.90	-0.97	1.07	0.74	0.75	-1.72	0.32	-0.01
11777.50	0.90	-1.66	0.38	0.78	0.75	-2.42	-0.37	0.02
11851.50	0.92	-1.15	0.89	0.73	0.76	-1.92	0.12	-0.03
11889.00	0.93	-1.12	0.92	0.99	0.77	-1.89	0.15	0.22
11894.29	0.94	-0.87	1.17	1.09	0.77	-1.64	0.40	0.32
11897.82	0.95	-0.86	1.18	1.14	0.77	-1.63	0.41	0.36
11955.68	0.96	-0.98	1.06	1.15	0.78	-1.76	0.28	0.37
12043.24	1.00	-0.84	1.20	1.12	0.79	-1.63	0.41	0.33
12059.00	1.01	-0.89	1.15	1.10	0.79	-1.69	0.36	0.30
12108.92	1.03	-1.05	0.99	1.10	0.79	-1.85	0.19	0.29
12196.49	1.07	-0.96	1.08	1.11	0.80	-1.76	0.28	0.29
12284.05	1.11	-1.02	1.03	1.12	0.83	-1.85	0.19	0.30
12299.00	1.12	-0.75	1.29	1.11	0.84	-1.59	0.45	0.30
12349.73	1.14	-0.79	1.25	1.13	0.86	-1.64	0.40	0.20
12415.41	1.17	-1.01	1.03	1.15	0.88	-1.89	0.15	0.30
12499.00	1.25	-1.34	0.70	1.22	0.91	-2.25	-0.21	0.30
12546.76	1.23	-0.39	1.65	1.24	0.92	-1.31	0.73	0.35
12634.32	1.27	-0.66	1.38	1.31	0.94	-1.60	0.44	0.33
12699.00	1.30	-0.48	1.57	1.32	0.94	-1.42	0.63	0.46
12701.09	1.32	-1.03	1.01	1.30	0.94	-1.97	0.07	0.35
12704.36	1.38	-0.65	1.39	1.22	0.94	-1.59	0.45	0.28
12704.45	1.40	-0.92	1.12	1.20	0.94	-1.86	0.18	0.22
12706.55	1.42	-1.03	1.01	1.25	0.94	-1.97	0.07	0.28
12707.18	1.45	-0.77	1.27	1.30	0.94	-1.71	0.33	0.42
12709.82	1.48	-0.71	1.33	1.34	0.94	-1.65	0.39	0.39

Cal yr BP	Depth (mbsf)	G. ruber $\delta^{18}\text{O}$	G. ruber $\delta^{18}\text{O}$ (normalised)	Smoothed G. ruber $\delta^{18}\text{O}$ (normalised)	$\delta^{18}\text{O}$ (GIV effect)	G. ruber $\Delta\delta^{18}\text{O}$ ($\delta^{18}\text{O}$ - GIV effect)	G. ruber $\Delta\delta^{18}\text{O}$ (normalised)	Smoothed G. ruber $\Delta\delta^{18}\text{O}$ (normalised)
12709.91	1.50	0.04	2.08	1.33	0.94	-0.90	1.14	0.39
12712.55	1.53	-1.09	0.95	1.36	0.94	-2.03	0.01	0.40
12715.27	1.58	-1.00	1.04	1.32	0.94	-1.94	0.10	0.46
12718.00	1.63	-0.74	1.30	1.24	0.94	-1.68	0.36	0.27
12718.09	1.65	-0.41	1.63	1.18	0.94	-1.35	0.69	0.18
12720.73	1.68	-0.92	1.12	1.18	0.94	-1.86	0.18	0.26
12723.55	1.75	-1.52	0.52	1.24	0.94	-2.46	-0.42	0.27
12726.18	1.78	-0.60	1.44	1.28	0.94	-1.54	0.50	0.36
12728.91	1.83	-0.72	1.32	1.36	0.94	-1.66	0.38	0.39
12729.00	1.85	0.06	2.11	1.46	0.94	-0.88	1.17	0.53
12732.40	1.88	-0.80	1.24	1.58	0.94	-1.74	0.30	0.64
12736.40	1.93	-0.82	1.22	1.59	0.94	-1.76	0.28	0.75
12737.33	1.95	-0.01	2.03	1.59	0.94	-0.95	1.09	0.55
12740.40	1.98	-0.20	1.85	1.56	0.94	-1.14	0.91	0.66
12748.40	2.08	-0.93	1.11	1.52	0.94	-1.87	0.17	0.64
12751.81	2.13	-0.25	1.79	1.41	0.94	-1.19	0.85	0.45
12754.82	2.18	-0.88	1.16	1.37	0.94	-1.82	0.22	0.32
12757.83	2.23	-0.99	1.06	1.38	0.94	-1.93	0.12	0.53
12760.84	2.28	-0.85	1.19	1.42	0.94	-1.79	0.25	0.47
12763.86	2.33	-0.52	1.52	1.50	0.94	-1.46	0.58	0.58
12766.87	2.38	-1.11	0.93	1.54	0.94	-2.05	-0.01	0.66
12769.22	2.46	-0.24	1.80	1.56	0.94	-1.18	0.86	0.57
12769.88	2.43	-0.43	1.61	1.59	0.94	-1.37	0.67	0.61
12772.89	2.48	-0.34	1.70	1.66	0.94	-1.28	0.76	0.78
12775.90	2.53	-0.33	1.71	1.69	0.94	-1.27	0.77	0.77
12779.90	2.59	-0.27	1.77	1.59	0.94	-1.21	0.83	0.69
12785.52	2.69	-0.28	1.76	1.48	0.94	-1.22	0.82	0.48
12787.95	2.73	-0.85	1.20	1.35	0.94	-1.79	0.26	0.46
12790.96	2.78	-1.36	0.68	1.28	0.94	-2.30	-0.26	0.30
12791.13	2.79	-0.46	1.58	1.25	0.94	-1.40	0.64	0.26
12793.98	2.83	-1.06	0.98	1.23	0.94	-2.00	0.04	0.36
12796.75	2.89	-0.47	1.57	1.21	0.94	-1.41	0.63	0.25
12796.99	2.88	-0.37	1.67	1.18	0.94	-1.31	0.73	0.21
12885.59	2.98	-0.66	1.38	1.09	0.95	-1.60	0.44	0.18
13056.78	3.08	-0.80	1.24	1.09	0.96	-1.76	0.28	-0.02
13142.37	3.13	-0.82	1.22	1.10	0.97	-1.78	0.26	0.22
13227.97	3.18	-1.35	0.69	1.20	0.97	-2.32	-0.28	0.20

Cal yr BP	Depth (mbsf)	G. ruber $\delta^{18}\text{O}$	G. ruber $\delta^{18}\text{O}$ (normalised)	Smoothed G. ruber $\delta^{18}\text{O}$ (normalised)	$\delta^{18}\text{O}$ (GIV effect)	G. ruber $\Delta\delta^{18}\text{O}$ ($\delta^{18}\text{O}$ - GIV effect)	G. ruber $\Delta\delta^{18}\text{O}$ (normalised)	Smoothed G. ruber $\Delta\delta^{18}\text{O}$ (normalised)
13246.05	3.20	-0.65	1.39	1.24	0.97	-1.62	0.42	0.27
13313.56	3.23	-0.75	1.30	1.34	0.98	-1.72	0.32	0.32
13399.15	3.28	-0.44	1.61	1.41	0.98	-1.42	0.62	0.51
13411.62	3.30	-0.54	1.50	1.47	0.99	-1.53	0.52	0.45
13484.75	3.33	-0.39	1.65	1.48	0.99	-1.38	0.66	0.49
13570.34	3.38	-0.90	1.14	1.49	1.00	-1.90	0.14	0.52
13577.20	3.40	-0.52	1.52	1.47	1.00	-1.52	0.53	0.46
13741.53	3.48	-0.28	1.76	1.44	1.00	-1.29	0.75	0.44
13742.77	3.49	-0.82	1.23	1.42	1.01	-1.83	0.22	0.42
13846.20	3.58	-0.44	1.60	1.34	1.01	-1.45	0.59	0.36
13850.43	3.58	-1.02	1.02	1.33	1.02	-2.04	0.00	0.21
13884.13	3.63	-0.77	1.27	1.31	1.02	-1.80	0.25	0.37
13914.40	3.69	-1.02	1.02	1.34	1.02	-2.05	-0.01	0.29
13917.83	3.68	0.01	2.05	1.36	1.02	-1.01	1.03	0.29
13951.52	3.73	-0.85	1.19	1.41	1.03	-1.88	0.17	0.42
13970.20	3.78	-0.99	1.05	1.45	1.03	-2.01	0.03	0.45
13985.22	3.78	-0.15	1.89	1.44	1.03	-1.18	0.86	0.40
14018.91	3.83	-0.84	1.21	1.48	1.03	-1.87	0.18	0.39
14032.20	3.86	-0.22	1.82	1.52	1.03	-1.25	0.79	0.55
14052.61	3.88	-0.94	1.11	1.58	1.03	-1.97	0.08	0.53
14086.30	3.93	-0.16	1.88	1.57	1.03	-1.19	0.85	0.56
14120.00	3.98	-0.24	1.80	1.55	1.03	-1.27	0.77	0.54
14207.50	4.03	-0.72	1.32	1.48	1.03	-1.75	0.29	0.48
14245.00	4.07	-0.31	1.73	1.43	1.03	-1.34	0.70	0.33
14295.00	4.08	-1.25	0.79	1.39	1.03	-2.28	-0.24	0.39
14350.00	4.13	-0.91	1.14	1.36	1.03	-1.94	0.10	0.38
14383.33	4.18	0.05	2.10	1.33	1.03	-0.98	1.07	0.22
14450.00	4.28	-0.74	1.30	1.36	1.03	-1.77	0.27	0.29
14483.33	4.33	-1.09	0.95	1.41	1.03	-2.13	-0.09	0.49
14516.67	4.38	-0.93	1.11	1.40	1.03	-1.97	0.07	0.35
14550.00	4.43	0.11	2.15	1.35	1.04	-0.93	1.11	0.27
14616.67	4.53	-0.65	1.39	1.33	1.04	-1.68	0.36	0.32
14650.00	4.58	-1.10	0.94	1.26	1.04	-2.14	-0.10	0.30
14783.33	4.78	-0.86	1.18	1.14	1.04	-1.90	0.14	0.05
14816.67	4.83	-1.01	1.04	1.04	1.05	-2.05	-0.01	-0.07
14850.00	4.88	-1.11	0.94	1.01	1.06	-2.16	-0.12	-0.03
14935.00	4.93	-1.23	0.81	1.03	1.06	-2.29	-0.25	-0.03

Cal yr BP	Depth (mbsf)	G. ruber $\delta^{18}\text{O}$	G. ruber $\delta^{18}\text{O}$ (normalised)	Smoothed G. ruber $\delta^{18}\text{O}$ (normalised)	$\delta^{18}\text{O}$ (GIV effect)	G. ruber $\Delta\delta^{18}\text{O}$ ($\delta^{18}\text{O}$ - GIV effect)	G. ruber $\Delta\delta^{18}\text{O}$ (normalised)	Smoothed G. ruber $\Delta\delta^{18}\text{O}$ (normalised)
15020.00	4.98	-0.88	1.16	1.04	1.06	-1.94	0.10	-0.03
15105.00	5.03	-0.87	1.18	1.08	1.06	-1.93	0.11	0.01
15190.00	5.08	-0.98	1.06	1.12	1.06	-2.04	0.00	0.09
15275.00	5.13	-0.90	1.14	1.14	1.06	-1.96	0.08	0.07
15360.00	5.18	-0.82	1.22	1.15	1.06	-1.88	0.16	0.08
15445.00	5.23	-0.98	1.06	1.18	1.06	-2.04	0.00	0.12
15530.00	5.28	-0.80	1.24	1.23	1.06	-1.86	0.18	0.17
15710.00	5.33	-0.80	1.24	1.27	1.06	-1.85	0.19	0.21
15890.00	5.38	-0.69	1.35	1.29	1.06	-1.74	0.30	0.19
16430.00	5.53	-0.51	1.54	1.54	1.14	-1.64	0.40	0.18
16610.00	5.58	-0.97	1.08	1.08	1.17	-2.14	-0.09	0.27
16726.15	5.63	-0.72	1.32	1.32	1.19	-1.92	0.13	0.37
17190.77	5.83	-0.26	1.78	1.78	1.16	-1.42	0.62	0.39
17306.92	5.88	-0.10	1.94	1.94	1.15	-1.25	0.79	0.59
17423.08	5.93	-0.37	1.67	1.67	1.15	-1.52	0.52	0.73
17655.38	6.03	0.05	2.09	2.09	1.19	-1.14	0.90	0.78
17771.54	6.08	-0.03	2.01	2.01	1.20	-1.24	0.80	0.76
17887.69	6.13	0.07	2.11	2.11	1.22	-1.15	0.89	0.82
18003.85	6.18	-0.12	1.92	1.92	1.24	-1.36	0.68	0.75
18120.00	6.23	0.05	2.09	2.09	1.24	-1.19	0.85	0.75
18332.86	6.28	-0.26	1.78	1.78	1.23	-1.49	0.55	0.71
18545.71	6.33	-0.03	2.01	2.01	1.21	-1.24	0.80	0.71
18971.43	6.43	-0.19	1.85	1.85	1.17	-1.36	0.68	0.68
19184.29	6.48	-0.20	1.84	1.84	1.16	-1.37	0.67	0.72
19397.14	6.53	-0.21	1.83	1.83	1.16	-1.36	0.68	0.65
19610.00	6.58	-0.15	1.89	1.89	1.15	-1.29	0.75	0.60
20390.00	6.83	-0.39	1.65	1.65	1.19	-1.58	0.46	0.60
20702.00	6.93	-0.41	1.63	1.63	1.21	-1.62	0.42	0.54
20858.00	6.98	-0.13	1.91	1.91	1.22	-1.36	0.69	0.49
21014.00	7.03	-0.44	1.60	1.60	1.23	-1.67	0.37	0.51
21170.00	7.08	-0.30	1.74	1.74	1.22	-1.52	0.52	0.55
21390.00	7.13	-0.25	1.79	1.79	1.22	-1.48	0.57	0.56
21660.00	7.20	-0.23	1.82	1.82	1.22	-1.44	0.60	0.67
22886.67	7.60	-0.17	1.87	1.87	1.11	-1.28	0.76	0.75
23040.00	7.65	-0.01	2.03	2.03	1.13	-1.14	0.90	0.83
23346.67	7.75	0.00	2.04	2.04	1.14	-1.14	0.90	0.84
23500.00	7.80	0.03	2.07	2.07	1.10	-1.07	0.97	0.80

Cal yr BP	Depth (mbsf)	G. ruber $\delta^{18}\text{O}$	G. ruber $\delta^{18}\text{O}$ (normalised)	Smoothed G. ruber $\delta^{18}\text{O}$ (normalised)	$\delta^{18}\text{O}$ (GIV effect)	G. ruber $\Delta\delta^{18}\text{O}$ ($\delta^{18}\text{O}$ - GIV effect)	G. ruber $\Delta\delta^{18}\text{O}$ (normalised)	Smoothed G. ruber $\Delta\delta^{18}\text{O}$ (normalised)
23653.33	7.85	-0.32	1.72	1.72	1.06	-1.38	0.66	0.71
23806.67	7.90	-0.44	1.60	1.60	1.03	-1.48	0.56	0.61
24152.50	8.00	-0.50	1.54	1.54	1.09	-1.59	0.45	0.52
24537.50	8.10	-0.51	1.53	1.53	1.12	-1.63	0.41	0.51
24730.00	8.15	-0.32	1.72	1.72	1.10	-1.42	0.62	0.57
24922.50	8.20	-0.24	1.80	1.80	1.09	-1.33	0.71	0.62
25115.00	8.25	-0.35	1.70	1.70	1.10	-1.45	0.59	0.64
25307.50	8.30	-0.28	1.76	1.76	1.11	-1.39	0.65	0.67
25500.00	8.35	-0.31	1.73	1.73	1.10	-1.41	0.63	0.67
25808.33	8.40	-0.16	1.88	1.88	1.11	-1.27	0.77	0.71
26425.00	8.50	-0.20	1.84	1.84	1.12	-1.32	0.72	0.75
26733.33	8.55	-0.20	1.84	1.84	1.09	-1.29	0.75	0.81
27350.00	8.65	-0.14	1.90	1.90	1.01	-1.15	0.89	0.78
27662.50	8.80	-0.17	1.87	1.87	0.96	-1.14	0.90	0.73
27975.00	8.95	-0.39	1.65	1.65	1.00	-1.39	0.65	0.73
28037.50	8.98	-0.59	1.45	1.45	1.01	-1.59	0.45	0.72
28599.00	9.25	-0.23	1.81	1.81	1.03	-1.27	0.77	0.64
28799.00	9.34	-0.25	1.79	1.79	1.00	-1.24	0.80	0.63
30034.29	9.70	-0.60	1.44	1.44	0.90	-1.51	0.53	0.73
30446.06	9.77	-0.58	1.46	1.46	0.88	-1.46	0.58	0.77
30940.18	10.00	-0.18	1.86	1.86	0.90	-1.08	0.96	0.77
31492.31	10.10	-0.29	1.75	1.75	0.80	-1.09	0.95	0.83
31599.00	10.13	-0.40	1.64	1.64	0.80	-1.20	0.84	0.89
31682.76	10.15	-0.40	1.64	1.64	0.80	-1.20	0.84	0.85
31889.66	10.20	-0.39	1.65	1.65	0.80	-1.20	0.84	0.81
32096.55	10.25	-0.46	1.58	1.58	0.80	-1.26	0.78	0.83
32253.55	10.29	-0.47	1.57	1.57	0.80	-1.27	0.77	0.82
32303.45	10.30	-0.30	1.74	1.74	0.80	-1.10	0.94	0.83
32510.34	10.35	-0.46	1.59	1.59	0.80	-1.25	0.79	0.83
32717.24	10.40	-0.40	1.65	1.65	0.79	-1.18	0.86	0.85
32799.00	10.42	-0.44	1.60	1.60	0.78	-1.22	0.82	0.86
32920.00	10.45	-0.44	1.60	1.60	0.75	-1.19	0.85	0.95
33040.00	10.48	-0.31	1.73	1.73	0.73	-1.04	1.00	0.93
33199.00	10.51	-0.10	1.94	1.94	0.71	-0.81	1.23	0.96
33599.00	10.62	-0.52	1.52	1.52	0.76	-1.28	0.76	0.97
33960.54	10.82	-0.29	1.75	1.75	0.78	-1.07	0.97	0.90
34322.08	11.02	-0.36	1.68	1.68	0.80	-1.16	0.88	0.78

34683.62	11.22	-0.58	1.46	1.46	0.82	-1.41	0.63	0.72
35045.15	11.42	-0.52	1.52	1.52	0.89	-1.41	0.63	0.72
35551.31	11.78	-0.77	1.27	1.27	0.80	-1.56	0.48	0.66
35949.00	12.00	-0.33	1.71	1.71	0.74	-1.07	0.97	0.61
36269.31	12.27	-0.58	1.46	1.46	0.89	-1.47	0.57	0.58
36589.63	12.47	-0.71	1.33	1.33	0.91	-1.62	0.42	0.65
36909.94	12.67	-0.81	1.23	1.23	0.79	-1.60	0.44	0.61
37230.25	12.89	-0.48	1.56	1.56	0.69	-1.17	0.87	0.65
37550.56	13.02	-0.62	1.42	1.42	0.66	-1.28	0.76	0.77
37999.00	13.27	-0.55	1.49	1.49	0.71	-1.26	0.79	0.86
38991.16	13.49	-0.39	1.66	1.66	0.68	-1.07	0.98	0.84
39893.12	13.69	-0.48	1.57	1.57	0.64	-1.12	0.92	0.82

Appendix 2: *G. sacculifer* (sac form)

Cal yr BP	Depth (mbsf)	<i>G. sacculifer</i> (sac) $\delta^{18}\text{O}$	<i>G. sacculifer</i> (sac) $\delta^{18}\text{O}$ (normalised)	Smoothed <i>G. sacculifer</i> (sac) $\delta^{18}\text{O}$ (normalised)	$\delta^{18}\text{O}$ (GIV effect)	<i>G. sacculifer</i> (sac) $\Delta\delta^{18}\text{O}$ ($\delta^{18}\text{O}$ - GIV effect)	<i>G. sacculifer</i> (sac) $\Delta\delta^{18}\text{O}$ (normalised)	Smoothed <i>G. sacculifer</i> (sac) $\Delta\delta^{18}\text{O}$ (normalised)
1.00	0.00	-1.69	0.00	0	0.00	-1.69	0.00	0
89.42	0.01	-1.52	0.17	0.02	0.00	-1.52	0.16	0.02
177.84	0.02	-1.79	-0.11	0.06	0.00	-1.79	-0.11	0.05
266.26	0.04	-1.58	0.11	0.01	0.00	-1.58	0.10	0.01
354.68	0.05	-1.65	0.03	0.10	0.01	-1.66	0.03	0.10
443.11	0.07	-1.52	0.17	0.08	0.01	-1.53	0.16	0.08
531.53	0.08	-1.63	0.06	0.04	0.01	-1.64	0.05	0.03
619.95	0.09	-1.78	-0.09	0.04	0.01	-1.79	-0.10	0.03
708.37	0.10	-1.53	0.15	0.04	0.01	-1.55	0.14	0.03
796.79	0.11	-1.62	0.06	0.10	0.01	-1.63	0.05	0.09
885.21	0.12	-1.59	0.09	0.08	0.01	-1.60	0.08	0.07
1062.05	0.14	-1.59	0.09	0.13	0.01	-1.61	0.08	0.12
1150.47	0.15	-1.48	0.20	0.18	0.02	-1.50	0.19	0.16
1238.89	0.16	-1.45	0.24	0.23	0.02	-1.47	0.22	0.21
1327.32	0.17	-1.45	0.24	0.18	0.02	-1.47	0.22	0.16
1415.74	0.18	-1.62	0.06	0.13	0.02	-1.64	0.04	0.11
1504.16	0.19	-1.59	0.09	0.10	0.02	-1.61	0.07	0.08
1679.00	0.21	-1.54	0.14	0.19	0.02	-1.57	0.12	0.16
1681.00	0.21	-1.36	0.33	0.18	0.02	-1.38	0.31	0.15
1785.38	0.22	-1.62	0.06	0.19	0.03	-1.65	0.04	0.16
1887.75	0.23	-1.52	0.16	0.10	0.03	-1.55	0.14	0.07
1889.75	0.23	-1.62	0.06	0.12	0.03	-1.65	0.04	0.09
1992.13	0.24	-1.55	0.13	0.11	0.03	-1.58	0.10	0.08
1994.13	0.24	-1.55	0.14	0.07	0.03	-1.58	0.11	0.04
2097.50	0.25	-1.73	-0.05	0.12	0.03	-1.76	-0.08	0.09
2098.50	0.25	-1.41	0.28	0.10	0.03	-1.44	0.25	0.07
2200.88	0.26	-1.61	0.08	0.12	0.03	-1.64	0.04	0.09
2202.88	0.26	-1.68	0.00	0.12	0.03	-1.72	-0.03	0.08
2307.25	0.27	-1.41	0.28	0.12	0.04	-1.45	0.24	0.08
2409.63	0.28	-1.62	0.07	0.15	0.04	-1.66	0.03	0.12
2411.63	0.28	-1.57	0.11	0.09	0.04	-1.61	0.08	0.05
2515.00	0.29	-1.60	0.08	0.13	0.04	-1.64	0.04	0.10
2516.00	0.29	-1.48	0.21	0.13	0.04	-1.52	0.17	0.09
2618.38	0.30	-1.59	0.10	0.24	0.04	-1.63	0.06	0.20
2619.38	0.30	-1.28	0.40	0.23	0.04	-1.32	0.36	0.19
2620.38	0.30	-1.48	0.20	0.34	0.04	-1.52	0.16	0.30

Cal yr BP	Depth (mbsf)	G. sacculifer (sac) $\delta^{18}\text{O}$	G. sacculifer (sac) $\delta^{18}\text{O}$ (normalised)	Smoothed G. sacculifer (sac) $\delta^{18}\text{O}$ (normalised)	$\delta^{18}\text{O}$ (GIV effect)	G. sacculifer (sac) $\Delta\delta^{18}\text{O}$ ($\delta^{18}\text{O}$ - GIV effect)	G. sacculifer (sac) $\Delta\delta^{18}\text{O}$ (normalised)	Smoothed G. sacculifer (sac) $\Delta\delta^{18}\text{O}$ (normalised)
2723.75	0.31	-1.26	0.42	0.26	0.04	-1.31	0.38	0.22
2724.75	0.31	-1.54	0.15	0.21	0.04	-1.58	0.11	0.17
2828.13	0.32	-1.63	0.05	0.13	0.04	-1.68	0.01	0.08
2932.50	0.33	-1.51	0.18	0.18	0.05	-1.56	0.13	0.14
3035.88	0.34	-1.36	0.32	0.19	0.05	-1.41	0.27	0.14
3141.25	0.35	-1.63	0.06	0.19	0.05	-1.68	0.01	0.14
3244.63	0.36	-1.50	0.19	0.10	0.05	-1.55	0.14	0.05
3245.63	0.36	-1.63	0.06	0.15	0.05	-1.68	0.01	0.10
3349.00	0.37	-1.49	0.20	0.16	0.05	-1.54	0.14	0.11
3518.67	0.38	-1.46	0.22	0.20	0.05	-1.52	0.17	0.15
3686.33	0.39	-1.49	0.20	0.18	0.05	-1.54	0.15	0.13
3687.33	0.39	-1.57	0.12	0.15	0.05	-1.62	0.07	0.10
3855.00	0.40	-1.55	0.14	0.10	0.05	-1.60	0.09	0.05
4024.67	0.41	-1.65	0.04	0.12	0.04	-1.69	0.00	0.08
4192.33	0.42	-1.50	0.18	0.06	0.04	-1.54	0.14	0.02
4193.33	0.42	-1.74	-0.05	0.09	0.04	-1.78	-0.09	0.04
4362.00	0.43	-1.56	0.13	0.07	0.04	-1.60	0.08	0.03
4530.67	0.44	-1.54	0.14	0.13	0.05	-1.59	0.09	0.08
4698.33	0.45	-1.56	0.13	0.16	0.06	-1.61	0.07	0.11
4699.33	0.45	-1.47	0.22	0.17	0.06	-1.52	0.16	0.12
4868.00	0.46	-1.52	0.17	0.25	0.06	-1.58	0.11	0.19
5035.67	0.47	-1.33	0.35	0.19	0.06	-1.39	0.29	0.13
5036.67	0.47	-1.64	0.05	0.17	0.06	-1.70	-0.01	0.11
5204.33	0.48	-1.57	0.11	0.12	0.06	-1.63	0.05	0.06
5205.33	0.48	-1.48	0.20	0.21	0.06	-1.54	0.15	0.15
5374.00	0.49	-1.39	0.30	0.17	0.06	-1.45	0.24	0.11
5541.67	0.50	-1.68	0.00	0.09	0.06	-1.75	-0.06	0.03
5542.67	0.50	-1.70	-0.02	0.04	0.06	-1.77	-0.08	-0.02
5710.33	0.51	-1.54	0.14	0.10	0.07	-1.61	0.08	0.04
5711.33	0.51	-1.50	0.18	0.24	0.07	-1.57	0.11	0.17
5879.00	0.52	-1.30	0.38	0.23	0.07	-1.38	0.31	0.16
5880.00	0.52	-1.56	0.13	0.29	0.07	-1.63	0.06	0.21
6046.36	0.53	-1.33	0.36	0.28	0.09	-1.42	0.27	0.18
6211.73	0.54	-1.34	0.34	0.35	0.12	-1.47	0.22	0.23
6212.73	0.54	-1.35	0.34	0.25	0.13	-1.47	0.21	0.12
6379.09	0.55	-1.62	0.06	0.26	0.14	-1.76	-0.08	0.12
6544.45	0.56	-1.32	0.37	0.16	0.14	-1.46	0.23	0.02

6545.45	Cal yr BP	0.56	Depth (mbsf)	-1.63	G. sacculifer (sac) $\delta^{18}\text{O}$	0.05	G. sacculifer (sac) $\delta^{18}\text{O}$ (normalised)	0.26	Smoothed G. sacculifer (sac) $\delta^{18}\text{O}$ (normalised)	0.14	$\delta^{18}\text{O}$ (GIV effect)	-1.78	G. sacculifer (sac) $\Delta\delta^{18}\text{O}$ ($\delta^{18}\text{O}$ - GIV effect)	-0.09	G. sacculifer (sac) $\Delta\delta^{18}\text{O}$ (normalised)	0.12	Smoothed G. sacculifer (sac) $\Delta\delta^{18}\text{O}$ (normalised)
6710.82		0.57		-1.34		0.35		0.24		0.14		-1.47		0.21		0.10	
6711.82		0.57		-1.38		0.31		0.30		0.14		-1.52		0.17		0.16	
6878.18		0.58		-1.46		0.23		0.29		0.13		-1.59		0.10		0.16	
7043.55		0.59		-1.37		0.32		0.35		0.12		-1.49		0.20		0.23	
7044.55		0.59		-1.17		0.51		0.40		0.12		-1.30		0.39		0.28	
7209.91		0.60		-1.31		0.38		0.38		0.12		-1.43		0.26		0.26	
7210.91		0.60		-1.44		0.25		0.39		0.12		-1.55		0.13		0.27	
7377.27		0.61		-1.14		0.54		0.39		0.14		-1.28		0.41		0.25	
7542.64		0.62		-1.31		0.37		0.47		0.16		-1.47		0.22		0.31	
7709.00		0.63		-1.20		0.49		0.47		0.18		-1.38		0.31		0.30	
7710.00		0.63		-1.14		0.55		0.59		0.18		-1.32		0.37		0.41	
7890.91		0.64		-0.96		0.73		0.58		0.19		-1.15		0.54		0.39	
8071.82		0.65		-1.23		0.46		0.52		0.19		-1.42		0.26		0.32	
8206.50		0.65		-1.31		0.38		0.50		0.22		-1.53		0.16		0.29	
8252.73		0.66		-1.03		0.66		0.50		0.22		-1.25		0.44		0.27	
8433.64		0.67		-1.22		0.47		0.51		0.24		-1.46		0.23		0.27	
8455.25		0.66		-1.29		0.39		0.48		0.24		-1.53		0.16		0.24	
8614.55		0.68		-1.10		0.59		0.49		0.25		-1.35		0.33		0.22	
8952.75		0.69		-1.20		0.48		0.50		0.32		-1.52		0.17		0.20	
8976.36		0.70		-1.27		0.42		0.45		0.32		-1.58		0.10		0.13	
9157.27		0.71		-1.23		0.46		0.46		0.33		-1.56		0.12		0.12	
9450.25		0.73		-1.18		0.51		0.48		0.37		-1.55		0.14		0.10	
9699.00		0.74		-1.22		0.47		0.52		0.44		-1.65		0.03		0.11	
9700.00		0.74		-1.09		0.59		0.67		0.44		-1.53		0.15		0.21	
9830.91		0.75		-0.75		0.94		0.71		0.48		-1.23		0.46		0.23	
9961.82		0.76		-1.08		0.61		0.71		0.52		-1.60		0.08		0.19	
10091.73		0.77		-1.11		0.57		0.61		0.54		-1.65		0.03		0.07	
10092.73		0.77		-1.04		0.64		0.51		0.54		-1.58		0.10		-0.03	
10223.64		0.78		-1.36		0.32		0.49		0.55		-1.91		-0.22		-0.05	
10353.55		0.79		-1.17		0.52		0.53		0.56		-1.72		-0.04		-0.02	
10354.55		0.79		-0.93		0.75		0.63		0.56		-1.49		0.19		0.07	
10485.45		0.80		-1.07		0.62		0.65		0.57		-1.64		0.05		0.08	
10615.36		0.81		-1.09		0.60		0.68		0.58		-1.67		0.01		0.10	
10616.36		0.81		-0.86		0.83		0.65		0.58		-1.44		0.25		0.06	
10747.27		0.82		-1.17		0.52		0.64		0.60		-1.77		-0.08		0.04	
10877.18		0.83		-1.12		0.57		0.65		0.63		-1.74		-0.06		0.03	

Cal yr BP	Depth (mbsf)	G. sacculifer (sac) $\delta^{18}\text{O}$	G. sacculifer (sac) $\delta^{18}\text{O}$ (normalised)	Smoothed G. sacculifer (sac) $\delta^{18}\text{O}$ (normalised)	$\delta^{18}\text{O}$ (GIV effect)	G. sacculifer (sac) $\Delta\delta^{18}\text{O}$ ($\delta^{18}\text{O}$ - GIV effect)	G. sacculifer (sac) $\Delta\delta^{18}\text{O}$ (normalised)	Smoothed G. sacculifer (sac) $\Delta\delta^{18}\text{O}$ (normalised)
10878.18	0.83	-0.82	0.86	0.66	0.63	-1.45	0.23	0.02
11008.09	0.84	-1.14	0.55	0.66	0.66	-1.80	-0.11	0.01
11009.09	0.84	-1.12	0.57	0.64	0.66	-1.78	-0.09	-0.03
11139.00	0.85	-0.88	0.80	0.80	0.69	-1.57	0.12	0.13
11140.00	0.85	-0.64	1.05	0.88	0.69	-1.33	0.36	0.18
11439.00	0.87	-0.89	0.80	0.88	0.73	-1.62	0.07	0.17
11440.00	0.87	-0.89	0.80	0.82	0.73	-1.61	0.07	0.09
11739.00	0.89	-0.82	0.86	0.87	0.75	-1.57	0.12	0.13
11740.00	0.89	-0.73	0.96	0.87	0.75	-1.47	0.21	0.12
11776.50	0.90	-0.89	0.79	0.69	0.75	-1.65	0.04	-0.07
11777.50	0.90	-1.38	0.31	0.65	0.75	-2.13	-0.45	-0.10
11851.50	0.92	-0.82	0.86	0.73	0.76	-1.59	0.10	-0.03
11889.00	0.93	-0.67	1.01	1.09	0.77	-1.44	0.24	0.32
11894.29	0.94	-0.30	1.39	1.26	0.77	-1.07	0.61	0.49
11897.82	0.95	-0.29	1.39	1.24	0.77	-1.07	0.62	0.47
11955.68	0.96	-0.73	0.96	1.23	0.78	-1.51	0.18	0.45
12043.24	1.00	-0.35	1.33	1.24	0.79	-1.14	0.54	0.45
12059.00	1.01	-0.40	1.29	1.19	0.79	-1.19	0.50	0.40
12108.92	1.03	-0.48	1.20	1.24	0.79	-1.28	0.41	0.44
12196.49	1.07	-0.54	1.15	1.20	0.80	-1.34	0.35	0.39
12284.05	1.11	-0.46	1.23	1.16	0.83	-1.29	0.40	0.34
12299.00	1.20	-0.58	1.10	1.13	0.84	-1.42	0.27	0.29
12349.73	1.14	-0.57	1.12	1.19	0.86	-1.42	0.26	0.33
12415.41	1.17	-0.65	1.03	1.18	0.88	-1.53	0.15	0.30
12499.00	1.25	-0.23	1.46	1.49	0.91	-1.13	0.55	0.59
12546.76	1.23	-0.51	1.17	1.52	0.92	-1.44	0.25	0.60
12634.32	1.27	0.98	2.66	1.84	0.94	0.04	1.72	0.91
12699.00	1.30	-0.42	1.27	1.80	0.94	-1.36	0.33	0.87
12701.09	1.32	0.94	2.63	1.92	0.94	0.00	1.69	0.98
12704.45	1.40	-0.40	1.29	1.67	0.94	-1.34	0.35	0.73
12706.55	1.42	0.08	1.77	1.84	0.94	-0.86	0.83	0.90
12707.18	1.45	-0.30	1.38	1.62	0.94	-1.24	0.44	0.68
12709.82	1.48	0.46	2.15	1.74	0.94	-0.48	1.21	0.80
12709.91	1.50	-0.18	1.51	1.67	0.94	-1.12	0.57	0.73
12712.55	1.53	0.22	1.91	1.83	0.94	-0.72	0.97	0.89
12718.09	1.65	-0.30	1.38	1.59	0.94	-1.24	0.44	0.65
12720.73	1.68	0.50	2.19	1.68	0.94	-0.44	1.25	0.74

APPENDICES

12726.18	1.78	-0.75	0.94	1.64	0.94	-1.69	0.00	0.70
12728.91	1.83	0.28	1.96	1.78	0.94	-0.66	1.02	0.84
12732.40	1.88	0.02	1.71	1.78	0.94	-0.92	0.77	0.84
12736.40	1.93	0.39	2.08	1.82	0.94	-0.55	1.14	0.88
12740.40	1.98	0.54	2.23	1.88	0.94	-0.40	1.29	0.94
12748.40	2.08	-0.56	1.13	1.97	0.94	-1.50	0.19	1.03
12751.81	2.13	0.56	2.25	2.05	0.94	-0.38	1.31	1.11
12754.82	2.18	0.49	2.18	2.04	0.94	-0.45	1.24	1.10
12763.86	2.33	0.76	2.45	2.10	0.94	-0.18	1.51	1.16
12766.87	2.38	0.52	2.21	1.85	0.94	-0.42	1.27	0.91
12769.22	2.46	-0.29	1.40	1.79	0.94	-1.23	0.46	0.85
12769.88	2.43	-0.67	1.01	1.82	0.94	-1.61	0.07	0.88
12772.89	2.48	0.21	1.90	1.72	0.94	-0.73	0.96	0.78
12775.90	2.53	0.89	2.58	1.77	0.94	-0.05	1.64	0.83
12785.52	2.69	0.01	1.69	1.90	0.94	-0.93	0.75	0.96
12787.95	2.73	-0.01	1.68	1.84	0.94	-0.95	0.74	0.90
12790.96	2.78	-0.06	1.63	1.65	0.94	-1.00	0.69	0.71
12793.98	2.83	-0.05	1.63	1.69	0.94	-0.99	0.69	0.75
12796.75	2.89	-0.07	1.62	1.69	0.94	-1.01	0.68	0.75
12796.99	2.88	0.22	1.91	1.72	0.94	-0.72	0.97	0.78
12885.59	2.98	-0.01	1.67	1.75	0.95	-0.96	0.73	0.80
13056.78	3.08	0.09	1.78	1.85	0.96	-0.87	0.82	0.89
13142.37	3.13	0.09	1.78	1.80	0.97	-0.87	0.81	0.84
13227.97	3.18	0.41	2.09	1.77	0.97	-0.57	1.12	0.80
13246.05	3.20	-0.02	1.67	1.87	0.97	-0.99	0.70	0.89
13313.56	3.23	-0.18	1.51	1.89	0.98	-1.15	0.53	0.91
13399.15	3.28	0.59	2.27	1.81	0.98	-0.40	1.29	0.83
13411.62	3.30	0.21	1.89	1.82	0.99	-0.78	0.91	0.84
13484.75	3.33	0.02	1.70	1.83	0.99	-0.97	0.71	0.84
13570.34	3.38	0.05	1.73	1.69	1.00	-0.95	0.74	0.70
13577.20	3.40	-0.12	1.56	1.61	1.00	-1.12	0.57	0.61
13741.53	3.48	-0.11	1.57	1.53	1.01	-1.12	0.56	0.53
13742.77	3.49	-0.20	1.48	1.50	1.01	-1.21	0.47	0.49
13846.20	3.58	-0.37	1.32	1.57	1.02	-1.39	0.30	0.56
13850.43	3.58	-0.12	1.57	1.45	1.02	-1.14	0.55	0.43
13884.13	3.63	0.23	1.92	1.62	1.02	-0.79	0.89	0.60
13914.40	3.69	-0.72	0.97	1.63	1.02	-1.74	-0.05	0.61

Cal yr BP	Depth (mbsf)	G. sacculifer (sac) $\delta^{18}\text{O}$	G. sacculifer (sac) $\delta^{18}\text{O}$ (normalised)	Smoothed G. sacculifer (sac) $\delta^{18}\text{O}$ (normalised)	$\delta^{18}\text{O}$ (GIV effect)	G. sacculifer (sac) $\Delta\delta^{18}\text{O}$ ($\delta^{18}\text{O}$ - GIV effect)	G. sacculifer (sac) $\Delta\delta^{18}\text{O}$ (normalised)	Smoothed G. sacculifer (sac) $\Delta\delta^{18}\text{O}$ (normalised)
13917.83	3.68	0.63	2.32	1.71	1.02	-0.39	1.29	0.68
13951.52	3.73	-0.31	1.37	1.65	1.03	-1.34	0.35	0.62
13985.22	3.78	0.27	1.96	1.71	1.03	-0.76	0.93	0.69
14018.91	3.83	-0.05	1.63	1.41	1.03	-1.08	0.60	0.38
14032.20	3.86	-0.40	1.29	1.56	1.03	-1.43	0.26	0.53
14052.61	3.88	-0.87	0.81	1.40	1.03	-1.90	-0.22	0.37
14086.30	3.93	0.40	2.09	1.36	1.03	-0.63	1.06	0.33
14120.00	3.98	-0.50	1.19	1.34	1.03	-1.53	0.16	0.31
14207.50	4.03	-0.29	1.40	1.39	1.03	-1.32	0.37	0.36
14245.00	4.07	-0.48	1.21	1.35	1.03	-1.51	0.18	0.32
14295.00	4.08	-0.63	1.06	1.58	1.03	-1.66	0.03	0.55
14350.00	4.13	0.22	1.91	1.64	1.03	-0.81	0.87	0.61
14383.33	4.18	0.66	2.34	1.73	1.03	-0.38	1.31	0.70
14450.00	4.28	-0.02	1.67	1.80	1.03	-1.05	0.64	0.77
14483.33	4.33	0.00	1.69	1.83	1.03	-1.03	0.65	0.80
14516.67	4.38	-0.28	1.40	1.58	1.03	-1.32	0.37	0.55
14550.00	4.43	0.38	2.06	1.48	1.04	-0.66	1.03	0.44
14616.67	4.53	-0.59	1.09	1.31	1.04	-1.63	0.05	0.27
14650.00	4.58	-0.54	1.14	1.21	1.04	-1.58	0.10	0.17
14683.33	4.63	-0.84	0.84	1.07	1.04	-1.89	-0.20	0.02
14716.67	4.68	-0.77	0.91	0.97	1.05	-1.82	-0.13	-0.08
14783.33	4.78	-0.35	1.34	0.98	1.05	-1.40	0.29	-0.07
14816.67	4.83	-1.08	0.60	1.07	1.05	-2.14	-0.45	0.02
14850.00	4.88	-0.50	1.19	1.16	1.06	-1.56	0.13	0.10
14935.00	4.93	-0.38	1.31	1.12	1.06	-1.44	0.25	0.06
15020.00	4.98	-0.35	1.34	1.23	1.06	-1.41	0.28	0.17
15105.00	5.03	-0.53	1.16	1.26	1.06	-1.59	0.09	0.19
15190.00	5.08	-0.51	1.17	1.26	1.06	-1.58	0.11	0.20
15275.00	5.13	-0.39	1.30	1.27	1.06	-1.45	0.24	0.21
15360.00	5.18	-0.35	1.34	1.40	1.06	-1.41	0.28	0.34
15445.00	5.23	-0.30	1.39	1.47	1.06	-1.36	0.33	0.41
15530.00	5.28	0.11	1.80	1.50	1.06	-0.94	0.74	0.44
15710.00	5.33	-0.17	1.51	1.52	1.06	-1.23	0.46	0.46
15890.00	5.38	-0.24	1.45	1.47	1.06	-1.30	0.39	0.40
16070.00	5.43	-0.22	1.47	1.47	1.07	-1.29	0.40	0.40
16250.00	5.48	-0.57	1.12	1.12	1.10	-1.67	0.01	0.01
16430.00	5.53	-0.13	1.56	1.56	1.14	-1.27	0.42	0.42

16610.00	5.58	-0.36	1.32	1.32	1.17	-1.53	0.15	0.15
16726.15	5.63	-0.12	1.56	1.56	1.19	-1.32	0.37	0.37
17074.62	5.78	0.21	1.90	1.90	1.18	-0.97	0.72	0.72
17190.77	5.83	0.33	2.01	2.01	1.16	-0.83	0.85	0.85
17306.92	5.88	0.09	1.77	1.77	1.15	-1.06	0.62	0.62
17423.08	5.93	0.25	1.93	1.93	1.15	-0.90	0.79	0.79
17539.23	5.98	0.28	1.96	1.96	1.17	-0.89	0.80	0.80
17771.54	6.08	0.09	1.78	1.78	1.20	-1.11	0.57	0.57
17887.69	6.13	0.36	2.05	2.05	1.22	-0.86	0.83	0.83
18003.85	6.18	0.55	2.23	2.23	1.24	-0.70	0.99	0.85
18120.00	6.23	0.34	2.02	2.02	1.24	-0.90	0.78	0.78
18332.86	6.28	0.29	1.98	1.98	1.23	-0.94	0.75	0.75
18545.71	6.33	0.31	1.99	1.99	1.21	-0.90	0.78	0.78
18758.57	6.38	0.28	1.97	1.97	1.19	-0.91	0.78	0.78
18971.43	6.43	0.35	2.04	2.04	1.17	-0.82	0.87	0.87
19397.14	6.53	0.35	2.04	2.04	1.16	-0.80	0.89	0.89
19610.00	6.58	0.42	2.11	2.11	1.15	-0.72	0.96	0.96
20390.00	6.83	0.19	1.88	1.88	1.19	-0.99	0.69	0.69
20702.00	6.93	0.39	2.07	2.07	1.21	-0.82	0.86	0.86
20858.00	6.98	0.35	2.04	2.04	1.22	-0.87	0.82	0.82
21014.00	7.03	0.35	2.03	2.03	1.23	-0.88	0.81	0.81
21170.00	7.08	0.39	2.08	2.08	1.22	-0.83	0.85	0.85
21390.00	7.13	0.19	1.88	1.88	1.22	-1.03	0.66	0.66
21660.00	7.20	0.09	1.78	1.78	1.22	-1.12	0.56	0.56
22886.67	7.60	0.16	1.85	1.85	1.11	-0.95	0.74	0.74
23040.00	7.65	0.04	1.72	1.72	1.13	-1.09	0.59	0.59
23500.00	7.80	-0.04	1.64	1.64	1.10	-1.14	0.54	0.54
23653.33	7.85	0.00	1.69	1.69	1.06	-1.06	0.63	0.63
23806.67	7.90	-0.04	1.65	1.65	1.03	-1.07	0.61	0.61
23960.00	7.95	0.07	1.76	1.76	1.05	-0.98	0.71	0.71
24152.50	8.00	0.01	1.70	1.70	1.09	-1.08	0.60	0.60
24635.11	8.08	0.10	1.79	1.79	1.11	-1.01	0.68	0.68
24730.00	8.15	-0.01	1.68	1.68	1.10	-1.10	0.58	0.58
24922.50	8.20	0.18	1.86	1.86	1.09	-0.91	0.77	0.77
25115.00	8.25	0.15	1.83	1.83	1.10	-0.96	0.73	0.73
25307.50	8.30	0.06	1.74	1.74	1.11	-1.05	0.64	0.64
25500.00	8.35	0.07	1.75	1.75	1.10	-1.04	0.65	0.65

APPENDICES

Cal yr BP	Depth (mbsf)	G. sacculifer (sac) $\delta^{18}\text{O}$	G. sacculifer (sac) $\delta^{18}\text{O}$ (normalised)	Smoothed G. sacculifer (sac) $\delta^{18}\text{O}$ (normalised)	$\delta^{18}\text{O}$ (GIV effect)	G. sacculifer (sac) $\Delta\delta^{18}\text{O}$ ($\delta^{18}\text{O}$ - GIV effect)	G. sacculifer (sac) $\Delta\delta^{18}\text{O}$ (normalised)	Smoothed G. sacculifer (sac) $\Delta\delta^{18}\text{O}$ (normalised)
25808.33	8.40	0.18	1.86	1.86	1.11	-0.93	0.76	0.76
26116.67	8.45	0.26	1.94	1.94	1.15	-0.89	0.79	0.79
26425.00	8.50	0.37	2.05	2.05	1.12	-0.75	0.93	0.93
26733.33	8.55	0.43	2.11	2.11	1.09	-0.66	1.02	1.02
27350.00	8.65	0.01	1.70	1.70	1.01	-1.00	0.69	0.69
27662.50	8.80	-0.02	1.66	1.66	0.96	-0.99	0.70	0.70
27870.83	8.90	0.04	1.72	1.72	0.98	-0.95	0.74	0.74
27975.00	8.95	-0.19	1.50	1.50	1.00	-1.19	0.50	0.50
28037.50	8.98	-0.16	1.52	1.52	1.01	-1.17	0.52	0.52
28599.00	9.25	-0.02	1.67	1.67	1.03	-1.05	0.64	0.64
28799.00	9.34	0.03	1.72	1.72	1.00	-0.96	0.72	0.72
30034.29	9.70	-0.02	1.66	1.66	0.90	-0.93	0.76	0.76
30446.06	9.77	-0.12	1.56	1.56	0.88	-1.00	0.69	0.69
30940.18	10.00	0.17	1.86	1.86	0.90	-0.73	0.96	0.96
31492.31	10.10	-0.10	1.58	1.58	0.80	-0.91	0.78	0.78
31599.00	10.13	0.00	1.69	1.69	0.80	-0.80	0.88	0.88
31682.76	10.15	-0.04	1.64	1.64	0.80	-0.85	0.84	0.84
31889.66	10.20	0.07	1.75	1.75	0.80	-0.74	0.95	0.95
32096.55	10.25	-0.14	1.55	1.55	0.80	-0.94	0.75	0.75
32253.55	10.29	-0.13	1.55	1.55	0.80	-0.93	0.75	0.75
32303.45	10.30	-0.08	1.61	1.61	0.80	-0.88	0.81	0.81
32510.34	10.35	0.05	1.74	1.74	0.80	-0.75	0.94	0.94
32717.24	10.40	0.04	1.73	1.73	0.79	-0.75	0.94	0.94
32799.00	10.42	-0.06	1.62	1.62	0.78	-0.84	0.84	0.84
32920.00	10.45	-0.02	1.67	1.67	0.75	-0.77	0.92	0.92
33040.00	10.48	0.15	1.83	1.83	0.73	-0.58	1.10	1.10
33199.00	10.51	0.14	1.83	1.83	0.71	-0.57	1.11	1.11
33599.00	10.62	-0.07	1.62	1.62	0.76	-0.83	0.86	0.86
33960.54	10.82	-0.08	1.61	1.61	0.78	-0.86	0.83	0.83
34322.08	11.02	-0.03	1.65	1.65	0.80	-0.84	0.85	0.85
34683.62	11.22	-0.26	1.43	1.43	0.82	-1.08	0.60	0.60
35045.15	11.42	-0.18	1.51	1.51	0.89	-1.07	0.61	0.61
35551.31	11.78	-0.26	1.42	1.42	0.80	-1.06	0.63	0.63
35949.00	12.00	-0.05	1.63	1.63	0.74	-0.79	0.90	0.90
36269.31	12.27	-0.44	1.24	1.24	0.89	-1.33	0.35	0.35
36589.63	12.47	-0.45	1.24	1.24	0.91	-1.36	0.33	0.33
36909.94	12.67	-0.23	1.45	1.45	0.79	-1.02	0.66	0.66

37230.25	12.89	-0.15	1.53	1.53	0.69	-0.84	0.84	0.84
37550.56	13.02	-0.04	1.64	1.64	0.66	-0.71	0.98	0.98
37999.00	13.27	-0.26	1.42	1.42	0.71	-0.97	0.72	0.72
38991.16	13.49	-0.35	1.34	1.34	0.68	-1.03	0.66	0.66
39893.12	13.69	-0.10	1.59	1.59	0.64	-0.74	0.94	0.94

Cal yr BP

Depth (mbsf)

G. sacculifer (sac) $\delta^{18}\text{O}$ G. sacculifer (sac) $\delta^{18}\text{O}$
(normalised)Smoothed G. sacculifer
(sac) $\delta^{18}\text{O}$ (normalised) $\delta^{18}\text{O}$ (GIV effect)G. sacculifer (sac)
 $\Delta\delta^{18}\text{O}$ ($\delta^{18}\text{O}$ - GIV
effect)G. sacculifer (sac)
 $\Delta\delta^{18}\text{O}$ (normalised)Smoothed G. sacculifer
(sac) $\Delta\delta^{18}\text{O}$
(normalised)

Appendix 3: *G. sacculifer* (non sac form)

1.00	Cal yr BP	0.00	Depth (mbsf)	-1.88	G. sacculifer (non sac) $\delta^{18}\text{O}$	0.00	G. sacculifer (non sac) $\delta^{18}\text{O}$ (normalised)	0	Smoothed G. sacculifer (non sac) $\delta^{18}\text{O}$ (normalised)	0.00	$\delta^{18}\text{O}$ (GIV effect)	-1.88	G. sacculifer (non sac) $\Delta\delta^{18}\text{O}$ ($\delta^{18}\text{O}$ - GIV effect)	0.00	G. sacculifer (non sac) $\Delta\delta^{18}\text{O}$ (normalised)	0	Smoothed G. sacculifer (non sac) $\Delta\delta^{18}\text{O}$ (normalised)
177.84		0.02		-1.57		0.00		0.21		0.00		-1.57		0.00		0.31	0.21
266.26		0.04		-1.56		0.32		0.31		0.00		-1.57		0.31		0.31	0.31
354.68		0.05		-1.58		0.30		0.30		0.01		-1.58		0.30		0.30	0.30
531.53		0.08		-1.60		0.28		0.33		0.01		-1.60		0.28		0.28	0.33
619.95		0.09		-1.47		0.41		0.31		0.01		-1.48		0.40		0.40	0.30
708.37		0.10		-1.64		0.24		0.29		0.01		-1.65		0.23		0.23	0.28
796.79		0.11		-1.66		0.22		0.12		0.01		-1.67		0.21		0.21	0.11
885.21		0.12		-1.97		-0.09		0.13		0.01		-1.98		-0.10		-0.10	0.12
973.63		0.14		-1.62		0.26		0.18		0.01		-1.63		0.25		0.25	0.16
1238.89		0.15		-1.51		0.37		0.33		0.02		-1.53		0.35		0.35	0.31
1327.32		0.16		-1.52		0.36		0.33		0.02		-1.54		0.34		0.34	0.31
1415.74		0.17		-1.61		0.27		0.27		0.02		-1.63		0.25		0.25	0.25
1592.58		0.19		-1.71		0.17		0.33		0.02		-1.73		0.15		0.15	0.31
1679.00		0.21		-1.33		0.55		0.21		0.02		-1.36		0.52		0.52	0.19
1681.00		0.21		-1.97		-0.09		0.11		0.02		-2.00		-0.12		-0.12	0.08
1785.38		0.22		-2.02		-0.14		0.03		0.03		-2.04		-0.16		-0.16	0.00
1887.75		0.23		-1.56		0.32		0.21		0.03		-1.59		0.29		0.29	0.18
1889.75		0.23		-1.43		0.45		0.38		0.03		-1.46		0.42		0.42	0.35
1992.13		0.24		-1.51		0.37		0.37		0.03		-1.54		0.34		0.34	0.34
1994.13		0.24		-1.59		0.29		0.31		0.03		-1.62		0.26		0.26	0.28
2097.50		0.25		-1.62		0.26		0.33		0.03		-1.65		0.23		0.23	0.30
2098.50		0.25		-1.44		0.44		0.34		0.03		-1.47		0.40		0.40	0.31
2200.88		0.26		-1.54		0.33		0.40		0.03		-1.58		0.30		0.30	0.37
2202.88		0.26		-1.44		0.44		0.37		0.03		-1.48		0.40		0.40	0.33
2307.25		0.27		-1.55		0.33		0.40		0.04		-1.59		0.29		0.29	0.36
2409.63		0.28		-1.45		0.43		0.39		0.04		-1.49		0.39		0.39	0.36
2411.63		0.28		-1.45		0.43		0.36		0.04		-1.49		0.39		0.39	0.33
2515.00		0.29		-1.64		0.24		0.37		0.04		-1.68		0.20		0.20	0.33
2516.00		0.29		-1.43		0.45		0.36		0.04		-1.46		0.42		0.42	0.32
2618.38		0.30		-1.49		0.39		0.31		0.04		-1.53		0.35		0.35	0.27
2619.38		0.30		-1.80		0.08		0.26		0.04		-1.84		0.04		0.04	0.22
2620.38		0.30		-1.57		0.31		0.25		0.04		-1.61		0.27		0.27	0.21
2723.75		0.31		-1.52		0.36		0.33		0.04		-1.56		0.32		0.32	0.29
2724.75		0.31		-1.55		0.33		0.32		0.04		-1.59		0.29		0.29	0.28
2828.13		0.32		-1.60		0.28		0.31		0.04		-1.64		0.24		0.24	0.27

2932.50	0.33	-1.56	0.32	0.30	0.05	-1.61	0.27	0.26
3035.88	0.34	-1.58	0.30	0.36	0.05	-1.62	0.26	0.31
3141.25	0.35	-1.43	0.45	0.35	0.05	-1.47	0.41	0.30
3244.63	0.36	-1.59	0.29	0.34	0.05	-1.64	0.24	0.29
3245.63	0.36	-1.59	0.29	0.29	0.05	-1.64	0.24	0.24
3349.00	0.37	-1.58	0.29	0.35	0.05	-1.64	0.24	0.29
3518.67	0.38	-1.42	0.46	0.41	0.05	-1.48	0.40	0.35
3686.33	0.39	-1.41	0.47	0.44	0.05	-1.46	0.42	0.39
3687.33	0.39	-1.49	0.39	0.42	0.05	-1.54	0.34	0.37
3855.00	0.40	-1.50	0.38	0.43	0.05	-1.54	0.34	0.39
3856.00	0.40	-1.35	0.53	0.42	0.05	-1.40	0.48	0.38
4024.67	0.41	-1.53	0.35	0.41	0.04	-1.57	0.31	0.37
4192.33	0.42	-1.52	0.36	0.25	0.04	-1.56	0.32	0.21
4193.33	0.42	-1.83	0.05	0.34	0.04	-1.87	0.00	0.29
4362.00	0.43	-1.28	0.60	0.39	0.04	-1.32	0.56	0.34
4530.67	0.44	-1.37	0.51	0.51	0.05	-1.42	0.46	0.46
4698.33	0.45	-1.47	0.41	0.35	0.06	-1.52	0.36	0.30
4699.33	0.45	-1.75	0.13	0.35	0.06	-1.80	0.08	0.30
4868.00	0.46	-1.36	0.52	0.34	0.06	-1.42	0.46	0.28
5035.67	0.47	-1.51	0.37	0.39	0.06	-1.57	0.31	0.33
5036.67	0.47	-1.61	0.27	0.31	0.06	-1.67	0.21	0.25
5204.33	0.48	-1.60	0.28	0.35	0.06	-1.66	0.22	0.29
5205.33	0.48	-1.38	0.50	0.41	0.06	-1.43	0.45	0.35
5374.00	0.49	-1.44	0.44	0.42	0.06	-1.50	0.38	0.36
5541.67	0.50	-1.57	0.31	0.37	0.06	-1.63	0.25	0.30
5542.67	0.50	-1.53	0.35	0.30	0.06	-1.60	0.28	0.24
5710.33	0.51	-1.64	0.24	0.30	0.07	-1.70	0.18	0.23
5711.33	0.51	-1.58	0.30	0.36	0.07	-1.64	0.24	0.29
5879.00	0.52	-1.33	0.55	0.43	0.07	-1.41	0.47	0.36
5880.00	0.52	-1.43	0.45	0.41	0.07	-1.50	0.38	0.33
6046.36	0.53	-1.64	0.24	0.42	0.09	-1.74	0.14	0.33
6211.73	0.54	-1.30	0.58	0.40	0.12	-1.43	0.45	0.28
6212.73	0.54	-1.50	0.38	0.48	0.13	-1.63	0.25	0.35
6379.09	0.55	-1.40	0.48	0.46	0.14	-1.54	0.34	0.32
6544.45	0.56	-1.36	0.52	0.39	0.14	-1.50	0.38	0.25
6545.45	0.56	-1.72	0.16	0.39	0.14	-1.86	0.02	0.25
6710.82	0.57	-1.40	0.48	0.38	0.14	-1.53	0.35	0.24

6711.82	0.57	-1.39	0.49	0.41	0.14	-1.53	0.35	0.28
6878.18	0.58	-1.61	0.27	0.45	0.13	-1.74	0.14	0.32
7043.55	0.59	-1.30	0.58	0.52	0.12	-1.42	0.46	0.39
7044.55	0.59	-1.18	0.70	0.57	0.12	-1.30	0.58	0.45
7209.91	0.60	-1.44	0.44	0.55	0.12	-1.56	0.32	0.43
7210.91	0.60	-1.37	0.51	0.47	0.12	-1.49	0.39	0.35
7377.27	0.61	-1.40	0.48	0.55	0.14	-1.54	0.34	0.41
7542.64	0.62	-1.23	0.65	0.55	0.16	-1.38	0.50	0.40
7543.64	0.62	-1.36	0.52	0.57	0.16	-1.51	0.37	0.41
7709.00	0.63	-1.35	0.53	0.56	0.18	-1.52	0.36	0.39
7710.00	0.63	-1.26	0.62	0.52	0.18	-1.44	0.44	0.34
7890.91	0.64	-1.46	0.42	0.60	0.19	-1.66	0.22	0.41
8071.82	0.65	-1.10	0.78	0.59	0.21	-1.31	0.57	0.38
8206.50	0.65	-1.32	0.56	0.64	0.22	-1.54	0.34	0.42
8252.73	0.66	-1.31	0.57	0.61	0.22	-1.53	0.35	0.38
8433.64	0.67	-1.18	0.70	0.65	0.24	-1.42	0.46	0.42
8455.25	0.66	-1.19	0.69	0.68	0.24	-1.43	0.45	0.44
8614.55	0.68	-1.23	0.65	0.69	0.25	-1.48	0.40	0.42
8952.75	0.69	-1.17	0.71	0.74	0.32	-1.48	0.40	0.44
8976.36	0.70	-1.03	0.85	0.79	0.32	-1.35	0.53	0.47
9157.27	0.71	-1.08	0.80	0.81	0.33	-1.41	0.47	0.48
9338.18	0.72	-1.10	0.78	0.79	0.35	-1.45	0.43	0.43
9450.25	0.73	-1.11	0.77	0.77	0.37	-1.48	0.40	0.40
9519.09	0.73	-1.12	0.76	0.77	0.38	-1.51	0.37	0.37
9699.00	0.74	-1.11	0.77	0.84	0.44	-1.55	0.33	0.42
9700.00	0.74	-0.89	0.99	0.82	0.44	-1.33	0.55	0.37
9830.91	0.75	-1.17	0.71	0.81	0.48	-1.66	0.22	0.32
9961.82	0.76	-1.16	0.72	0.74	0.52	-1.68	0.20	0.23
10091.73	0.77	-1.08	0.80	0.76	0.54	-1.62	0.26	0.22
10092.73	0.77	-1.13	0.75	0.82	0.54	-1.67	0.21	0.28
10223.64	0.78	-0.96	0.92	0.81	0.55	-1.51	0.37	0.26
10353.55	0.79	-1.13	0.75	0.89	0.56	-1.69	0.19	0.34
10354.55	0.79	-0.87	1.01	0.95	0.56	-1.42	0.46	0.38
10485.45	0.80	-0.80	1.08	0.99	0.57	-1.37	0.51	0.42
10615.36	0.81	-1.01	0.87	1.01	0.58	-1.60	0.28	0.43
10616.36	0.81	-0.81	1.07	1.03	0.58	-1.39	0.49	0.44
10747.27	0.82	-0.72	1.16	0.99	0.60	-1.32	0.56	0.39

10877.18	0.83	-1.13	0.75	0.89	0.63	-1.76	0.12	0.28
10878.18	0.83	-1.10	0.78	0.78	0.63	-1.73	0.15	0.14
11008.09	0.84	-1.08	0.80	0.83	0.66	-1.74	0.14	0.18
11009.09	0.84	-0.98	0.90	0.86	0.66	-1.64	0.24	0.19
11139.00	0.85	-1.00	0.88	0.91	0.69	-1.68	0.20	0.24
11140.00	0.85	-0.92	0.96	0.96	0.69	-1.60	0.28	0.26
11439.00	0.87	-0.84	1.04	1.01	0.73	-1.56	0.32	0.29
11739.00	0.89	-0.87	1.01	0.93	0.75	-1.62	0.26	0.19
11740.00	0.89	-1.16	0.72	0.91	0.75	-1.91	-0.03	0.17
11776.50	0.90	-0.87	1.01	0.95	0.75	-1.62	0.26	0.20
11777.50	0.90	-0.77	1.11	1.08	0.75	-1.53	0.35	0.32
11851.50	0.92	-0.76	1.12	1.16	0.76	-1.52	0.36	0.40
11889.00	0.93	-0.62	1.26	1.23	0.77	-1.39	0.49	0.46
11894.29	0.94	-0.57	1.31	1.38	0.77	-1.34	0.54	0.60
11897.82	0.95	-0.33	1.55	1.46	0.77	-1.10	0.78	0.69
11955.68	0.96	-0.35	1.53	1.50	0.78	-1.13	0.75	0.72
12043.24	1.00	-0.47	1.41	1.49	0.79	-1.26	0.62	0.71
12059.00	1.02	-0.45	1.43	1.48	0.79	-1.24	0.63	0.69
12108.92	1.03	-0.32	1.56	1.42	0.79	-1.12	0.76	0.62
12196.49	1.07	-0.39	1.49	1.44	0.80	-1.19	0.69	0.63
12284.05	1.11	-0.65	1.23	1.43	0.83	-1.48	0.40	0.61
12299.00	1.13	-0.38	1.50	1.37	0.84	-1.21	0.67	0.53
12349.73	1.14	-0.52	1.36	1.29	0.86	-1.38	0.50	0.43
12415.41	1.17	-0.59	1.29	1.36	0.88	-1.47	0.41	0.48
12499.00	1.25	-0.80	1.08	1.24	0.91	-1.71	0.17	0.34
12546.76	1.26	-0.33	1.55	1.30	0.92	-1.25	0.63	0.38
12634.32	1.27	-0.97	0.91	1.32	0.94	-1.91	-0.03	0.39
12699.00	1.30	-0.22	1.66	1.40	0.94	-1.16	0.72	0.46
12704.36	1.38	-0.48	1.40	1.43	0.94	-1.42	0.46	0.49
12704.45	1.40	-0.41	1.47	1.61	0.94	-1.35	0.53	0.67
12706.55	1.42	-0.19	1.69	1.54	0.94	-1.13	0.75	0.60
12707.18	1.45	-0.03	1.85	1.68	0.94	-0.97	0.91	0.74
12709.82	1.48	-0.58	1.30	1.55	0.94	-1.52	0.36	0.61
12709.91	1.50	0.20	2.08	1.54	0.94	-0.74	1.14	0.60
12712.55	1.53	-1.04	0.84	1.53	0.94	-1.98	-0.10	0.59
12715.27	1.58	-0.22	1.66	1.60	0.94	-1.16	0.72	0.66
12718.00	1.63	-0.11	1.77	1.34	0.94	-1.05	0.83	0.40

12720.73	1.68	-0.23	1.65	1.50	0.94	-1.17	0.71	0.56
12723.55	1.75	-1.08	0.80	1.48	0.94	-2.02	-0.14	0.54
12726.18	1.78	-0.22	1.66	1.43	0.94	-1.16	0.72	0.49
12728.91	1.83	-0.34	1.54	1.45	0.94	-1.28	0.60	0.51
12729.00	1.85	-0.37	1.51	1.62	0.94	-1.31	0.57	0.68
12732.40	1.88	-0.13	1.75	1.55	0.94	-1.07	0.81	0.61
12736.40	1.93	-0.26	1.62	1.72	0.94	-1.20	0.68	0.78
12740.40	1.98	-0.58	1.30	1.69	0.94	-1.52	0.36	0.75
12745.67	2.06	0.52	2.40	1.63	0.94	-0.42	1.46	0.69
12748.40	2.08	-0.51	1.37	1.56	0.94	-1.45	0.43	0.62
12751.81	2.13	-0.42	1.46	1.75	0.94	-1.36	0.52	0.81
12754.82	2.18	-0.61	1.27	1.62	0.94	-1.55	0.33	0.68
12757.83	2.23	0.36	2.24	1.83	0.94	-0.58	1.30	0.89
12760.84	2.28	-0.13	1.75	1.97	0.94	-1.07	0.81	1.03
12763.86	2.33	0.53	2.41	2.05	0.94	-0.41	1.47	1.11
12766.87	2.38	0.31	2.18	2.01	0.94	-0.63	1.24	1.07
12769.22	2.46	-0.24	1.64	2.08	0.94	-1.18	0.70	1.14
12772.89	2.48	0.16	2.04	2.02	0.94	-0.78	1.10	1.08
12775.90	2.53	0.24	2.11	1.92	0.94	-0.70	1.17	0.98
12785.52	2.69	0.24	2.12	1.99	0.94	-0.70	1.18	1.05
12787.95	2.73	-0.19	1.69	2.06	0.94	-1.13	0.75	1.12
12790.96	2.78	0.12	2.00	1.97	0.94	-0.82	1.06	1.03
12793.98	2.83	0.51	2.39	1.86	0.94	-0.43	1.45	0.92
12796.75	2.89	-0.21	1.67	1.76	0.94	-1.15	0.73	0.82
12796.99	2.88	-0.35	1.53	1.77	0.94	-1.29	0.59	0.82
12800.00	2.93	-0.69	1.19	1.75	0.94	-1.63	0.25	0.81
12885.59	2.98	0.18	2.06	1.92	0.95	-0.77	1.11	0.97
13056.78	3.08	0.44	2.32	2.09	0.96	-0.52	1.36	1.14
13080.48	3.10	0.61	2.49	2.07	0.96	-0.35	1.53	1.11
13142.37	3.13	0.52	2.40	2.01	0.97	-0.45	1.43	1.05
13227.97	3.18	-0.80	1.08	2.02	0.97	-1.77	0.10	1.05
13246.05	3.20	-0.10	1.78	1.95	0.97	-1.07	0.81	0.98
13313.56	3.23	0.46	2.34	1.82	0.98	-0.52	1.36	0.84
13399.15	3.28	0.29	2.17	2.03	0.98	-0.70	1.18	1.05
13411.62	3.30	-0.14	1.74	2.10	0.99	-1.12	0.76	1.12
13484.75	3.33	0.24	2.12	2.07	0.99	-0.75	1.13	1.07
13570.34	3.38	0.27	2.15	1.90	1.00	-0.73	1.15	0.91

13577.20	3.40	0.27	2.15	1.94	1.00	-0.73	1.15	0.94
13655.93	3.43	-0.54	1.34	1.79	1.00	-1.54	0.34	0.78
13741.53	3.48	0.04	1.92	1.62	1.01	-0.97	0.91	0.62
13742.77	3.49	-0.50	1.38	1.59	1.01	-1.51	0.37	0.58
13850.43	3.58	-0.55	1.33	1.66	1.02	-1.57	0.31	0.64
13884.13	3.63	0.12	2.00	1.73	1.02	-0.91	0.97	0.71
13914.40	3.69	-0.22	1.66	1.89	1.02	-1.24	0.64	0.86
13917.83	3.68	0.39	2.27	2.07	1.02	-0.63	1.25	1.04
13951.52	3.73	0.29	2.17	1.99	1.03	-0.74	1.14	0.97
13985.22	3.78	0.36	2.24	1.91	1.03	-0.66	1.22	0.88
14018.91	3.83	-0.26	1.62	1.72	1.03	-1.29	0.59	0.69
14052.61	3.88	-0.66	1.22	1.71	1.03	-1.69	0.19	0.68
14086.30	3.93	-0.56	1.32	1.54	1.03	-1.59	0.29	0.51
14120.00	3.98	0.27	2.15	1.57	1.03	-0.76	1.12	0.54
14207.50	4.03	-0.48	1.40	1.67	1.03	-1.51	0.37	0.64
14245.00	4.07	-0.13	1.75	1.65	1.03	-1.16	0.72	0.62
14295.00	4.08	-0.17	1.71	1.78	1.03	-1.20	0.68	0.75
14350.00	4.13	-0.67	1.21	1.82	1.03	-1.70	0.18	0.79
14383.33	4.18	0.96	2.84	1.96	1.03	-0.07	1.81	0.92
14450.00	4.28	-0.30	1.58	2.12	1.03	-1.33	0.55	1.09
14516.67	4.38	0.56	2.44	2.14	1.03	-0.48	1.40	1.10
14550.00	4.43	0.66	2.54	1.83	1.04	-0.38	1.50	0.80
14616.67	4.53	-0.59	1.29	1.73	1.04	-1.63	0.25	0.69
14650.00	4.58	-0.54	1.34	1.46	1.04	-1.58	0.30	0.42
14683.33	4.63	-0.84	1.04	1.26	1.04	-1.89	-0.01	0.22
14716.67	4.68	-0.77	1.11	1.16	1.05	-1.82	0.06	0.11
14783.33	4.78	-0.35	1.53	1.17	1.05	-1.40	0.48	0.12
14816.67	4.83	-1.08	0.80	1.26	1.05	-2.14	-0.26	0.21
14850.00	4.88	-0.50	1.38	1.35	1.06	-1.56	0.32	0.29
14935.00	4.93	-0.38	1.50	1.31	1.06	-1.44	0.44	0.25
15020.00	4.98	-0.35	1.53	1.43	1.06	-1.41	0.47	0.37
15105.00	5.03	-0.53	1.35	1.45	1.06	-1.59	0.29	0.39
15190.00	5.08	-0.51	1.37	1.46	1.06	-1.58	0.30	0.39
15275.00	5.13	-0.39	1.49	1.47	1.06	-1.45	0.43	0.40
15360.00	5.18	-0.35	1.53	1.59	1.06	-1.41	0.47	0.53
15445.00	5.23	-0.30	1.58	1.66	1.06	-1.36	0.52	0.60
15530.00	5.28	0.11	1.99	1.69	1.06	-0.94	0.94	0.63

15710.00	5.33	-0.17	1.71	1.72	1.06	-1.23	0.65	0.66
15890.00	5.38	-0.24	1.64	1.66	1.06	-1.30	0.58	0.59
16070.00	5.43	-0.22	1.66	1.66	1.07	-1.29	0.59	0.59
16250.00	5.48	-0.57	1.31	1.31	1.10	-1.67	0.21	0.21
16430.00	5.53	-0.13	1.75	1.75	1.14	-1.27	0.61	0.61
16610.00	5.58	-0.36	1.52	1.52	1.17	-1.53	0.35	0.35
16726.15	5.63	-0.12	1.76	1.76	1.19	-1.32	0.56	0.56
17074.62	5.78	0.21	2.09	2.09	1.18	-0.97	0.91	0.91
17190.77	5.83	0.33	2.21	2.21	1.16	-0.83	1.05	1.05
17306.92	5.88	0.09	1.97	1.97	1.15	-1.06	0.82	0.82
17423.08	5.93	0.25	2.13	2.13	1.15	-0.90	0.98	0.98
17539.23	5.98	0.28	2.16	2.16	1.17	-0.89	0.99	0.99
17771.54	6.08	0.09	1.97	1.97	1.20	-1.11	0.77	0.77
17887.69	6.13	0.36	2.24	2.24	1.22	-0.86	1.02	1.02
18003.85	6.18	0.55	2.43	2.43	1.24	-0.70	1.18	0.95
18120.00	6.23	0.34	2.22	2.22	1.24	-0.90	0.98	0.98
18332.86	6.28	0.29	2.17	2.17	1.23	-0.94	0.94	0.94
18545.71	6.33	0.31	2.19	2.19	1.21	-0.90	0.98	0.98
18758.57	6.38	0.28	2.16	2.16	1.19	-0.91	0.97	0.97
18971.43	6.43	0.35	2.23	2.23	1.17	-0.82	1.06	1.06
19397.14	6.53	0.35	2.23	2.23	1.16	-0.80	1.08	1.08
19610.00	6.58	0.42	2.30	2.30	1.15	-0.72	1.16	1.16
20390.00	6.83	0.19	2.07	2.07	1.19	-0.99	0.89	0.89
20702.00	6.93	0.39	2.27	2.27	1.21	-0.82	1.06	1.06
20858.00	6.98	0.35	2.23	2.23	1.22	-0.87	1.01	1.01
21014.00	7.03	0.35	2.23	2.23	1.23	-0.88	1.00	1.00
21170.00	7.08	0.39	2.27	2.27	1.22	-0.83	1.05	1.05
21390.00	7.13	0.19	2.07	2.07	1.22	-1.03	0.85	0.85
21660.00	7.20	0.09	1.97	1.97	1.22	-1.12	0.76	0.76
22886.67	7.60	0.16	2.04	2.04	1.11	-0.95	0.93	0.93
23040.00	7.65	0.20	2.08	2.08	1.13	-0.93	0.95	0.95
23193.33	7.70	-0.30	1.58	1.58	1.15	-1.45	0.43	0.43
23346.67	7.75	0.13	2.01	2.01	1.14	-1.01	0.87	0.87
23500.00	7.80	-0.12	1.76	1.76	1.10	-1.23	0.65	0.65
23653.33	7.85	-0.01	1.87	1.87	1.06	-1.06	0.82	0.82
23806.67	7.90	0.14	2.02	2.02	1.03	-0.89	0.99	0.99
23960.00	7.95	0.07	1.95	1.95	1.05	-0.98	0.90	0.90

24537.50	8.10	0.07	1.95	1.95	1.12	-1.05	0.83	0.83
24635.11	8.12	0.27	2.15	2.15	1.11	-0.84	1.04	1.04
24730.00	8.15	-0.01	1.87	1.87	1.10	-1.10	0.78	0.78
24922.50	8.20	0.18	2.06	2.06	1.09	-0.91	0.97	0.97
25115.00	8.25	0.15	2.03	2.03	1.10	-0.96	0.92	0.92
25307.50	8.30	0.06	1.94	1.94	1.11	-1.05	0.83	0.83
25500.00	8.35	0.07	1.95	1.95	1.10	-1.04	0.84	0.84
25808.33	8.40	0.18	2.06	2.06	1.11	-0.93	0.95	0.95
26116.67	8.45	0.26	2.14	2.14	1.15	-0.89	0.99	0.99
26425.00	8.50	0.37	2.25	2.25	1.12	-0.75	1.13	1.13
26733.33	8.55	0.43	2.30	2.30	1.09	-0.66	1.22	1.22
27350.00	8.65	0.01	1.89	1.89	1.01	-1.00	0.88	0.88
27662.50	8.80	-0.02	1.86	1.86	0.96	-0.99	0.89	0.89
27870.83	8.90	0.04	1.92	1.92	0.98	-0.95	0.93	0.93
27975.00	8.95	-0.19	1.69	1.69	1.00	-1.19	0.69	0.69
28037.50	8.98	-0.16	1.72	1.72	1.01	-1.17	0.71	0.71
28599.00	9.25	-0.04	1.84	1.84	1.03	-1.07	0.81	0.81
28799.00	9.34	0.02	1.90	1.90	1.00	-0.98	0.90	0.90
29622.53	9.60	-0.37	1.51	1.51	0.94	-1.31	0.57	0.57
30034.29	9.70	-0.11	1.77	1.77	0.90	-1.01	0.87	0.87
30446.06	9.77	-0.15	1.73	1.73	0.88	-1.03	0.85	0.85
30940.18	10.00	0.12	2.00	2.00	0.90	-0.78	1.10	1.10
31492.31	10.10	0.17	2.05	2.05	0.80	-0.63	1.25	1.25
31599.00	10.13	0.03	1.91	1.91	0.80	-0.77	1.11	1.11
31682.76	10.15	0.08	1.96	1.96	0.80	-0.73	1.15	1.15
31889.66	10.20	0.16	2.04	2.04	0.80	-0.65	1.23	1.23
32096.55	10.25	-0.21	1.67	1.67	0.80	-1.01	0.87	0.87
32253.55	10.29	-0.19	1.69	1.69	0.80	-0.99	0.89	0.89
32303.45	10.30	0.03	1.91	1.91	0.80	-0.77	1.11	1.11
32510.34	10.35	-0.18	1.70	1.70	0.80	-0.97	0.91	0.91
32717.24	10.40	0.02	1.90	1.90	0.79	-0.77	1.11	1.11
32799.00	10.42	0.05	1.93	1.93	0.78	-0.73	1.15	1.15
32920.00	10.45	-0.21	1.67	1.67	0.75	-0.96	0.92	0.92
33040.00	10.48	-0.06	1.82	1.82	0.73	-0.80	1.08	1.08
33199.00	10.51	0.13	2.01	2.01	0.71	-0.58	1.30	1.30
33599.00	10.62	-0.19	1.69	1.69	0.76	-0.95	0.93	0.93
33960.54	10.82	-0.13	1.75	1.75	0.78	-0.91	0.97	0.97

34322.08	11.02	0.09	1.97	1.97	0.80	-0.71	1.17	1.17
34683.62	11.22	-0.38	1.50	1.50	0.82	-1.20	0.68	0.68
35045.15	11.42	-0.23	1.65	1.65	0.89	-1.13	0.75	0.75
35551.31	11.78	-0.53	1.35	1.35	0.80	-1.33	0.55	0.55
35949.00	12.00	-0.15	1.73	1.73	0.74	-0.89	0.99	0.99
36269.31	12.27	-0.41	1.47	1.47	0.89	-1.30	0.58	0.58
36589.63	12.47	-0.52	1.36	1.36	0.91	-1.43	0.45	0.45
36909.94	12.67	-0.52	1.36	1.36	0.79	-1.30	0.58	0.58
37230.25	12.89	-0.28	1.60	1.60	0.69	-0.98	0.90	0.90
37550.56	13.02	-0.35	1.53	1.53	0.66	-1.02	0.86	0.86
37999.00	13.27	-0.29	1.59	1.59	0.71	-0.99	0.89	0.89
38991.16	13.49	-0.38	1.50	1.50	0.68	-1.06	0.82	0.82
39893.12	13.69	-0.14	1.74	1.74	0.64	-0.78	1.10	1.10

Appendix 4: *N. dutertrei*

Cal yr BP	Depth (mbsf)	<i>N. dutertrei</i> $\delta^{18}\text{O}$	<i>N. dutertrei</i> $\delta^{18}\text{O}$ (normalised)	Smoothed <i>N. dutertrei</i> $\delta^{18}\text{O}$ (normalised)	$\delta^{18}\text{O}$ (GIV effect)	<i>N. dutertrei</i> $\Delta\delta^{18}\text{O}$ ($\delta^{18}\text{O}$ - GIV effect)	<i>N. dutertrei</i> $\Delta\delta^{18}\text{O}$ (normalised)	Smoothed <i>N. dutertrei</i> $\Delta\delta^{18}\text{O}$ (normalised)
1.00	0.00	-1.26	0.00	0	0.00	0.00	0.00	0
89.42	0.01	-1.09	0.17	0.16	0.00	0.17	0.17	0.16
177.84	0.02	-0.95	0.31	0.27	0.00	0.30	0.30	0.27
266.26	0.04	-0.93	0.33	0.38	0.00	0.33	0.33	0.38
443.11	0.07	-0.76	0.50	0.36	0.01	0.50	0.50	0.35
531.53	0.08	-1.03	0.23	0.32	0.01	0.22	0.22	0.31
619.95	0.09	-1.04	0.22	0.16	0.01	0.21	0.21	0.15
708.37	0.10	-1.24	0.02	0.22	0.01	0.01	0.01	0.20
796.79	0.11	-0.86	0.40	0.20	0.01	0.39	0.39	0.19
1062.05	0.14	-1.07	0.19	0.23	0.01	0.17	0.17	0.22
1150.47	0.15	-1.16	0.10	0.30	0.02	0.08	0.08	0.28
1238.89	0.16	-0.66	0.60	0.27	0.02	0.58	0.58	0.25
1327.32	0.17	-1.15	0.11	0.55	0.02	0.09	0.09	0.53
1415.74	0.18	-0.32	0.94	0.61	0.02	0.92	0.92	0.58
1504.16	0.19	-0.50	0.76	0.74	0.02	0.74	0.74	0.72
1592.58	0.20	-0.75	0.51	0.55	0.02	0.49	0.49	0.52
1679.00	0.21	-0.89	0.36	0.43	0.02	0.34	0.34	0.40
1681.00	0.21	-0.86	0.40	0.53	0.02	0.38	0.38	0.51
1785.38	0.22	-0.42	0.84	0.61	0.03	0.81	0.81	0.58
1887.75	0.23	-0.68	0.58	0.55	0.03	0.55	0.55	0.52
1889.75	0.23	-1.04	0.22	0.39	0.03	0.19	0.19	0.37
1992.13	0.24	-0.88	0.38	0.36	0.03	0.35	0.35	0.33
1994.13	0.24	-0.77	0.49	0.40	0.03	0.46	0.46	0.37
2097.50	0.25	-0.93	0.33	0.39	0.03	0.30	0.30	0.36
2098.50	0.25	-0.92	0.34	0.42	0.03	0.31	0.31	0.39
2200.88	0.26	-0.66	0.60	0.55	0.03	0.56	0.56	0.52
2201.88	0.26	-0.54	0.72	0.63	0.03	0.68	0.68	0.60
2306.25	0.27	-0.67	0.59	0.62	0.04	0.55	0.55	0.59
2307.25	0.27	-0.69	0.57	0.49	0.04	0.53	0.53	0.46
2409.63	0.28	-0.94	0.32	0.46	0.04	0.29	0.29	0.42
2410.63	0.28	-0.77	0.49	0.47	0.04	0.45	0.45	0.43
2411.63	0.28	-0.67	0.59	0.53	0.04	0.55	0.55	0.49
2515.00	0.29	-0.74	0.52	0.56	0.04	0.48	0.48	0.52
2516.00	0.29	-0.68	0.58	0.53	0.04	0.54	0.54	0.49
2618.38	0.30	-0.78	0.48	0.39	0.04	0.44	0.44	0.35
2619.38	0.30	-1.15	0.11	0.48	0.04	0.07	0.07	0.44

2620.38	0.30	-0.40	0.86	0.36	0.04	0.82	0.82	0.31
2723.75	0.31	-1.16	0.10	0.51	0.04	0.06	0.06	0.47
2724.75	0.31	-0.68	0.58	0.35	0.04	0.54	0.54	0.30
2828.13	0.32	-0.90	0.36	0.48	0.04	0.32	0.32	0.44
2932.50	0.33	-0.76	0.50	0.46	0.05	0.45	0.45	0.41
3035.88	0.34	-0.74	0.52	0.57	0.05	0.47	0.47	0.53
3141.25	0.35	-0.56	0.70	0.61	0.05	0.65	0.65	0.57
3244.63	0.36	-0.64	0.62	0.51	0.05	0.57	0.57	0.46
3245.63	0.36	-1.05	0.21	0.53	0.05	0.16	0.16	0.48
3349.00	0.37	-0.50	0.76	0.52	0.05	0.71	0.71	0.47
3350.00	0.37	-0.66	0.60	0.60	0.05	0.55	0.55	0.55
3518.67	0.38	-0.81	0.45	0.55	0.05	0.40	0.40	0.49
3686.33	0.39	-0.68	0.58	0.58	0.05	0.53	0.53	0.53
3687.33	0.39	-0.56	0.70	0.62	0.05	0.65	0.65	0.58
3855.00	0.40	-0.67	0.59	0.64	0.05	0.54	0.54	0.59
4024.67	0.41	-0.64	0.62	0.53	0.04	0.58	0.58	0.49
4192.33	0.42	-0.87	0.39	0.64	0.04	0.35	0.35	0.60
4193.33	0.42	-0.36	0.90	0.55	0.04	0.86	0.86	0.51
4362.00	0.43	-0.90	0.36	0.48	0.04	0.32	0.32	0.44
4530.67	0.44	-1.08	0.18	0.39	0.05	0.13	0.13	0.34
4698.33	0.45	-0.62	0.64	0.50	0.06	0.59	0.59	0.44
4868.00	0.46	-0.59	0.67	0.65	0.06	0.61	0.61	0.60
5035.67	0.47	-0.61	0.65	0.57	0.06	0.59	0.59	0.51
5036.67	0.47	-0.86	0.40	0.57	0.06	0.34	0.34	0.51
5204.33	0.48	-0.59	0.67	0.58	0.06	0.61	0.61	0.52
5205.33	0.48	-0.58	0.68	0.64	0.06	0.62	0.62	0.58
5374.00	0.49	-0.69	0.57	0.61	0.06	0.51	0.51	0.55
5541.67	0.50	-0.68	0.58	0.58	0.06	0.51	0.51	0.52
5542.67	0.50	-0.66	0.60	0.54	0.06	0.54	0.54	0.47
5711.33	0.51	-0.83	0.43	0.65	0.07	0.37	0.37	0.58
5879.00	0.52	-0.33	0.93	0.81	0.07	0.85	0.85	0.74
5880.00	0.52	-0.19	1.07	0.85	0.07	1.00	1.00	0.77
6046.36	0.53	-0.69	0.56	0.72	0.09	0.47	0.47	0.63
6211.73	0.54	-0.73	0.53	0.53	0.12	0.41	0.41	0.41
6212.73	0.54	-0.77	0.49	0.65	0.13	0.36	0.36	0.53
6379.09	0.55	-0.32	0.94	0.71	0.14	0.80	0.80	0.58
6544.45	0.56	-0.56	0.70	0.80	0.14	0.56	0.56	0.66

6545.45	0.56	-0.51	0.75	0.73	0.14	0.60	0.60	0.60	0.59
6711.82	0.57	-0.51	0.75	0.68	0.14	0.61	0.61	0.61	0.55
6878.18	0.58	-0.71	0.55	0.67	0.13	0.42	0.42	0.42	0.54
7043.55	0.59	-0.54	0.72	0.67	0.12	0.60	0.60	0.60	0.55
7044.55	0.59	-0.51	0.75	0.81	0.12	0.63	0.63	0.63	0.69
7209.91	0.60	-0.29	0.97	0.97	0.12	0.85	0.85	0.85	0.84
7377.27	0.61	-0.07	1.19	1.04	0.14	1.05	1.05	1.05	0.90
7542.64	0.62	-0.29	0.97	1.03	0.16	0.81	0.81	0.81	0.88
7543.64	0.62	-0.34	0.92	0.89	0.16	0.76	0.76	0.76	0.72
7709.00	0.63	-0.49	0.77	0.96	0.18	0.59	0.59	0.59	0.79
7710.00	0.63	-0.07	1.19	0.88	0.18	1.01	1.01	1.01	0.70
7890.91	0.64	-0.57	0.69	0.98	0.19	0.50	0.50	0.50	0.79
8071.82	0.65	-0.21	1.05	0.92	0.19	0.85	0.85	0.85	0.72
8206.50	0.65	-0.23	1.03	1.00	0.22	0.81	0.81	0.81	0.78
8252.73	0.66	-0.34	0.92	1.00	0.22	0.69	0.69	0.69	0.78
8433.64	0.67	-0.19	1.07	0.98	0.24	0.83	0.83	0.83	0.74
8455.25	0.66	-0.31	0.94	1.01	0.24	0.71	0.71	0.71	0.77
8614.55	0.68	-0.23	1.02	0.99	0.25	0.77	0.77	0.77	0.72
8952.75	0.69	-0.26	0.99	1.01	0.32	0.68	0.68	0.68	0.70
9157.27	0.71	-0.26	1.00	1.00	0.33	0.66	0.66	0.66	0.67
9338.18	0.72	-0.24	1.02	0.99	0.35	0.67	0.67	0.67	0.64
9450.25	0.73	-0.30	0.96	1.01	0.37	0.59	0.59	0.59	0.64
9519.09	0.73	-0.22	1.04	1.00	0.38	0.66	0.66	0.66	0.61
9699.00	0.74	-0.25	1.01	1.10	0.44	0.57	0.57	0.57	0.68
9700.00	0.74	0.00	1.26	1.10	0.44	0.82	0.82	0.82	0.65
9830.91	0.75	-0.23	1.03	1.18	0.48	0.55	0.55	0.55	0.70
9961.82	0.76	0.00	1.26	1.09	0.52	0.73	0.73	0.73	0.57
10091.73	0.77	-0.28	0.98	1.04	0.54	0.44	0.44	0.44	0.50
10092.73	0.77	-0.38	0.88	1.03	0.54	0.34	0.34	0.34	0.49
10223.64	0.78	-0.02	1.24	1.02	0.55	0.69	0.69	0.69	0.48
10353.55	0.79	-0.32	0.94	1.10	0.56	0.39	0.39	0.39	0.55
10354.55	0.79	-0.15	1.11	1.19	0.56	0.56	0.56	0.56	0.63
10485.45	0.80	0.26	1.52	1.18	0.57	0.95	0.95	0.95	0.62
10615.36	0.81	-0.34	0.92	1.26	0.58	0.34	0.34	0.34	0.68
10616.36	0.81	0.07	1.33	1.26	0.58	0.75	0.75	0.75	0.67
10747.27	0.82	0.26	1.52	1.30	0.60	0.92	0.92	0.92	0.69
10877.18	0.83	-0.22	1.03	1.22	0.63	0.41	0.41	0.41	0.60

10878.18	Cal yr BP	0.83	Depth (mbsf)	-0.16	N. dutertrei $\delta^{18}\text{O}$	1.10	N. dutertrei $\delta^{18}\text{O}$ (normalised)	1.05	Smoothed N. dutertrei $\delta^{18}\text{O}$ (normalised)	0.63	$\delta^{18}\text{O}$ (GIV effect)	0.47	N. dutertrei $\Delta\delta^{18}\text{O}$ ($\delta^{18}\text{O}$ - GIV effect)	0.47	N. dutertrei $\Delta\delta^{18}\text{O}$ (normalised)	0.41	Smoothed N. dutertrei $\Delta\delta^{18}\text{O}$ (normalised)
11008.09		0.84		-0.24		1.02		1.06		0.66		0.36		0.36		0.41	
11009.09		0.84		-0.20		1.06		1.10		0.66		0.40		0.40		0.43	
11139.00		0.85		-0.04		1.22		1.26		0.69		0.53		0.53		0.58	
11140.00		0.85		0.23		1.49		1.33		0.69		0.81		0.81		0.63	
11439.00		0.87		0.02		1.28		1.31		0.73		0.55		0.55		0.60	
11440.00		0.87		-0.09		1.17		1.28		0.73		0.44		0.44		0.55	
11739.00		0.89		0.13		1.39		1.32		0.75		0.65		0.65		0.58	
11740.00		0.89		0.14		1.40		1.37		0.75		0.66		0.66		0.63	
11776.50		0.90		0.07		1.33		1.34		0.75		0.57		0.57		0.59	
11777.50		0.90		0.03		1.28		1.36		0.75		0.53		0.53		0.60	
11851.50		0.92		0.20		1.45		1.39		0.76		0.69		0.69		0.62	
11889.00		0.93		0.16		1.42		1.42		0.77		0.65		0.65		0.65	
11894.29		1.02		0.12		1.38		1.57		0.77		0.61		0.61		0.80	
11897.82		1.08		0.64		1.90		1.78		0.77		1.13		1.13		1.00	
11955.68		0.96		0.78		2.04		1.85		0.78		1.26		1.26		1.07	
12043.24		1.00		0.34		1.60		1.79		0.79		0.81		0.81		1.00	
12059.00		1.14		0.30		1.56		1.73		0.79		0.77		0.77		0.94	
12108.92		1.03		0.56		1.82		1.69		0.79		1.02		1.02		0.89	
12196.49		1.07		0.35		1.61		1.63		0.80		0.81		0.81		0.82	
12284.05		1.11		0.60		1.86		1.65		0.83		1.03		1.03		0.82	
12299.00		1.20		0.05		1.31		1.62		0.84		0.47		0.47		0.78	
12349.73		1.14		0.37		1.62		1.61		0.86		0.77		0.77		0.75	
12415.41		1.17		0.43		1.69		1.42		0.88		0.81		0.81		0.54	
12499.00		1.25		0.32		1.57		1.59		0.91		0.67		0.67		0.69	
12546.76		1.23		-0.35		0.91		1.63		0.92		-0.01		-0.01		0.71	
12634.32		1.27		0.87		2.13		1.55		0.94		1.19		1.19		0.62	
12699.00		1.30		0.58		1.84		1.33		0.94		0.90		0.90		0.39	
12701.09		1.32		0.05		1.31		1.54		0.94		0.37		0.37		0.60	
12704.36		1.38		-0.80		0.46		1.29		0.94		-0.48		-0.48		0.35	
12707.18		1.45		0.70		1.96		1.21		0.94		1.02		1.02		0.27	
12709.82		1.48		-0.36		0.90		1.10		0.94		-0.04		-0.04		0.16	
12709.91		1.50		0.17		1.43		1.14		0.94		0.49		0.49		0.20	
12712.55		1.53		-0.50		0.76		1.13		0.94		-0.18		-0.18		0.19	
12718.00		1.63		-0.63		0.63		1.21		0.94		-0.31		-0.31		0.27	
12718.09		1.65		0.65		1.91		1.06		0.94		0.97		0.97		0.12	
12720.73		1.68		0.07		1.32		1.18		0.94		0.38		0.38		0.24	

Cal yr BP	Depth (mbsf)	N. dutertrei $\delta^{18}\text{O}$	N. dutertrei $\delta^{18}\text{O}$ (normalised)	Smoothed N. dutertrei $\delta^{18}\text{O}$ (normalised)	$\delta^{18}\text{O}$ (GIV effect)	N. dutertrei $\Delta\delta^{18}\text{O}$ ($\delta^{18}\text{O}$ - GIV effect)	N. dutertrei $\Delta\delta^{18}\text{O}$ (normalised)	Smoothed N. dutertrei $\Delta\delta^{18}\text{O}$ (normalised)
12723.55	1.75	-0.56	0.70	1.26	0.94	-0.24	-0.24	-0.24
12726.18	1.78	0.07	1.32	1.33	0.94	0.38	0.38	0.39
12728.91	1.83	-0.22	1.04	1.35	0.94	0.10	0.10	0.41
12729.00	1.85	0.98	2.24	1.63	0.94	1.30	1.30	0.69
12732.40	1.88	0.17	1.43	1.78	0.94	0.49	0.49	0.84
12736.40	1.93	0.84	2.10	1.92	0.94	1.16	1.16	0.98
12740.40	1.98	0.82	2.08	1.80	0.94	1.14	1.14	0.86
12748.40	2.08	0.52	1.78	1.78	0.94	0.84	0.84	0.84
12757.83	2.23	0.38	1.64	1.59	0.94	0.70	0.70	0.65
12760.84	2.28	0.04	1.30	1.59	0.94	0.36	0.36	0.65
12766.87	2.38	-0.08	1.18	1.65	0.94	0.24	0.24	0.71
12769.22	2.46	0.80	2.06	1.72	0.94	1.12	1.12	0.78
12772.89	2.48	0.80	2.06	1.92	0.94	1.12	1.12	0.98
12775.90	2.53	0.73	1.99	1.99	0.94	1.05	1.05	1.05
12779.90	2.59	1.07	2.33	1.87	0.94	1.39	1.39	0.93
12781.93	2.63	0.23	1.49	1.79	0.94	0.55	0.55	0.85
12787.95	2.73	0.22	1.48	1.74	0.94	0.54	0.54	0.80
12790.96	2.78	0.38	1.64	1.41	0.94	0.70	0.70	0.47
12791.13	2.79	0.50	1.76	1.47	0.94	0.82	0.82	0.53
12793.98	2.83	-0.56	0.70	1.51	0.94	-0.24	-0.24	0.57
12796.75	2.89	0.51	1.77	1.46	0.94	0.83	0.83	0.52
12796.99	2.88	0.42	1.68	1.60	0.94	0.74	0.74	0.66
12800.00	2.93	0.15	1.41	1.92	0.94	0.47	0.47	0.98
12885.59	2.98	1.21	2.46	2.06	0.95	1.52	1.52	1.11
13056.78	3.08	1.02	2.28	2.15	0.96	1.32	1.32	1.19
13080.48	3.10	1.20	2.46	2.24	0.96	1.50	1.50	1.28
13142.37	3.13	0.86	2.12	2.09	0.97	1.15	1.15	1.12
13227.97	3.18	0.62	1.88	1.93	0.97	0.91	0.91	0.96
13246.05	3.20	0.46	1.72	1.87	0.97	0.74	0.74	0.89
13313.56	3.23	0.24	1.50	1.87	0.98	0.52	0.52	0.90
13399.15	3.28	0.86	2.12	1.96	0.98	1.13	1.13	0.98
13411.62	3.30	0.90	2.16	2.03	0.99	1.18	1.18	1.04
13484.75	3.33	1.05	2.31	2.04	0.99	1.32	1.32	1.05
13570.34	3.38	0.79	2.05	1.93	1.00	1.05	1.05	0.94
13577.20	3.40	0.31	1.57	1.88	1.00	0.57	0.57	0.88
13741.53	3.48	0.32	1.58	1.83	1.01	0.57	0.57	0.82
13742.77	3.49	0.62	1.88	1.78	1.01	0.87	0.87	0.76

Cal yr BP	Depth (mbsf)	N. dutertrei $\delta^{18}\text{O}$	N. dutertrei $\delta^{18}\text{O}$ (normalised)	Smoothed N. dutertrei $\delta^{18}\text{O}$ (normalised)	$\delta^{18}\text{O}$ (GIV effect)	N. dutertrei $\Delta\delta^{18}\text{O}$ ($\delta^{18}\text{O}$ - GIV effect)	N. dutertrei $\Delta\delta^{18}\text{O}$ (normalised)	Smoothed N. dutertrei $\Delta\delta^{18}\text{O}$ (normalised)
13846.20	3.58	0.81	2.07	1.90	1.02	1.05	1.05	0.88
13850.43	3.58	0.53	1.79	2.01	1.02	0.77	0.77	0.99
13884.13	3.63	0.91	2.17	1.99	1.02	1.15	1.15	0.97
13917.83	3.68	0.88	2.14	2.06	1.02	1.11	1.11	1.04
13951.52	3.73	0.54	1.80	2.03	1.03	0.78	0.78	1.00
13970.20	3.78	1.16	2.42	1.95	1.03	1.39	1.39	0.92
13985.22	3.78	0.35	1.61	1.90	1.03	0.58	0.58	0.88
14018.91	3.83	0.52	1.78	1.97	1.03	0.75	0.75	0.94
14032.20	3.86	0.65	1.91	1.97	1.03	0.88	0.88	0.94
14052.61	3.88	0.87	2.13	2.00	1.03	1.10	1.10	0.97
14086.30	3.93	1.14	2.40	1.95	1.03	1.37	1.37	0.92
14120.00	3.98	0.50	1.76	1.85	1.03	0.73	0.73	0.82
14207.50	4.03	0.27	1.53	1.84	1.03	0.50	0.50	0.81
14245.00	4.07	0.17	1.43	1.71	1.03	0.40	0.40	0.67
14295.00	4.08	0.82	2.08	1.72	1.03	1.05	1.05	0.69
14383.33	4.18	0.47	1.73	1.75	1.03	0.70	0.70	0.72
14450.00	4.28	0.57	1.83	1.93	1.03	0.79	0.79	0.90
14483.33	4.33	0.42	1.68	1.89	1.03	0.65	0.65	0.86
14516.67	4.38	1.08	2.34	1.84	1.03	1.31	1.31	0.81
14550.00	4.43	0.62	1.87	1.74	1.04	0.84	0.84	0.70
14816.67	4.83	0.24	1.50	1.83	1.05	0.44	0.44	0.78
14850.00	4.88	0.05	1.31	1.71	1.06	0.26	0.26	0.66
14935.00	4.93	0.86	2.12	1.72	1.06	1.06	1.06	0.66
15020.00	4.98	0.50	1.76	1.82	1.06	0.70	0.70	0.76
15105.00	5.03	0.65	1.91	2.03	1.06	0.84	0.84	0.96
15190.00	5.08	0.74	2.00	1.96	1.06	0.94	0.94	0.90
15275.00	5.13	1.09	2.35	2.01	1.06	1.28	1.28	0.94
15360.00	5.18	0.52	1.78	2.02	1.06	0.72	0.72	0.96
15445.00	5.23	0.74	2.00	2.03	1.06	0.94	0.94	0.97
15530.00	5.28	0.69	1.95	1.92	1.06	0.90	0.90	0.87
15710.00	5.33	0.82	2.08	2.01	1.06	1.02	1.02	0.95
15890.00	5.38	0.55	1.81	1.81	1.06	0.75	0.75	0.96
16070.00	5.43	0.96	2.22	2.22	1.07	1.15	1.15	1.15
16250.00	5.48	0.85	2.11	2.11	1.10	1.00	1.00	1.00
16430.00	5.53	0.54	1.80	1.80	1.14	0.67	0.67	0.67
16610.00	5.58	0.89	2.15	2.15	1.17	0.98	0.98	0.98
16726.15	5.63	0.99	2.25	2.25	1.19	1.05	1.05	1.05

17074.62	5.78	1.28	2.53	2.53	1.18	1.36	1.36	1.36
17190.77	5.83	1.25	2.51	2.51	1.16	1.35	1.35	1.35
17306.92	5.88	0.88	2.14	2.14	1.15	0.99	0.99	0.99
17423.08	5.93	0.93	2.19	2.19	1.15	1.04	1.04	1.04
17539.23	5.98	1.22	2.48	2.48	1.17	1.32	1.32	1.32
17655.38	6.03	1.16	2.42	2.42	1.19	1.24	1.24	1.24
17771.54	6.08	0.65	1.91	1.91	1.20	0.70	0.70	0.70
17887.69	6.13	0.38	1.64	1.64	1.22	0.42	0.42	0.42
18003.85	6.18	0.33	1.59	1.59	1.24	0.35	0.35	0.35
18120.00	6.23	0.81	2.07	2.07	1.24	0.84	0.84	0.84
18332.86	6.28	0.28	1.54	1.54	1.23	0.31	0.31	0.31
18545.71	6.33	0.59	1.85	1.85	1.21	0.64	0.64	0.64
18758.57	6.38	0.95	2.21	2.21	1.19	1.02	1.02	1.02
18971.43	6.43	0.73	1.99	1.99	1.17	0.81	0.81	0.81
19184.29	6.48	0.52	1.78	1.78	1.16	0.62	0.62	0.62
19397.14	6.53	1.13	2.39	2.39	1.16	1.24	1.24	1.24
19610.00	6.58	0.92	2.18	2.18	1.15	1.04	1.04	1.04
20390.00	6.83	0.89	2.15	2.15	1.19	0.96	0.96	0.96
20702.00	6.93	0.76	2.02	2.02	1.21	0.81	0.81	0.81
20858.00	6.98	0.98	2.24	2.24	1.22	1.02	1.02	1.02
21014.00	7.03	1.02	2.28	2.28	1.23	1.05	1.05	1.05
21170.00	7.08	1.34	2.60	2.60	1.22	1.38	1.38	1.38
22886.67	7.60	1.02	2.28	2.28	1.11	1.17	1.17	1.17
23040.00	7.65	1.05	2.31	2.31	1.13	1.18	1.18	1.18
23346.67	7.75	0.56	1.82	1.82	1.14	0.68	0.68	0.68
23500.00	7.80	0.82	2.08	2.08	1.10	0.97	0.97	0.97
23653.33	7.85	0.65	1.91	1.91	1.06	0.85	0.85	0.85
23806.67	7.90	0.91	2.17	2.17	1.03	1.14	1.14	1.14
24152.50	8.00	0.80	2.06	2.06	1.09	0.96	0.96	0.96
24537.50	8.10	0.68	1.94	1.94	1.12	0.82	0.82	0.82
24635.11	9.08	0.68	1.94	1.94	1.11	0.83	0.83	0.83
24730.00	8.15	0.74	2.00	2.00	1.10	0.91	0.91	0.91
24922.50	8.20	1.24	2.50	2.50	1.09	1.41	1.41	1.41
25115.00	8.25	0.49	1.75	1.75	1.10	0.65	0.65	0.65
25307.50	8.30	1.18	2.44	2.44	1.11	1.33	1.33	1.33
25500.00	8.35	1.10	2.36	2.36	1.10	1.26	1.26	1.26
25808.33	8.40	0.62	1.88	1.88	1.11	0.77	0.77	0.77

Cal yr BP	Depth (mbsf)	N. dutertrei $\delta^{18}\text{O}$	N. dutertrei $\delta^{18}\text{O}$ (normalised)	Smoothed N. dutertrei $\delta^{18}\text{O}$ (normalised)	$\delta^{18}\text{O}$ (GIV effect)	N. dutertrei $\Delta\delta^{18}\text{O}$ ($\delta^{18}\text{O}$ - GIV effect)	N. dutertrei $\Delta\delta^{18}\text{O}$ (normalised)	Smoothed N. dutertrei $\Delta\delta^{18}\text{O}$ (normalised)
26116.67	8.45	1.29	2.54	2.54	1.15	1.39	1.39	1.39
26425.00	8.50	1.03	2.29	2.29	1.12	1.17	1.17	1.17
26733.33	8.55	1.00	2.26	2.26	1.09	1.17	1.17	1.17
27350.00	8.65	0.90	2.16	2.16	1.01	1.15	1.15	1.15
27662.50	8.80	0.91	2.16	2.16	0.96	1.20	1.20	1.20
27870.83	8.90	0.90	2.16	2.16	0.98	1.18	1.18	1.18
27975.00	8.95	0.65	1.91	1.91	1.00	0.91	0.91	0.91
28037.50	8.98	0.76	2.02	2.02	1.01	1.01	1.01	1.01
28599.00	9.25	0.71	1.97	1.97	1.03	0.94	0.94	0.94
28799.00	9.34	0.95	2.21	2.21	1.00	1.21	1.21	1.21
29622.53	9.60	0.50	1.76	1.76	0.94	0.82	0.82	0.82
30034.29	9.70	0.62	1.88	1.88	0.90	0.97	0.97	0.97
30446.06	9.77	0.53	1.79	1.79	0.88	0.91	0.91	0.91
30940.18	10.00	0.82	2.08	2.08	0.90	1.18	1.18	1.18
31492.31	10.10	0.53	1.79	1.79	0.80	0.98	0.98	0.98
31599.00	10.13	0.61	1.87	1.87	0.80	1.06	1.06	1.06
31682.76	10.15	0.93	2.19	2.19	0.80	1.38	1.38	1.38
31889.66	10.20	0.87	2.13	2.13	0.80	1.33	1.33	1.33
32096.55	10.25	0.83	2.09	2.09	0.80	1.29	1.29	1.29
32253.55	10.29	0.62	1.88	1.88	0.80	1.08	1.08	1.08
32303.45	10.30	0.76	2.02	2.02	0.80	1.22	1.22	1.22
32510.34	10.35	0.89	2.15	2.15	0.80	1.36	1.36	1.36
32717.24	10.40	0.72	1.97	1.97	0.79	1.19	1.19	1.19
32799.00	10.42	0.76	2.02	2.02	0.78	1.24	1.24	1.24
32920.00	10.45	0.81	2.06	2.06	0.75	1.31	1.31	1.31
33040.00	10.48	0.77	2.03	2.03	0.73	1.30	1.30	1.30
33199.00	10.51	0.53	1.79	1.79	0.71	1.08	1.08	1.08
33599.00	10.62	0.55	1.81	1.81	0.76	1.05	1.05	1.05
33960.54	10.82	0.77	2.03	2.03	0.78	1.25	1.25	1.25
34322.08	11.02	0.74	2.00	2.00	0.80	1.19	1.19	1.19
34683.62	11.22	0.52	1.78	1.78	0.82	0.95	0.95	0.95
35045.15	11.42	0.57	1.83	1.83	0.89	0.94	0.94	0.94
35551.31	11.78	0.64	1.90	1.90	0.80	1.11	1.11	1.11
35949.00	12.00	0.35	1.61	1.61	0.74	0.87	0.87	0.87
36269.31	12.27	0.38	1.64	1.64	0.89	0.75	0.75	0.75
36589.63	12.47	0.34	1.60	1.60	0.91	0.69	0.69	0.69
36909.94	12.67	0.17	1.43	1.43	0.79	0.64	0.64	0.64

37230.25	12.89	0.56	1.82	1.82	0.69	1.13	1.13	1.13
37550.56	13.02	0.51	1.77	1.77	0.66	1.10	1.10	1.10
37999.00	13.27	0.48	1.74	1.74	0.71	1.03	1.03	1.03
38991.16	13.49	0.48	1.73	1.73	0.68	1.05	1.05	1.05
39893.12	13.69	0.49	1.75	1.75	0.64	1.11	1.11	1.11
	Cal yr BP							
	Depth (mbsf)							
	N. dutertrei $\delta^{18}\text{O}$							
	N. dutertrei $\delta^{18}\text{O}$ (normalised)							
	Smoothed N. dutertrei $\delta^{18}\text{O}$ (normalised)							
	$\delta^{18}\text{O}$ (GIV effect)							
	N. dutertrei $\Delta\delta^{18}\text{O}$ ($\delta^{18}\text{O}$ - GIV effect)							
	N. dutertrei $\Delta\delta^{18}\text{O}$ (normalised)							
	Smoothed N. dutertrei $\Delta\delta^{18}\text{O}$ (normalised)							

Appendix 5: *G. truncatulinoides*

Cal yr BP	Depth (mbsf)	G. truncatulinoides $\delta^{18}\text{O}$	G. truncatulinoides $\delta^{18}\text{O}$ (normalised)	Smoothed G. truncatulinoides $\delta^{18}\text{O}$ (normalised)	$\delta^{18}\text{O}$ (GIV effect)	G. truncatulinoides $\Delta\delta^{18}\text{O}$ ($\delta^{18}\text{O}$ - GIV effect)	G. truncatulinoides $\Delta\delta^{18}\text{O}$ (normalised)	Smoothed G. truncatulinoides $\Delta\delta^{18}\text{O}$ (normalised)
89.42	0.01	1.92	0.00	0	0.00	1.92	0.00	0
177.84	0.02	0.31	-1.61	-0.67	0.00	0.31	-1.61	-0.67
354.68	0.04	1.51	-0.41	-0.63	0.01	1.50	-0.42	-0.64
708.37	0.08	2.04	0.12	-0.20	0.01	2.03	0.12	-0.21
796.79	0.09	1.59	-0.33	-0.51	0.01	1.58	-0.34	-0.52
1415.74	0.18	0.61	-1.31	-0.80	0.02	0.59	-1.33	-0.82
1504.16	0.19	1.15	-0.77	-1.07	0.02	1.13	-0.79	-1.09
1592.58	0.20	0.79	-1.13	-0.78	0.02	0.77	-1.15	-0.81
1679.00	0.21	1.47	-0.45	-0.70	0.02	1.44	-0.47	-0.72
1681.00	0.21	1.40	-0.52	-0.67	0.02	1.37	-0.54	-0.70
1785.38	0.23	0.87	-1.05	-0.84	0.03	0.84	-1.07	-0.86
1992.13	0.24	0.98	-0.94	-0.80	0.03	0.95	-0.97	-0.83
1994.13	0.24	1.52	-0.40	-0.58	0.03	1.49	-0.43	-0.60
2098.50	0.25	1.54	-0.38	-0.61	0.03	1.51	-0.41	-0.64
2200.88	0.26	0.88	-1.04	-1.06	0.03	0.85	-1.07	-1.09
2202.88	0.26	0.15	-1.77	-1.67	0.03	0.12	-1.80	-1.70
2306.00	0.27	-0.28	-2.20	-1.82	0.04	-0.32	-2.23	-1.85
2307.25	0.27	0.43	-1.49	-1.74	0.04	0.40	-1.52	-1.78
2409.63	0.28	0.38	-1.54	-1.12	0.04	0.35	-1.57	-1.15
2411.63	0.28	1.59	-0.33	-0.71	0.04	1.55	-0.36	-0.75
2516.00	0.29	1.65	-0.27	-0.95	0.04	1.61	-0.31	-0.99
2618.38	0.30	-0.33	-2.25	-1.43	0.04	-0.37	-2.29	-1.47
2620.38	0.30	-0.30	-2.22	-1.57	0.04	-0.34	-2.26	-1.61
2724.75	0.31	1.20	-0.72	-1.80	0.04	1.15	-0.76	-1.84
2828.13	0.32	-0.54	-2.46	-1.33	0.04	-0.59	-2.51	-1.37
3035.88	0.34	1.12	-0.80	-1.61	0.05	1.07	-0.84	-1.66
3141.25	0.35	0.34	-1.58	-1.43	0.05	0.29	-1.63	-1.47
3244.63	0.36	0.02	-1.90	-1.83	0.05	-0.03	-1.95	-1.88
3245.63	0.36	-0.09	-2.01	-2.22	0.05	-0.15	-2.06	-2.26
3687.33	0.39	-0.81	-2.73	-1.92	0.05	-0.86	-2.78	-1.97
4024.67	0.41	0.90	-1.02	-1.92	0.04	0.86	-1.06	-1.96
4192.33	0.42	-0.10	-2.02	-1.50	0.04	-0.14	-2.06	-1.54
4193.33	0.42	0.47	-1.45	-1.88	0.04	0.43	-1.49	-1.92
4362.00	0.43	-0.24	-2.16	-1.78	0.04	-0.29	-2.21	-1.82
4530.67	0.44	0.21	-1.71	-1.78	0.05	0.16	-1.76	-1.83
4698.33	0.45	0.45	-1.47	-1.51	0.06	0.39	-1.53	-1.56

APPENDICES

4699.33	0.45	G. truncatulinoides $\delta^{18}\text{O}$	-1.35	G. truncatulinoides $\delta^{18}\text{O}$ (normalised)	-1.63	Smoothed G. truncatulinoides $\delta^{18}\text{O}$ (normalised)	0.06	$\delta^{18}\text{O}$ (GIV effect)	0.51	G. truncatulinoides $\Delta\delta^{18}\text{O}$ ($\delta^{18}\text{O}$ - GIV effect)	-1.41	G. truncatulinoides $\Delta\delta^{18}\text{O}$ (normalised)	-1.69	Smoothed G. truncatulinoides $\Delta\delta^{18}\text{O}$ (normalised)
4868.00	0.46	-0.15	-2.07	-1.74	0.06	-0.21	-2.13	-1.80						
5035.67	0.47	0.12	-1.80	-2.01	0.06	0.06	-1.86	-2.07						
5036.67	0.47	-0.25	-2.16	-1.75	0.06	-0.30	-2.22	-1.80						
5204.33	0.48	0.65	-1.27	-1.95	0.06	0.59	-1.33	-2.01						
5205.33	0.48	-0.50	-2.42	-2.04	0.06	-0.56	-2.48	-2.10						
5374.00	0.49	-0.50	-2.42	-2.08	0.06	-0.56	-2.48	-2.14						
5541.67	0.50	0.51	-1.40	-1.87	0.06	0.45	-1.47	-1.93						
5710.33	0.51	0.14	-1.78	-1.55	0.07	0.07	-1.85	-1.61						
5711.33	0.51	0.47	-1.45	-1.64	0.07	0.40	-1.52	-1.71						
5880.00	0.52	0.23	-1.69	-1.53	0.07	0.16	-1.76	-1.60						
6046.36	0.53	0.48	-1.44	-1.55	0.09	0.39	-1.53	-1.64						
6211.73	0.54	0.41	-1.51	-1.67	0.12	0.29	-1.63	-1.79						
6212.73	0.54	-0.15	-2.07	-1.71	0.13	-0.27	-2.19	-1.84						
6379.09	0.55	0.37	-1.55	-0.90	0.14	0.23	-1.69	-1.03						
6544.45	0.56	2.85	0.93	0.12	0.14	2.71	0.79	-0.02						
6710.82	0.57	2.89	0.97	0.03	0.14	2.76	0.84	-0.11						
6711.82	0.57	0.10	-1.82	-0.96	0.14	-0.04	-1.96	-1.10						
6878.18	0.58	-0.12	-2.04	-1.83	0.13	-0.25	-2.17	-1.96						
7043.55	0.59	0.28	-1.63	-1.69	0.12	0.16	-1.76	-1.81						
7044.55	0.59	0.53	-1.39	-1.47	0.12	0.41	-1.51	-1.59						
7209.91	0.60	0.54	-1.38	-1.69	0.12	0.42	-1.50	-1.81						
7210.91	0.60	-0.37	-2.29	-1.81	0.12	-0.49	-2.41	-1.93						
7377.27	0.61	0.17	-1.74	-1.88	0.14	0.04	-1.88	-2.01						
7542.64	0.62	0.33	-1.59	-1.72	0.16	0.17	-1.75	-1.87						
7543.64	0.62	0.10	-1.82	-1.66	0.16	-0.06	-1.97	-1.82						
7709.00	0.63	0.36	-1.56	-1.62	0.18	0.18	-1.74	-1.79						
7710.00	0.63	0.42	-1.50	-1.64	0.18	0.24	-1.67	-1.82						
7890.91	0.64	0.06	-1.86	-1.66	0.19	-0.13	-2.05	-1.85						
8071.82	0.65	0.30	-1.62	-1.72	0.19	0.10	-1.82	-1.92						
8206.50	0.65	0.24	-1.68	-1.68	0.22	0.02	-1.90	-1.89						
8252.73	0.66	0.19	-1.73	-1.56	0.22	-0.03	-1.95	-1.78						
8433.64	0.67	0.66	-1.26	-1.48	0.24	0.42	-1.49	-1.71						
8455.25	0.66	0.48	-1.44	-1.47	0.24	0.24	-1.68	-1.72						
8614.55	0.68	0.20	-1.72	-1.59	0.25	-0.06	-1.98	-1.86						
8952.75	0.69	0.30	-1.62	-1.63	0.32	-0.02	-1.94	-1.92						
8976.36	0.70	0.39	-1.53	-1.62	0.32	0.07	-1.85	-1.94						

APPENDICES

9157.27	0.71	0.21	-1.71	-1.58	0.33	-0.13	-2.05	-1.91
9338.18	0.72	0.44	-1.48	-1.60	0.35	0.08	-1.83	-1.95
9450.25	0.73	0.33	-1.59	-1.49	0.37	-0.04	-1.96	-1.86
9519.09	0.73	0.51	-1.41	-1.57	0.38	0.13	-1.79	-1.96
9699.00	0.74	0.22	-1.70	-1.56	0.44	-0.22	-2.14	-1.98
9700.00	0.74	0.34	-1.58	-1.66	0.44	-0.10	-2.02	-2.12
9830.91	0.75	0.21	-1.71	-1.56	0.48	-0.27	-2.19	-2.04
9961.82	0.76	0.52	-1.40	-1.61	0.52	-0.01	-1.92	-2.13
10091.73	0.77	0.19	-1.73	-1.47	0.54	-0.35	-2.27	-2.00
10092.73	0.77	0.64	-1.28	-1.43	0.54	0.10	-1.82	-1.97
10223.64	0.78	0.65	-1.27	-1.42	0.55	0.11	-1.81	-1.97
10353.55	0.79	0.19	-1.72	-1.45	0.56	-0.36	-2.28	-2.00
10354.55	0.79	0.57	-1.35	-1.39	0.56	0.01	-1.91	-1.95
10485.45	0.80	0.82	-1.10	-1.41	0.57	0.25	-1.67	-1.98
10615.36	0.81	0.14	-1.78	-1.33	0.58	-0.45	-2.36	-1.91
10616.36	0.81	0.81	-1.11	-1.36	0.58	0.23	-1.69	-1.95
10747.27	0.82	0.74	-1.18	-1.30	0.60	0.13	-1.78	-1.91
10877.18	0.83	0.30	-1.62	-1.60	0.63	-0.33	-2.25	-2.22
10878.18	0.83	-0.07	-1.99	-1.72	0.63	-0.70	-2.62	-2.36
11008.09	0.84	0.37	-1.55	-1.52	0.66	-0.29	-2.21	-2.16
11009.09	0.84	0.90	-1.02	-1.36	0.66	0.25	-1.67	-2.03
11139.00	0.85	0.39	-1.53	-1.29	0.69	-0.30	-2.21	-1.98
11439.00	0.87	0.58	-1.34	-1.36	0.73	-0.15	-2.06	-2.07
11440.00	0.87	0.71	-1.21	-1.34	0.73	-0.01	-1.93	-2.08
11739.00	0.89	0.43	-1.49	-1.36	0.75	-0.31	-2.23	-2.10
11740.00	0.89	0.54	-1.38	-1.38	0.75	-0.21	-2.12	-2.13
11776.50	0.90	0.63	-1.29	-1.07	0.75	-0.12	-2.04	-1.82
11777.50	0.90	1.39	-0.53	-0.84	0.75	0.63	-1.29	-1.59
11851.50	0.92	1.22	-0.70	-0.60	0.76	0.46	-1.46	-1.36
11889.00	0.93	1.36	-0.56	-0.59	0.77	0.58	-1.33	-1.36
11894.29	0.95	1.42	-0.50	-0.47	0.77	0.64	-1.27	-1.24
11897.82	0.96	1.58	-0.34	-0.33	0.77	0.81	-1.11	-1.10
11955.68	0.98	1.78	-0.14	-0.21	0.78	1.00	-0.92	-0.99
12043.24	1.00	1.76	-0.16	-0.40	0.79	0.96	-0.95	-1.19
12059.00	1.01	1.01	-0.91	-0.80	0.79	0.22	-1.69	-1.59
12108.92	1.03	0.59	-1.33	-0.74	0.79	-0.20	-2.12	-1.54
12196.49	1.07	1.44	-0.48	-0.97	0.80	0.64	-1.28	-1.78

APPENDICES

12284.05	1.11	1.08	-0.84	-0.93	0.83	0.25	-1.67	-1.75
12299.00	1.20	0.64	-1.28	-0.81	0.84	-0.20	-2.11	-1.66
12415.41	1.17	1.21	-0.71	-0.86	0.88	0.33	-1.59	-1.74
12499.00	1.25	1.16	-0.76	-0.77	0.91	0.26	-1.66	-1.67
12546.76	1.23	1.20	-0.72	-0.70	0.92	0.28	-1.64	-1.62
12634.32	1.27	1.53	-0.39	-0.74	0.94	0.59	-1.33	-1.67
12699.00	1.30	0.98	-0.94	-0.84	0.94	0.04	-1.88	-1.77
12701.09	1.32	1.01	-0.91	-0.92	0.94	0.07	-1.85	-1.86
12704.36	1.38	0.68	-1.24	-1.10	0.94	-0.26	-2.18	-2.04
12704.45	1.40	0.78	-1.14	-1.10	0.94	-0.16	-2.08	-2.04
12706.55	1.42	0.66	-1.26	-1.12	0.94	-0.28	-2.20	-2.05
12707.18	1.45	0.95	-0.97	-0.99	0.94	0.01	-1.91	-1.93
12709.82	1.48	0.95	-0.97	-0.85	0.94	0.01	-1.91	-1.79
12709.91	1.50	1.32	-0.60	-0.76	0.94	0.38	-1.53	-1.70
12712.55	1.53	1.47	-0.45	-0.66	0.94	0.53	-1.39	-1.60
12715.27	1.58	1.08	-0.84	-0.72	0.94	0.14	-1.77	-1.66
12718.00	1.63	1.46	-0.46	-0.72	0.94	0.52	-1.40	-1.66
12718.09	1.65	0.67	-1.25	-0.74	0.94	-0.27	-2.19	-1.68
12720.73	1.68	1.33	-0.59	-0.72	0.94	0.39	-1.53	-1.66
12723.55	1.75	1.35	-0.57	-0.84	0.94	0.41	-1.51	-1.77
12726.18	1.78	1.20	-0.72	-0.64	0.94	0.26	-1.66	-1.58
12728.91	1.83	0.87	-1.05	-0.56	0.94	-0.07	-1.99	-1.50
12729.00	1.85	1.63	-0.29	-0.44	0.94	0.69	-1.23	-1.38
12732.40	1.88	1.73	-0.19	-0.29	0.94	0.79	-1.13	-1.23
12736.40	1.93	1.97	0.05	-0.15	0.94	1.03	-0.89	-1.09
12737.33	1.95	1.96	0.04	-0.08	0.94	1.02	-0.90	-1.02
12740.40	1.98	1.55	-0.37	-0.13	0.94	0.61	-1.30	-1.07
12745.67	2.06	1.99	0.07	-0.17	0.94	1.05	-0.86	-1.11
12748.40	2.08	1.48	-0.44	-0.18	0.94	0.54	-1.38	-1.12
12751.81	2.13	1.77	-0.15	-0.22	0.94	0.83	-1.09	-1.16
12754.82	2.18	1.89	-0.03	-0.32	0.94	0.95	-0.97	-1.26
12757.83	2.23	1.35	-0.57	-0.34	0.94	0.41	-1.51	-1.28
12760.84	2.28	1.50	-0.42	-0.55	0.94	0.56	-1.36	-1.49
12763.86	2.33	1.39	-0.53	-0.62	0.94	0.45	-1.47	-1.56
12766.87	2.38	0.70	-1.22	-0.78	0.94	-0.24	-2.16	-1.71
12769.22	2.46	1.58	-0.34	-0.77	0.94	0.64	-1.28	-1.71
12769.88	2.43	0.55	-1.37	-0.70	0.94	-0.39	-2.30	-1.64

Cal yr BP	Depth (mbsf)	G. truncatulinoides $\delta^{18}\text{O}$	G. truncatulinoides $\delta^{18}\text{O}$ (normalised)	Smoothed G. truncatulinoides $\delta^{18}\text{O}$ (normalised)	$\delta^{18}\text{O}$ (GIV effect)	G. truncatulinoides $\Delta\delta^{18}\text{O}$ ($\delta^{18}\text{O}$ - GIV effect)	G. truncatulinoides $\Delta\delta^{18}\text{O}$ (normalised)	Smoothed G. truncatulinoides $\Delta\delta^{18}\text{O}$ (normalised)
12772.89	2.48	1.51	-0.41	-0.52	0.94	0.57	-1.35	-1.46
12775.90	2.53	1.75	-0.17	-0.79	0.94	0.81	-1.11	-1.73
12779.90	2.59	1.60	-0.32	-0.62	0.94	0.66	-1.26	-1.56
12781.93	2.63	0.24	-1.68	-0.76	0.94	-0.70	-2.62	-1.69
12785.52	2.69	1.41	-0.51	-0.86	0.94	0.47	-1.45	-1.80
12787.95	2.73	0.82	-1.10	-0.82	0.94	-0.12	-2.04	-1.76
12790.96	2.78	1.24	-0.68	-0.59	0.94	0.30	-1.62	-1.53
12791.13	2.79	1.80	-0.12	-0.53	0.94	0.86	-1.06	-1.47
12793.98	2.83	1.39	-0.52	-0.39	0.94	0.45	-1.46	-1.33
12796.75	2.89	1.69	-0.23	-0.31	0.94	0.75	-1.17	-1.25
12796.99	2.88	1.54	-0.38	-0.41	0.94	0.60	-1.32	-1.35
12885.59	2.98	1.64	-0.28	-0.27	0.95	0.69	-1.23	-1.22
13056.78	3.08	1.30	-0.62	-0.28	0.96	0.35	-1.57	-1.23
13080.48	3.10	2.08	0.16	-0.23	0.96	1.12	-0.80	-1.19
13142.37	3.13	1.64	-0.27	-0.28	0.97	0.68	-1.24	-1.25
13227.97	3.18	1.81	-0.11	-0.15	0.97	0.84	-1.08	-1.12
13246.05	3.20	1.35	-0.57	-0.18	0.97	0.37	-1.54	-1.15
13313.56	3.23	1.98	0.06	-0.26	0.98	1.00	-0.92	-1.24
13399.15	3.28	1.91	-0.01	-0.24	0.98	0.93	-0.99	-1.23
13411.62	3.30	1.24	-0.68	-0.04	0.99	0.26	-1.66	-1.03
13484.75	3.33	1.90	-0.02	-0.18	0.99	0.90	-1.01	-1.17
13570.34	3.38	2.35	0.43	-0.24	1.00	1.35	-0.57	-1.24
13577.20	3.40	1.33	-0.59	-0.26	1.00	0.33	-1.59	-1.26
13655.93	3.43	1.58	-0.34	-0.48	1.00	0.58	-1.34	-1.48
13741.53	3.48	1.14	-0.78	-0.61	1.01	0.13	-1.79	-1.62
13742.77	3.49	0.83	-1.09	-0.56	1.01	-0.18	-2.10	-1.57
13846.20	3.58	1.67	-0.25	-0.68	1.02	0.65	-1.27	-1.69
13850.43	3.58	1.59	-0.33	-0.76	1.02	0.58	-1.34	-1.77
13884.13	3.63	0.98	-0.94	-0.54	1.02	-0.04	-1.96	-1.56
13914.40	3.69	0.74	-1.18	-0.64	1.02	-0.28	-2.20	-1.66
13917.83	3.68	1.90	-0.02	-0.71	1.02	0.88	-1.04	-1.73
13951.52	3.73	1.18	-0.74	-0.70	1.03	0.15	-1.76	-1.73
13970.20	3.78	1.24	-0.68	-0.74	1.03	0.21	-1.71	-1.77
13985.22	3.78	1.02	-0.90	-0.81	1.03	0.00	-1.92	-1.84
14018.91	3.83	0.56	-1.36	-0.76	1.03	-0.47	-2.39	-1.79
14032.20	3.86	1.53	-0.39	-0.93	1.03	0.50	-1.42	-1.96
14086.30	3.93	1.43	-0.49	-1.10	1.03	0.40	-1.52	-2.13

14120.00	3.98	0.40	-1.52	-0.97	1.03	-0.63	-2.55	-2.00
14207.50	4.03	0.16	-1.76	-1.00	1.03	-0.87	-2.79	-2.03
14245.00	4.07	1.23	-0.69	-0.95	1.03	0.20	-1.72	-1.98
14295.00	4.08	1.38	-0.54	-0.71	1.03	0.35	-1.57	-1.74
14350.00	4.13	1.68	-0.24	-0.54	1.03	0.64	-1.27	-1.57
14383.33	4.18	1.60	-0.32	-0.63	1.03	0.56	-1.36	-1.67
14450.00	4.28	1.01	-0.91	-0.76	1.03	-0.02	-1.94	-1.79
14483.33	4.33	0.76	-1.16	-0.87	1.03	-0.27	-2.19	-1.90
14516.67	4.38	0.75	-1.17	-1.01	1.03	-0.29	-2.20	-2.04
14550.00	4.43	1.15	-0.77	-0.96	1.04	0.11	-1.80	-2.00
14616.67	4.53	0.87	-1.05	-0.85	1.04	-0.17	-2.09	-1.89
14650.00	4.58	1.26	-0.66	-0.78	1.04	0.22	-1.70	-1.82
14716.67	4.68	1.31	-0.61	-0.86	1.05	0.26	-1.66	-1.91
14783.33	4.78	1.11	-0.81	-0.81	1.05	0.06	-1.86	-1.86
14816.67	4.83	0.74	-1.18	-0.89	1.05	-0.32	-2.23	-1.95
14935.00	4.93	1.13	-0.79	-0.88	1.06	0.07	-1.85	-1.94
15020.00	4.98	0.85	-1.07	-0.87	1.06	-0.22	-2.14	-1.93
15105.00	5.03	1.35	-0.57	-0.74	1.06	0.29	-1.63	-1.80
15190.00	5.08	1.19	-0.73	-0.67	1.06	0.12	-1.80	-1.73
15275.00	5.13	1.38	-0.54	-0.55	1.06	0.32	-1.60	-1.61
15360.00	5.18	1.49	-0.43	-0.53	1.06	0.43	-1.49	-1.59
15445.00	5.23	1.45	-0.47	-0.34	1.06	0.40	-1.52	-1.39
15530.00	5.28	1.42	-0.50	-0.35	1.06	0.37	-1.55	-1.41
15710.00	5.33	2.17	0.25	-0.28	1.06	1.12	-0.80	-1.36
16070.00	5.43	1.30	-0.62	-0.38	1.07	0.23	-1.69	-1.49
16610.00	5.58	1.84	-0.08	-0.38	1.17	0.67	-1.25	-1.52
16726.15	5.63	0.95	-0.97	-0.97	1.19	-0.24	-2.16	-2.16
17074.62	5.78	1.42	-0.50	-0.50	1.18	0.24	-1.68	-1.68
17190.77	5.83	1.33	-0.59	-0.59	1.16	0.17	-1.74	-1.74
17306.92	5.88	1.68	-0.24	-0.24	1.15	0.53	-1.39	-1.39
17423.08	5.93	1.26	-0.66	-0.66	1.15	0.11	-1.81	-1.81
17539.23	5.98	1.37	-0.55	-0.55	1.17	0.20	-1.72	-1.72
17655.38	6.03	1.96	0.04	0.04	1.19	0.77	-1.15	-1.15
17771.54	6.08	2.08	0.16	0.16	1.20	0.88	-1.04	-1.04
17887.69	6.13	2.23	0.31	0.31	1.22	1.01	-0.91	-0.91
18003.85	6.18	2.06	0.14	0.14	1.24	0.82	-1.10	-1.10
18120.00	6.23	2.08	0.16	0.16	1.24	0.84	-1.08	-1.08

Cal yr BP	Depth (mbsf)	G. truncatulinoides $\delta^{18}\text{O}$	G. truncatulinoides $\delta^{18}\text{O}$ (normalised)	Smoothed G. truncatulinoides $\delta^{18}\text{O}$ (normalised)	$\delta^{18}\text{O}$ (GIV effect)	G. truncatulinoides $\Delta\delta^{18}\text{O}$ ($\delta^{18}\text{O}$ - GIV effect)	G. truncatulinoides $\Delta\delta^{18}\text{O}$ (normalised)	Smoothed G. truncatulinoides $\Delta\delta^{18}\text{O}$ (normalised)
18332.86	6.28	2.30	0.38	0.38	1.23	1.07	-0.85	-0.85
18758.57	6.38	2.73	0.81	0.81	1.19	1.54	-0.38	-0.38
18971.43	6.43	1.88	-0.04	-0.04	1.17	0.71	-1.21	-1.21
19184.29	6.48	2.08	0.16	0.16	1.16	0.92	-1.00	-1.00
19397.14	6.53	1.88	-0.04	-0.04	1.16	0.72	-1.19	-1.19
19610.00	6.58	1.66	-0.25	-0.25	1.15	0.52	-1.40	-1.40
20390.00	6.83	1.44	-0.48	-0.48	1.19	0.26	-1.66	-1.66
20702.00	6.93	2.21	0.29	0.29	1.21	1.00	-0.92	-0.92
20858.00	6.98	1.57	-0.35	-0.35	1.22	0.34	-1.57	-1.57
21014.00	7.03	1.61	-0.31	-0.31	1.23	0.38	-1.53	-1.53
21170.00	7.08	2.29	0.37	0.37	1.22	1.06	-0.86	-0.86
21390.00	7.13	2.02	0.10	0.10	1.22	0.80	-1.12	-1.12
21660.00	7.20	2.28	0.36	0.36	1.22	1.06	-0.86	-0.86
22886.67	7.60	1.24	-0.68	-0.68	1.11	0.13	-1.79	-1.79
23040.00	7.65	1.01	-0.91	-0.91	1.13	-0.12	-2.04	-2.04
23193.33	7.70	1.46	-0.46	-0.46	1.15	0.30	-1.61	-1.61
23346.67	7.75	1.44	-0.48	-0.48	1.14	0.30	-1.62	-1.62
23500.00	7.80	1.38	-0.54	-0.54	1.10	0.27	-1.64	-1.64
23653.33	7.85	1.83	-0.09	-0.09	1.06	0.77	-1.15	-1.15
23806.67	7.90	2.38	0.46	0.46	1.03	1.35	-0.57	-0.57
23960.00	7.95	1.93	0.01	0.01	1.05	0.88	-1.04	-1.04
24152.50	8.00	2.05	0.13	0.13	1.09	0.96	-0.96	-0.96
24537.50	8.10	0.90	-1.02	-1.02	1.12	-0.22	-2.14	-2.14
24635.11	8.13	1.38	-0.54	-0.54	1.11	0.27	-1.65	-1.65
24730.00	8.15	2.40	0.48	0.48	1.10	1.31	-0.61	-0.61
24922.50	8.20	2.22	0.30	0.30	1.09	1.13	-0.78	-0.78
25115.00	8.25	1.67	-0.25	-0.25	1.10	0.57	-1.35	-1.35
25307.50	8.30	2.15	0.23	0.23	1.11	1.05	-0.87	-0.87
25500.00	8.35	2.22	0.30	0.30	1.10	1.12	-0.80	-0.80
25808.33	8.40	2.15	0.23	0.23	1.11	1.04	-0.88	-0.88
26116.67	8.45	1.78	-0.14	-0.14	1.15	0.63	-1.29	-1.29
26425.00	8.50	2.45	0.53	0.53	1.12	1.33	-0.59	-0.59
26733.33	8.55	2.64	0.72	0.72	1.09	1.55	-0.37	-0.37
27350.00	8.65	2.65	0.73	0.73	1.01	1.64	-0.28	-0.28
27662.50	8.80	2.49	0.57	0.57	0.96	1.53	-0.39	-0.39
27870.83	8.90	2.40	0.48	0.48	0.98	1.42	-0.50	-0.50
28037.50	8.98	2.33	0.41	0.41	1.01	1.32	-0.60	-0.60

Cal yr BP	Depth (mbsf)	G. truncatulinoides $\delta^{18}\text{O}$	G. truncatulinoides $\delta^{18}\text{O}$ (normalised)	Smoothed G. truncatulinoides $\delta^{18}\text{O}$ (normalised)	$\delta^{18}\text{O}$ (GIV effect)	G. truncatulinoides $\Delta\delta^{18}\text{O}$ ($\delta^{18}\text{O}$ - GIV effect)	G. truncatulinoides $\Delta\delta^{18}\text{O}$ (normalised)	Smoothed G. truncatulinoides $\Delta\delta^{18}\text{O}$ (normalised)
28799.00	9.34	2.17	0.25	0.25	1.00	1.18	-0.74	-0.74
30034.29	9.70	1.81	-0.11	-0.11	0.90	0.91	-1.01	-1.01
30446.06	9.77	2.01	0.09	0.09	0.88	1.14	-0.78	-0.78
30940.18	10.00	1.80	-0.12	-0.12	0.90	0.90	-1.02	-1.02
31492.31	10.10	1.01	-0.91	-0.91	0.80	0.20	-1.71	-1.71
31599.00	10.13	2.30	0.38	0.38	0.80	1.50	-0.42	-0.42
31682.76	10.15	1.92	0.00	0.00	0.80	1.12	-0.80	-0.80
31889.66	10.20	2.78	0.86	0.86	0.80	1.97	0.05	0.05
32096.55	10.25	1.41	-0.51	-0.51	0.80	0.61	-1.31	-1.31
32253.55	10.29	1.64	-0.27	-0.27	0.80	0.84	-1.07	-1.07
32303.45	10.30	1.79	-0.13	-0.13	0.80	0.99	-0.93	-0.93
32510.34	10.35	1.56	-0.36	-0.36	0.80	0.76	-1.16	-1.16
32717.24	10.40	1.67	-0.25	-0.25	0.79	0.88	-1.03	-1.03
32799.00	10.42	1.67	-0.25	-0.25	0.78	0.89	-1.03	-1.03
32920.00	10.45	1.62	-0.30	-0.30	0.75	0.87	-1.05	-1.05
33040.00	10.48	2.18	0.26	0.26	0.73	1.45	-0.47	-0.47
33199.00	10.51	1.71	-0.21	-0.21	0.71	0.99	-0.93	-0.93
33599.00	10.62	1.83	-0.09	-0.09	0.76	1.07	-0.84	-0.84
33960.54	10.82	1.91	-0.01	-0.01	0.78	1.13	-0.79	-0.79
34322.08	11.02	1.45	-0.47	-0.47	0.80	0.64	-1.27	-1.27
34683.62	11.22	1.39	-0.53	-0.53	0.82	0.57	-1.35	-1.35
35045.15	11.42	1.58	-0.34	-0.34	0.89	0.68	-1.23	-1.23
35551.31	11.78	2.72	0.81	0.81	0.80	1.93	0.01	0.01
35949.00	12.00	1.77	-0.15	-0.15	0.74	1.03	-0.89	-0.89
36269.31	12.27	1.37	-0.55	-0.55	0.89	0.48	-1.44	-1.44
36589.63	12.47	1.41	-0.51	-0.51	0.91	0.50	-1.42	-1.42
36909.94	12.67	1.36	-0.56	-0.56	0.79	0.57	-1.35	-1.35
37230.25	12.89	1.79	-0.13	-0.13	0.69	1.09	-0.82	-0.82
37550.56	13.02	0.56	-1.36	-1.36	0.66	-0.11	-2.02	-2.02
37999.00	13.27	1.34	-0.58	-0.58	0.71	0.64	-1.28	-1.28
38991.16	13.49	1.84	-0.08	-0.08	0.68	1.16	-0.76	-0.76
39893.12	13.69	0.94	-0.98	-0.98	0.64	0.29	-1.63	-1.63